Structure, Magnetic and Dielectric properties study of some 3d/4f metal ions doped ZnO nanomaterials

Thesis submitted for the award of
Doctor of Philosophy (Science)
of
Jadavpur University
2022

By
Tanumoy Debnath
Department of Physics,
Jadavpur University,
Kolkata-700032,
India

Certificate from the Supervisors

This is to certify that the thesis entitled **"Structure, Magnetic and Dielectric properties study of some 3d/4f metal ions doped ZnO nanomaterials"** Submitted by Sri Tanumoy Debnath (Index No.: 136/19/Phys./26) who got his name registered on 14.11.2019 for the award of Ph. D. (Science) degree of Jadavpur University, is absolutely based upon his own work under the supervision of Prof. (Dr.) Sukhen Das, Professor, Department of Physics, Jadavpur University, Kolkata-700032 and Dr. Soumyaditya Sutradhar, Assistant Professor, Department of Physics, Jadavpur University, Kolkata-700032 that neither this thesis nor any part of it has been submitted for either any degree/diploma or any other academic award any where before.

Soumyaditya Sutradhar
16/03/2022

Dr. Soumyaditya Sutradhar
Assistant Professor
Department of Physics
Jadavpur University
Kolkata-700032, India

Dr. Soumyaditya Sutradhar
Assistant Professor
Department of Physics
Jadavpur University
Kolkata-700032

Sukhen Das

Prof. (Dr.) Sukhen Das 16/03/2022
Professor
Department of Physics
Jadavpur University
Kolkata- 700032, India

Prof. Sukhen Das
Department of Physics,
Jadavpur University
Kolkata-700032

Certificate of similarity check

This is to certify that the plagiarism checking for this thesis authored by Tanumoy Debnath has been performed using professional plagiarism prevention software iThenticate. According to the report generated after plagiarism checking there is 10% similarity in this thesis, which is in category "Level 0" (minor similarities) as per the "Promotion of Academic Integrity and Prevention of Plagiarism in Higher Educational Institutions Regulations, 2018" of the University Grant Commission (UGC) of India. The common knowledge or coincidental terms up to 10 (ten) consecutive words (as prescribed in the above said UGC Regulation up to 14 (fourteen) terms for such common knowledge or coincidental terms can be excluded) and own works of the candidate published in various peer-reviewed journals (those are attached in the thesis) are excluded from the similarity checking. It is certified that the present thesis submitted by Tanumoy Debnath is plagiarism free and he has followed standard norms of academic integrity and scientific ethics.

Soumyaditya Sutradhar
16/03/2022

Dr. Soumyaditya Sutradhar
Department of Physics,
Jadavpur University
Kolkata- 700032, India

Dr. Soumyaditya Sutradhar
Assistant Professor
Department of Physics
Jadavpur University
Kolkata-700032

Sukhen Das
16/03/2022

Prof. (Dr.) Sukhen Das
Department of Physics,
Jadavpur University
Kolkata- 700032, India

Prof. Sukhen Das
Department of Physics,
Jadavpur University
Kolkata-700032

DECLARATION

I declare that the matter described in the thesis entitled, **“Structure, Magnetic and Dielectric properties study of some 3d/4f metal ions doped ZnO nanomaterials”** is the result of investigation carried out by me at Department of Physics, Jadavpur University, Kol- 700032, India under the supervision of **Prof. (Dr.) Sukhen Das and Dr. Soumyaditya Sutradhar** and that it has not submitted elsewhere for the award of any degree or diploma.

I declare that this written document represents my ideas, in my own words and I have adhered to all principles of academic honesty and integrity and have not misrepresented or fabricated or falsified any idea/data/fact/source in my submission.

In keeping with the general practice in reporting scientific observations, due acknowledgement and citation has been made whenever the work described based on the findings of other investigators. Any omission that might have occurred by oversight or error of judgement is regretted.

Date: 16.03.2022

Tanumoy Debnath
....

Tanumoy Debnath
(Index No: 136/19/Phys./26)
Department of Physics,
Jadavpur University
Kolkata- 700032, India

Dedicated to:

My Beloved Parent, My Family

&

My Supervisors

For their endless Support and

Motivation

Acknowledgement

An execution of research work and writing a thesis is such an enormous job that it cannot be done alone. There are a few people alongside me who have contributed considerably for the fulfillment of this research work. If anybody gets curious aspect from my research work then it is not only me but also those who have participated to the present work.

The most important persons to be acknowledged are my honorable supervisors Prof. (Dr.) Sukhen Das, Professor, Department of Physics, Jadavpur University, Kolkata-700032, India and Dr. Soumyaditya Sutradhar, Assistant Professor, Department of Physics, Jadavpur University, Kolkata-700032, India (formerly affiliated in Department of Physics, Amity University, Kolkata-700135) for suggesting the problems in the field of semiconducting nanomaterials. They have guided and motivated me from time to time and have backed me a lot to fulfill my research work regardless of several difficulties in the way. I have truly enjoyed the friendly atmosphere of the laboratory. I am obligated to Dr. D. Das, Scientist G, UGC-DAE CSR, Kolkata, Dr. Atul Bandyopadhyay, Department of Physics, University of Gour Banga, Malda, West Bengal-732103, India and Dr. Abhik Sinha Mahapatra, Department of Physics, JIS University for furnishing me with various facilities during my research work in their respective laboratories.

I am also grateful to Mrs. Papiya Saha, Miss Nesla Patra, Mr. Tanmoy Chakraborty, Mr. Shivam Sharma, Mr. Koustav Das, Dr. Susmita Singh, Miss Suman Saha, Dr. Rama Ranjan Bhattacharjee in our group and all the co-researchers in our Department for their co-operation during the term of my work.

ACKNOWLEDGEMENT

I am cordially thankful to the authority of Department of Physics, Jadavpur University, Jadavpur, Kolkata-700032 for furnishing me with all kinds of facilities viz., Laboratory, Library, etc. which were mostly crucial for my work.

It would be impossible for me without Prof. (Dr.) Papiya Nandy, Dr. Ruma Basu and Dr. Alakananda Bhattacharya for their enormous cooperation, support and encouragement throughout my research period. I am also thankful to Dr. Arnab Ghosh, Dr. Sujan Ghosh, Dr. Subrata Kar, Dr. Niranjan Bala, Dr. Arpon Kool, Dr. Biplab Paul, Dr. Pradip Thakur, Dr. Noor Amin Haque and all my labmates specially Mr. Santanu Das, Mr. Shubham Roy, Miss. Souravi Bardhan, Dr. Dheeraj Mondal, Mrs. Silpa Maity, Miss Debbethi Bera, Mr. Debmalya Sarkar for their help and inspirations.

I must give my hearty respect and gratitude to my parents, who have braced me affectionately and financially throughout my life. The inspiration of my mother Mrs. Reba Debnath, my elder sister Mrs. Tanusree Nath and my better half Mrs. Mousumi Debnath played an important part during my research work. It was unfeasible to fulfill my research without their support. Finally, I want to acknowledge those people whose names I may be leaved out unintentionally.

Tanumoy Debnath

Tanumoy Debnath

Department of Physics,

Jadavpur University,

Kolkata-700032,

India

Chapter-1: Synopsis

Chapter-2: Experimental

Chapter-3: Optical, Magnetic and Dielectric Properties of Yttrium doped ZnO Nanorods Synthesized by Hydrothermal Method

Chapter-4: Dielectric property study of undoped and Chromium doped semiconducting ZnO nanorods

Chapter-5: Structural and ferromagnetic properties of Chromium doped ZnO nanomaterials

Chapter-6: Structural, morphological and charge transport properties study of Chromium doped ZnO nanomaterials

List of Published and Communicated papers

(1) Optical, magnetic and dielectric properties of ZnO:Y nanoparticles synthesized by hydrothermal Method.

Tanumoy Debnath, Sukhen Das, Dipankar Das, Soumyaditya Sutradhar.

Journal of Alloys and Compounds, 696 (2017)670-681.

(2) Hydrothermal process assists undoped and Cr-doped semiconducting ZnO nanorods: Frontier of Dielectric property.

Tanumoy Debnath, Papiya Saha, Nesla Patra, Sukhen Das, Soumyaditya Sutradhar.

Journal of Applied Physics, 123 (2018)194101.

(3) Influence of different Cr concentrations on the structural and ferromagnetic properties of ZnO nanomaterials prepared by hydrothermal synthesis route.

Tanumoy Debnath, Atul Bandyopadhyay, Tanmoy Chakraborty, Sukhen Das, Soumyaditya

Sutradhar.

Materials Research Bulletin, 118 (2019)110480.

(4) Modulation of structural, morphological and electrical charge transport property of Cr doped ZnO nanomaterials prepared by chemical process. (Communicated paper)

Tanumoy Debnath, Tanmoy Chakraborty, Atul Bandyopadhyay, Shivam Sharma, Abhik Sinha Mahapatra, Sukhen Das, Soumyaditya Sutradhar

(5) Site Selective Response of Cr^{3+} and Y^{3+} Cationic Dopants in Semiconducting ZnO Nanomaterials: Modulation of Optical, Dielectric and Magnetic Behaviors. (Communicated paper)

Tanumoy Debnath, Tanmoy Chakraborty, Atul Bandyopadhyay, Koustav Das, Susmita Singh, Suman Saha, Rama Ranjan Bhattacharjee, Sukhen Das, Soumyaditya Sutradhar.

(6) β-Phase improved Mn-Zn-Cu-ferrite-PVDF nanocomposite film: A metamaterial for enhanced microwave absorption.

Papiya Saha, Tanumoy Debnath, Sukhen Das, Souvik Chatterjee, Soumyaditya Sutradhar.

Materials Science and Engineering: B, 245 (2019) 17-29.

(7) Effect of hydrothermal synthesis on physical property modulation and biological activity of ZnO nanorods.

Soumyaditya Sutradhar, Atul Bandyopadhyay, Tanumoy Debnath, Tanmoy Chakraborty, Sukanta Majumdar, Shohini Chakraborty, Sukhen Das.

Materials Research Express, 6 (2019) 1250f7.

(8) Enhancement of EMI shielding effectiveness of flexible Co2U-type hexaferrite (Ba4Co2Fe36O60)-poly(vinylidene fluoride) heterostructure composite materials: An improved radar absorbing material to combat against electromagnetic pollution.

Tanmoy Chakraborty, Tanumoy Debnath, Somashree Bhowmick, Atul Bandyopadhyay, Arup Karmakar, Sukhen Das, Abhik Sinha Mahapatra, Soumyaditya Sutradhar.

Journal of Applied Physics,128 (2020) 095301.

(9) Fabrication of heterostructure composites of Ni-Zn-Cu-Ferrite-C3N4-Poly(vinylidene fluoride) films for the enhancement of electromagnetic interference shielding effectiveness.

Tanmoy Chakraborty, Shivam Sharma, Tanumoy Debnath, Abhik Sinha Mahapatra, Abhyavartin Selvam, Sandip Chakrabarti, Soumyaditya Sutradhar.

Chemical Engineering Journal, 420(2) (2021) 127683.

List of Figures

List of Tables

Abstract

The synthesis and study of nanomaterials have become a major rising area of research over the past few years. Semiconducting nanoparticles play a vital role in several latest technologies, which give rise to their potential applications in the fields of field emitters, photo detectors, nano lasers, light emitting diodes, chemical sensors, photo-electrodes and supercapacitors etc. One of the most popular topics of nanostructured materials is the transition metal ions/ rare earth ions doped ZnO nanoparticles. The synthesis process is a key factor for the doped ZnO nanoparticles considering the factors of quantum size effect and the position of dopant ions within the nanostructred ZnO. It is to be noted that several interesting phenomena like high luminescence quantum efficiency, shift and broadening of spectrum have been observed.

Influence of synthesis route on the morphology of the grain and there by modulation of different properties like optical, magnetic and dielectric of the undoped and doped semiconducting ZnO nanoparticles have been investigated in this research work. X-ray diffraction study exhibits that all the samples are polycrystalline in phase with hexagonal structure (wurtzite). FESEM analysis shows that all the nanomaterials are rod like structure. UV-Vis measurement reveals the remarkable control over the charge density of semiconducting host nanomaterial with the occupancy of dopant ions within the ZnO lattice structure. In photoluminescence spectra, sharp peaks have been observed in the UV region but no convincing peak has been detected in visible region. The synthesis mechanism dependent morphology and morphology oriented properties of all samples are the characteristic aspects of our research work. Till now this has not been used considerably by anyone else to modulate the dielectric properties. The dielectric property depending upon frequency as well as temperature of all samples has been investigated minutely. The well known, hydrothermal synthesis mechanism leverages the growth process of the nanomaterials favoring the rod like morphology and the co-precipitation synthesis method allows the growth mechanism of the nanoparticles mostly towards spherical in nature and the dopant influences the charge density, the defect density and the nature of defects within the structure of ZnO nanomaterials which have been suggested by the dielectric measurement. All the observation of semiconducting ZnO nanomaterials make it more productive for convenient applications in various magneto-dielectric appliances.

Different theoretical models introduced by various research groups have been presented in our work.

Soumyaditya Sutradhar
16/03/2022
Dr. Soumyaditya Sutradhar
Assistant Professor
Department of Physics
Jadavpur University

Tanumoy Debnath

Sukhen Das
16/03/2022
Prof. Sukhen Das
Department of Physics,
Jadavpur University
Kolkata-700032

Organization of the thesis

Chapter 1 gives an introduction and a brief literature review of the thesis. The novelty of our research work and the objective of the thesis are also provided in this chapter. All together, the doped ZnO systems are very much influential for leading electronic, optoelectronic, spintronic and quantum device fabrications.

Chapter 2 describes different preparation and characterization techniques used in this thesis. For the synthesis of undoped and doped ZnO nanoparticles, co-precipitation and hydrothermal synthesis method have been used. Mainly XRD and FESEM instrument have been used to characterize the synthesized nanoparticles and to study various properties of the nanomaterials, UV-VIS and PL spectroscopy, SQUID magnetometer and Dielectric measurement instrument have been used.

Chapter 3 discusses the optical, magnetic and dielectric properties of undoped and yttrium doped ZnO nanorods. Here, the structural parameters have been extracted from the XRD patterns. The synthesized nanoparticles are rodlike in nature. The optical property study shows that the doping may enhances the oxygen vacancies and intrinsic defects. So, these nanomaterials are suitable in various device applications.

Chapter 4 describes the dielectric property study of undoped and chromium doped ZnO nanorods. The increase in band gap with the decrease in particles size which has been observed for all the rodlike samples is called quantum confinement. Also, the high value of dielectric constant makes it useful in charge storage devices.

Chapter 5 addresses the structural and ferromagnetic properties of chromium doped ZnO nanoparticles. Here, the synthesis mechanism is considered to be favorable to produce lattice strain within the structure of the lattice to regulate the optical and magnetic properties. The oxygen vacancy defect plays the crucial role to increase the ferromagnetic ordering within the specimens.

Chapter 6 gives the structural, morphological and charge transport properties study of chromium doped ZnO nanomaterials. Here, synthesis mechanism dependent properties have been studied. The structural parameters of Cr-doped ZnO nanomaterial synthesized by co-precipitation and hydrothermal method have been calculated from Rietveld analysis. The dielectric constant of hydrothermally synthesized rod like nanomaterials is complementary to that of the spherical nanoparticles synthesized by co-precipitation method.

Chapter 7 addresses the reprint of the published papers.

Soumyaditya Sutradhar
16/03/2022

Dr. Soumyaditya Sutradhar
Assistant Professor
Department of Physics
Jadavpur University
Kolkata-700032

Sukhen Das
16/03/2022

Prof. Sukhen Das
Department of Physics,
Jadavpur University
Kolkata-700032

Tanumoy Debnath

CHAPTER 1

Synopsis

1.1 Introduction

In recent times, much attention has been given on the various properties like, optical, magnetic and dielectric of various cationic elements doped IV, III–V and II–VI semiconducting nanomaterials. ZnO is a known II-VI semiconducting material accompanying with a direct band energy gap of 3.37 eV and a large excitonic binding energy of 60 meV. It has also allured phenomenal interest of the researchers [1-3]. ZnO nanoparticles have been considered for research since the past decades, but the low-dimensional undoped and doped ZnO nanostructures like nanospheres, nanorods, nanowires, nanotubes, etc. have been focused enormously due to its new elementary physical properties along with many fascinating applications in future devices [4-7]. In this regard, transition metal (TM) ions and rare earth element (REE) ions doped ZnO nanostructures have attracted substantial attention as promising dilute magnetic semiconductor (DMS) due to the possibility of its band gap modulation, strong emission in the visible region, induced room temperature (RT) ferromagnetic ordering and enhanced dielectric behavior. All together, these doped ZnO systems are very much important and interesting materials for advanced optoelectronic, spintronic, electrical and quantum device applications [8-13].

1.2 Literature Review

Many articles, it also been reported that the existence of oxygen vacancies give rise to room temperature ferromagnetism within the doped ZnO nanoparticles [14]. Again, the dielectric property of the doped ZnO nanoparticles have been extremely organised due to the existence of indigenous defects designated as zinc vacancies, zinc interstitials, oxygen vacancies, dandling bond etc., by the result of a true selection of dopants as well as doping mechanism, which is the principal topic of our research. The undoped and doped ZnO nanomaterials have many other electrifying physical and chemical properties like large electron mobility, high chemical stability and excellent optical emission. These can be obtained by the appropriate choice of synthesis process among the standard method such as sol-gel method, co-precipitation method, hydrothermal method, solid state reaction method, mechanical milling method, pulsed laser deposition method, etc. [15-18].

Undoped and doped semiconducting ZnO nanoparticles, synthesized by the above synthesis mechanism are extremly relevent for photovoltaic and ultraviolet device applications like light-emitting diodes, photodetectors, nanolasers, chemical sensors, field emitters, supercapacitors and photoelectrodes, etc. [19-27]. More over the selection of the synthesis mechanism, the remarkable control over the several materialistic properties like conductivity, charge density and dielectric constant, etc., can be obtained by the proper selection of doping ions. Both these above factors, play a crucial role in the tuning of some physical properties. By the proper choice of transition metal ions (Ni^{2+}, Co^{2+}, Mn^{2+}, Cu^{2+}, etc.) and/or rare earth ions (Eu^{3+}, Er^{3+}, Gd^{3+}, Yb^{3+} Tb^{3+}, etc.), modification of the properties of ZnO is anticipated [28-31].

In rare-earth ions doped zinc oxide nanomaterials, magnetic ordering can be attributed to carrier mediated coupling between dopant 4f and host s electrons. Although, Assadi et al. published that Eu ions, located in the nearest neighbor sites can produce magnetic coupling [32]. Shi et al. reported that electron doping can be attributed to the ferromagnetic ordering in Gd doped zinc oxide [33]. Though, Bantounas et al. suggested that such long-range magnetic ordering does not present in a similar doped ZnO nanomaterials [34]. Recently, Venkatesh et al. published magnetic coupling in Gd doped zinc oxide thin films attributed to defect band. This defect band has been attributed to oxygen vacancy related defects, which are required to demonstrate the ferromagnetic ordering [35].

1.3 Novelty of our Research Work

Until now, we have gathered few knowledge that the optical properties of doped ZnO have been suggested by various research groups but the specific exploration of dielectric and magnetic properties of doped ZnO have not been investigated yet. Now, we are about to explore a clear investigation of magnetic and dielectric properties of doped ZnO nanomaterials along with optical properties. For the preparation of doped ZnO nanostructures we have selected easier, secure and less costly hydrothermal method for the synthesis of ZnO nanomaterials. Hydrothermal synthesis mechanism of ZnO provides an expected growth of the nanoparticles together with desired surface morphology.

1.4 Objective of the Thesis

In many articles, it has been investigated that various physical and chemical properties of Zinc Oxide nanomaterials can be modulated by the selection of proper dopants and doping mechanism [36-38]. Based on the atomic radius and charge valence state of selective dopants, give rise to massive effect on the growth of the nanoparticles and also the development of native defects inside the nanostructures are very much dependent on the selection of dopants and doping mechanism. In our research work, we have reported that doping with a 3^+ valence state can generate various types of vacancies by means of zinc vacancies and oxygen vacancies [39]. These native defects by means of vacancies give rise to quantum confinement by decreasing the average size of the ZnO nanoparticles. The change in the band gap of the nanomaterials towards a higher frequency region is generally known as a blue shift which is due to quantum confinement [40, 41].

In our research work, hydrothermal synthesis process has been preferred for the synthesis of undoped and doped zinc oxide nanomaterials. In this synthesis mechanism, the structure of the nanoparticles can be fabricated rod like and this matter has been established [42-46]. Furthermore, the superior selections of the pH value, temperature and time of hydrothermal synthesis are the fundamental factors for the growth of the expected rod like shape of undoped and doped zinc oxide nanomaterials. The rod like structures can modulate some specific physical properties, the study of which is the goal of our present work.

References:

[1] Z. L. Wang, J. Phys.: Condens. Mat. 16 (2004) R829-R858.

[2] N. Tahir et al., J. Phys. Chem. C 117 (2013) 8968-8973.

[3] G. Li et al., Nanoscale Res. Lett. 10 (2015) 112-119.

[4] V. Gandhi, R. Ganesan, H. H. A. Syedahamed, M. Thaiyan, J. Phys. Chem. C 118 (2014) 9715-9725.

[5] C. Wu, L. Shen, Y. C. Zhang, Q. Huang, Mater. Lett. 65 (2011) 1794-1796.

[6] L. W. Yang, X. L. Wu, T. Qiu, G. G. Siu, P. K. Chu, J. Appl. Phys. 99 (2006) 074303-074307.

[7] K. Jaynthi, S. Chawla, A. G. Joshi, Z. H. Khan, R. K. Kotnala, J. Phys. Chem. C 114 (2010) 18429-18434.

[8] Z. Dai et al., J. Chem. Phys. 134 (2011) 104706-104710.

[9] P. Kaur et al., Appl. Nanosci. 5 (2015) 975-981.

[10] C. H. Lee et al., Nanotechnology 22 (2011) 055205-055210.

[11] J. Pan et al., ACS Photonics 3 (2016) 215-222.

[12] J. Pan et al., RSC Adv. 5 (2015) 82192-82198.

[13] L. Qian, Y. Zheng, J. Xue, P. H. Holloway, Nature Photonics 5 (2012) 543548.

[14] W. Yan, Q. Jiang, Z. Sun, T. Yao, F. Hu, and S. Wei, J. Appl. Phys. 108 (2010) 013901.

[15] P. P. Murmu, J. K. Kennedy, B. J. Ruck, A. Markwitz, G. V. M. Williams, and S. Rubanov, Nucl. Instrum. Methods Phys. Res., Sect. B 272 (2012) 100.

[16] H. M. Zhou, D. Q. Yi, Z. M. Yu, L. R. Xiao, and J. Li, Thin Solid Films 515 (2007) 6909.

[17] N. Fathy and M. Ichimura, J. Cryst. Growth 294 (2006) 191.

[18] M. Jin, J. Feng, Z. De-heng, M. Hong-lei, and L. Shu-ying, Thin Solid Films 357 (1999) 98.

[19] Y. Wang, N. Liu, Y. Chen, C. Yang, W. Liu, J. Su, L. Lia, and Y. Gao, RSC Adv. 5 (2015) 104386.

[20] C. E. Small, S. Chen, J. Subbiah, C. M. Amb, S. W. Tsang, T. H. Lai, J. R. Reynolds, and F. So, Nat. Photonics 6 (2012) 115.

[21] S. C. Pillai, J. M. Kelly, R. Ramesh, and D. E. McCormack, J. Mater. Chem. C 1 (2013) 3268.

[22] M. H. Huang, S. Mao, and H. Feick, Science 292 (2001) 1897.

[23] G. S. Kino and R. S. Wagner, J. Appl. Phys. 44 (1973) 1480.

[24] P. K. Shrestha, Y. T. Chun, and D. Chu, Light: Sci. Appl. 4 (2015) e259.

[25] Y. Y. Lai, Y. P. Lan, and T. C. Lu, Light: Sci. Appl. 2 (2013) e76.

[26] G. Li-li, L. Jun-sheng, Z. Miao, and Z. Yue-lin, Chin. J. Liq. Cryst. Disp. 29 (2014) 499.

[27] G. Li-li, L. Song-fei, C. Tian-fu, and Z. Xue, Chin. J. Liq. Cryst. Disp. 30 (2015) 925.

[28] A. S. H. Hameed, C. Karthikeyan, A. P. Ahamed, N. Thajuddin, N. S. Alharbi, S. A. Alharbi, and G. Ravi, Sci. Rep. 6 (2016) 24312.

[29] W. H. Nam, Y. S. Lim, S. M. Choi, W. S. Seo, and J. Y. Lee, J. Mater. Chem. 22 (2012) 14633.

[30] C. J. Cong, L. Liao, J. C. Li, L. X. Fan, and K. L. Zhang, Nanotechnology 16 (2005) 981.

[31] J. Luo, J. K. Liang, Q. L. Liu, F. S. Liu, and Y. Zhang, J. Appl. Phys. 97 (2005) 086106.

[32] M. H. N. Assadi, Y. Zhang, R. K. Zheng, S. P. Ringer, and S. Li, Nanoscale Res. Lett. 6 (2011) 357.

[33] H. Shi, P. Zhang, S. S. Li, and J. B. Xia, J. Appl. Phys. 106 (2009) 023910.

[34] I. Bantounas, S. Goumri-Said, M. B. Kanoun, A. Manchon, I. Roqan, and U. Schwingenschlögl, J. Appl. Phys. 109 (2011) 083929.

[35] S. Venkatesh, J. B. Franklin, M. P. Ryan, J. S. Lee, H. Ohldag, M. A. McLachlan, N. M. Alford, and I. S. Roqan, J. Appl. Phys. 117 (2015) 013913.

[36] V. Ney, S. Ye, T. Kammermeier, A. Ney, H. Zhou, J. Fallert, H. Kalt, F.- Y. Lo, A. Melnikov, and A. D. Wieck, J. Appl. Phys. 104 (2008) 083904.

[37] H. S. Hsu, J. C. A. Huang, Y. H. Huang, Y. F. Liao, M. Z. Lin, C. H. Lee, J. F. Lee, S. F. Chen, L. Y. Lai, and C. P. Liu, Appl. Phys. Lett. 88 (2006) 242507.

[38] V. Gandhi, R. Ganesan, H. H. A. Syedahamed, and M. Thaiyan, J. Phys. Chem. C 118 (2014) 9715.

[39] T. Debnath, S. Das, D. Das, and S. Sutradhar, J. Alloys Compd. 696 (2017) 670.

[40] H. Yu, J. Li, R. A. Loomis, L.-W. Wang, and W. E. Buhro, Nat. Mater. 2 (2003) 517.

[41] K.-F. Lin, H. M. Cheng, H.-C. Hsu, and W.-F. Hsieh, Appl. Phys. Lett. 88 (2006) 263117.

[42] O. Lupan, T. Pauport_e, B. Viana, V. V. Ursaki, I. M. Tiginyanu, V. Sontea, and L. Chow, J. Nanoelectron. Optoelectron. 7 (2012) 712.

[43] S. Baruah and J. Dutta, Sci. Technol. Adv. Mater. 10 (2009) 013001.

[44] F. Sol_ıs-Pomar, E. Mart_ınez, M. F. Mel_endrez, and E. P_erez-Tijerina, Nanoscale Res. Lett. 6 (2011) 524.

[45] S. Lopez-Romero and M. Garc_ıa-H, World J. Condens. Matter Phys. 3 (2013) 152.

[46] S. B. Kondawar, S. A. Acharya, and S. R. Dhakate, Adv. Mater. Lett. 2 (2011) 362.

CHAPTER 2

Experimental

2.1 Preparation technique

In our research work, the semiconducting nanoparticles of undoped and doped with different concentration of rare earth and/or transition metal ions have been prepared by two different techniques, one is co-precipitation method and the other is hydrothermal method.

2.1.1 Co-precipitation method

For the preparation of semiconducting oxide nanomaterials, the co precipitation technique is a fruitful method. In the case of undoped and doped semiconducting system, it is normally restricted to the cations of chemically alike properties. In this method, the needed ions are mixed together in the aqueous solution. To get the precipitated metal ions, the pH of the resultant solution adjusted at a certain value by the addition of aqueous solution of ammonium hydroxide. The precipitation is collected after removing the supernatant and washed several times with double distilled water. Then the precipitated particles dried in vacuum atmosphere and sintered at a particular temperature without agglomeration.

2.1.2 Hydrothermal method

The synthesis of single crystals depending on the solubility of minerals at a certain temperature and high pressure can be defined as hydrothermal technique. In a steel vessel known as autoclave, the crystal growth is executed by filling up the Teflon lined autoclave with nutrients along with sufficient water and a temperature gradient is maintained to ensure the seeds to grow in a particular direction. The potentiality to produce crystalline phases which may not stable at melting point is the important advantages of hydrothermal synthesis route over other synthesis mechanism. The materials which can also be synthesized by hydrothermal method having high vapour pressure near their melting points. For the improvement of sizeable superior-quality crystals maintaining proper control over the nutrients, this synthesis method is quite worthy.

2.2 Characterization techniques

The measuring instruments and experimental set up operated for the characterization of structural, morphological and physical properties study of different nanocrystalline systems have been discussed in this chapter. Following the synthesis of the nanomaterials in different procedures, the most crucial requirement is to determine the crystallographic phase of all the nanocrystalline and it has been executed by using X-ray diffractometer. The size of the nanocrystallite, lattice parameters and the formation of impure phase, if any are relevant information of the nanocrystalline. Such types of information are extracted from the XRD patterns. In this particular chapter a few fundamental understanding of the X-ray diffractometer and the technique of analysis of the XRD data has been introduced. The microstructural and morphological characterization of the nanocrystalline systems are evaluated from Field Effect Scanning Electron microscope (FESEM). FESEM is a key experimental instrument for the reckoning of the morphology and the microstructural knowledge of nanostructured samples. FESEM are used to determine the microstructural characterization of a few selected nanocrystalline systems and various compatible quantities like average crystallite size and its distribution from the micrographs are evaluated. The UV-Visible absorption spectrum of the as-prepared nanoparticles was performed by l25 spectrophotometer, Perkin Elmer, Germany within the range of 240-340 nm. A Perkin Elmer Germany, Spectroflurometer was employed to study the photoluminescence (PL) spectroscopy at an excitation wavelength of 320 nm. The technique of electrical conduction was explored by dielectric measurements using Agilent 4294A Precision Impedance Analyzer.

An illustration of the instruments and the technique of data analysis are incorporated in this particular chapter. The dynamic magnetic performance and the ac magnetizations of different samples are taken by a 16 bit computer controlled digital hysteresis loop tracer associated with a computer. This measurement has been carried out to study various magnetic properties like, ac magnetization, saturation to remanence ratio, coercive field, hysteresis loss etc. Static magnetic behavior i.e., field vs. magnetization (M-H curve) as well as zero-field cooled (ZFC) and field cooled (FC) curves at various temperatures are analyzed using SQUID (Superconducting Quantum Interference Device) magnetometer and a few magnetic quantities have been evaluated from the study. Concise explanations of these magnetic measuring equipments have been given in this chapter.

2.3 X-Ray Diffraction

The structural and microstructural characteristic study of materials has been done by the X-ray diffraction (XRD) technique which is a vital analytical mechanism. For the recognition of crystallographic phase and to calculate the particulars of crystallographic property of a substance, XRD is an essential instrument. von Laue's discovered in 1912 that that crystals diffract X-rays which is beneficial to determine the structure of the crystal. Previously, to determine the crystal structure, X-ray diffraction had been used and now a days the method not only applied to evaluate structural information but also to study chemical analysis and stress measurement. Also, a few information like crystallite strain, shape, lattice parameters etc. are calculated by the broadening of reflections peak in a powder diffraction pattern.

The structural characterization of the materials has been done by using Brukers Advanced D8 diffractometer with Cu K_α radiation (λ = 1.5425 Å). Fig. 2.1 shows the photograph of an X-ray diffractometer. The germanium (022) monochromator has been used for Cu K_α radiation from an eminently stabilized Bruker X-ray generator (K 780) and is operated in the θ-2θ mode. The incident X-rays interacts with the samples and thereby producing constructive interference which satisfies the Bragg's Law $n\lambda = 2d\sin\theta$, corresponding diffracted rays are gained, where λ represents the wavelength of the X-ray, d shows the inter planner spacing and θ denotes the glancing angle. Then the diffracted X-rays have been detected, evaluated and studied. Due to random orientation of different planes of the crystallite, the diffractions from all possible directions of the lattice were obtained by scanning the samples with a range of 2θ angles.

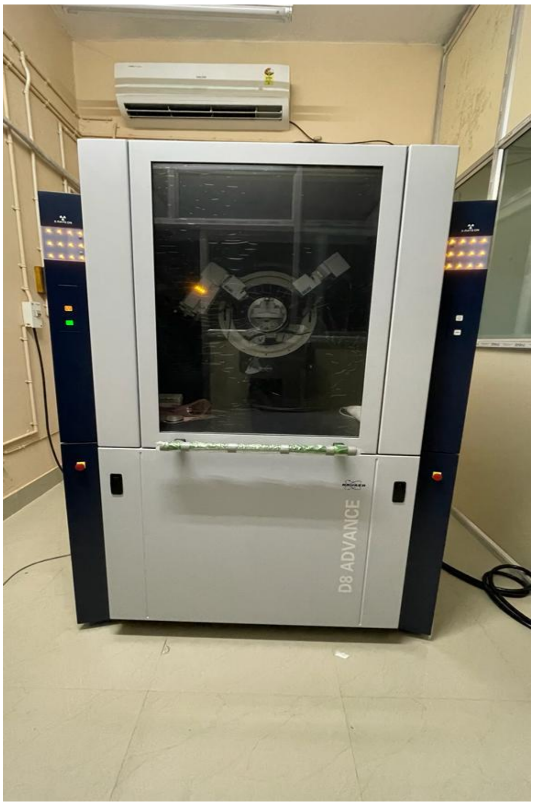

Fig. 2.1 Brukers Advanced D8 diffractometer

2.3.1 Estimation of nanocrystallite size from Debye-Scherrer formula

From the diffraction angle of different peak positions, the lattice spacing may be calculated and for first order diffraction, the Bragg's equation represents by

$$2d_{hkl} \sin\theta = \lambda, \qquad \text{for } n = 1,\ldots.. \qquad 2.1$$

Where (hkl) denote the Miller indices of lattice planes.

To calculate the nanocrystallite size (D), Debye-Scherrer equation is introduced,

$$< D > = \frac{0.89\,\lambda}{\beta_{1/2}\cos\theta} \qquad 2.2$$

Where D denotes the crystallite size and θ represents the position of most intense peak in XRD pattern and also the full width at half maximum (FWHM) of the sharpest peak is denoted by

$$\beta_{1/2} = \sqrt{\left\{\left(\beta_{1/2}\right)_0^2 - b_0^2\right\}} \qquad 2.3$$

Here b_0 represents the same for large crystallites.

2.4.1 Field Emission Scanning Electron Microscope (FESEM)

Field Emission Scanning Electron Microscope (FESEM) is one of the most important instruments for the investigation and analysis of the microstructure and chemical composition of nanostructured materials. To realize the basic of electron microscopy, it is required to know the fundamental of optics. Since the electron may be deflected by the magnetic field in various investigations, the light source has been replaced by high energy electron beam to develop the electron microscopy. To get a range of signals on the surface of the solid materials, He SEM with high energy electrons has been introduced. The information about the materials like morphology, chemical composition, and crystalline structure have been revealed by the signal obtained from the electron sample interactions. Normally, a two dimensional image is procured by the collected data over a preferred area of the surface of nanostructured materials. A selected point location on the nanomaterials can also be analyzed with the help of a SEM. Such kind of approach is convenient in determination of chemical compositions. There is a secondary electron detector in a SEM. The secondary electrons produce the signal which is detected and image is produced. To obtain the virtual 3-D image of specimen, thee scan rate of electron beam may be enhanced. Also by using standard photography, the image can be captured.

Fig. 2.2 Picture of INSPECT F50 FESEM

2.4.2 Energy dispersive x-ray analysis (EDX)

The energy dispersive x-ray (EDX) is a powerful technique of scanning electron microscope to obtain the chemical composition of materials. This analysis is an integral part of a SEM. This technique has been used to determine the elemental composition of specimen sample. The sample is bombered with an electron beam during an EDX analysis inside the scanning electron microscope. As a result of this collision between colliding electron and specimen atoms, some of them are knocked off. An ejected inner shell electron leaves a vacant position which is eventually inhabited by an outer shell higher energy electron. The transmitted outer electrons in this process must emit some energy in the form of x- rays. The energy emitted by transmitting electrons depends on which shell it is transferring to and which shell it is transferred from. The amount of energy releases is unique for the atom of each element during the transferring process. During the electron bombardment, the amount of energy in the X-rays being measured which establishes the identity of atom.

The spectrum of each energy level is the output of EDX. The peaks corresponding to each energy level have been displayed by EDX spectrum. This unique peak corresponding to an atom represents a single element. More the sharpness of a peak in the spectrum, the more assembled the elements in the sample.

2.5 Raman Spectroscopy

Raman spectroscopy is one of the most versatile techniques for the investigation of various features of nanocrystalline and nanocomposites [1,2]. The phenomenon of Raman spectroscopy can be realized in connection with quantum theory of radiations. The radiation having frequency ν comprising with stream of particles named photon with energy hν, here h denotes Plank’s constant. When photons collide with the molecules, they will be deflected unaffectedly if the collision is perfectly elastic. The energy of the incident photon can be collected with a detector placed at right angles to an incident beam. For inelastic collision, there is an exchange of energy between photon and molecule during collision. In this process, in conformation with quantum laws the molecule may gain or lose some amounts of energy which is represented by the change in vibrational or rotational energy ΔE of the molecule. The photon will be dispersed with energy ΔE= hν, when the molecule acquire energy and the radiation will possess frequency ν-ΔE/h is referred to as Stoke’s radiation. On the other hand, when the molecule losses energy ΔE, the radiation will have frequency ν+ΔE/h is referred to as anti Stoke’s radiation.

To study the vibrational and rotational properties of molecules, Raman scattering have been used widely. To probe these levels, infrared spectroscopy is normally needed. Though, these levels can be excited using visible light in Raman spectroscopy. The H_2 molecule has not any electric dipole (even in excited vibrational states), there is no possibility to obtain any emission line for such transition [3]. In this case, Raman spectroscopy is the only solution to study the transitions.

Raman Spectrophotometer (J. Y. HORIBA) having Ar^+ laser with 514.5 nm as excitation wavelength has been used to study Raman Spectra. Fig. 2.4 represents the Raman spectrophotometer.

Fig. 2.3 Picture of T64000 Raman Spectrophotometer (J. Y. HORIBA).

2.6 Electron Paramagnetic Resonance

Electron Paramagnetic Resonance (EPR) is a magnetic resonance spectroscopy that uses microwave to probe species with unpaired electrons, like cations and triplet in the presence of externally applied static magnetic field. EPR spectroscopy has various applications, such as study the kinetics and mechanism of reactive radical to obtain the information about the interactions between paramagnetic metal ions, study the conducting electrons in semiconducting materials. EPR spectrometer appeared in the year 1980 and has become extensively used for biological and electronic field. An electron is a negatively charged particle having two moments, one is orbital magnetic moment and the other is spin magnetic moment. The unpaired electron's spin magnetic moment is given by

$$M_s = \sqrt{S(S+1)}\frac{h}{2\Pi}$$

Where, M_s represents the total spin angular momentum, S represents the spin quantum number and h is Planck's constant.

The fundamental basis of EPR spectroscopy is the energy difference between the energy levels broaden until it become equivalent with the microwave radiation with the increasing of intensity of the applied magnetic field and ensure the absorption of photons. EPR spectrometer normally vary the magnetic field to confine the microwave frequency and available in various frequency ranges. Currently, the X band is the most often used.

Fig. 2.4 Picture of EPR spectroscopy

2.7 UV-VIS spectroscopy study

From a visible and/or UV light source, a beam of light is divided into its component wavelengths by a prism or diffraction grating. By using a half mirrored device, each monochromatic beam is split into two equal intensity beams. One beam i.e. the sample beam moves through a transparent container (cuvette) holding a solution of the specimen being investigated in a transparent solvent. On the other hand, the reference beam travels through an identical container (cuvette) holding the solvent only. The intensities of the light beam are computed by detectors and then analyzed by comparing these two. The intensity of the reference light beam endured a little or no light absorption is designated as I_0 and the intensity of the sample light beam is designated as I. The spectrometer impulsively scans all the component wavelengths rapidly. At various wavelengths, the absorption is different and is the characteristic of the specimen. This characteristic parameter is known as absorbance.

The spectrometer exhibit the intensity of absorbance on the vertical axis. The wavelength corresponding to the maximum absorbance is a characteristic quantity and is defined as λ_{max}, different compound possess different absorption maxima.

Fig. 2.5 Picture of UV-VIS spectroscopy

2.8 Photoluminescence spectroscopy

Photoluminescence spectroscopy is an important tool to study the optical property of nanomaterials. Photoluminescence (PL) is a mechanism in which a specimen absorbs electromagnetic radiation and then releases photon energy. This phenomena can be described Quantum mechanically and can be explained as an excitation to a higher energy state and return back to the lower energy state with the emission of photon energy. The emission of light by a material through any mechanism other than black body radiation is known as Luminescence. The easiest photoluminescence mechanism is resonant radiation. In this process, a specific wavelength photon gets absorbed and a similar photon is radiated and no remarkable internal energy transitions of chemical substrate is involved which is exceptionally fast in the order of 10 nano seconds. This kind of effect is very familiar and is known as fluorescence in which a few original energies are scattered so that the radiated light photons have lower energy than that of the absorbed.

To measure the purity and crystalline quality of semiconductors, photoluminescence is an important tool. In PL, by using photons to instigate excited electronic state within the materials we measure physical and chemical properties and analyze the optical emission. It is to be noted here that this method is non destructive exploring the electronic structure of materials.

Fig. 2.6 Picture of PL spectroscopy

2.9 dc magnetic measurements

Superconducting Quantum Interference Device (SQUID)

The photograph of SQUID magnetometer is shown in Fig. 2.7. The measurement of magnetic properties of various specimen have been investigated by Quantum Design MPMS7 SQUID magnetometer. Different magnetic measurements like magnetization, coercive field, field cooled and zero field cooled magnetization, saturation to remanance ratio and superparamagnetic relaxation etc. can be measured by using this equipment which is a very sensitive device. This device comprising with a superconducting magnet, a superconducting detection coil named as pick-up coil, a SQUID and superconducting magnetic shield.

The magnetometer performs like a magnetic flux to voltage converter. The magnetic signal of the sample which is located in a liquid helium bath is procured from the superconducting pick-up coil which is a part of the SQUID device. A gelatin capsule which has weak diamagnetic signal has been loaded with the sample. Also, the gelatin capsule is filled with cotton to curb the movement of the specimen during the measurement. Then the capsule has been located within a plastic straw which is hooked to the MPMS sample probe. SQUID magnetometer has two modes of measurement, one is reciprocating sample oscillation mode (RSO) and the other is direct current mode (DC). In case of RSO mode, the oscillation of the sample is carried out using a servo motor that rapidly oscillates the sample, on the other hand in DC mode, the specimen has been moved inside the coil in discrete steps. Due to fast data acquisition time and extreme sensitivity, the RSO mode of action is more superior over DC mode. The RSO mode incorporated with digital signal processor (DSP) favors for faster data collection than the DC mode. When the data is measured in DC mode, the magnetic noise will be relatively high during measurement. So, the RSO mode of data collection will be more effective and reliable to minimize the effect of magnetic noise by virtue of non-linear SQUID drift. An alternative magnetic flux in pick-up coil has been produced when the specimen is moving up and down which produces an alternating output voltage in the SQUID instrument. Then the amplified alternating voltage is studied by the magnetometer electronics. A magnetic field generated by the superconducting magnet can magnetize the sample and the read out signal will be proportional to the magnetic moment of the specimen. The operational temperature of MPMS is in the range from 2 to 400 K with an external applied magnetic field up to 7 T.

Fig. 2.7 Picture of SQUID magnetometer (Quantum Design MPMS).

2.10 Dielectric measurements

Dielectrics are material which resists the flow of electric field through it and it is a material in which the electrostatic field may exist for a long period of time in the expense of minimal energy dissipation in the form of heat. Under the effect of an external electric field, the short range motion of charge carriers influences the dielectric effect. The electrons in each atom are polarizes due to the presence of external applied electric field to a dielectric material and there by producing a dipole moment. In response to the applied alternating electric field, the behavior of dielectric material is frequency dependent and generally known as dielectric response. Due to the electronic polarization of the charged particles, the storing of electric field by the material is measured in terms of dielectric constant or permittivity (ε). Due to the presence of dielectric material between a capacitor plates, the performance of a material i.e. the Relative permittivity, ε_r is measured with respect to the permittivity of free space (ε_0) and that has been defined as fractional increase in the stored charge per unit voltage.

Considering the dielectric within a parallel plate capacitor, the capacitance C is given by,

$$C = \varepsilon_r \varepsilon_0 A / d \qquad 2.12$$

Here, A is the area and d is the thickness of the parallel plate capacitor and other symbols are already been signified.

In the presence of an applied alternating potential, $V = V_0 \exp(j\omega t)$, the total current in the dielectric is represented by,

$$I = j\omega r C_0 V \qquad 2.13$$

Here, V_0 is the amplitude of peak voltage and C_0 represents the maximum amplitude of the capacitance.

Since, 'r' represents a complex quantity ($r = r' - jr''$), 'I' may be written as,

$$I = j\omega (r' - jr'') C_0 V \qquad 2.14$$

As, $\exp(j\omega t) = \cos(\omega t) + j \sin(\omega t)$, the current and the voltage are presented by the magnitude of the respective vectors and the subsequent current is $\pi/2$ rad out of phase against the applied voltage. Only for an ideal dielectric, Eq. 2.14 is significant. Actually, due to losses in the wires, electrodes, dielectric loss, dc resistance and inertia of the charge carriers, the capacitor experiences energy dissipation and the resulting current is not comprehensively $\pi/2$ rad out of phase against the applied voltage. Therefore the resulting current for real dielectric leads by an angle of $(90^0–\delta)$ with the applied voltage, here 'δ' is the "loss angle". The '$\tan \delta$' i.e. the tangent of the loss angle represents the loss tangent or "dissipation factor", a dimensionless quantity which exhibits the energy losses by a capacitor and is represented as,

$$\tan \delta = r'' / r' \qquad 2.15$$

In this thesis, the dielectric measurement has been investigated by using Agilent 4294A Precision Impedance Analyzer. The photograph of the instrument has been shown in the Fig. 2.8 At first, the specimen in the powder form are pelletized using a hydraulic press pelletizer. A pressure of 150 kg/cm^2 has been applied for 5 minutes during the making of pellets which have diameter of 10 mm. At room temperature as well as at high temperature, the capacitance

(C) and dissipation factor (D) of all the specimen have been measured as a function of frequency of the applied field in the range from 50 Hz to 1.4 MHz. From the measured value of C and D, the real and imaginary part of dielectric constant have been calculated by using the relations

$$\varepsilon' = C.d / \varepsilon_0 A \qquad 2.16$$

and,

$$\varepsilon'' = \varepsilon' . D \qquad 2.17$$

Fig. 2.8 Dielectric measurement setup.

2.11 Theoretical modeling

Rietveld Analysis

Rietveld analysis of a XRD pattern has been carried out using MAUD software to get the structural information of a sample under investigation. The Rietveld analysis of a XRD pattern provide information about the lattice parameters, grain size, micro-strain, atomic positions and occupancies etc. The detected XRD pattern of the samples is compared with the theoretical pattern produced by the Rietveld method, formulated on the user defined model of the crystal structure. By repetitive refinement of various structural, microstructural and background functional parameters, the difference between the theoretical and experimentally calculated pattern has been minimized. The figure of each Bragg peak has been fitted with a Pseudo-Voit type function and a fourth order polynomial has been considered for the backgrounds. Standard Si powder having large crystallite is used to determine the instrumental function. By the analytical convolution of true line broadening and symmetric part of instrumental function followed by the numerical convolution of the asymmetric part of instrumental function, the entire pattern has been generated. To determine the shape parameters of the profile function of specimen, the parameters of crystallite/coherent domain size and rms micro-strain have been refined. The values of the parameters evaluated from the standard material have been kept fixed. With the JCPDS file, the simulation of the XRD pattern of the sample has been carried out.

References:

1. C. P. Bean, J. D. Livingston, J. Appl. Phys. 30 (1959) 120S.
2. S. Yan, J. Geng, J. Chen, L. Yin, Y. Zhou, and E. Zhou, J. Crystal Growth 262 (2004) 415.
3. J. P. Singh, R.C. Srivastava, H.M. Agrawal, and R. Kumar, J. Raman Spectroscopy 42 (2011) 1510.
4. D. A. Long, The Raman Effect, John Wiley & Sons Ltd., (2002).

CHAPTER 3

Optical, Magnetic and Dielectric Properties of Yttrium doped ZnO Nanorods Synthesized by Hydrothermal Method

3.1 Introduction

Due to exciting physical properties and application in future technologies, ZnO has attracted considerable interest of the researchers [1-3]. Due to new physical properties and potential applications in nanodevices, interests are concentrated on the low-dimensional nanostructures like nanoparticles, nanorods, nanowires, and nanotubes [4-7]. By various growth mechanism such as sol-gel, co-precipitation method, hydrothermal methods and pulsed laser deposition method and by doping with proper dopants, such as Li, P, and Ag, a performance enrichment of these ZnO based nanomaterials for many device applications have been executed [8-14]. Apart from, by using modified carbothermic reduction process, an effective mass production of ZnO nanowires has been claimed [15]. A few investigations indicated that nanostructured ZnO with high surface to volume ratio is highly acceptable for ultraviolet and photovoltaic device applications, like nanolasers, light-emitting diodes, field emitters, photodetectors, photo-electrodes in dye-sensitized solar cells, and chemical sensors [16-21]. In recent times, ferromagnetic orientation at room temperature (RT) as well as high Curie temperature in III-V and II-VI semiconducting nanomaterials has also been observed [22-24].In theory transition metal ions doped ZnO nanoparticles has been proven which was established by experiments with RT ferromagnetic ordering for spintronic device applications [25,26]. ZnO nanoparticles have been doped with magnetic metal ions, such as Co, Ni, or Mn to fabricate diluted magnetic semiconductors (DMSs) [27].Recently, some researchers have revealed that ferromagnetic ordering observed in undoped and doped ZnO nanostructures and said to be influenced by intrinsic defects [28]. Also, RT ferromagnetism has been observed in non-magnetic elements, like Li or Bi doped ZnO nanoparticles [29,30]. By incorporating proper rare-earth dopant, modification of the optical, magnetic and dielectric properties can be anticipated. Recently, many researchers have been explored on rare-earth (Gd^{3+}, Dy^{3+}, Tm^{3+},Tb^{3+}, etc.) doped ZnO nanostructures. Due to the presence of intrinsic defects in the rare-earth doped ZnO nanostructure, an enhancement in the optical, magnetic and dielectric properties have been observed. Since, the dopants ionic radius are incomparable to that of the host zinc ions, various types of intrinsic defects such as, oxygen vacancies, zinc vacancies, zinc interstitials and others in the doped ZnO nanostructures have been developed. The ionic radius of yttrium ion (0.89 Å) is extremely higher than the ionic radius of the zinc ion (0.74 Å). Therefore, large size yttrium ion doped ZnO nanostructures can generate huge internal strain which in turn can produce large numbers of intrinsic defects in the ZnO nanostructures. Also yttrium doping are beneficiary as (i) it can decrease the band energy gap of ZnO [31] (ii) Y^{3+} surface upgrade crystallite growth [32] (iii) the surface confinement of Y^{3+} increases oxygen vacancies [32]. All these, inspired us to investigate the optical, magnetic and dielectric properties of yttrium ions doped ZnO nanomaterials [33-35].

3.2 Experimental

3.2.1 Materials:

Y^{3+}ions doped ZnO nanoparticles were synthesized by hydrothermal method. Zinc acetate dihydrate $Zn(CH_3COO)_2 \cdot 2H_2O$ (Sigma Aldrich, 99%), yttrium nitrate hexahydrate $YN_3O_9 \cdot 6H_2O$ (Sigma Aldrich, 99%), and ammonium hydroxide NH_4OH (concentration ~ 25%) are used as precursor material with analytical grade to synthesize $Zn_{1-x}Y_xO$ (x = 0.03, 0.05 and 0.07).

3.2.2 Synthesis of Y^{3+}ions doped ZnO nanostructures by co-precipitation method

Y^{3+}ions doped ZnO Nanoparticles were prepared by using two step method. The precursor materials are taken in milli-Q water and the aqueous solutions are taken in a beaker which is placed on a magnetic stirrer. 3, 5, and 7% molar concentration of yttrium to that of the molar concentration of zinc salt has been taken in the aqueous solution. The mixed solution has been stirred for four hrs. to get homogeneous solution. To maintain the pH of the solution at ~ 10, NH_4OH solution is added in the previous solution for precipitation. Then the co-precipitated particles are collected for washing many times by using milli-Q water.

3.2.3 Nucleation of Y^{3+}ions doped ZnO nanoparticles

The washed precipitate is diluted in milli-Q water and taken in Teflon jacket. The Teflon jacket is placed in an autoclave at 160 °C for 48 hours. The atmosphere within the Teflon jacket is favourable for the surface growth of ZnO nanoparticles to rod like structure. After cooling down to room temperature, the supernatant is eliminated and the solid precipitate is collected and washed many times with milli-Q water. Then for drying the sample, it is desiccated at RT. To achieve better crystallographic phase formation, the dried powder is sintered at 400 °C in vacuum atmosphere. The sample name and related specifications are given in the Table 3.1.

Table 3.1. The sample name and its corresponding specifications.

Sample specification	Sample details
ZnO	Undoped ZnO
ZnOY3	3% yttrium ions doped ZnO ($Zn_{0.97}Y_{0.03}O$)
ZnOY5	5% yttrium ions doped ZnO ($Zn_{0.95}Y_{0.05}O$)
ZnOY7	7% yttrium ions doped ZnO ($Zn_{0.93}Y_{0.07}O$)

3.2.4 Characterization techniques

X-ray diffractograms of undoped and Y^{3+} ions doped ZnO nanoparticles are recorded in the range of 2θ from 10 to 80° in powder X-ray diffractometer, Model D8, BRUKER AXS, using Cu K_α radiation (λ = 1.5405 Å). The structural morphology of all the samples has been observed by using Field emission scanning electron microscope (FESEM), INSPECT F50 (FEI, Netherland). The chemical bonding existing in the samples are recorded by Fourier transform infra-red (FTIR) spectrometer, JASCO FTIR instrument - 410 (USA). The photoluminescence spectroscopy (PL) has been carried out with an excitation wavelength (λ_{ex}) of 325 nm at RT by a spectroflurometer, Perkin Elmer Germany. The Raman spectroscopy study has been employed using Newport RS 2000TM. The Magnetization versus applied magnetic field (M-H) data of all the samples at RT and at various low temperature has been studied by using a SQUID magnetometer (MPMS XL 7, Quantum Design) with a maximum applied field of 50 kOe. The Electrical conductivity has been explored with dielectric measurement by using an Impedance Analyzer, Agilent 4294A.

3.3 Result and discussions

3.3.1 XRD and FESEM analysis

Fig. 3.1 illustrates the XRD patterns of undoped ZnO and Y^{3+} ions doped ZnO nanoparticles. All the peaks have been indexed to hexagonal wurtzite structure of ZnO with the help of the JCPDS (file no. 36-1451, space group $P6_3mc$). Also, it is evident that there are no extra peaks corresponding to any impurity phase like Y_2O_3 etc. This data indicates homogeneous doping of the Y^{3+} ions in the tetrahedral (Zn^{2+}) site of the ZnO wurtzite structure. The average crystallite size of all samples has been calculated from the broadening of the peak (101) by using the Debye-Scherrer equation.

$$< D >_{(101)} = \frac{0.9\lambda}{\beta_{\frac{1}{2}}\cos\theta} \tag{3.1}$$

With the Y^{3+} concentration increasing in the ZnO nanoparticles, the average nanocrystallite diameter increases. Distortion in the host ZnO lattice occurs due to the addition of the Y^{3+} ions which also induce particle size change. The micro strain (ε) of the doped ZnO nanoparticles is also calculated using the formula below and shown in Table 3.2.

$$Micro\ strain\ (\varepsilon) = \frac{\beta_{\frac{1}{2}}cos\theta}{4} \tag{3.2}$$

From the microstructural analysis of the samples, other important data such as unit cell parameters ‘a’ and ‘c’, c/a ratio, volume per unit cell(V), bond length(L), internal positional parameter(u), and dislocation density(δ) have been calculated from the XRD and shown in Table 3.2. It is observed that the lattice parameter ‘a’ for Y^{3+} ions doped ZnO nanoparticles is comparatively higher than undoped ZnO nanoparticles. Also, ‘c’ is found to be lower for doped ZnO nanoparticles as compared to undoped ZnO nanoparticles.

With the increase of doping concentration in the ZnO nanostructure, the lattice constants increase/decrease which proves the substitution of Y^{3+} ions at tetrahedral site of Zn. Due to the difference in the ionic radius of the host and the dopant internal lattice strain is developed. The measured ratio of c/a also shows a perfect agreement with hexagonal close packed (hcp) structure. By using the following equation, the unit cell volume for has been measured,

$$V = 0.866 \times a^2 \times c \tag{3.3}$$

Increased value of volume of unit cell (V) illustrates the substitution of Y^{3+} ions in the Zn sites. The presence of defects in the doped ZnO samples is prominently signified by Dislocation density (δ). Dislocation density has been calculated using the following equation

$$\delta = \frac{1}{D^2} \tag{3.4}$$

By using the following relationship, the Zn-O bond length has been calculated

$$\mathrm{L} = \sqrt{\frac{a^2}{3} + \left(\frac{1}{2} - u\right)^2 c^2} \tag{3.5}$$

Where the positional parameter (u) for wurtzite structure can be measured using the equation

$$u = \frac{a^2}{3c^2} + 0.25 \tag{3.6}$$

It is observed that with the increased doping of Y^{3+} ions in the ZnO nanoparticles, the bond length increases moderately. This is due to the fact that, Y-O bond is developed due to the replacement of Zn^{2+} ions by Y^{3+} ions, the bond length of which is larger than Zn-O bond length.

Table 3.2. Structural parameters evaluated from XRD.

Sample	Avg. crystallite diameter D (nm) (101)	Lattice parameter (Å)		c/a ratio	Micro strain (ε) (10^{-4})	Unit cell volume V $(Å)^3$	ZnO bond length (Å)	Dislocation density $(Å)^{-2}$ δ (10^{-6})
		a	c					
ZnO	84.44	3.2514	5.212	1.605	3.728	47.66	1.9783	1.158
ZnOY3	87.06	3.2516	5.209	1.603	3.966	47.69	1.9787	1.312
ZnOY5	88.86	3.2518	5.207	1.601	4.061	47.74	1.9791	1.375
ZnOY7	89.19	3.2520	5.204	1.600	4.132	47.78	1.9796	1.432

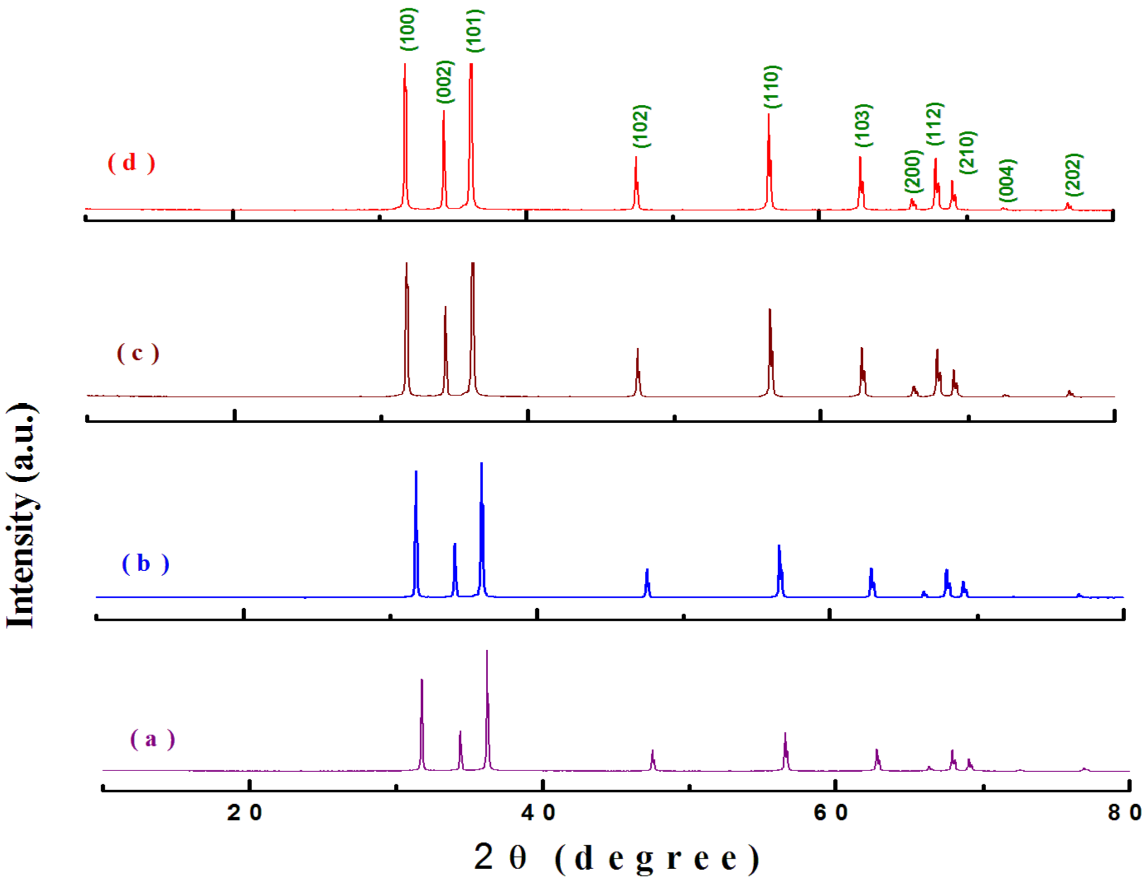

Fig. 3.1 XRD patterns of the samples (a) ZnO, (b) ZnOY3, (c) ZnOY5 and (d) ZnOY7.

Fig. 3.2 shows some micrographs which is the structural morphology of all the samples. FESEM micrographs in Figs. 3.2a-d represent the structural morphology of undoped and doped ZnO nanostructures. From the Figs. 3.2a-d it is evident that all the micrographs are rod like in nature including hexagonal cross-section. It can also be observed that all rod like structures are crystalline and very much observable from one another. The micrographs of ZnOY3, ZnOY5 and ZnOY7 nanoparticles are shown in Fig. 3.2b-d respectively. With the increase in doping percentages of Y^{3+} ions, the morphology is changed which represents the true incorporation of the Y^{3+} ions in ZnO nanostructures.

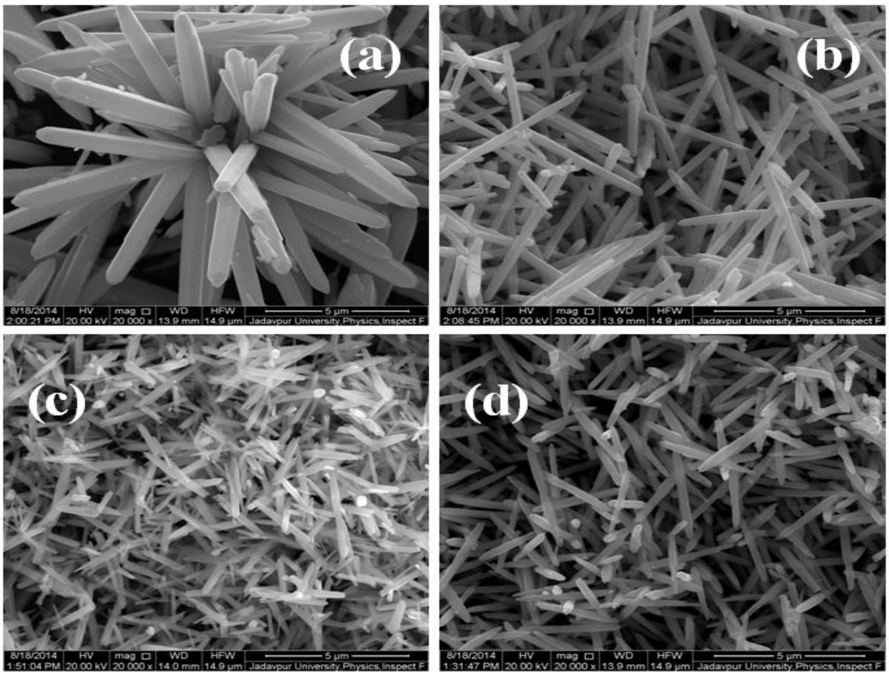

Fig. 3.2 SEM images of the samples (a) ZnO, (b) ZnOY3, (c) ZnOY5 and (d) ZnOY7.

3.3.2 FTIR studies

Fig. 3.3 shows the FTIR spectra of undoped and Y^{3+} ions doped ZnO nanoparticles. It enables us to study the atomic vibrational mode of molecules in the powder samples calcined at 400^o C. Due to the existence of CO_2 molecule in air, a weak doublet nearly 2366, 2348, 2347 and 2357cm^{-1} of undoped and doped ZnO (ZnOY3, ZnOY5 and ZnOY7) have been shown respectively [36]. This might have occurred due to the absorption of CO_2 from the atmosphere during measurement and the trapped CO_2 molecules raises these modes. Due to the C=O stretching (symmetric and asymmetric) mode appears from the trapped CO_2 residing on the surface of the ZnO nanomaterials, peak around1513, 1529, 1536, 1348 cm^{-1}of pristine ZnO and 1406, 1413, 1401, 1404 cm^{-1} of the ZnOY3, ZnOY5 and ZnOY7, respectively, arises [37]. The two strong absorption bands corresponding to 443-452 cm^{-1}, might have occurred due to Zn-O stretching.

Due to the formation of oxygen vacancies (V_o) in the structure during annealing process, a band at 525-531 cm^{-1} is observed. Moreover, different types of defects such as oxygen vacancies, zinc vacancies and zinc interstitials in the ZnO nanoparticles are attributed to the discrepancy between the ionic radius of Zn^{2+}ion (~ 0.74 Å) and Y^{3+}ion (~ 0.89Å).

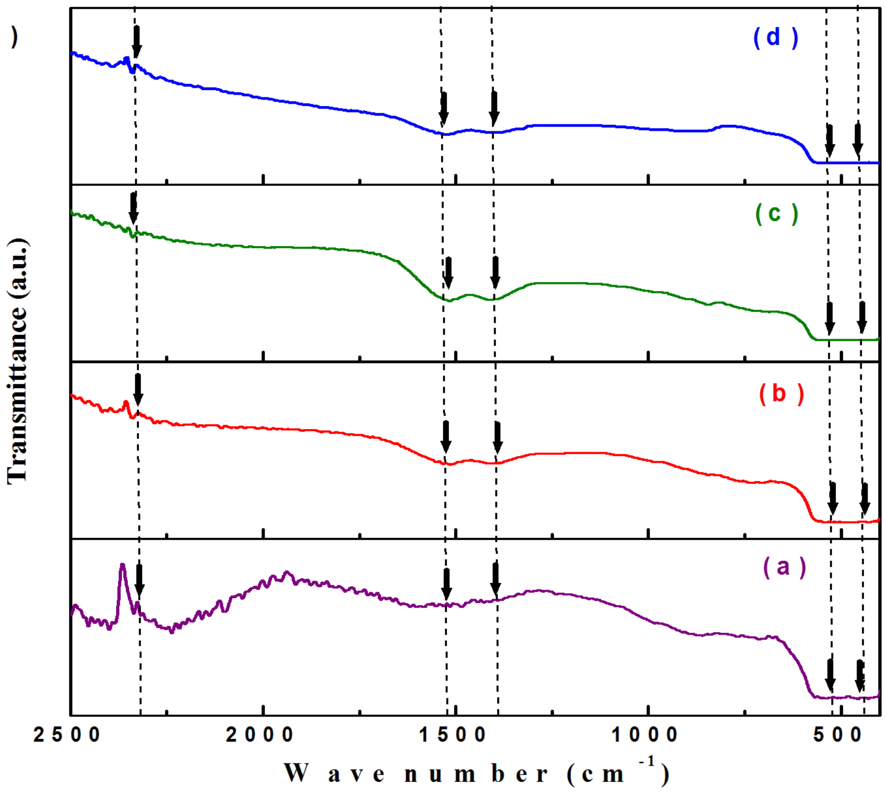

Fig. 3.3 FTIR transmittance spectra of the samples (a) ZnO, (b) ZnOY3, (c) ZnOY5 and (d) ZnOY7.

3.3.3 Photoluminescence studies

The optical properties of undoped ZnO and Y^{3+} ions doped ZnO nanorods have been studied using PL spectroscopy with an excitation wavelength of 325 nm at RT and are given in the Figs. 3.4(I)(a-d) respectively. The PL spectra for all the samples exhibit a sharp ultraviolet emission at 360nm and 388 nm almost at the same position. These peaks develop due to the recombination of free excitons and are normally attributed to near-band-edge (NBE) emission. A violet emission located at 411 nm in the visible region is designated to the electronic transition occurring from zinc interstitial (I_{Zn}) level to the top of the valance band. In the visible region, a blue emission at 454 nm is assigned to the electronic transition from zinc interstitial (I_{Zn}) to zinc vacancy (V_{Zn}) level for all samples [38]. A green emission observed at 498 nm is attributed to electronic transition from the bottom of conduction band to the oxygen vacancy (V_o) level. Due to the incorporation of Y^{3+} ions into ZnO matrix, a clear red shift of the excitonic emission peak has been detected for all the samples. The relative intensity of Y^{3+} ions doped ZnO nanorods is negligible as compared to undoped ZnO nanorods, which demonstrates that the doping may improve the intrinsic defects and oxygen vacancies in the system [39-42].

3.3.4 Raman spectroscopy studies

To obtain more information such as, quality of crystallinity, intrinsic defect and structural disorder about the microstructure of undoped and doped ZnO nanorods, Raman spectroscopy has been introduced. It is a nondestructive procedure. The spectra are taken for all the samples in the range of 50-550 cm^{-1}. Figs. 3.4(II)(a) shows the Raman spectrum corresponding to six different Raman-active phonon modes at 101[E_2(low)],225 [$2E_2$(low)], 330 (E_{2H}-E_{2L}), 380 [A_1(TO)], 410[E_1(TO)] and 437 cm^{-1} [E_2(high)] respectively, at RT for wurtzite ZnO [43-45]. The low frequency E_2 mode [E_2(low)] in doped ZnO nanoparticles as compared to undoped ZnO shows a blue shift from 100 cm^{-1} to 108 cm^{-1}. The high frequency E_2 mode [E_2(high)] in Y^{3+} ions doped ZnO nanomaterials as compared to undoped ZnO presents a blue shift from 428 cm^{-1} to 437 cm^{-1}. Due to the production of structural defects, the shift in the position and minimization in intensity of Raman modes are appeared. This demonstrates the incorporation of dopant ions at the position of Zn^{2+} lattice sites within the ZnO matrix. The lattice distortions in the nanostructured system have occurred due to the mismatch of the ionic radii of the Zn^{2+} and Y^{3+} ions. The peak corresponding to 329 cm^{-1} is attributed to E_2 (high)–E_2 (low) mode (E_{2H}-E_{2L}) which is coming from zone-boundary phonon scattering. A peak nearly 530-560 cm^{-1} arises because of E_1 symmetry with LO modes and assumed to be caused by oxygen vacancy, zinc interstitial defect and free carriers. This is because proper doping of Y^{3+} ions in ZnO nanoparticles creates large number of oxygen vacancies or zinc interstitials. Also, the position of E_{2H} mode (428-437 cm^{-1}) for different doping percentages of Y^{3+} ions in ZnO nanostructures compared to the undoped ZnO is a characteristic of wurtzite structure. The local defect, lattice strain or distortion causes phonon localization that give rise to corresponding peak shift which exhibits variation in frequency.

These changes did not occur due to laser activated heating in the nanoparticles. Therefore, it can be mentioned that the variation in isotopic mass of atom forming ZnO by the incorporation of Y atom.

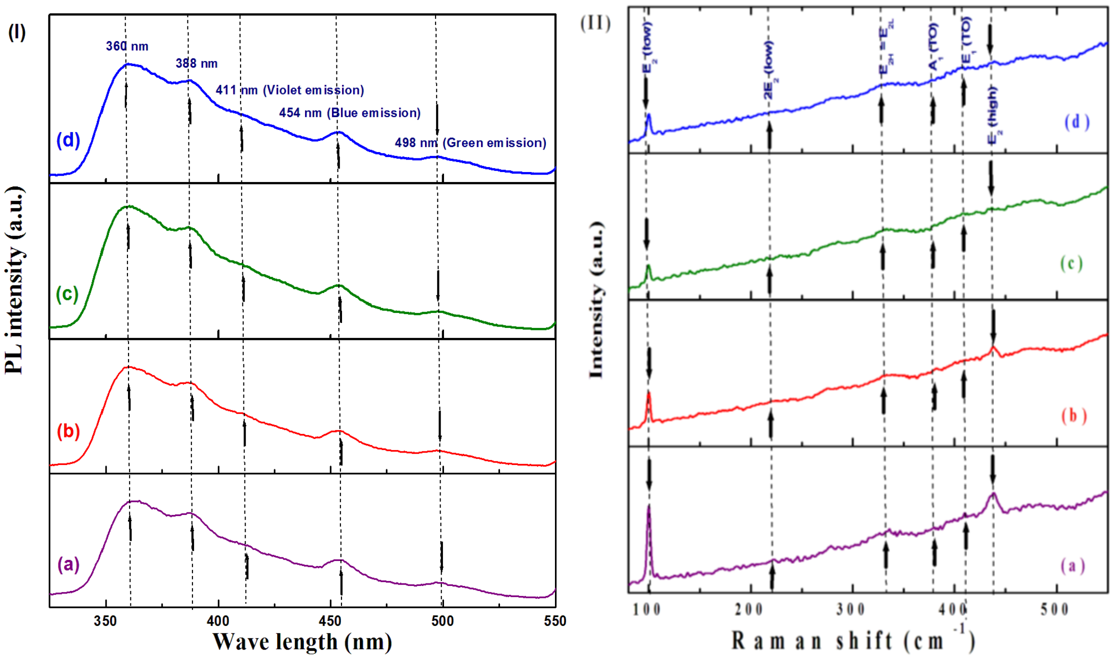

Fig. 3.4 (I) Photoluminescence spectra of the samples (a) ZnO, (b) ZnOY3, (c) ZnOY5 and (d) ZnOY7 and (II) Characteristic Raman vibrational modes of the samples (a) ZnO, (b) ZnOY3, (c) ZnOY5 and (d) ZnOY7.

3.3.5 Static magnetic measurement

The Magnetization (M) vs. Field (H) data for all the samples within the applied magnetic field of 0-50 kOe have been studied at different temperatures (300K, 150K and 10 K) using SQUID magnetometer. ZnOY3 and ZnOY7 show ferromagnetic (FM) phase including almost saturation magnetization for the M-H curve at RT (see Figs. 3.5a, and f). The measured hysteresis loops at low temperature (10 K) are not saturated implying the co-existence of paramagnetic (PM) and ferromagnetic (FM) phase [46,47]. At lower temperatures, the PM contribution is larger than the FM contribution. The hysteresis loops of ZnOY5 are unsaturated for all temperatures even at the highest applied magnetic field, this suggests the co-existence of PM phase with FM phase for all temperatures (Figs. 3.5c, d and e). This result is incompatible with the results gained by the various other researchers. As for example, Liu et al. investigated for V-doped ZnO nanoparticles where PM phase dominates over weak FM phase [48]. Jing et al. obtained for Er-doped ZnO system where they report co-existence of PM and FM phase in their work [49]. The magnetic information such as maximum magnetization (M_{max}), remanent magnetization (M_r) and coercive field (H_c), extracted from the hysteresis loops of all the Y^{3+} ions doped ZnO samples have been shown in Table 3.3. Identical results established by other researchers, for Nd doped ZnO and transition metal ions doped ZnO nanoparticles have also been reported previously [50, 51]. According to the previous literatures, the no. of structural defects/oxygen vacancy is an undeniable factor about the origin of ferromagnetism in Y^{3+} ions doped ZnO at RT. The presence of single wurtzite structure without secondary phases for all the Y^{3+} ions doped ZnO samples have been verified from FTIR, Raman spectra and PL spectra. So, the contribution of secondary impurity on the magnetic data can be eliminated in the present case. The detected ferromagnetism must not appear from carrier-mediated technique because electron concentration in Y^{3+} ions doped ZnO samples is low which is established by the dielectric property study later on in the report. The dielectric constant of all the samples exhibits semi-insulating nature which doesn’t match with the theory given by Dietl et al. [52]. The theory behind intrinsic ferromagnetism in ZnO nanostructure is still under scanner, though the defects are treated as the most vital factor which plays an essential role in ferromagnetism.

The electronic structure and formation energies of point defects in ZnO nanostructures have been calculated using the first-principle potential method, by Kohan et al. [53]. Their calculation proved that, oxygen vacancy and zinc vacancy (V_o and V_{Zn}) are the two most common defects in ZnO. The formation energy for oxygen vacancy (V_o) is lower when compared to that of zinc vacancy (V_{Zn}) and must be abundant in Zn-rich conditions, so as zinc vacancy (V_{Zn}) should command in O-rich conditions. So, it can be concluded that a part of oxygen vacancy and abundant zinc vacancy co-exist in the Y^{3+} ions doped ZnO nanoparticles. As the doping of trivalent ions induce huge oxygen vacancy (V_o), the contribution of oxygen vacancy (V_o) is greater than zinc vacancy (V_{Zn}) for the dilute ferromagnetism [54].

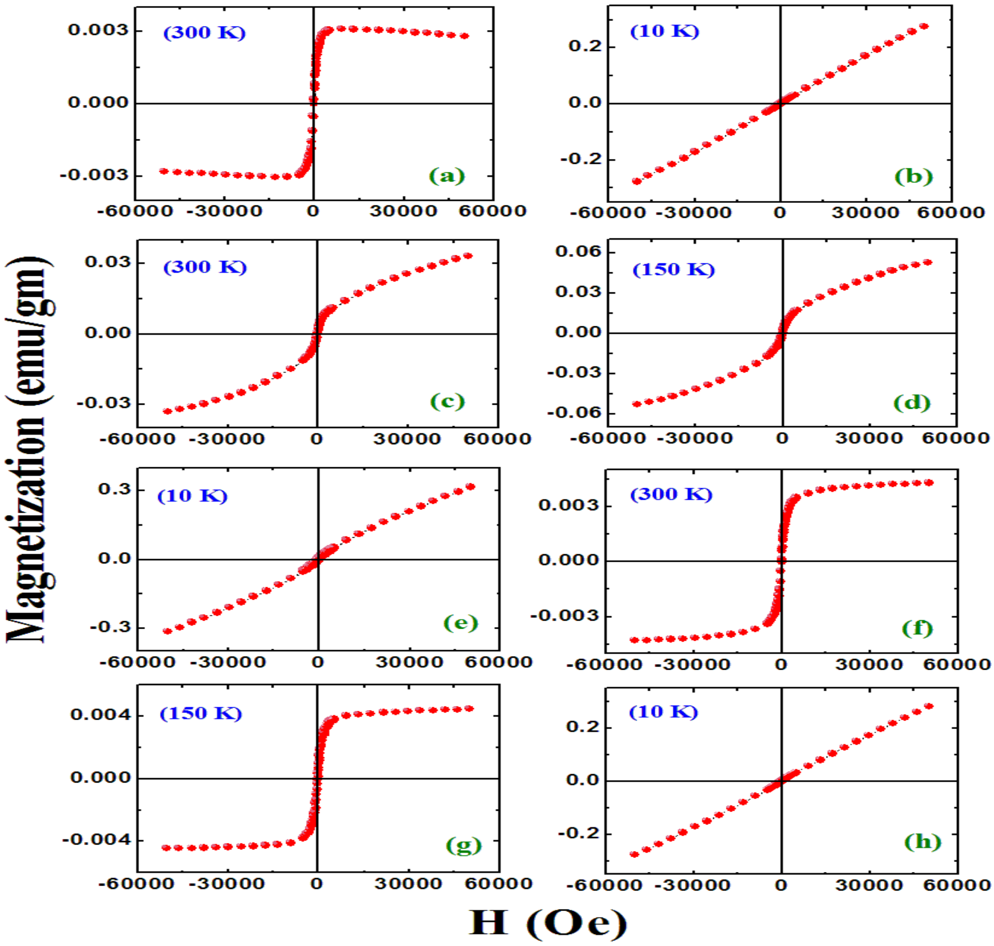

Fig. 3.5 Static hysteresis (M-H) loops of different sample ZnOY3 (a) 300 K and (b) 10 K, ZnOY5 (c) 300 K, (d) 150 K and (e) 10 K and ZnOY7 (f) 300 K, (g) 150 K and (h) 10 K.

Coey et.al. introduced BMP model to explain ferromagnetism by taking into consideration the dopant density and unsaturated hysteresis loop at low temperatures which might be suitable for low conductive or high resistive (as viewed from dielectric nature) samples with confined carriers [55]. In this case, a localized electron in oxygen vacancy (V_o) plays a significant role for the spin orientations of neighboring Y^{3+} ions. The exchange interaction of oxygen vacancies (V_o) with Y^{3+} ions and some of the Y^{3+} spins are aligned around the oxygen vacancies (V_o) which forming the BMPs. If sufficient oxygen vacancies (V_o) are not present in the sample, adjacent Y^{3+} ions are coupled by oxygen bond (super exchange interaction), initiating magnetic ordering destruction.

Hence, oxygen vacancies (V_o) lead a crucial role in RTFM. Coey's model suggests that the recorded magnetization due to interaction between BMPs can be written as [56]

$$\mathrm{M} = \mathrm{M_0 L(x)} + \chi_{\mathrm{m}}\mathrm{H} \tag{3.7}$$

The first term represents the contribution owing to BMP and the second term denotes the paramagnetic part [57]. The equation mentioned above shows that the sample is perceived by the mixed-up state of BMPs where trapped electron strongly interacts with Y^{3+} ions. The no. of Y^{3+} ions which don't participate in the BMP interaction are assumed to be an independent paramagnetic component that contributes to paramagnetism.

Also, the spontaneous moment of the system may be described as

$$M_0 = N m_s \tag{3.8}$$

Where the term m_s represents the actual spontaneous moment of each BMP and N signifies the number of BMPs per unit volume. The Langevin function is written as

$$(x) = \ coth x - \frac{1}{x} \tag{3.9}$$

Here, the term x can be written as

$$x = {}^{Hm_{eff}}\!\big/_{TK_B} \tag{3.10}$$

Where, m_{eff} is the effective spontaneous magnetic moment of each BMP. It is to be noted here that the interaction between the BMPs have ignored and thus fitting technique is done by pretending$m_s = m_{eff}$.Figs. 3.6(a-c) denotes the fittings of M-H curve of all the samples at RT. It is noticeable from the fitting that the paramagnetic contribution for ZnOY5 sample is nearly ~ 40 times larger than other two samples.

Due to the presence of PM phase, the hysteresis loop at room temperature of ZnOY5 does not attain to the saturation value as compare to the other two doped samples. For all the samples the BMPs concentration is of the order of ~ 10^{13}-10^{14} at RT, whereas the temperature decreases the BMPs concentration increases sharply around ~ 10^{17}-10^{18}. The Y^{3+} ions are distributed as isolated BMPs or uncoupled spin and leads to a fraction of BMPs may overlap which results PM phase mixed with FM phase. At lower temperature, the number of polaron increases and over lapping of this polaron contributes to FM and there by a clear hysteresis loop with larger magnetization, coercivity and remanence have been recorded for some samples. Although, with the decrease of temperature the paramagnetic contribution increases that leads to the robust increase of magnetization along with non-saturation of hysteresis loop. At lower temperature, the low value of m_{eff} can be attributed to the reduced size of the BMPs [58]. The presence of competing magnetic interaction might have reduced BMP size [59]. The variation of Y^{3+} ions in ZnO host matrix may be assumed as (i) Y^{3+} ions coupled with AFM which have minimum one neighboring Y^{3+} ions, (ii) isolated Y^{3+} ions behaving paramagnetically which contribute to magnetization at lower temperature and (iii) the Y^{3+} ions couple with donor electrons associated with defects behave ferromagnetically. Modification of Y^{3+} ions in ZnO host matrix favor variations in the character of magnetic coupling, leading to a change of magnetic state. The average distance between two neighboring Y atoms in ZnOY7 decreases with the increasing number of Y^{3+} ions (7 wt %) which leads to direct exchange interaction. As the Y d-states overlap with the valence band, the coupling between Y-Y neighbors in ZnO is assumed to be antiferromagnetic. Hence, concentration of Y^{3+} ions above 5% increases the antiferromagnetic exchange interaction between neighboring Y^{3+} ions thus resulting in the reduction of magnetization of ZnOY7 sample as compared to the others.

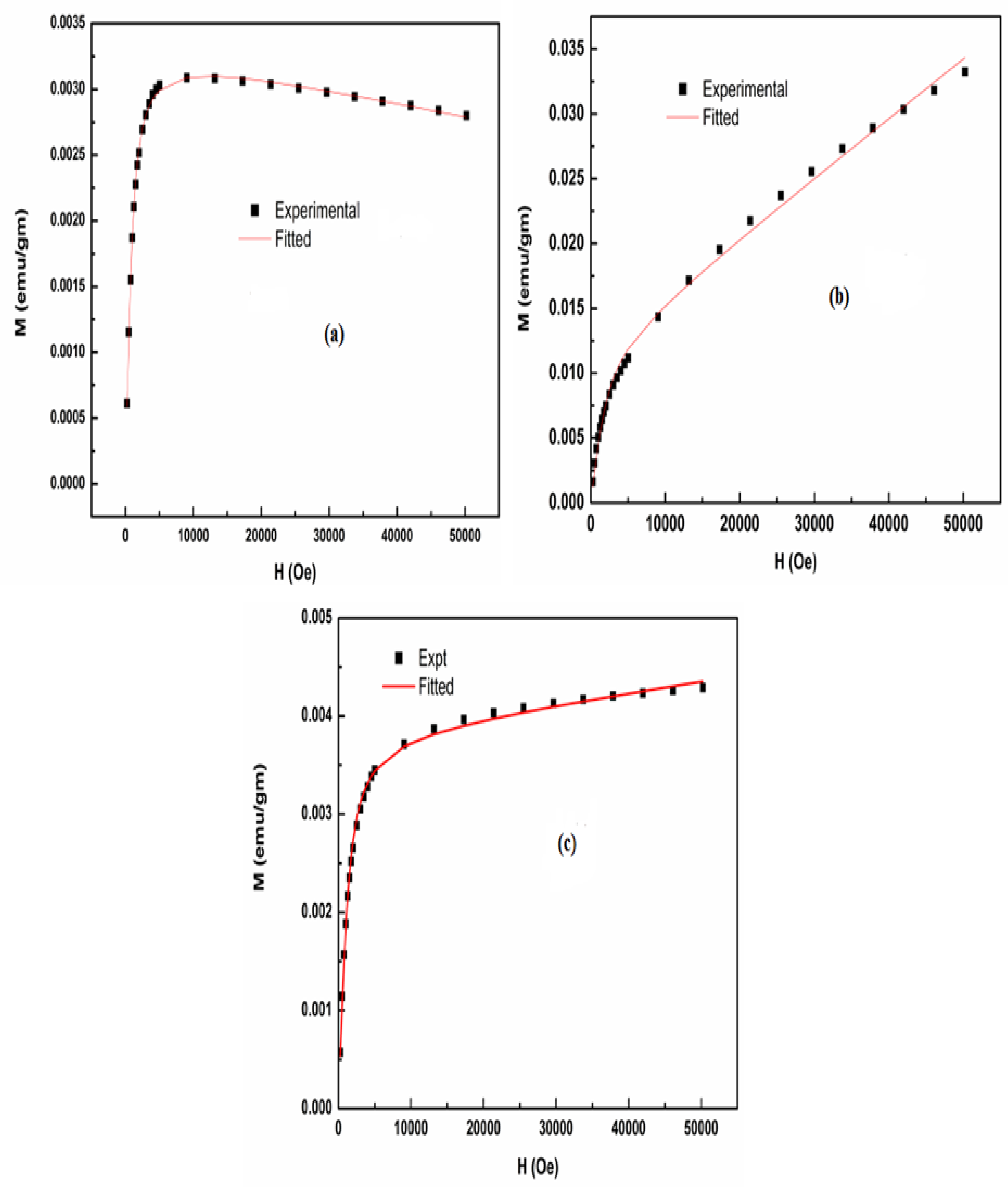

Fig. 3.6 Initial Magnetization vs field curve fitted by BMP model at 300 K (a) ZnOY3, (b) ZnOY5 and (c) ZnOY7.

Table 3.3. Maximum Magnetization (M_{max}), Remanence (M_r), Coercivity (H_c) of ZnOY3, (b) ZnOY5 and (c) ZnOY7 recorded at different temperature from 300 K to 10K.

Sample ID	Measuring Temperature (T) (In K)	Maximum Magnetization (M_{max}) (emu/g)	Remanence (M_r) (emu/g)	Coactivity (H_c) (Oe)
ZnOY3	300	0.0028	0.000165	59.18
	10	0.2755	0.000720	89.44
ZnOY5	300	0.0334	0.000662	80.05
	150	0.0530	0.000730	155.97
	10	0.3173	0.006301	464.25
ZnOY7	300	0.0043	0.000108	40.25
	150	0.0044	0.000365	124.30
	10	0.2809	0.001070	160.13

3.3.6 Dielectric measurement

The effect of temperature dependent applied alternating electric field with dielectric constant (ε′) and loss tangent (tanδ) of all samples have been recorded. To understand the reality of storing ability of electrostatic energy and dissipation of energy, the value of dielectric constant (ε′) and loss tangent (tanδ) have been recorded applying alternating electric field. For all samples, the real part of complex permittivity (ε′) has been determined by using the formula

$$\varepsilon' = \frac{Cd}{\varepsilon_0 A} \tag{3.11}$$

Where, C is capacitance, d is thickness and A is area, respectively of the pelletized sample and ε_0 is the permittivity at free space. The variation of frequency dependent (ε') at various temperature for undoped and Y^{3+} ions doped ZnO nanoparticles, in the frequency range of 40 Hz to 10^6 Hz is shown in Fig.3.7. The electron hopping between Y^{3+} and Zn^{2+} ions in the doped ZnO nanostructure acting as electric dipoles under the applied alternating electric field causes large value of real part of dielectric constant (ε'). The dielectric behavior can also be explained on the basis of Maxwell-Wagner type of relaxation. Also, electronic, ionic, dipolar and space charge polarization etc. remarkably contribute to the dielectric value of the samples. The high value of dielectric constant at low frequency region can be attributed to the space charge polarization. Different types of polarization are originating from various defects like oxygen vacancies, grain boundary defects etc. for Y^{3+} ions doped ZnO nanostructures. The observed value of real part of dielectric constant (ε') decreases with increasing frequency and becomes frequency independent at higher frequency region [60,61]. The polarization is decreasing with increase in frequency as it is lagging behind the external electric field because the hopping of electrons goes out of phase with the external applied alternating electric field at the higher frequency region. Fig. 3.8 represents the frequency dependent dielectric loss ($\tan\delta$) in the range from 40 Hz to 10^6 Hz for various temperatures. The energy dissipation is represented by dielectric loss ($\tan\delta$) in the system. Initially the dielectric loss increases with increase in frequency and beyond a certain value it decreases with the increase in frequency for all samples due to the occupancy of space charge polarization in the nanostructured samples. Although, the dielectric loss is lower for 3% and 5% Y^{3+} ions doped ZnO as compared to the undoped ZnO nanoparticles and for 7% Y^{3+} ions doped ZnO nanoparticles, it increases again. Therefore, for high frequency device applications Y^{3+} ions doped ZnO nanostructure can be adapted. The real part of dielectric constant (ε') with the variation of temperature in the range from 30 ^{o}C to 350 ^{o}C has been shown in Fig. 3.9. For three different frequencies i.e., 1 kHz, 10 kHz and 100 kHz, respectively, the measurement has been recorded. Ferroelectric to paraelectric transition is occurred for all samples but the transitional temperatures are different for each sample [62]. It can be mentioned that due to the presence of interfacial polarization the real part of the dielectric constant is very high.

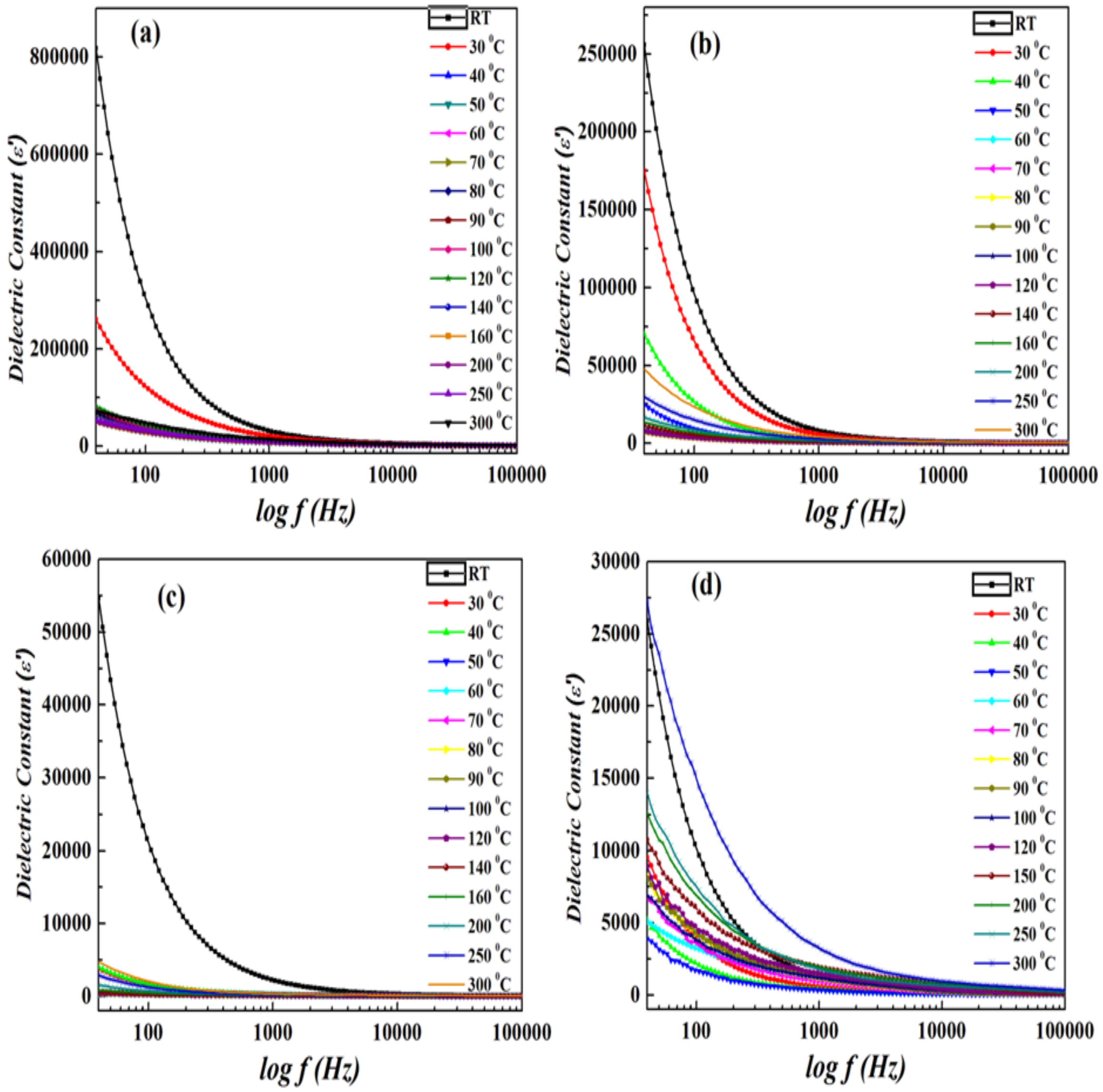

Fig. 3.7 Variation of Dielectric constant with frequency for samples (a) ZnO, (b) ZnOY3, (c) ZnOY5 and (d) ZnOY7.

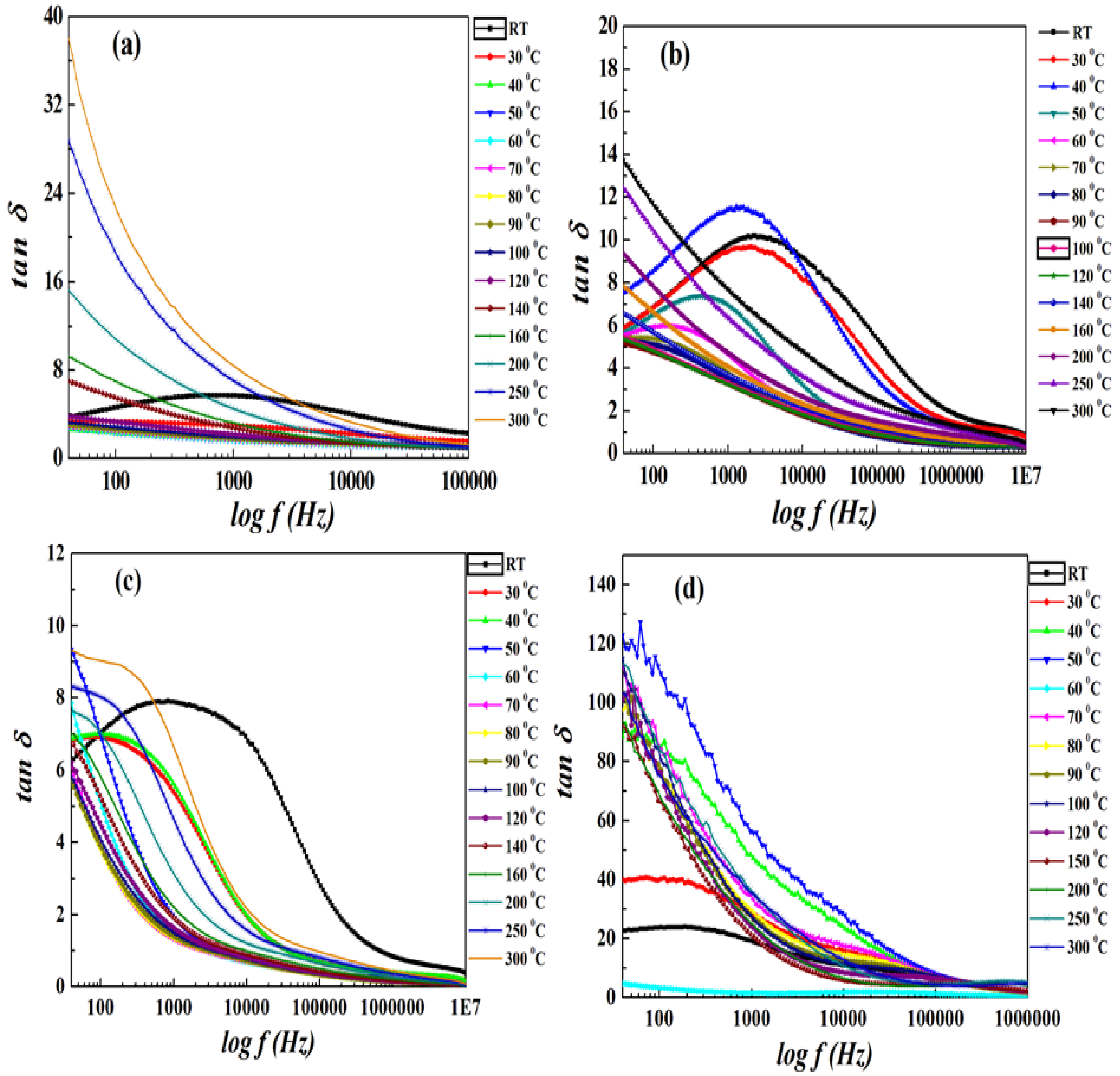

Fig. 3.8 Plot of loss tangent (tanδ) vs frequency at different temperature for the samples (a) ZnO, (b) ZnOY3, (c) ZnOY5 and (d) ZnOY7.

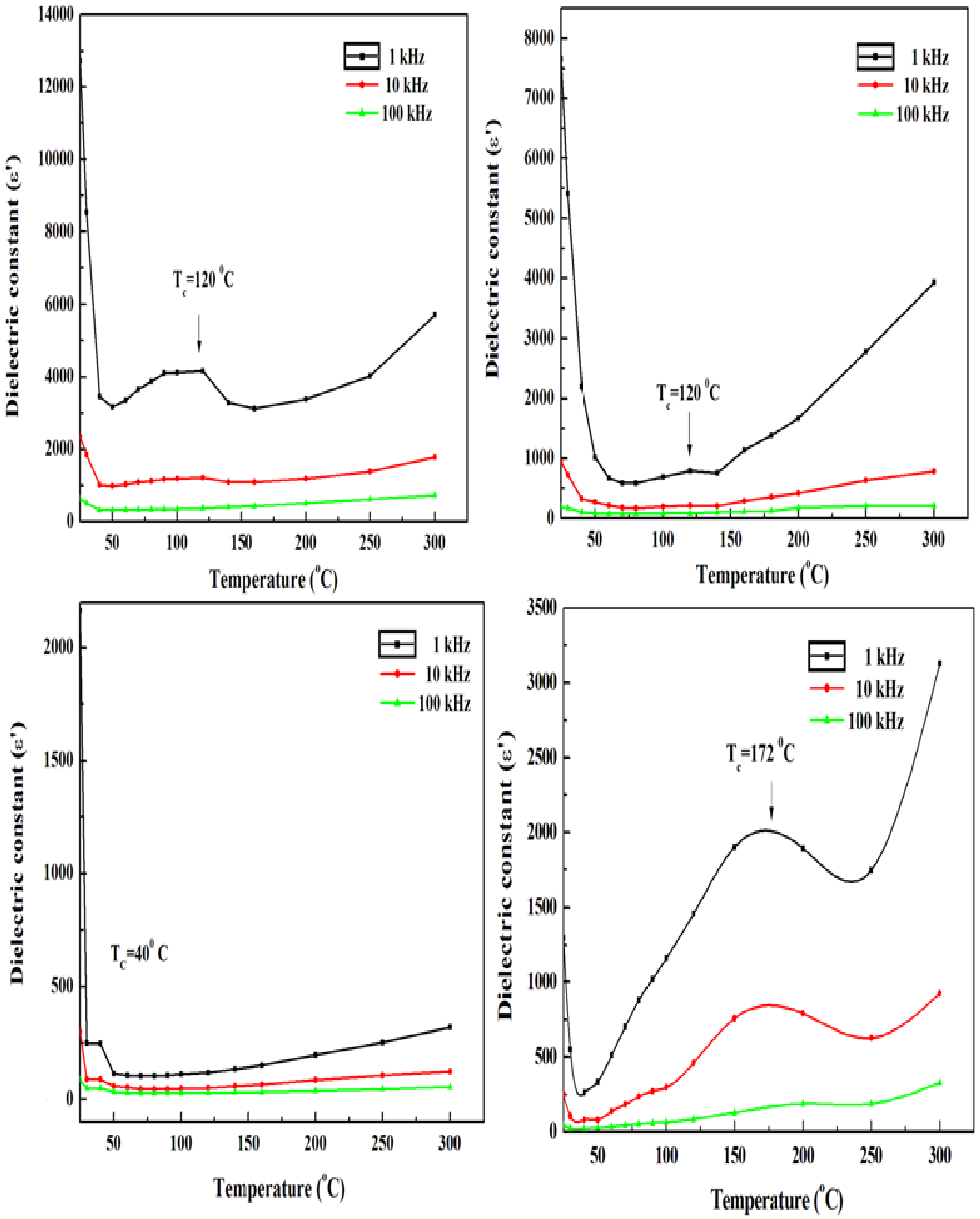

Fig. 3.9 Variation of dielectric constant with temperature for the samples (a) ZnO, (b) ZnOY3, (c) ZnOY5 and (d) ZnOY7.

3.4 Conclusions

By using co-precipitation method followed by hydrothermal synthesis route, Y^{3+} ions doped ZnO nanoparticles have been synthesized successfully. The connection between the induced intrinsic defects in Y^{3+} ions doped ZnO nanorods and the structural, optical, magnetic and dielectric properties have been investigated properly in the present study. It can be noted that the doping of Y^{3+} ions in ZnO host lattice leads to the increase of various intrinsic defects which induces structural, optical, magnetic and dielectric properties study. The crystallization is lowered by the doping of Y^{3+} ions properly in the ZnO nanorods which is suggested by the XRD spectra. The doping of Y^{3+} ions generate more intrinsic defects in the ZnO nanorods which has been proved by increase in visible emission of PL spectra at room temperature and E_1(LO) intensity of Raman spectra. The magnetization data demonstrates room temperature ferromagnetism in doped ZnO nanorods together with a maximum coercivity for 5% Y^{3+} ions doped sample. The dielectric study reveals that the nanostructured ZnO are acceptable for high frequency device applications. Finally, all measurements demonstrate that the defects are vital and enhance the RT ferromagnetism by selecting proper doping percentage.

Reference

[1] Z.L. Wang, J. Phys.: Condens. Mat. 16 (2004) 829.

[2] N. Tahir, A. Karim, K.A. Persson, S.T. Hussain, A.G. Cruz, Md. Usman, Md. Naeem, R. Qiao, W. Yang, Y.D. Chuang, Z. Hussain, J. Phys. Chem. C 117 (2013) 8968.

[3] G. Li, H. Wang, Q. Wang, Y. Zhao, Z. Wang, J. Du, Y. Ma, Nano. Research Lett. 10 (2015) 112.

[4] V. Gandhi, R. Ganesan, H.H.A. Syedahamed, M. Thaiyan, J. Phys. Chem. C 11 (2014) 9715.

[5] C. Wu, L. Shen, Y.C. Zhang, Q. Huang, Materials Lett. 65 (2011) 1794.

[6] L.W. Yang, X.L. Wu, T. Qiu, G.G. Siu, P.K. Chu, J. Appl. Phys. 99 (2006) 074303.

[7] K. Jayanthi, S. Chawla, A.G. Joshi, Z.H. Khan, R.K. Kotnala, J. Phys. Chem. C 114 (2010) 18429.

[8] G.M. Kumar, P. Elanchezhiyan, J. Kawakita, M. Subramanian, R. Jayavel, Cryst. Eng. Comm. 12 (2010) 1887.

[9]F.F. Comjani, U. Willer, S. Kontermann, W. Schade, Phys. Status Solidi A 210, 10 (2013) 2219.

[10]C. Xu, K. Yang, Y. Liu, L. Huang, H. Lee, J. Cho, H. Wang, J. Phys. Chem. C 112 (2008) 19236.

[11] L. Mino, D. Gianolio, F. Bardelli, C. Prestipino, E. S. Kumar, F. Bellarmine, M. Ramanjaneyulu, C. Lamberti, M.S. Ramachandra Rao, J. Phys.: Condens. Matter, 25 (2013) 385402.

[12]C.X. Mei, J. Yong, G.X. Yong, Z.X. Wei, Chin. Phys. B 21 (2012) 116801.

[13]Z. Zhang, K.E. Knutsen, T. Merz, A.Y. Kuznetsov, B.G. Svensson, L.J. Brillson, J. Phys. D: Appl.Phys. 45 (2012) 375301.

[14]S. Sarkar, D. Basak, RSC Adv. 4 (2014) 39095-39100.

[15]C.S. Kim, Y.B. Chung, W.K. Youn, N.M. Hwang, Aerosol Science and Technology 43 (2009) 120.

[16] D.K. Hwang, M.S. Oh, J.H. Lim, Y.S. Choi, S.J. Park, Appl. Phys. Lett 91 (2007) 121113.

[17] G. Visimberga1, E.E. Yakimov, A.N. Redkin, A.N. Gruzintsev, V.T. Volkov, S. Romanov, G.A. Emelchenko, Phys. Status Solidi C 7 (2010) 1668.

[18] C.H. Chen, S.J. Chang, S.P. Chang, M.J. Li, I.C. Chen, T.J. Hsueh, C.L. Hsu, Chem. Phys. Lett. 476 (2009) 69.

[19] C.C. Lin, W.H. Lin, C.Y. Hsiao, K.M. Lin, Y.Y. Li, J. Phys. D: Appl. Phys. 41 (2008)

045301.

[20] T. Zhang, Y. Zeng, H.T. Fan, L.J. Wang, R. Wang, W.Y. Fu, H.B. Yang, J. Phys. D: Appl. Phys. 42 (2009) 045103.

[21] A. Umar, A. Al-Hajry, Y.B. Hahn, D.H. Kim, Electrochem. Acta 54 (2009) 5358.

[22] B. Pal, P.K. Giri, J. Appl. Phys. 108 (2010) 084322.

[23] J.J. Wu, S.C. Liu, M.H. Yang, Appl. Phys. Lett. 85 (2004) 6.

[24] X.W. Zhang, W.J. Fan, Y.H. Zheng, S.S. Li, J.B. Xia, Appl. Phys. Lett. 90 (2007) 253110

[25] Z. Dai, A. Nurbawono, A. Zhang, M. Zhou, Y.P. Feng, G.W. Ho, C. Zhang, Chem. Phys. 134 (2011) 104706.

[26] P. Kaur, S.K. Pandey, S. Kumar, N.S. Negi, C.L. Chen, S.M. Rao, M.K. Wu, Appl. Nanosci. 5 (2015) 975-981.

[27] Z.Y. Chen, Z.Q. Chen, B. Zou, X.G. Zhao, Z. Tang, S.J. Wang, J. Appl. Phys. 112 (2012) 083905.

[28] J. Yun, R. Qu, Z. Zhang, J. Li, Adv. Condens, Matter Phys. 2014 (2014) 627975.

[29] R.T. Ginting, H.B. Lee, S.T. Tan, C.H. Tan, Md. H.H. Jumali, C.C. Yap, J.W.Kang, Md. Yahaya, J. Phys. Chem. C 120 (2016) 771.

[30] C.L. Pueyo, S. Dilger, M.R. Wagner, M. Gerigk, A. Hoffmann, S. Polarz, Cryst. Eng. Comm. 16 (2014) 1525.

[31] T.M. Hammad, J.K. Salem, R.G. Harrison, Nano 4 (2009) 225.

[32] I. Atriabak, A. Bueno-Lopez, A. Garcia-Garcia, J. Mol. Catal. A: Chem. 300 (2009) 103.

[33] J. Yang, R. Wang, L. Yang, J. Lang, M. Wei, M. Gao, X. Liu, J. Cao, X. Li, N. Yang, J. Alloys Compd. 509 (2011) 3606.

[34] J.H. Zheng, J.L. Song, Q. Jiang, J.S. Lian, Applied Surface Science 258 (2012) 6735.

[35] S.K. Sharma, D.Y. Kim, Journal of Materials Science & Technology 32 (2016) 12-16.

[36]S. Anandan, S. Muthukumara, Opt. Mater. 35 (2013) 2241.

[37] C. Gua, J. Huanga, Y. Wua, M. Zhaia, Y. Sunc, J. Liub, J. Alloys Compd.509 (2011) 4499.

[38] X. Wei, B. Man, J. Appl. Phys. 45 (2006) 8586.

[39] P.P. Murmu, J. Kennedy, B.J. Ruck, G.V.M. Williams, A. Markwitz, S. Rubanov, AIP Conf. Proc 1525 (2013) 300-304.

[40] J. Kennedy, P.P. Murmu, E. Manikandan, S.Y. Lee, J. Alloys Compd. 616 (2014) 614.

[41] P.P. Murmu, J. Kennedy, B.J. Ruck, S. Rubanov, Electronic Materials Letters 11 (2015) 998.

[42] J. Kennedy, B. Sundrakannan, R.S. Katiyar, A. Markwitz, Z. Li, W. Gao, Current Applied Physics 8 (2008) 291.

[43] R.P. Wang, G. Xu, P. Jin, Phys. Rev. B. 69 (2004) 113303.

[44] J.B. Wang, H.M. Zhong, Z.F. Li, W. Lu, J. Appl. Phys. 97 (2005) 086105.

[45] J.D. Ye, S.L. Gu, S.M. Liu, Y. Shi, Q. Chen, Appl. Phys. Lett. 88 (2006) 101905.

[46] J. Kennedy, G.V.M. Williams, P.P. Murmu, B.J. Ruck, Phys. Rev. B 88 (2013) 214423.

[47] P.P. Murmu, J. Kennedy, G.V.M. Williams, B.J. Ruck, S. Granville, S.V. Chong, Appl. Phys. Lett. 101 (2012) 082408

[48] S.H. Liu, H.S. Hsu, C.R. Lin, C.S. Lue, J.C. Huang, Appl. Phys. Lett. 90 (2007) 222505.

[49] J. Qi, D. Gao, J. Liu, W. Yang, Q. Wang, J. Zhou, Y. Yang, J. Liu, Appl. Phys. A, 100 (2010) 79.

[50] A. Dakhel, M. El-Hilo, J. Appl. Phys. 107 (2010) 123905.

[51] J. Anghel, A. Thurber, D.A. Tenne, C.B. Hanna, A. Punnoose, J. Appl. Phys. 107(2010) 314.

[52] T. Dietl, Nat. Mater.9 (2010) 965.

[53] A.F. Kohan, G. Ceder, D. Morgan,Phys. Rev. B 61 (2000) 15019.

[54] H. Shi, P. Zhang, S.S. Li, J.B. Xia,J. Appl. Phys. 106 (2009) 023910.

[55] J.M.D. Coey, M. Venkatesan, C.B. Fitzgerald, Nat. Mater. 4 (2005) 173.

[56] A. Bandyopadhyay, S. Sutradhar, B.J. Sarkar, A. K. Deb, P.K. Chakrabarti,Appl. Phys. Lett. 100 (2012) 25241.

[57] A. Bandyopadhyay, A.K. Deb, S. Kobayashi, K. Yoshimura, P.K. Chakrabarti,611 (2014) 324.

[58] S. Mohanty, S. Ravi, Solid State Communications 150 (2010) 1570.

[59] T. Bora, B. Samantaray, S. Mohanty,IEEE Transactions on Magnetics 47 (2011) 3991.

[60] S. Bhattacharya, S.K. Saha, D. Chakravorty, Appl. Phys. Lett. 76 (2000) 3896.

[61] M.K. Gupta, N. Sinha, B. Kumar,J. Appl. Phys. 112 (2012) 014303.

[62] M.K. Gupta, B. Kumar, J. Alloys Compd. 509 (2011)L208.

CHAPTER 4

Dielectric property study of undoped and Chromium doped semiconducting ZnO nanorods

4.1 Introduction

Since nanoparticles have small grain size, large grain boundary, large surface to volume ratio and quantum size effect, they have obtained much attention by different research groups on theoretical and experimental grounds as prominent research topic [1-3]. The modulation of structural symmetry, band gap, charge density, grain morphology, micro strain and various intrinsic defects due to the choice of selective synthesis mechanism and nature of dopants leads to the upgrade of physical properties of nanomaterials like microstructural, thermal, optical, magnetic and dielectric [4-7]. Recently, different semiconducting metal oxide nanoparticles e.g titanium oxide (TiO_2), indium oxide (In_2O_3), tin oxide (SnO_2), silicon oxide (SiO_2), zirconium oxide (ZrO_2), zinc oxide (ZnO) etc have been investigated comprehensively for their interesting physical properties and various device applications [8-20]. In this purpose, ZnO is an n type II-VI semiconducting material with a direct band gap of 3.37 eV and a high excitonic binding energy of 60 meV [21-23]. Though, doped ZnO nanomaterials can be both n-type and p-type in nature. Here, it is to be mentioned that the nature (n-type/p-type) of the semiconducting nanomaterials depends on the proper choice of dopant [24-30]. Various properties of ZnO nanoparticles can be regulated by the proper choice of doping technique and dopant [31-33]. The growth mechanism of nanomaterials and development of native defects in the nanostructures are heavily depends on the atomic radius and charge valance of state of the selected dopants. We have demonstrated that dopants having 3^+ valance state produces various types of vacancies such as oxygen and zinc vacancies in our earlier publication [5,12]. These defects oriented vacancies give rise to quantum confinement by decreasing the average size of ZnO nanoparticles which leads to the change in band gap towards a higher frequency region generally known as blue shift [34,35]. Room temperature ferromagnetism in doped ZnO nanoparticles is observed due to the presence of oxygen vacancy [36]. By selecting proper dopant and doping mechanism, the defects modulated grain size, oxygen vacancies, zinc vacancies, zinc interstitials and dandling bond, etc. are the important factor to enhance the dielectric property of ZnO nanoparticles. The synthesis route such as sol-gel method, co-precipitation method, hydrothermal method, mechanical milling method, solid state reaction method, pulsed laser deposition method etc. plays an important role to modulate the physical and chemical properties like high electron mobility, superior chemical stability and excellent optical emission [37-40]. These nanostructured ZnO nanoparticles are efficient to produce ultraviolet and photovoltaic device applications like field emitters, photo detectors, nano lasers, light emitting diodes, chemical sensors and supercapacitors etc [41-49]. Also the modulation of physical properties of ZnO is expected in the desired direction by proper choice of metal ions (Cu^{2+}, Ni^{2+}, Co^{2+}, Mn^{2+} etc.) as well as rare earth ions (Er^{3+}, Eu^{3+}, Gd^{3+}, Yb^{3+}, Sm^{3+}, Tb^{3+} etc.) [50-53]. In our present work, undoped and Cr^{3+} ions doped ZnO nanomaterials have been synthesized by using hydrothermal technique. It has already been proved by other research groups that by using hydrothermal synthesis tecnnique morphology of the nanoparticles can be modulated to rod like and cylindrical structure [54-58]. Such rod like morphology plays an important role for modulation of physical properties. The dielectric properties of undoped and doped ZnO synthesized by hydrothermal process is the main feature of our present work as compared to the dielectric properties studied by earlier research work in various synthesis mechanism. In this report, we have focused on synthesis dependent dielectric property. In this work, modulation of various physical properties such as optical, magnetic and dielectric has been done by doping with chromium (Cr) ions. As the radius of Zn^{2+} (0.74 Ǻ) is larger as compared to the radius of Cr^{3+} (0.63 Ǻ), the doping with Cr^{3+}ions at the lattice point of wurtzite structure of ZnO produces large amount of micro strain and various defects inside the lattice. The amount of free charge density consist at the surface of the poorly conducting grain boundaries in the ZnO nanomaterials in presence of the externally applied electric field has been developed by using the selective cationic dopant i.e. Cr^{3+} ions. Also, various intrinsic defects such as oxygen vacancy, zinc vacancy, interstitials and dandling bond etc. are attributed to substitution of Cr^{3+} ions. These various intrinsic defects and the increase of charge density in the ZnO lattice structure are modulated due to the selection of proper hydrothermal synthesis mechanism and existence of both ionic radius dissimilarity and 3^+ vacant sites of the chromium atoms. Also, due to the reliable usefulness in the memory device and other applications, optimized ferromagnetic behavior of doped ZnO nanomaterials of two cations have been investigated [59-60]. In our present work, the dielectric properties of undoped and Cr^{3+} ion doped ZnO nanoparticles have been investigated.

4.2 Experimental

4.2.1 Materials:

Undoped and doped ZnO nanomaterials of $Zn_{1-x}Cr_xO$ (x = 0.03, 0.05 and 0.07) have been synthesized by co-precipitation process and there after followed by hydrothermal synthesis route for controlled nucleation. The preparation method was also shown in our earlier work [5,12]. The precursor materials, Zinc acetate dehydrate $Zn(O_2CCH_3)_2{\cdot}2H_2O$ (Sigma Aldrich, 99%), chromium acetate $Cr(CH_3COO)_3$ (Sigma Aldrich, 99%) and ammonium hydroxide NH_4OH (concentration ~ 25%) with analytical grade have been used without further purification.

4.2.2 Synthesis of Cr^{3+} ions doped ZnO nanoparticles by co-precipitation method

Cr^{3+} ions doped ZnO nanomaterials have been synthesized by co-precipitation method. Zinc acetate dihydrate $Zn(CH_3COO)_2{\cdot}2H_2O$ and chromium acetate $Cr(CH_3COO)_3$ are the precursor materials grasped in a beaker with distilled water and placed it on a magnetic stirrer. The percentage of chromium salt is fixed at three concentrations as 3, 5, and 7% to that of the zinc salt. To get the homogeneous solution of the mixed precursor salt, it has been stirred for several hours. Then NH_4OH solution has been added to the previous solution for precipitation and the final ph kept at ~ 10. After rigorous stirring, the newly produced colloidal suspension of $Zn(OH)_2$ for undoped ZnO and colloidal mixture of $Zn(OH)_2$ and $Cr(OH)_3$ for Cr^{3+} doped ZnO have been collected. To eliminate the extra ions and to neutralize the pH value of the co-precipitated particles washing has been done many times by using distilled water and ethyl alcohol.

4.2.3 Nucleation of Cr^{3+} ions doped ZnO nanoparticles by hydrothermal process

The newly produced colloidal solutions of different samples have been dissolved in 40 ml of triple distilled water and taken into a Teflon jacket that has been taken in the autoclave which is placed in an oven at 160 ^oC for 2 days. Under the effect of high pressure of air present in the Teflon jacket, the nucleation process of undoped and Cr^{3+} doped ZnO nanoparticles has been initiated towards rod like structure. The surface and the interfacial growth of undoped and Cr^{3+} ions doped ZnO into rod like structures have been favoured by the ambience inside the Teflon. After the nucleation, the autoclave has been allowed to cool down to RT naturally. After removing the supernatant, the suspension has been collected and washed many times to remove unreacted ions with distilled water. The nanoseeds are then dried at RT keeping these in a vacuum desiccators. Now to acquire crystallographic phase and to remove the unreacted precursor, the dried powder has been sintered at 400 ^oC in vacuum atmosphere. Table 4.1 shows the sample name and corresponding sample specifications.

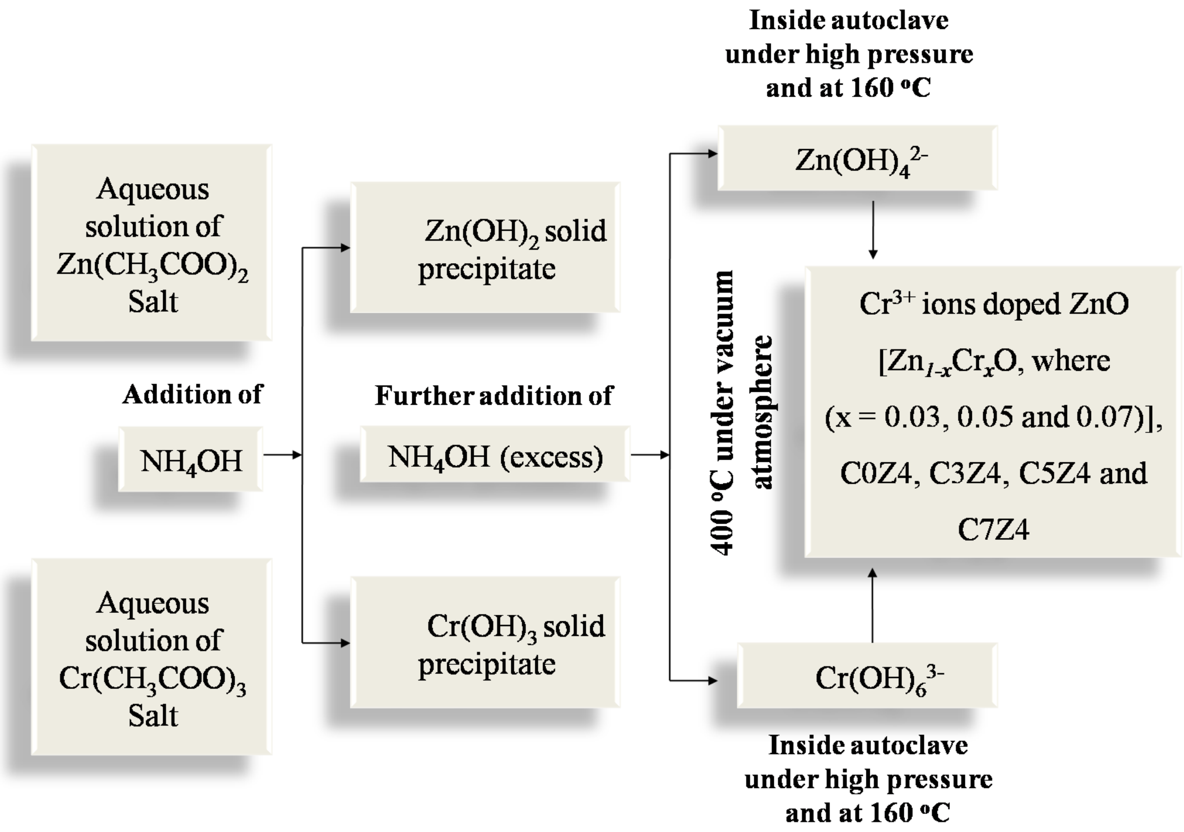

Fig. 4.1 Flowchart of the preparation of undoped and Cr^{3+} ion doped ZnO by hydrothermal synthesis route.

Table 4.1. The sample name and the corresponding sample specifications for undoped and Cr^{+3} ions doped ZnO samples.

Sample name	Sample specification
PZ4	undoped ZnO sintered at 400 °C
CZ34	3% Cr^{3+} ions doped ZnO ($Zn_{0.97}Cr_{0.03}O$) sintered at 400 °C
CZ54	5% Cr^{3+} ions doped ZnO ($Zn_{0.95}Cr_{0.05}O$) sintered at 400 °C
CZ74	7% Cr^{3+} ions doped ZnO ($Zn_{0.93}Cr_{0.07}O$) sintered at 400 °C

4.2.4 Characterization techniques

The XRD pattern has been recorded in the range of 2θ from 20 to 80° for all the samples in powder X-ray diffractometer, Model D8, BRUKER AXS, using Cu K_α radiation (λ = 1.5405 Å). For morphological study, Field emission scanning electron microscope (FESEM) has been employed using INSPECT F50 (FEI, Netherland). Using l25 spectrophotometer, Perkin Elmer, Germany, the absorption (UV-Visible) spectra of all the synthesized nanoparticles has been recorded in the range of 240-350 nm. Also, the photoluminescence (PL) emission spectroscopy study has been done with an excitation wavelength (λ_{ex}) of 300 nm by using a spectroflurometer, Perkin Elmer Germany. The dielectric measurements of all the samples have been executed by using Agilent 4294A Precision Impedance Analyzer.

4.3 Result and discussions

4.3.1 XRD analysis

Fig. 4.2 depicts the X-ray diffraction of undoped ZnO assigned as PZ4 and Cr^{3+} ions doped ZnO nanostructures assigned as CZ34, CZ54 and CZ74 respectively. For undoped and Cr^{3+} ions doped ZnO nanoparticles, position and relative intensities of diffraction peaks match very well with the hexagonal wurtzite structures of ZnO (space group $P6_3mc$) and also the peaks have been designated with the JCPDS (file no. 36-1451). Also, no other impurity phase has been identified in the XRD patterns which suggests that the doping of Cr^{3+} ions at the tetrahedral site of ZnO wurtzite structure is homogeneous.

For undoped and Cr^{3+} ions doped ZnO nanomaterials, the average crystallite diameters have been calculated by broadening of peak (100) of each sample by executing the renouned Debye-Scherrer equation.

$$< D >_{(100)} = \frac{0.9\lambda}{\beta_{\frac{1}{2}}\cos\theta} \tag{4.1}$$

Here, D represents crystallite diameter, λ represents wavelength of incident X-ray beam, θ corresponds to Braggs angle, $\beta_{\frac{1}{2}}$ is full width at half maximum (FWHM) of (100) peak. For various samples the crystallite diameters (D) have been raised within the range of 34 to 40 nm. The interplaner spacing (d) of each sample have been calculated from the Bragg's equation.

$$2dsin\theta = n\lambda \tag{4.2}$$

Where 'n' represents order of diffraction, 'λ' signifies wavelength of X-rays and 'θ' shows the angle of diffraction. For undoped and Cr^{3+} ions doped ZnO, the lattice parameter has been calculated using the relation

$$\frac{1}{d^2} = \frac{4}{3}\frac{h^2+hk+k^2}{a^2} + \frac{l^2}{c^2} \tag{4.3}$$

Here 'a' and 'c' represent the lattice parameters and h, k and l represents the Miller indices, respectively. D signifies the interplaner spacing of specific plane (hkl). For PZ4, CZ34, CZ54 and CZ74 nanostructure, the crystallite diameters and the lattice parameters have been shown in Table 4.2 respectively. It is to mention here that both the said calculated value get decreased with the increase of doping percentage of Cr^{3+} ions. Along the (002) crystalline plane, the peak intensity of Cr^{3+} ions doped ZnO nanostructure reduces and the peak intensity along (100) crystalline plane increases with regard to the undoped nanoparticles. The accepted growth of doped ZnO nanostructure along (100) plane is recognized by the said change in crystalline plane which proves the proper substitution of Cr^{3+} ions inside the ZnO nanostructure. Due to existence of micro strain in the ZnO lattice by the substitution of Cr^{3+} ions, the change in crystallite diameter and lattice parameter have been observed. To maintain the charge equality, more and more amount of zinc vacancies would create with the increase of Cr^{3+} ions in the wurtzite ZnO nanostructure. Such kind of cationic vacancies/zinc vacancies induced by doping with Cr^{3+} ions are accountable for the reduction in crystallite diameter. The effective diameter of nanocrystallite has been decreased with respect to undoped ZnO is due to the fact that during substitution three Zn^{2+} ions get substituted by the two Cr^{3+} ions. The average nanocrystalline diameter decreases moderately with the increase of doping percentages of Cr^{3+} ions. This proves the proper substitution of Cr^{3+} ions in the host ZnO lattice. Also, the XRD pattern reveals that there is no unwanted impurity phase detect in any of the doped samples. The internal lattice strain inside the lattice structure of doped ZnO is due to difference in the dimension of ionic radius i.e. radius of Cr^{3+} ion (0.63 Å) is unmatched with the radius of Zn^{2+} ion (0.74 Å).

As compared to the undoped ZnO, the Cr^{3+} ions doped ZnO nanoparticles have larger internal lattice strain/micro strain (ϵ) and with the increasing of doping percentage of Cr^{3+} ions in the nanosructured ZnO, the internal lattice strain/micro strain is increases gradually.

Table 4.2 shows the values of the internal lattice strain/micro strain (ϵ) of all the samples using the relation

$$\text{Micro strain } (\epsilon) = \frac{\beta_{\frac{1}{2}} \cos\theta}{4} \tag{4.4}$$

Using the following equation, the volume of unit cell for hexagonal nanostructure has been calculated

$$V = 0.866 \times a^2 \times c \tag{4.5}$$

Also, with the increase of doping percentage of Cr^{3+} ions, value of the unit cell volume (V) is decreasing which indicates the proper substitution of Cr^{3+} ions in the tetrahedral site of ZnO nanomaterials.

The presence of several forms of defects in Cr^{3+} ions doped ZnO nanoparticles is signified by the Dislocation density (δ). It can be specified by the length of dislocation lines present per unit volume inside the lattice structure and can be calculated by using proper equation,

$$\delta = \frac{1}{D^2} \tag{4.6}$$

It is to be noted from the dislocation density (δ) value that the magnitude of dislocation density increases with the increase of doping percentage in the nanostructured ZnO. Hence the magnitude of defects increases with the increase of doping percentage.

Using the following formula, the Zn-O bond length has been measured

$$L = \sqrt{\frac{a^2}{3} + \left(\frac{1}{2} - u\right)^2 c^2} \tag{4.7}$$

Here, u is known as the positional parameter and can be measured from the following equation

$$u = \frac{a^2}{3c^2} + 0.25 \tag{4.8}$$

It can be observed that with the increase of Cr^{3+} ions in the ZnO nanostructure bond length increases gradually. Due to the proper substitution of the Cr^{3+} ions inside ZnO lattice, Cr-O bonds are also produced which have longer bond length than Zn-O bond. A comprehensive evidence of presence of irregularities/defects in doped ZnO nanostructure is proven by all the parameters bring out from the XRD analysis and thus helps the modulation of various physical properties significantly.

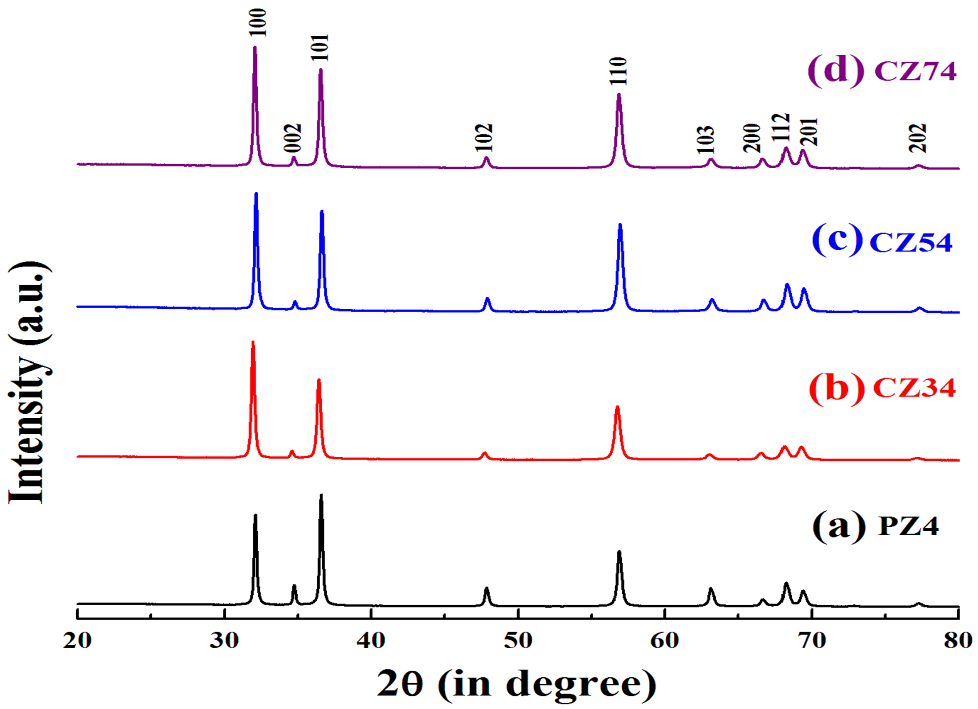

Fig. 4.2 XRD patterns of (a) PZ4, (b) CZ34, (c) CZ54 and (d) CZ74.

Table 4.2. Structural parameters are crystallite diameter (D), lattice parameters (a and c), micro strain (ε), unit cell volume (V), bond length (L) and dislocation density (δ).

Sample	Average crystallite diameter D (nm)	Lattice parameter (Å)		Micro strain (10^{-4})	Unit cell volume	Zn-O bond length (Å)	Dislocation density $(Å)^{-2}$
	(100)	a	c	ε	V $(Å)^3$		δ (10^{-6})
PZ4	39.62	3.24	5.18	8.787	47.09	1.9583	6.371
CZ34	36.47	3.23	5.17	9.581	46.71	1.9666	7.518
CZ54	35.83	3.21	5.15	9.671	45.95	1.9554	7.789
CZ74	34.73	3.20	5.13	10.022	45.49	1.9597	8.291

4.3.2 FESEM analysis

Different types of defects generated by the proper incorporation of Cr^{3+} ions in the ZnO nanostructure has been shown in the XRD analysis and these defects leads to the enrichment of the dielectric property. The growth mechanism of nanostructured ZnO is explained in the FESEM section shown in Fig. 4.3 with some representative micrographs. The growth mechanism of nanoparticles can be assumed to be the formation of growth units and comprising the growth units to form the crystal lattice at the interface. When the solution is taken under the autoclave, sufficiently high amount of growth units of $Zn(OH)_4^{2-}$ and $Cr(OH)_6^{3-}$ would have been developed at high pH value and at high temperature (~ 160 ºC). Under hydrothermal synthesis route, the growth units in the solution for undoped and doped ZnO have been shown in the Fig. 4.1. Now, due to the diffusion of ions and deregulation movement of molecules and ions, in the supersaturated solution, the growth units in the form of $Zn(OH)_4^{2-}$ and $Cr(OH)_6^{3-}$ are bounded by a dehydration reaction followed by a large size $Zn_iO_j(OH)_k^{(i-2j-2k)-}$ and $Cr_iO_j(OH)_k^{(i-2j-2k)-}$. Then the cluster of $Zn_iO_j(OH)_k^{(i-2j-2k)-}$ is precipitated when the critical size gains the value required for the development of ZnO nanoparticles. The subscript i, j and k demonstrate the numbers of Zn^{2+}, Cr^{3+}, O^{2-}, OH^- respectively. Then, due to the excessive surface energy and intermolecular forces, the ions are consumed in the primary nuclei to form the hexagonal rod like ZnO nanostructure from the nano seeds. Such types of morphology may be formed by high air pressure developed inside the Teflon jacket. Due to high pH value, the excessive NH_3 present in the solution generates high pressure. The adequate number of growth units will be diffused and decomposed into distinct rod like structure at such high pressure. In such way, the undoped and doped ZnO nanoseed grow into a rod like nano structure in this high pH and high pressure. The micrographs of all specimen are rod like in nature having hexagonal cross section which is the trademark morphology of ZnO nanoparticles by hydrothermal synthesis method been shown in the Fig. 4.3. The micrographs of PZ4 are rod like in nature and each rod is very much clear and distinguishable. The morphology of CZ54 is also rod like in nature shown in Fig. 4.3(b) which is similar to that of PZ4 but size of CZ54 microstructure is considerably large as compared to PZ4. From the XRD analysis, it has been found that the crystallite size of the doped ZnO decreases gradually with the increase of Cr^{3+} ions doping percentage as compared to the undoped ZnO but it is quite clear from the FESEM analysis that the size of the microstructure increases with the increase of Cr^{3+} ions doping. The fact is that, with the decreasing crystallite diameter of the nanoparticles the surface energy increases [47] and high surface energy provides the large growth rate of the crystallite at a certain temperature. As a result, the small nanocrystallites can generate large microstructure in hydrothermal process. Also the variation of microstructure with the increase in doping percentage of Cr^{3+} ions implies the proper incorporation of Cr^{3+} ions in the nanostructured ZnO. Although, for a particular sample all the nanorods in different micrographs are almost uniform in size.

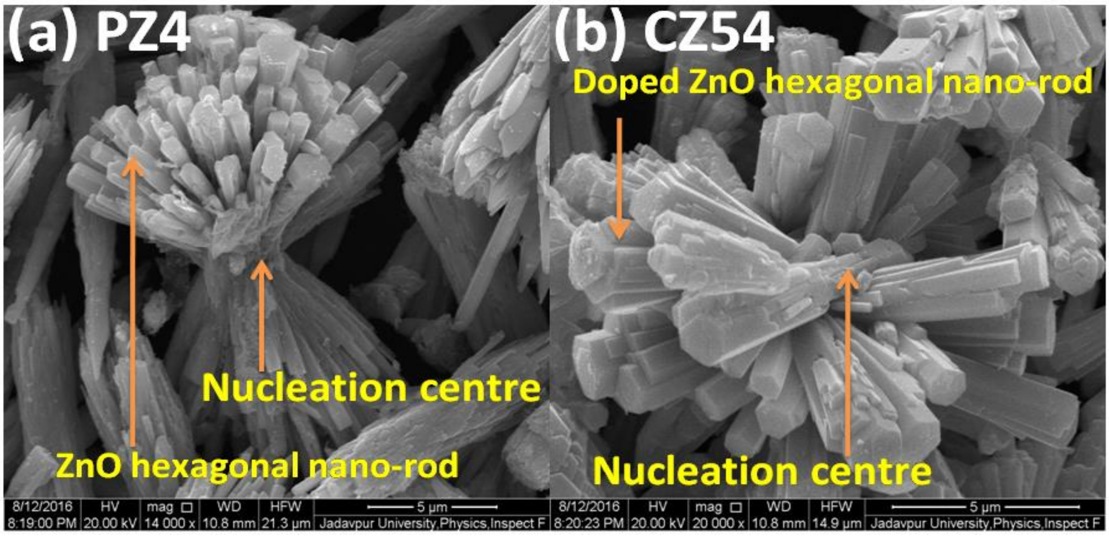

Fig. 4.3 SEM images of (a) PZ4 and (b) CZ54.

4.3.3 UV-Visible absorption study

To study the optical properties of direct band gap semiconductor, UV-Visible absorption spectroscopy has been introduced. By using UV-Visible absorption spectroscopy, the band energy gap of undoped ZnO and Cr^{3+} ions doped ZnO nanomaterials can also be evaluated. The defects develop within the nanomaterial by the doping of foreign elements changes the band energy gap of semiconducting materials. Fig. 4.4 depicts the absorption spectra of undoped ZnO and Cr^{3+} ions doped ZnO nanostructure measured in the wavelength range of 240-350 nm. With the increase of Cr^{3+} ions concentration within the ZnO lattice structure, different absorption peaks of doped ZnO with respect to the undoped ZnO show blue shift. The absorbance may vary with different key factors like particles size, oxygen vacancy, various defects in lattice structure and band gap etc. in the nanostructured ZnO.

The optical band gap of the ZnO nanoparticles has been calculated using the Tauc plot equation given below

$$\alpha h\nu = A(h\nu - E_g)^n \tag{4.9}$$

Here $h\nu$ is the photon energy, E_g is the optical band gap energy measured in eV respectively. The terms α denotes the absorption coefficient given by the equation, $\alpha = 2.303A/t$, here the constant A represents absorbance and t is the thickness of cuvett. Depending on the nature of electronic transition, the value of n = 1/2, 3/2, 2 or 3 and for direct band gap semiconducting material n = 1/2. The different values of optical band gap for different samples have been investigated on the linear region of $(\alpha h\nu)^2$ on the abscissa vs. photon energy ($h\nu$) by using the Tauc plot shown in Fig. 4.5. With the increase of Cr^{3+} ions in ZnO lattice leads to a increase in band gap energy from 4.32 to 4.40 eV that has also been reported by R. Mariappan et al [61]. The value of band energy gap of undoped nanostructured ZnO with respect to their bulk counterpart is comparatively higher which represents a clear blue shift in the absorption band and that can be assigned as well known quantum size effect of the direct band gap semiconducting materials, suggesting the increasing band gap with the decreasing particle size [62-64]. With the increase in Cr^{3+} ions doping percentage would create more and more zinc vacancies within nanostructured ZnO that has been expressed in the XRD section. The Cr^{3+} ions doped ZnO nanoparticles produces more and more cationic vacancies/zinc vacancies which leads to the decrease in particle size, lattice parameter and increase in the band energy gap that can be explained by Moss-Burstein effect. The n-type semiconducting ZnO have donor electrons. For Cr^{3+} ions doped nanostructured ZnO, to maintain the charge neutrality two Cr^{3+} ions substitute three Zn^{2+} ions. And now by releasing the two excess electrons present within the third oxygen (O^{2-}) becomes neutral. The resultant charge density of the doped nanostructured ZnO is increased by the excess electrons acts as donor electrons with the increasing in doping percentage of Cr^{3+} ions. Also, the donor electrons occupy the state at the bottom of conduction band in Cr^{3+} ions doped nanostructured ZnO. Pauli principle suggests that those electrons are confined to doubly occupied state. These valance electrons require extra energy to be transmitted to the higher energy state due to the vertical nature of the optical transition which leads to the broadening of band energy gap. Free charge carriers have been released in nanostructured ZnO when Cr^{3+} ions are substituted in the lattice structure. The top most electronic level of the valance band become unoccupied and the Fermi level transferred within the conduction band and there by filling all the electronic level just bellow it. Then, the absorption takes places between top valance band and Fermi level within the conduction band. The increase in band gap is observed due to the decreases in particle size is called quantum confinement and also the increase in free charge carrier or donor electrons within the nanostructure is called Moss-Burstein effect.

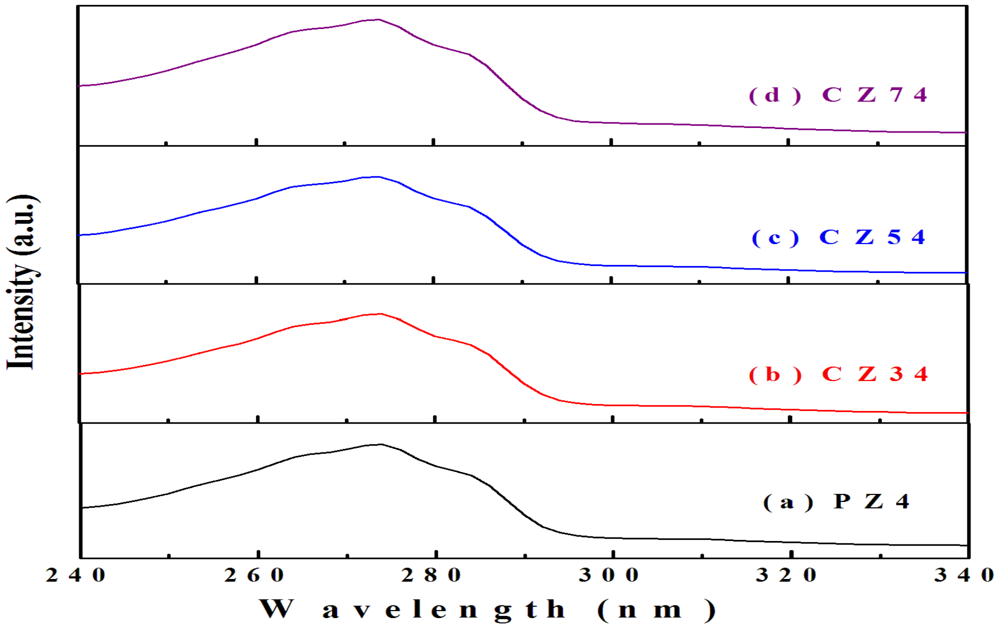

Fig. 4.4 UV-visible absorbance spectra of (a) PZ4, (b) CZ34, (c) CZ54 and (d) CZ74.

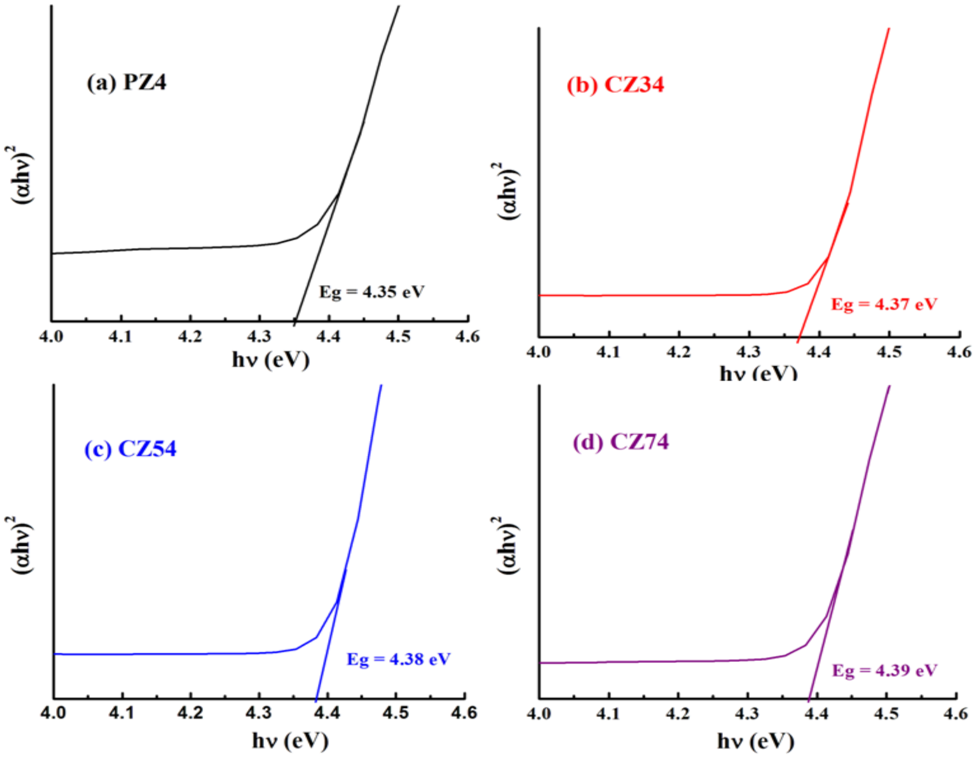

Fig. 4.5 Plot of $(\alpha h\upsilon)^2$ vs ($h\upsilon$) of (a) PZ4, (b) CZ34, (c) CZ54 and (d) CZ74.

4.3.4 Photoluminescence study

Fig. 4.6 represents the photoluminescence (PL) spectra at room temperature for undoped and all Cr^{3+} ions doped ZnO nanomaterials. For the betterment of the PL spectrum, it is necessary to the proper selection of preparation mechanism, choice of dopant, stoichiometry and post sintering process. The above mentioned factors mostly control the surface morphology and various structural defects for undoped and Cr^{3+} ions doped ZnO nanomaterials which directly affects the corresponding PL intensity. The excitation wavelength for PL study is 290 nm for all the samples. A prominent UV emission at 326 nm and 336 nm in the PL spectra of undoped and Cr^{3+} ions doped nanostructured ZnO have been observed. Such types of emission in the UV region are found nearly at the same position and these peaks are attributed to recombination of free excitons coming from exciton-exciton collision process and are known as near-band-edge (NBE) emission. A violet emission peak at 396 nm in the visible region for undopd and all Cr^{3+} ions doped ZnO samples have been observed and is assigned as electronic transition from the zinc interstitial level (I_{Zn}) to top of the valance band. Due to the incorporation of Cr^{3+} ions within ZnO nanostructures, a variation in intensity of the excitonic emission for all the doped samples has been observed. No prominent peaks corresponding to the blue, green and red emissions in the visible region have been detected in any of the measured samples. The nanocrystals with large size and nearly perfect crystal structure normally show stronger UV emission, along with that the UV emissions are competing with the visible emission that has been mentioned in the earlier reports. It has also been observed that the intensity ratio of UV emission to visible emission is very high for rod like nanostructure synthesized by hydrothermal process. The number of surface defects and the defect centers within the nanostructures give rise to the transfer of optical emission from UV region to the visible region along with their emission intensity. It is expected a large number of surface defects and large amount of defect centers to be present more in case of spherical nanostructure than rod like nanostructure and an electronic transition between two energy levels may occur but if the defect centers deep hole trapped levels of the valance band present at the surface, the free electrons will be trapped at the surface of Cr^{3+} ions doped ZnO nanostructure and thereby reducing the visible emission. In this case, Cr^{3+} ions doped ZnO nanostructure samples are rod like in nature which have small amount of surface defects and also the amount of defect centers related to oxygen vacancies, deep donor levels and deep acceptor levels are less and the defect centers belong to deep holes trapped levels at the surface. Hence, the observed FESEM and PL study suggest that the hydrothermally synthesized rod like ZnO nanostructure is not commendable for the modulation of the optical properties. Also from the Fig. 4.6, it may be observed that the UV intensity peaks of the PL spectrum decreases with the increase in Cr^{3+} ions doping percentage and the luminescence band corresponding to the Cr^{3+} ions doped ZnO nanostructure is larger as compared to the undoped ZnO suggests that the Cr^{3+} ions doping will increase the surface defects and oxygen vacancies.

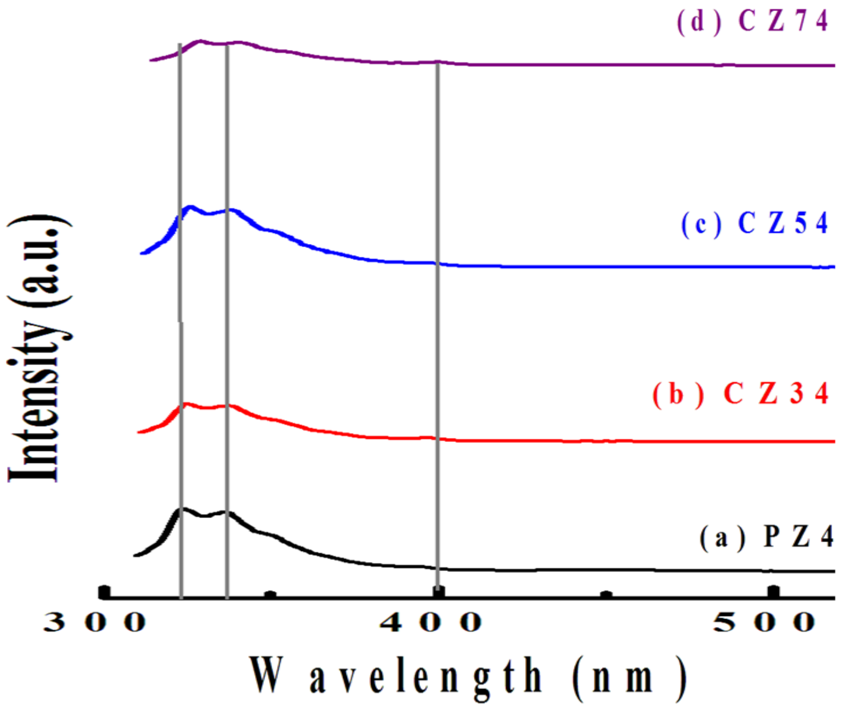

Fig. 4.6 Photoluminescence spectra of (a) PZ4, (b) CZ34, (c) CZ54 and (d) CZ74.

4.3.5 Dielectric study

For the advancement of science, the dielectric response regarding to shape and dopant dependency of undoped and doped ZnO nanomaterials is a dominant field of research. This mechanism helps us to control the dielectric response of the semiconducting nanomaterials. Till now, it has been declared in many articles that the dielectric property of the nanostructured ZnO is fairly dependent on their grain morphologies. Actually, various physical properties with regards to the morphology are competing with each other. In this regard, sol-gel, co-precipitation etc. produced spherical nanostructure have low value of dielectric constant but the hydrothermally synthesized rod like structured ZnO or any other metal oxide semiconductor possesses relatively high or ultra high dielectric responses. The value of dielectric constant in the range of 10^5 or 10^6 can be achieved for rod like structured nanomaterials and are known as super dielectric materials (SDM). Such types of SDMs are highly recommended in the research field of super capacitor, sensor applications, piezoelectric and ferroelectric device applications. Here, we have analyzed the dielectric response of undoped and Cr^{3+} ions doped nanostructured ZnO and the potential reasons behind the high values of dielectric constant of the nanomaterials. Also, the synthesis modulated dielectric response of the nanomaterials has been discussed in this section. The dielectric constant is given by the following relation,

$$\varepsilon = \varepsilon' - j\,\varepsilon'' \tag{4.10}$$

(ε') signifies the real part of the dielectric constant and (ε'') represents the imaginary part of dielectric constant. The value of ε' and ε'' of all the samples with response to externally applied electric field and temperature have been measured by using the formula

$$\varepsilon' = \frac{Cd}{\varepsilon_0 A} \tag{4.11}$$

and

$$\varepsilon'' = \varepsilon' \times \tan\delta \tag{4.12}$$

Here, C represents the capacitance of the sample, d is thickness and A is the area, respectively of the pellet and ε_0 signifies the free space permittivity. The frequency dependent ε' curve for undoped and Cr^{3+} ions doped nanostructured ZnO with the frequency range from 40 Hz to 1 kHz at different temperatures (From RT to 200 ^{o}C) is shown in Fig.4.7. Also, the variation of ε'' of all the samples with the same frequency range from 40 Hz to 1 kHz in the temperature range of RT to 80 ^{o}C have been represented in Fig. 4.8. The electron hopping between Zn^{2+} and Cr^{3+} ions acts as permanent electric dipole under the presence of externally applied alternating electric field and this will help the enrichment of both ε' and ε'' of Cr^{3+} ions doped nanostructured ZnO (CZ34, CZ54 and CZ74) as compared with the undoped ZnO nanomaterial (PZ4). With the help of Koop's theory which depends on Maxwell-Wagner-Sillars model for the nanostructures, the frequency dependent dielectric response can be explained [65-67]. According to it, a dielectric medium is made of well conducting grains and each of which is isolated from its surrounding with poorly conducting grain boundary. The free charge carriers (generated by the doping of Cr^{3+} ions within the ZnO) can easily drift inside the grains under the presence of externally applied alternating electric field and accumulated at the grain boundaries. The accumulated free charge carriers produce large polarizability within the materials which leads to a large polarization and high dielectric constant. The dielectric response can also be signified by some microscopic phenomena like electronic, ionic, dipolar and space charge polarization etc. At low frequency region, the dielectric constant is high which may appear due to the contribution of interfacial/space charge polarization of inhomogeneous nanostructures. Such types of polarization in Cr^{3+} ions doped ZnO nanoparticles can be observed due to the existence of different types of defects like grain boundary defects, vacancies, interstitials and dandling bonds etc. The observed values of both ε' and ε'' decreases with the increase in frequency of the applied alternating electric field and becomes frequency independent at the higher frequency region [68,1]. This type of nature observed due to the fact that beyond a certain frequency of the applied alternating electric field the hopping of the electrons between the metal cations (Zn^{2+}, Cr^{3+}) can not follow the frequency and lagging behind. In this work, the dielectric constants of CZ34, CZ54 and CZ74 are higher with reference to PZ4. This high value of dielectric constant for the sample CZ34 has been observed which is highest ever found for Cr^{3+} ions doped ZnO nanoparticles. The defects induced by the inhomogeneties in the nanostructures in enriched by the presence of Cr^{3+} ions within ZnO nanostructure. With the increase of Cr^{3+} ion concentration the observed value of ε' decreases. The formation of more number of microstructured grains of undoped or doped ZnO surrounded by insulating grain boundaries leads to the increase in the real part of dielectric constant (ε') and vice versa. As compared to CZ54 and CZ74, the grain size of CZ34 is lesser and gradually increases for both CZ54 and CZ74. Since dielectric constant is very much dependent on number of grains or effective grain boundary, the sample with large grain structure possess lesser number of grains and the amount of effective grain boundaries and thereby reducing the dielectric constant of the microstructure [64]. So the dielectric constant of CZ34, CZ54 and CZ74 decreases gradually.

It is to mention here that though the number of grains and the grain boundaries controls the dielectric constant but the rod like structure plays the vital role for the modulation of dielectric constant of the material. Also the increase of the dielectric constant of Cr^{3+} ions in the structure of ZnO i.e. for CZ34, CZ54 and CZ74 (electron hopping effect) with respect to PZ4 and the decrease of dielectric constant with the increase of Cr^{3+} ions within ZnO nanomaterials have been mentioned earlier. Such high dielectric values are very much acceptable for many device applications. In our work, due to hydrothermal synthesis process, the nanostructures are accumulated with a preferable growth along the c-axis within a microstructure. Each rod like structure acts like nano-dipole and all these nano dipoles within the microstructure cumulatively contribute to the resultant dielectric constant. The product of the number of the total charge with the free path length at the interface controls the dipole moment of each dipole. Now, as compared to undoped ZnO sample (PZ4), larger path length and more free charge carriers inside each microstructure have been found in doped ZnO sample (CZ34) and have larger dielectric constant. But with the increase of Cr^{3+} ions doping percentage within ZnO, the dielectric constant decreases gradually because the number of grain boundary and the effective grain boundary thickness decreases with the increase of doping percentage. The dielectric constant depends on the thickness of the effective grain boundary. The dielectric constant is higher for thin grain boundary layer. The grain boundary thickness of both CZ54 and CZ74 are larger than that of CZ34 as both CZ54 and CZ74 contain larger amount of growth units as compared to CZ34 and this reduces the dielectric constant of the nanomaterials respectively. The dielectric constant mainly depends on the presence of space charge polarization within the materials which directly depends on the amount of microstructural grains and grain boundaries.

Fig. 4.9 shows the variation of dielectric loss (tanδ) as a function of frequency with the presence of applied alternating electric field in the frequency range from 40 Hz to 10 kHz for various temperatures (RT to 80 ^{o}C). The energy dissipation within the dielectric system is represented by the dielectric loss (tanδ) which is caused by the domain wall resonance. The dielectric loss (tanδ) is designated by the ratio of the imaginary part (ε'') to the real part of the dielectric constant (ε') and is shown in Eq. (4.12). The dielectric loss (tanδ) decreases with the increase of frequency at different temperatures is shown in Fig. 4.9 and is due to the space charge polarization. It is to mention here that the dielectric loss (tanδ) is maximum for undoped materials and decreases with the increase of doping percentage of the Cr^{3+} ions gradually. From this observation it is clear that the doped samples are more capable to be used in high frequency device applications. In the higher frequency region no peak has been observed which reveals the relaxation processes or loss peaks and such behavior occurs due to the fact that the hopping frequency of localized electric charge carrier nearly equals to that of the frequency of externally applied alternating electric field. The real part of dielectric constant (ε′) as a function of temperature in the range from 25 to 120°C for undoped ZnO and Cr^{3+} ions doped ZnO nanoparticles has been shown in Fig. 4.10. The observed curves have been measured for three different frequencies at 1 kHz, 10 kHz and 100 kHz, respectively. The curves show ferroelectric to paraelectric transition for all the cases at almost 30 °C.

The Cr^{3+} ions doped ZnO (CZ34) sample has been found to have the highest value of dielectric constant (ε′) (~ 65595) at a frequency of 1 kHz and the dielectric constants (ε′) for all the samples are very high and such high value of dielectric constants (ε′) may be assigned to interfacial polarization present within the samples.

Now by doping of Cr^{3+} ions can enhances the charge density and the corresponding interfacial polarization which suggests that the substitution of Zn^{2+} ions with Cr^{3+} ions are proper [69]. To maintain the charge neutrality, three Zn^{2+} ions are replaced by two Cr^{3+} ions and due to this more free charge carriers and more zinc vacancies have been generated. Now the doubly ionized oxygen atom (O^{2-}) corresponding to each zinc vacancy releases excess electron to be neutralized itself. It is to mention here that the dielectric property mainly depends on the interfacial polarization of the nano grains and it is also dependent on the other factors like oxygen vacancy, zinc vacancy, zinc interstitial etc. so, the doping with trivalent cation like Cr^{3+} ions within the ZnO nanomaterials is the key factor for the proper enhancement of dielectric constant. Thus Cr^{3+} ions doped ZnO nanorods can be highly acceptable in various device applications.

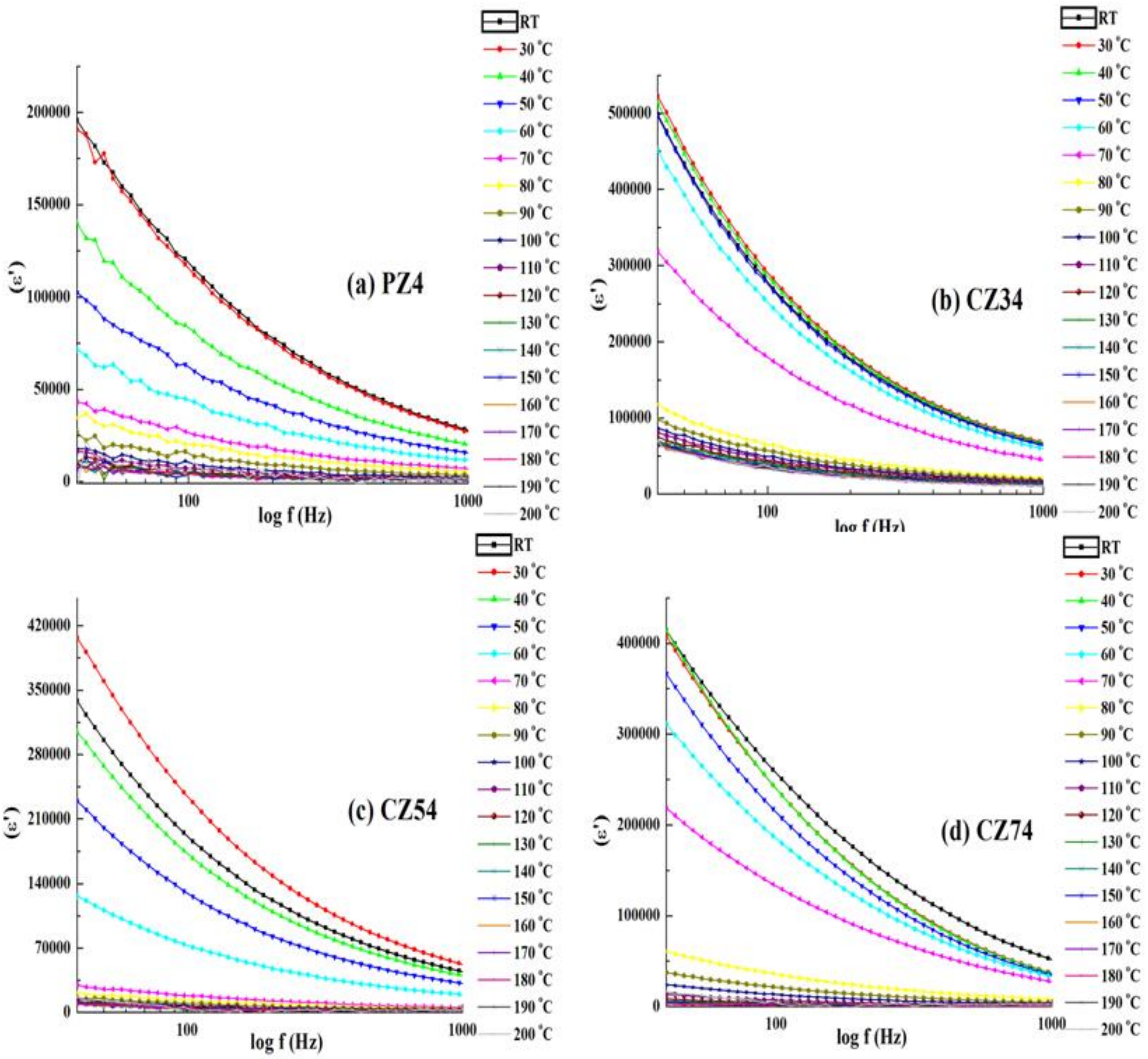

Fig. 4.7 Variation of real part of dielectric constant (ε′) with frequency at different temperatures of (a) PZ4, (b) CZ34, (c) CZ54 and (d) CZ74.

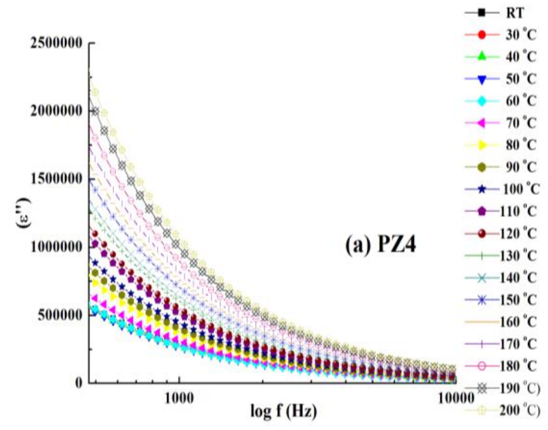

Fig. 4.8 Variation of imaginary part of dielectric constant (ε″) with frequency at different temperatures of (a) PZ4, (b) CZ34, (c) CZ54 and (d) CZ74.

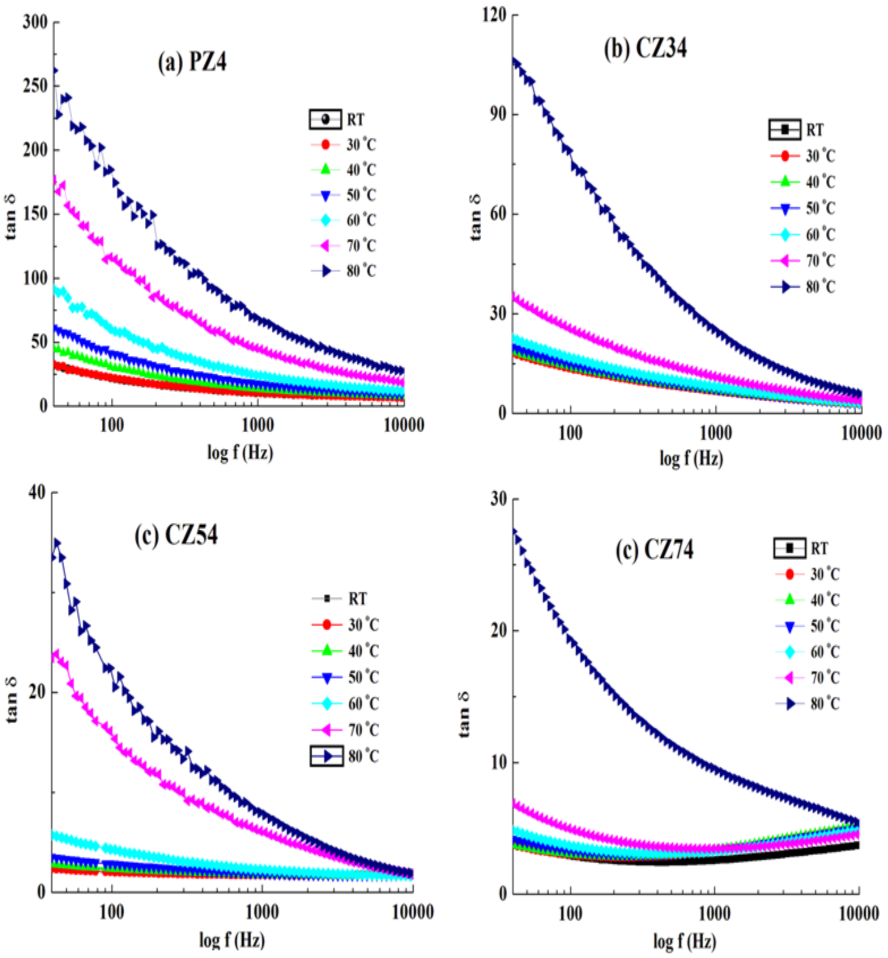

Fig. 4.9 Plot of dielectric loss (tanδ) vs frequency at different temperature of (a) PZ4, (b) CZ34, (c) CZ54 and (d) CZ74.

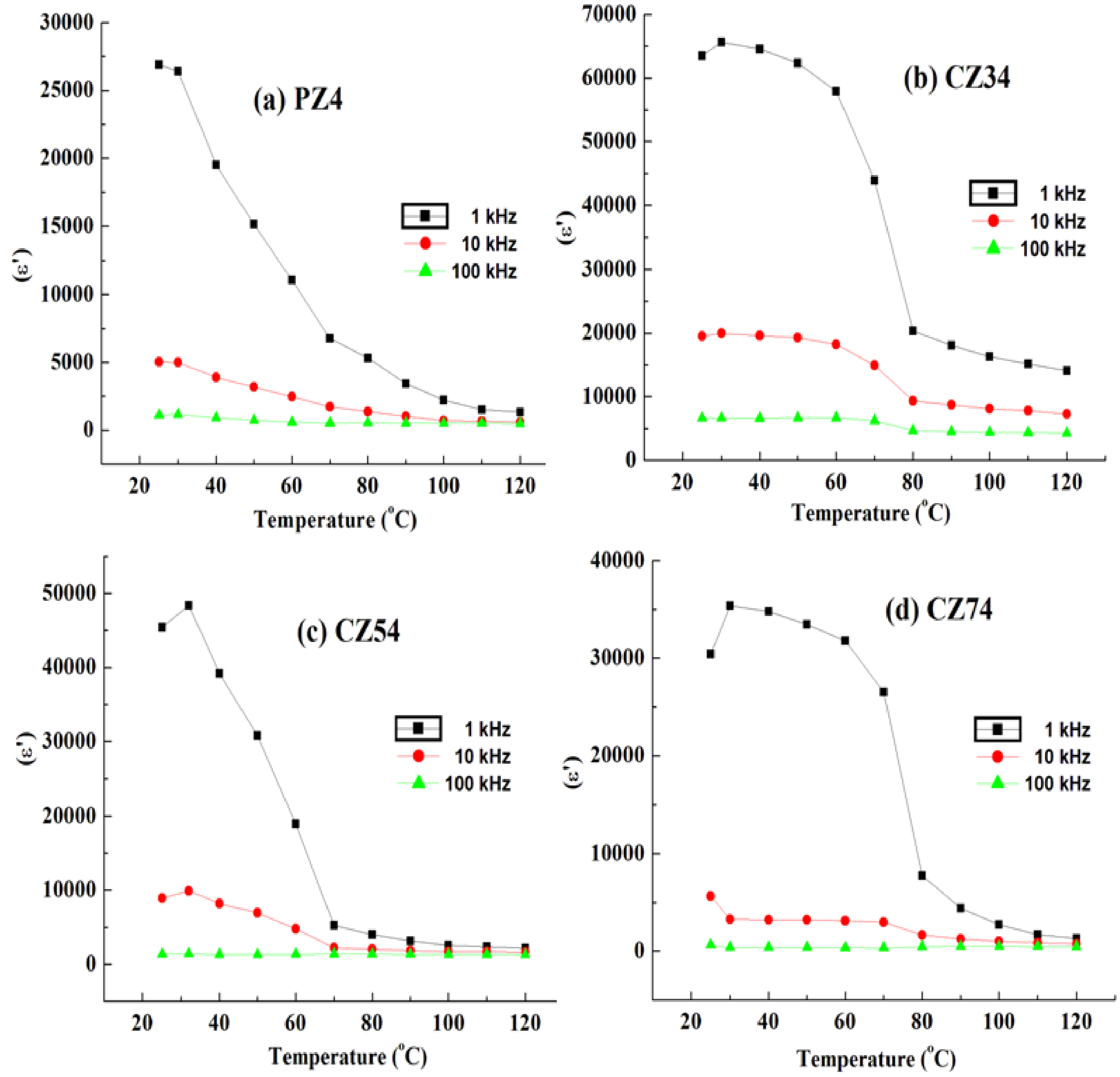

Fig. 4.10 Variation of real part of dielectric constant (ε′) with temperature at different frequencies of (a) PZ4, (b) CZ34, (c) CZ54 and (d) CZ74.

4.4 Conclusion

In this work, the dielectric property study modulated by the variation of Cr^{3+} ions doping percentage within the ZnO nanomaterials with high crystallinity prepared by hydrothermal synthesis route have been carried out and the synthesized nanoparticles are rod like in nature that have been confirmed by FESEM micrograph. These rod like morphology of the synthesized nanomaterials play the key role in modulating the dielectric property of the samples and super dielectric materials have been achieved by the formation of rod like nanostructure. So the hydrothermal synthesis route is very effective and inevitable for all semiconducting metal oxide in regard to the dielectric response. Also the Cr^{3+} ions substitution plays a crucial role in producing large amount of free charge carriers and enhancing the charge density which in turn enhances the dielectric response of the semiconducting ZnO nanomaterials. It is to be mention here that rod like structures with high dielectric constant can be achieved by using low cost hydrothermal synthesis mechanism and doping with proper TM or REE ions. Such high value of dielectric constant (~ 524160 at 40 Hz) in Cr^{3+} ions doped ZnO nanoparticles at low frequency with a ferroelectric to paraelectric phase transition at 30 ^{o}C improves the dielectric property of charge storage devices, ferroelectric or piezoelectric applications, sensor device applications, high electric breakdown strength materials which is the crucial requirement for device applications in modern technology.

Reference

[1] M. K. Gupta, N. Sinha, B. Kumar, J. Appl. Phys. 112 (2012) 014303.

[2] A. Kar, S. Kundu, A. Patra, J. Phys. Chem. C 115 (2011) 118.

[3] A. Patra, P. Ghosh, P. Saha Chowdhury, M. A. R. C. Alencar, W. Lozano B., N. Rakov, G. S. Maciel, J. Phys. Chem. B 109 (2005) 10142.

[4] K. L. Kelly, E. Coronado, L. L. Zhao, G. C. Schatz, J. Phys. Chem. B 107 (2003) 668.

[5] T. Debnath, S. Das, D. Das, S. Sutradhar, J. Alloys Compd. 696 (2017) 670.

[6] Y. Yang, W. Guo, X. Wang, Z. Wang, J. Qi, Y. Zhang,Nano Lett. 12 (2012) 1919.

[7] K. Jagiello, B. Chomicz, A. Avramopoulos, A. Gajewicz, A. Mikolajczyk, P. Bonifassi, M. G. Papadopoulos, J. Leszczynski, T. Puzyn,Struct. Chem. 28 (2017) 635.

[8] A. Kar, A. Patra, J. Phys. Chem. C 113 (2009) 4375.

[9] B. Liu, H. M. Chen, C. Liu, S. C. Andrews, C. Hahn, P. Yang, J. Am. Chem. Soc. 135 (2013) 9995.

[10] N. H. Hong, M. B. Kanoun, S. Goumri-Said, J. H. Song, E. Chikoidze, Y. Dumont, A. Ruyter, M. Kurisu, J. Phys.: Condens. Matter 25 (2013) 436003.

[11] N. H. Hong, J. Sakai, N. T. Huong, A. Ruyter, V. Brizé, J. Phys.: Condens. Matter 18 (2006) 6897.

[12] S. Das, S. Das, D. Das, S. Sutradhar, J. Alloys Compd. 691 (2017) 739.

[13] G. Z. Xing, Y. Wang, J. I. Wong, Y. M. Shi, Z. X. Huang, S. Li, H. Y. Yang, Appl. Phys. Lett. 105 (2014) 143905.

[14] G. Z. Xing, D. D. Wang, C.-J. Cheng, M. He, S. Li, T. Wu,, Appl. Phys. Lett. 103 (2013) 022402.

[15] Y. Sun, Q. Li, Chin. J., Liq. Crys. Disp. 31 (2016) 635.

[16] Z. Zhu, B. Bai, O. You, Q. Li, S. Fan, Light: Sci. Appl. 4 (2015) e296.

[17] A. Karabchevsky, A. Mosayyebi, A. V. Kavokin, Light: Sci. Appl. 5 (2016) e16164.

[18] C. Yuyu, T. Zhen, Chinese Optics 10(4.1) (2017) 86.

[19] L. Tong, Z. Mei-ling, W. Fei, Z. Da-ming, W. Guo-ping, Chinese Optic 10(4.2) (2017) 219.

[20] L. Ma, S. Ma, H. Chen, X. Ai, X. Huang, Applied Surface Science 257 (2011) 10036.

[21] Z. L. Wang, J. Phys. Condens. Mater. 16 (2004) 829.

[22] N. Tahir, A. Karim, K. A. Persson, S. T. Hussain, A. G. Cruz, Md. Usman, Md. Naeem, R. Qiao, W. Yang, Y. D. Chuang, Z. Hussain, J. Phys. Chem. C 117 (2013) 8968.

[23] G. Li, H. Wang, Q. Wang, Y. Zhao, Z. Wang, J. Du, Y. Ma, Nano. Res. Lett. 10 (2015) 112.

[24] X. Yang, A. Wolcott, G. Wang, A. Sobo, R. C. Fitzmorris, F. Qian, J. Z. Zhang, Y. Li, Nano Lett. 9 (2009) 2331.

[25] B. Chavillon, L. Cario, A. Renaud, F. Tessier, F. Cheviré, Md. Boujtita, Y. Pellegrin, E. Blart, A. Smeigh, L. Hammarström, F. Odobel, S. Jobic, J. Am. Chem. Soc.134 (2012) 464.

[26] K. Zhang, T. Holloway, M. Bahoura, A. K. Pradhan, R. Prabakaran, J. Pradhan, S. Smith, J. C. Hall, G. T. Ramesh, D. R. Sahu, J. L. Huang, Proc. SPIE7291 (2009) 729104.

[27] C. Chang, F. Kimura, T. Kimura, and H. Wada, Mater. Lett. 59 (2005) 1037.

[28] S. Li, H. Song, H. Yu, S. Lu, X. Bai, G. Pan, Y. Lei, L. Fan, and T. Wang, J. Lumin.122 (2007) 876.

[29] Y. Mao, J. Y. Huang, R. Ostroumov, K. L. Wang, J. P. Chang, J. Phys. Chem. C112 2278 (2008) 2278.

[30] Y. He, Y. Tian, Y. Zhu, Chem. Lett.32 (2003) 862.

[31] V. Ney, S. Ye, T. Kammermeier, A. Ney, H. Zhou, J. Fallert, H. Kalt, F.-Y. Lo, A. Melnikov, A. D. Wieck, J. Appl. Phys. 104 (2008) 083904.

[32] H. S. Hsu, J. C. A. Huang, Y. H. Huang, Y. F. Liao, M. Z. Lin, C. H. Lee, J. F. Lee, S. F. Chen, L. Y. Lai, C. P. Liu, Appl. Phys. Lett. 88 (2006) 242507.

[33] V. Gandhi,R. Ganesan,H. H. A. Syedahamed, M. Thaiyan, J. Phys. Chem. C 118 (2014) 9715.

[34] H. Yu, J. Li, R. A. Loomis, L.-W Wang, W. E. Buhro, Nat. Mater. 2 (2003) 517.

[35] K.-F. Lin, H,-M. Cheng, H.-C. Hsu, W.-F. Hsieh, Appl. Phys. Lett. 88 (2006) 263117.

[36] W. Yan, Q. Jiang, Z. Sun, T. Yao, F. Hu, S. Wei, J. Appl. Phys. 108 (2010) 013901.

[37] P. P. Murmu, J. K. Kennedy, B. J. Ruck, A. Markwitz, G. V. M. Williams, S. Rubanov, Nucl. Instrum. Methods Phys. Res. Sect. B: Beam Interact. Mater. Atoms 272 (2012) 100.

[38] H.M. Zhou, D.Q. Yi, Z.M. Yu, L.R. Xiao, J. Li, Thin Solid Films 515 (2007) 6909.

[39] N. Fathy, M. Ichimura, J. Cryst. Growth 294 (2006) 191.

[40] M. Jin, J. Feng, Z. De-heng, Ma Hong-lei, L. Shu-ying, Thin Solid Films 357 (1999) 98.

[41] Y. Wang, N. Liu, Y. Chen, C. Yang, W. Liu, J. Su, L. Lia, Y. Gao, RSC Adv. 5 (2015) 104386.

[42] C. E. Small, S. Chen, J. Subbiah, C. M. Amb, S. W. Tsang, T. H. Lai, J. R. Reynolds, F. So, Nat. Photonics 6 (2012) 115.

[43] S. C. Pillai, J. M. Kelly, R. Ramesh, D. E. McCormack, J. Mater. Chem. C 1 (2013) 3268.

[44] M. H. Huang, S. Mao, H. Feick, Science 292 (2001) 1897.

[45] G. S. Kino, R. S Wagner, J. Appl. Phys. 44 (1973) 1480.

[46] P. K. Shrestha, Y. T. Chun, D. Chu, Light: Sci. Appl. 4 (2015) e259.

[47] Y. Y. Lai, Y. P. Lan, T. C. Lu, Light: Sci. Appl. 2 (2013) e76.

[48] G. Li-li, L. Jun-sheng, Z. Miao, Z. Yue-lin, Chin., J. Liq. Crys. Disp. 29 (2014) 499.

[49] G. Li-li, L. Song-fei, C. Tian-fu, Z. Xue, Chin., J. Liq. Crys. Disp. 30 (2015) 925.

[50] A. S. H. Hameed, C. Karthikeyan, A. P. Ahamed, N. Thajuddin, N. S. Alharbi, S. A. Alharbi, G. Ravi, Scientific Reports 6 (2016) 24312.

[51] W. H. Nam, Y. S. Lim, S. M. Choi, W. S. Seo, J. Y. Lee, J. Mater. Chem. 22 (2012) 14633.

[52] C. J. Cong, L. Liao, J. C. Li, L. X. Fan, K. L. Zhang, Nanotechnology 16 (2005) 981.

[53] J. Luo, J. K. Liang, Q. L. Liu, F. S. Liu, Y. Zhang, J. Appl. Phys. 97 (2005) 086106.

[54] O. Lupan, T. Pauporté, B. Viana, V. V. Ursaki, I. M. Tiginyanu, V. Sontea, L. Chow, Journal of Nanoelectronics and Optoelectronics 7 (2012) 712.

[55] S. Baruah, J. Dutta,Sci. Technol. Adv. Mater. 10 (2009) 013001.

[56] F. Solís-Pomar, E. Martínez, M. F. Meléndrez, E. Pérez-Tijerina, Nanoscale Research Letters 6 (2011) 524.

[57] S. López-Romero, M. García-H, World Journal of Condensed Matter Physics 3 (2013) 152.

[58] S. B. Kondawar, S. A. Acharya, S. R. Dhakate, Adv. Mat. Lett. 2 (2011) 362.

[59] J. J. Lee, G. Z. Xing, J. B. Yi, T. Chen, M. Ionescu, S. Li, Appl. Phys. Lett. 104 (2014) 012405.

[60] D. D. Wang, G. Z. Xing, F. Yan, Y. S. Yan, S. Li, Appl. Phys. Lett. 104 (2014) 022412.

[61] R. Mariappan, V. Ponnuswamy, P. Suresh, R. Suresh, M.Ragavendar, Superlattices and Microstructures 59 (2013) 47.

[62] R. Viswanatha, S. Sapra, B. Satpati, P. V. Satya, B. N. Dev, D. D. Sarma, J. Mater. Chem. 14 (2004) 661.

[63] A. L.Schoenhalz, J. T. Arantes, A. Fazzio,G. M. Dalpian, J. Phys. Chem. C 114 (2010) 18293.

[64] A. Mclaren, T. Valdes-Solis, G. Li,S. C. Tsang, J. Am. Chem. Soc. 131 (2009) 12540.

[65] K. W. Wagner, Am. Phys. 40 (1973) 817.

[66] J. Maxwell, Electric and Magnetism 2New York Oxford University Press (1973).

[67] C. G. Koops, Phys. Rev. 83 (1951) 121.

[68] S. Bhattacharya, S.K. Saha, D. Chakravorty, Appl. Phys. Lett. 76 (2000) 3896.

[69] B. K. Roberts, A. B. Pakhomov, V. S. Shutthanandan, K. M. Krishnan, J. Appl. Phys. 97 (2005) 10D310.

CHAPTER 5

Structural and ferromagnetic properties of Chromium doped ZnO nanomaterials

5.1 Introduction

ZnO is the most valuable candidate for the fabrication of nano device with various morphologies like nanospheres, nanobolts, nanorods, nanoflowers, nanowires with modulated size exhibit interesting physical properties like optical, dielectric etc [1-3]. So far, the experimental observation of weak magnetic ordering has already been investigated for ZnO nanomaterials though the origin of it is still under ambiguity [4,5]. ZnO is a potential candidate for spintronic devices due to the small spin-orbit coupling and corresponding large spin coherence length [6]. To achieve some fascinating physical properties along with integrated magnetic response ZnO nanomaterials can be doped with transition metal (TM) ions which make it acceptable for the formulating spin-based devices like spin-valve transistors, logic device, non-volatile memory and many more [7,8]. Due to the possible presence of ferromagnetic secondary phases associated with the magnetic metal ions (Co, Ni, Fe, Mn, Mg), the room temperature ferromagnetism (RTFM) of TM doped ZnO nanomaterials is under debate. In any diluted magnetic semiconducting system, these secondary phases act a vital role as a source of magnetic signal [9,10]. To find out the origin of intrinsic ferromagnetism in a host ZnO lattice, a non magnetic element doping is the most effective way to be explained. In high speed data processing system the mere value of magnetization (nearly ~ 10^{-4} to 10^{-3} emu/g) of TM doped ZnO nanomaterials is a serious issue [11,12]. We have investigated the Cr doped ZnO nanomaterials to overcome this drawbacks related to TM doped ZnO and to fabricate the high speed next generation logic device. Here, we have chosen Cr as TM dopant for a few reasons, (i) FM in Cr-doped ZnO is more stable as compared to mostly studied Co-doped ZnO has been predicted by Sato and Katayama-Yoshida et al.[13], (ii) the radius of Cr^{3+} ion (0.63 Å) is smaller as compared to the atomic radius of Zn^{2+} ion (0.74 Å) and can easily substitute the Zn lattice point [14], (iii) Cr atom is antiferromagnetic below 311 K and paramagnetic at high temperature which helps it to distinguish intrinsic FM, (iv) the $3d^3$ high-spin configuration of trivalent Cr^{3+} ions produce huge magnetic moment in the host lattice and (v) also the trivalent chromium cations substitute the divalent zinc cations generates large amount of various defects like oxygen vacancy defect, as zinc vacancy defect, zinc interstitial defect and dandling bond etc. which initiate the magnetic ordering [15,16]. It is now accepted after various theoretical and experimental investigations that the structural defects are the main cause of RTFM in TM doped ZnO [17,18]. The another strong reason of magnetic ordering is the exchange interaction between the magnetic moments developed at the TM sites through free charge carriers established as Ruderman–Kittel–Kasuya–Yosida (RKKY) [19,20]. It is to mention that the ferromagnetic, paramagnetic or spin glass behavior for the same system have been reported earlier on the sample preparation parameters [21,22]. Thus the unprecedented magnetic ordering of Cr-doped ZnO nanomaterials is still a void work space for the researchers. To take on this we have synthesized 3, 5 and 7% of Cr^{3+} ions doped ZnO nanomaterials. The origin of the magnetic ordering and to reveal the influence of Cr ions substitution on the structural and magnetic properties of doped ZnO nanomaterials is our main aim of this study.

5.2 Experimental

5.2.1 Materials and methods

At first, Cr^{3+} ions doped ZnO nanomaterials have been synthesized using co-precipitation method. Zinc acetate dihydrate $Zn(CH_3COO)_2{\cdot}2H_2O$ and chromium acetate $Cr(CH_3COO)_3$ are the precursor materials are taken in a beaker with distilled water and placed on a magnetic stirrer. The percentage of Cr salt is specified at three concentrations as 3, 5, and 7% to that of the zinc salt. To get the homogeneous solution, it has been stirred for several hours. Then NH_4OH solution has been added drop wise to the previous solution for precipitation and the final ph be kept at ~ 10. After rigorous stirring, the produced colloidal suspension of $Zn(OH)_2$ for undoped ZnO and colloidal suspension of $Zn(OH)_2$ and $Cr(OH)_3$ for Cr^{3+} doped ZnO have been collected properly. To eliminate the excessive ions and to neutralize the pH value of the precipitated particles proper washing has been done several times by using distilled water/ethyl alcohol.

Then this colloidal solution of different samples have been dissolved in 40 ml of distilled water and taken into a Teflon jacket that has been kept in an autoclave which is placed in an oven at 160 ^oC for 2 days. Under the effect of high pressure of air present in the Teflon jacket, the nucleation process of undoped and Cr^{3+} doped ZnO nanoparticles has been initiated towards rod like structure. After the nucleation, the autoclave has been allowed to cool down to RT naturally. After removing the supernatant, the suspension has been collected and washed several times to remove unreacted ions with the distilled water. Then the nanoparticles are dried at RT keeping these samples in vacuum desiccators. Now to make a proper crystal the dried powder has been sintered at 400 ^oC in vacuum atmosphere.

Now on the basis of kinetic theory, the crystal growth of both undoped and Cr doped ZnO nanoparticles into rod like structure may be analyzed. For the assimilation of the microstructures into rod like nature, the high pH value ~ 10 of the aqueous solution plays a crucial role. A large amount of growth units like hydrated ions $Zn(OH)_4^{2-}$ and $Cr(OH)_6^{3-}$ have been produced by the addition of the excess NH_4OH. Now under high pressure within the autoclave, the hydrated ions are diffused into a particular c-axis direction and bounded together through a dehydration process. This will produce a large number of microstructure after get decomposed. After attaining a critical grain size, the cluster has been precipitated. Also this mechanism is helpful to produce internal lattice strain within the lattice structure which is an important factor for the modulation of different physical properties like optical and magnetic property that will be discussed in the XRD section.

5.2.2 Characterization techniques

XRD pattern of all the undoped and doped samples have been measured in powder X-ray diffractometer, Model D8, BRUKER AXS, using Cu K_α radiation ($\lambda = 1.5405$ Å) within the range of 2θ from 20 to 80°. For the morphological study, Field emission scanning electron microscope (FESEM) has been conducted using INSPECT F50 (FEI, Netherland). The photoluminescence (PL) emission spectroscopy has been employed by using spectroflurometer, Perkin Elmer Germany by applying an excitation wavelength (λ_{ex}) of 325 nm. For the EPR study, the measurement has been conducted by EPR spectroscopy model E500 Bruker. The Magnetization with the presence of applied magnetic field (M-H) data at RT and at various temperature have been recorded by a SQUID magnetometer (MPMS XL 7, Quantum Design) with a maximum applied field of 50000Oe.

5.3 Result and discussions

5.3.1 XRD analysis

The X-ray diffraction (XRD) patterns of undoped and Cr-doped ZnO nanomaterials (C0Z4, C3Z4, C5Z4 and C7Z4) have been represented in Fig. 1(a)-(d) for the study of structural properties. In this case, the Rietveld refinement corresponding to all samples suggests that all the nanostructured samples have a single phase of hexagonal wurtzite lattice of naostructured ZnO and no other impure phases have been detected. For high doping (7%), the vacant octahedral (Cr^{3+}) and tetrahedral (Cr^{6+}) sites may be occupied by the Cr ions which is the source of various secondary oxide phases like paramagnetic Cr_2O_3 and ferromagnetic CrO_2, antiferromagnetic Cr_2O_3 and $ZnCr_2O_4$ etc. Various forms of magnetic responses are originated from these secondary phases which are not intrinsic in nature [27]. To draw the conclusions about the intrinsic magnetic moment of FM ordering at RT, it is our matter of concern that the presence of any secondary phase within the Cr-doped ZnO nanomaterials can mislead us and other also. Under high pressure and temperature within the autoclave, due to the nucleation of undoped and Cr-doped nanostructured ZnO along (100) plane, a preferential growth along 'a' axis has been observed and the resultant ZnO nanomaterials to be evolved as rod like in nature. The (002) peaks with low intensity for all the samples are consistent with the fact that the growth of all the nanorods have been considered to be along 'a' axis rather than 'c' axis.

The relative texture coefficient illustrates the degree of a-orientation is represented in equation 5.1 [28]

$$TC_{100} = \frac{\frac{I_{100}}{I^0{}_{100}}}{\frac{I_{100}}{I^0{}_{100}} + \frac{I_{101}}{I^0{}_{101}}} \tag{5.1}$$

Here, the measured diffraction intensities are I_{100} and I_{101} corresponding to (100) and (101) planes and the diffraction intensities of standard ZnO are $I^0{}_{100}$ and $I^0{}_{101}$ as obtained from JCPDS (File no. 36-1451). The preferential growth of all the ZnO nanorods has been appeared along (100) plane which is indicated by the texture coefficients for C0Z4, C3Z4, C5Z4 and C7Z4 are 0.678, 0.672, 0.674 and 0.683 respectively.

At any diffraction angle (θ), the X-ray powder diffraction (XRPD) profile can be written as:

$$Y_c(2\theta) = [B \times (I_S \times I_A)](2\theta) + Bkg \tag{5.2}$$

Here B represents the true specimen broadening, I_S signifies the symmetric part of the instrumental function, I_A represents the asymmetric part of the instrumental function and Bkg represents the background of the diffraction pattern [29]. The Rietveld analysis with the help of MAUD software has been introduced to calculate the structural (lattice parameters, unit cell volume etc.) and the micro-structural (coherent domain size/crystallite size, micro-strain etc.) parameters [30]. All the nanoparticles are in single crystallographic phase that has been suggested by small values of χ^2 (goodness-of-fit quality factor) and different parameters like R_p (profile fitting R-value), R_{wp} (weighted profile R-value). The detected patterns are in well agreement with the observed patterns in the Rietveld refinement and the parameters are repeatable too. As a function of Cr doping concentration (x), the lattice parameters (*a* and *c*) calculated from Rietveld refinement have been plotted in Fig. 5.2 and the values of the lattice parameters (*a* and *c*), have been shown in Table 1. A small increment in the lattice parameter '*a'* and a small decrement in the lattice parameter '*c'* have been observed due to the increase in doping percentage of Cr in the host ZnO lattice (Fig. 5.2). A change in the lattice parameters (a and c) is observed due to the distortion effect produced by the incorporation of dopant. With the increase in the doping percentage of Cr^{3+} ions ($Zn_{1-x}Cr_xO$ (x = 0.03, 0.05 and 0.07)), to maintain the charge neutrality within the ZnO nanostructure more zinc vacancies would be produced which are responsible for the modulation of the lattice parameters (*a* and *c*). To maintain the electric charge during doping of Cr^{3+} ions, three Zn^{2+} ions have been removed by two Cr^{3+} ions and due to this fact the effective lattice parameters of doped nanomaterials are changed. Also, the substitution of smaller size Cr^{3+} ion (0.63 Å) at the lattice site of Zn^{2+} (0.74 Å) ions within the host ZnO may be the reason behind the decrement of the lattice parameter '*c*'. Normally, the base of Zn-tetrahedron is in the *ab*-plane and the apex along the *c*-direction in the hexagonal wurtzite structure of ZnO. Now, the average basal bond angles (O_b-Zn-O_b) of wurtzite structure of ZnO increases and the average base-apex angles (O_b-Zn-O_a) decreases as the substitution of Zn^{2+} ions by Cr^{3+} ions increases (here O_b is the oxygen atoms at the base and O_a is the oxygen atoms at the apex respectively of the tetrahedron) give rise to the small increment of the lattice parameter '*a'* and a small decrement of the lattice parameter '*c'* [31]. With the help of Rietveld analysis, we have calculated the bond angles and the bond lengths of all samples to substantiate the above explanation and the values are shown in Table 5.1. The value of base-apex angle decreases from 108.47° to 108.45° and the basal bond angle increases from 110.42° to 110.48°. Fig. 5.3 represents the crystal structure of 3% Cr-doped ZnO nanomaterial (C3Z4) that has been extracted from Rietveld analysis. Therefore, due to the modulations of bond length and bond angles within the lattice, the distortion effect arises in the Zn-tetrahedron. Also, Ozagur et al. proposed that the modulation of lattice constant may be due to the presence of zinc antisites, oxygen vacancies, and other defects [32]. In order to know the presence of oxygen occupancies in Cr-doped ZnO nanomaterial, an additional Rietveld refinement has been evaluated. The estimated values of oxygen occupancy are 1, 0.973, 0.952 and 0.928 for C0Z4, C3Z4, C5Z4 and C7Z4 nanomaterials. For each sample, the variation of oxygen occupancy is defined as [33]

$$\Delta g_{o(ZnO)} = g_{o(ZnO)} - \frac{g_{o(Cr-dopedZnO)}}{g_{o(ZnO)}} \tag{5.3}$$

Here, g_o represents the oxygen site occupancy. The oxygen vacancies increase with the increase of Cr doping concentration within the ZnO lattice that has been indicated in Table 5.1 where the values of all the Cr-doped ZnO nanomaterials are positive. Therefore, the conclusion can be driven that the Cr^{3+} ions are successfully substituted in the ZnO lattice structure which integrates the oxygen vacancies as well as lattice distortion.

The degree of distortion(R) is calculated by using the following equation:

$$R = \sqrt{\frac{8}{3}\frac{a}{c}} \tag{5.4}$$

For ideal structure the value of R is 1. Fig.5.4 shows the gradual increase of R which indicates that the R increases with the increase of Cr-concentration. Again by using the isotropic size strain model, the whole profile has been fitted to determine the size and strain parameters of undoped and Cr^{3+} ions doped ZnO nanomaterials. In the present study, when Cr doping concentration varies from 0% to 7%, the average crystallite size decreases from 57 to 29 nm which indicates that structural growth of the crystals grains has been prevented by the presence of Cr ions in ZnO lattice and also drag down the movement of grain boundaries. This interruption in the motion of grain boundary may be explained on the basis of Zener pinning [34]. Additionally, the incorporation of the Cr^{3+} ions in place of Zn^{2+} ions generates crystal defects which perform as the nucleation centre [35]. From Rietveld analysis, the lattice strain of C0Z4, C3Z4, C5Z4 and C7Z4 has been calculated and the corresponding values have been shown in Table 5.1. Now, under hydrothermal synthesis route, due to the high pressure within the autoclave, a large internal compressive stress on the crystal planes in the lattice structure of ZnO has been developed and due to this a large internal lattice strain has been developed in the undoped and Cr-doped ZnO nanomaterials. Now, the position of the XRD peaks can be shifted towards the higher 2θ value due to the large internal lattice strain. Since, the radius of Cr^{3+} ion (0.63 Å) is quite different from the radius of Zn^{2+} ion (0.74 Å). So the substitution produces an internal lattice strain within the lattice structure of Cr-doped ZnO nanomaterials. Table 5.1 represents the values of internal lattice strain/micro strain for all the nanomaterials (C0Z4, C3Z4, C5Z4 and C7Z4). Thus, the main reason behind this shift in diffraction peak positions in the XRD is the internal lattice strain produced by the incorporation of the Cr^{3+} ions in the structure of ZnO nanomaterials.

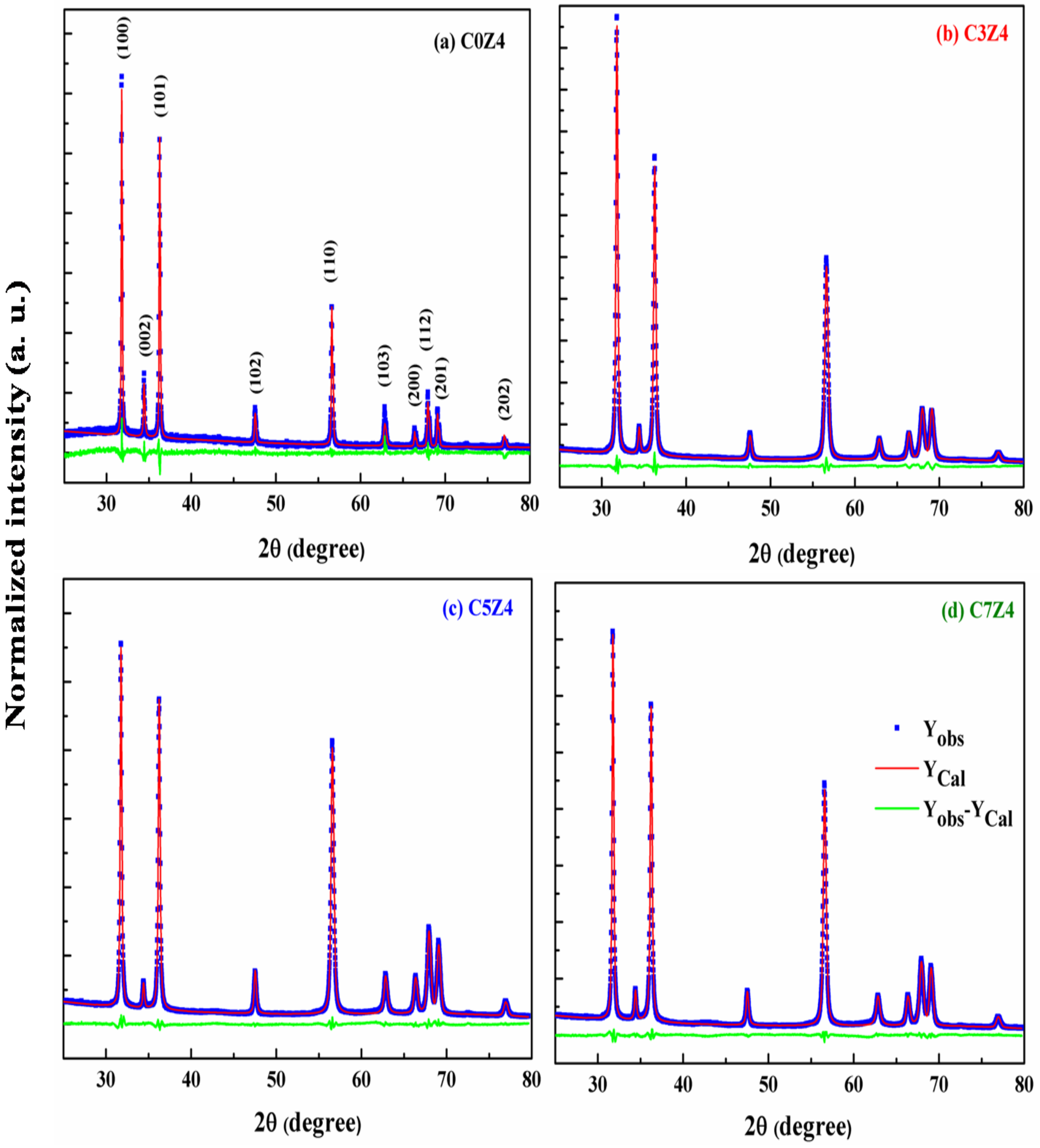

Fig. 5.1 XRD patterns along with the Rietveld analysis of (a) undoped ZnO (C0Z4), (b) 3% Cr-doped ZnO (CZ34), (c) 5% Cr-doped ZnO (CZ54) and (d) 7% Cr-doped ZnO (CZ74).

Table 5.1. Structural parameters of undoped and Cr-doped ZnO nanomaterials extracted from Rietveld analysis.

Parameters	C0Z4	C3Z4	C5Z4	C7Z4
Crystallite Size (nm)	57	44	35	29
a (Å)	3.249	3.251	3.252	3.252
c (Å)	5.208	5.207	5.205	5.204
B_{iso}	1.262	1.403	1.750	1.101
Δg_o	1.000	0.027	0.048	0.072
Degree of distortion (R)	1.018	1.019	1.020	1.020
$D_{Zn\text{-}O}$(Å)	1.977	1.978	1.978	1.978
O_b-Zn-O_a(in degree)	108.468	108.445	108.374	108.373
O_b-Zn-O_b(in degree)	110.422	110.479	110.559	110.549
Microstrain	5.62×10^{-4}	1.03×10^{-3}	1.5×10^{-3}	2.1×10^{-3}

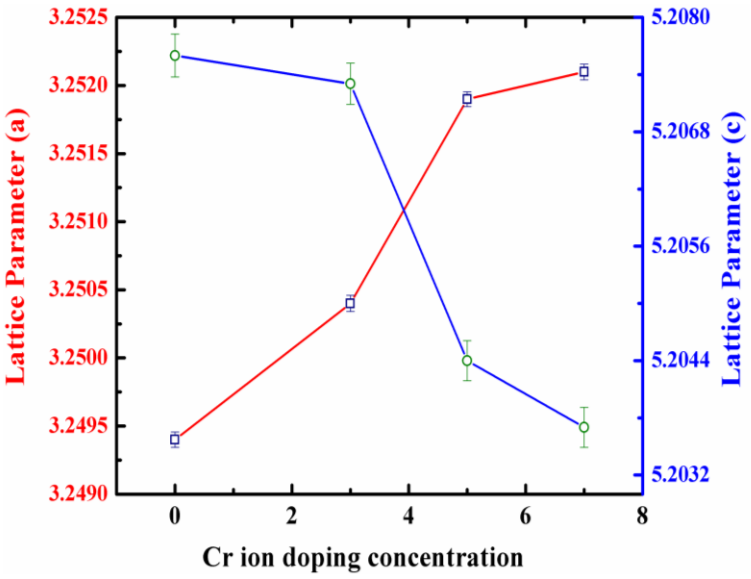

Fig. 5.2 Variations of lattice parameters ‘a’ and ‘c’ as a function of Cr ion doping concentration in ZnO.

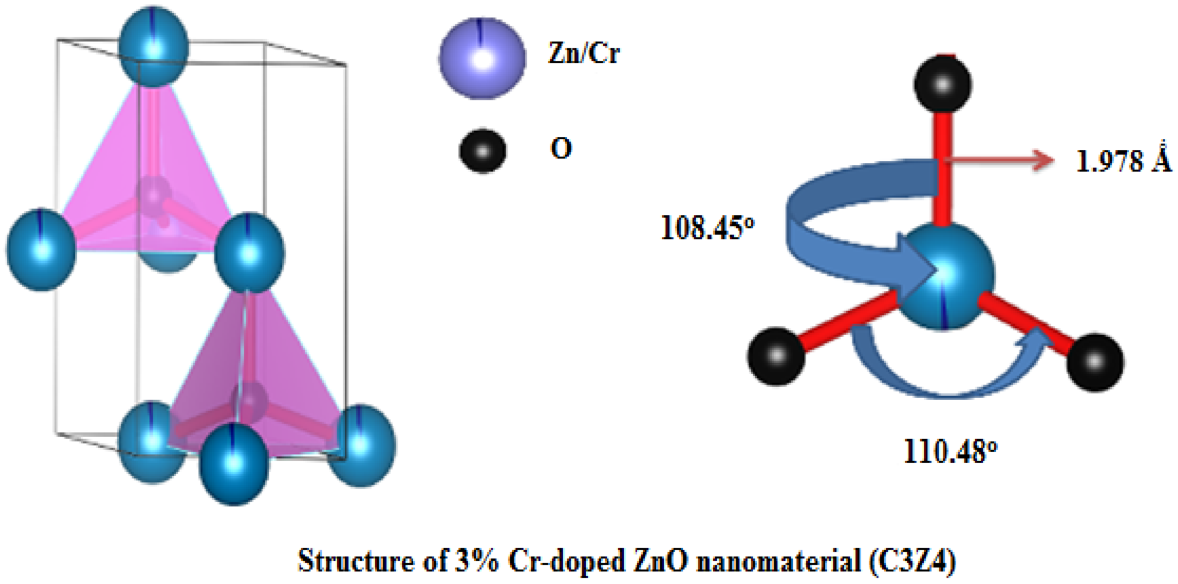

Fig. 5.3 Structure representation of 3% Cr-doped ZnO.

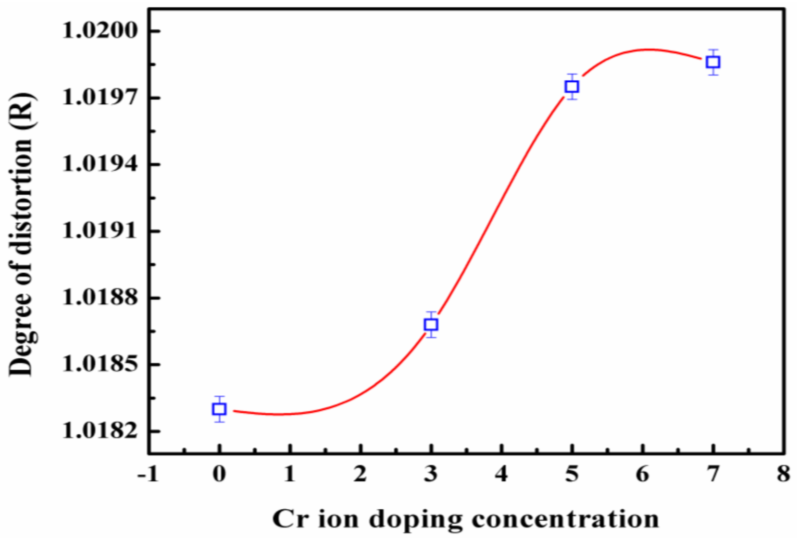

Fig. 5.4 Variations of degree of distortion (R) as a function of Cr ion concentration in ZnO.

5.3.2 FESEM analysis

The FESEM measurement has been conducted in order to clarify the growth and surface morphology of undoped and doped nanostructured ZnO and few selected micrographs have been represented in Fig. 5.5. The micrograph of undoped ZnO nanomaterial (C0Z4) in Fig. 5.5(a) represents rod like structure with needle like end. Though, the agglomeration effect at the growth centers cannot be eliminated, all the rods in the micrograph are very much clear and distinguishable. The micrograph of 5% Cr-doped ZnO nanomaterial (C5Z4) is shown in Fig. 5.5(b). The morphological nature of C5Z4 is rod like with hexagonal ends. Under high pH (~ 10), the growth units in the form of hydrated ions viz, $Zn(OH)_4^{2-}$ and $Cr(OH)_6^{3-}$ get diffused under high pressure and temperature (~ 160 ºC) within the aqueous solution. In our earlier publication, the complete growth mechanism of undoped and Cr-doped ZnO nanostructures has been given [23]. For both the rod like C0Z4 and C5Z4 nanomaterials, a clear structural difference has been observed. The morphology of C0Z4 shows a rod like structure with needle like end and the morphology of C5Z4 shows rod like structure with nearly uniform hexagonal end. Due to the presence of dissimilarities of elemental Cr^{3+} ions concentration of the undoped and Cr-doped ZnO nanomaterials, a change in the surface morphology between C0Z4 and C5Z4 nanomaterials have been observed. Under hydrothermal synthesis route as compared to undoped ZnO nanomaterials, due to the presence of Cr^{3+} ions the requisite conditions in making the precipitation of Cr-doped ZnO nanomaterials is quite different [36]. These structural changes with the presence of doping ions within the nanostructured ZnO shows the successful incorporation of the Cr^{3+} ions within the ZnO lattice. Incidentally, in different micrographs, the size of all the nanorods is almost uniform and the particles are not agglomerated.

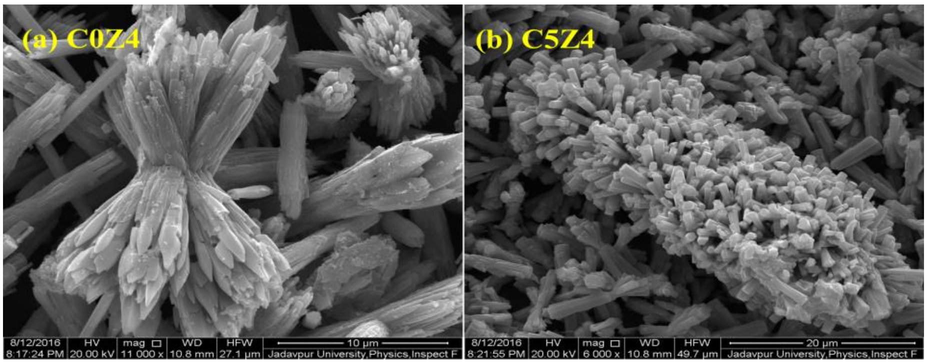

Fig. 5.5 FESEM images of (a) C0Z4 and (b) C5Z4.

5.3.3 Photoluminescence study

The photoluminescence (PL) spectra of all the specimens (C3Z4, C5Z4 and C7Z4) have been investigated and shown in Fig. 5.6(a-c). Fig. 5.6(d) shows the corresponding schematic diagram of band energy gap of PL spectra of each sample. It is known that the selection of dopant, doping percentage, stoichiometry, preparation technique and the annealing temperature are the important factors to control the PL emission spectra and these factors are sensitive for the desirable PL emission spectra. The above mention factors control the grain morphology and various native defects like, oxygen vacancy defects (V_o), oxygen interstitial defects (I_o), zinc vacancy defects (V_{Zn}), zinc interstitial defects (I_{Zn}) etc. related to the structure of Cr-doped ZnO nanoparticles which can be modulated and the corresponding PL spectra changes accordingly. The PL emission spectra of Cr-doped ZnO nanostructure has been studied with an excitation wavelength of 325 nm. The emission spectra of Cr-doped ZnO nanostructure (C3Z4, C5Z4 and C7Z4) exhibits a broad UV emission peak at 380 nm and the UV emission peak for all the samples has been detected nearly at the similar positions. The emission peak at the above mentioned position has been found due to the recombination of free excitons through exciton-exciton collision mechanism and is known as near-band-edge (NBE) emission [37]. For C3Z4, C5Z4 and C7Z4 nanomaterials, a broad peak centered at 442 nm has been detected. A blue emission peak in the visible region centered at 442 nm has been observed in Fig. 5.6. The cause of this emission is the electronic transition between the zinc interstitial (I_{Zn}) and the zinc vacancy (V_{Zn}) level [38]. Also, from the observed emission spectra, it is quite clear that no emission peak corresponding to any secondary phase like Cr_2O_3 has been detected. It is known that two Cr^{3+} ions substitute three Zn^{2+} ions within the hexagonal wurtzite structure of ZnO nanomaterials to maintain the charge neutrality and thereby produces Zn vacancies. These substituted Zn^{2+} ions will keep themselves into the interstitial positions within the ZnO lattice structure. Thus, the emission peak centered at 442 nm corresponding to the blue emission is due to the presence of Zn vacancies (V_{Zn}) and Zn interstitials (I_{Zn}) for C3Z4, C5Z4 and C7Z4 nanomaterials. A blue-green emission peak centered at 492 nm has been detected for C3Z4 and C7Z4 nanomaterials. This emission peak has been assigned due to the electronic transition between oxygen vacancy defects (V_o) and oxygen interstitial defects (I_o) attributed to the surface defects within the ZnO nanomaterials [38]. For C5Z4 nanomaterial, a peak at 540 nm corresponding to the green emission has been observed and this peak is attributed to the electronic transitions due to oxygen vacancies (V_o) [39]. During the sintering period, the defect states corresponding to oxygen vacancies (V_o) and oxygen interstitials (I_o) have been formed within the lattice. In this present study, the detected PL spectra of Cr-doped ZnO nanomaterials are in consistent with the research work of Kennedy et al. and Sathyaseelan et al. [40,41]. Finally, it is to be mention here that the oxygen vacancy (V_o) present within the doped system plays an important role for the enhancement of ferromagnetic.

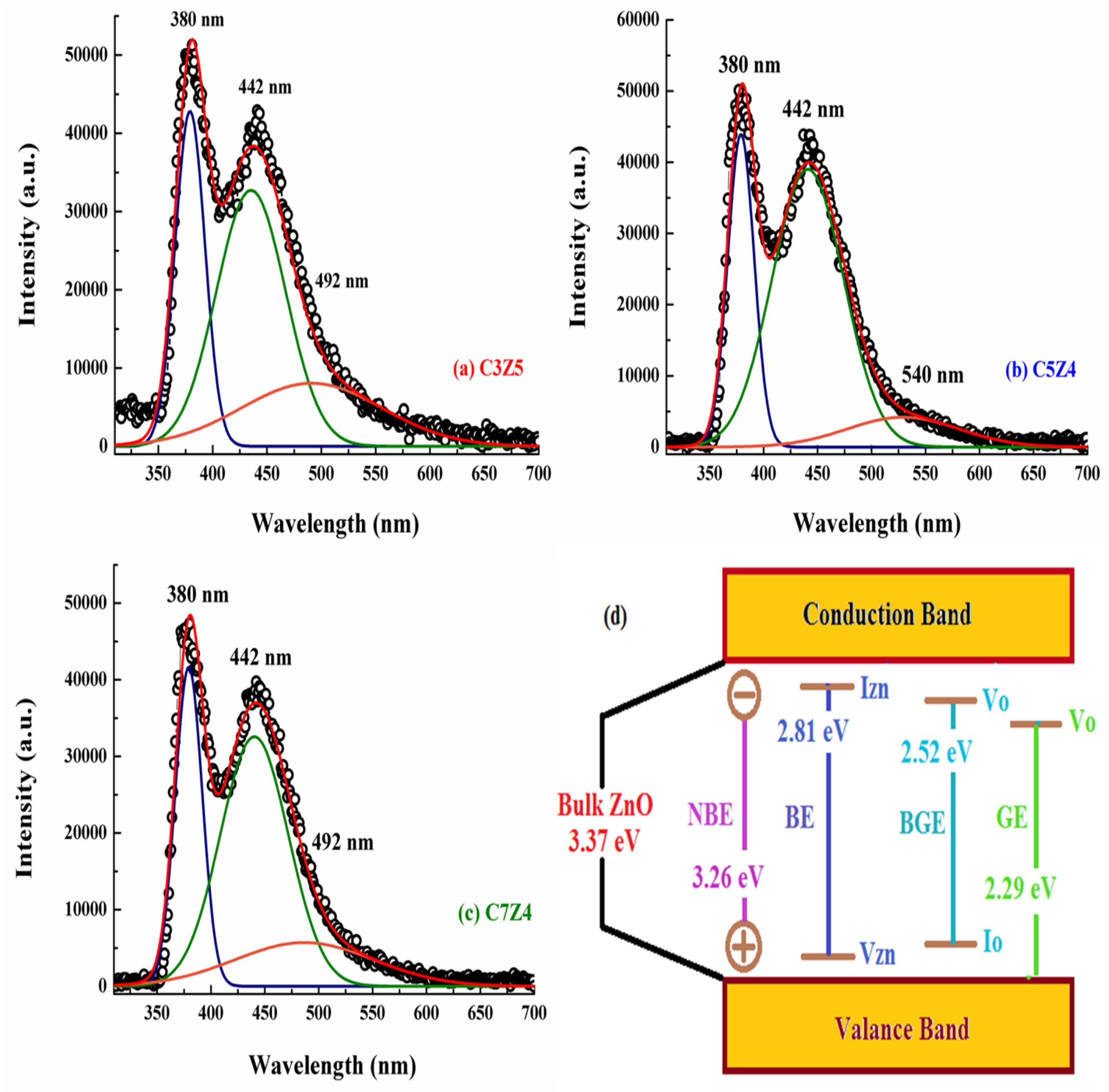

Fig. 5.6 Deconvoluted Photoluminescence spectra of (a) CZ34, (b) CZ54 and (c) CZ74 and (d) Schematic diagram proposed for different relaxation processes in Cr-doped ZnO nanomaterials.

5.3.4 EPR study

Room temperature electron paramagnetic resonance (EPR) study has been measured to identify the development of oxygen vacancy defect states produced within the Cr-doped ZnO nanomaterials. Ferromagnetic ordering has been detected in all the specimens in the static magnetic measurement and this particular observation energized us to do further research on EPR analysis of these samples. The variations of EPR spectra with the presence of magnetic field have been depicted in Fig. 5.7. The EPR spectra of C3Z4, C5Z4 and C7Z4 nanomaterials, have been depicted in Figs. 5.7(a), (b) and (c) respectively. For all the Cr-doped ZnO nanomaterials, the EPR spectra with broad line width have been found. From the figure it can be seen that with the increase of Cr concentration within the host ZnO nanomaterials, the line width of EPR spectra decreases and the intensity of EPR spectra increases. The patterns observed in the EPR spectra are nearly symmetrical Lorentzian in shape for all the doped samples. The resonant signal regarding to the effective value of g-factor of the specimens has been calculated by the following equation [42]

$$\mathrm{g} = \frac{h\gamma}{BH} \tag{5.5}$$

here, H signifies the static field (gauss), is the frequency (Hz), B represents the Bohr magnetron equal to 9.274×10^{-21} erg/gauss, and h represents the Planck's constant, the value f which is 6.626×10^{-27} erg-s/cycle. From the room temperature EPR spectra, the values of g-factors of specimens have been measured which shows the enhancement with the increase of doping concentration of Cr ions within the lattice structure. The enhancement of the number of paramagnetic centers, i.e., singly ionized oxygen vacancies (V_o^+) has been signified by the value of g-factor, where the value of g-factor increases with the increase in Cr concentration within the ZnO nanomaterials. The presence of paramagnetic centers or singly ionized oxygen vacancies (V_o^+) within the lattice structure of all the samples have been substantiated by the existence of paramagnetic and ferromagnetic ordering in static magnetic measurement. Also, the higher value of EPR intensity substantiates the higher concentration of paramagnetic centers in the C7Z4 nanomaterials. As compared to C3Z4 and C5Z4 nanomaterials, the EPR resonant peak of C7Z4 nanomaterial is sharper. The value of g-factor and the resonant peak of C7Z4 nanomaterial is higher as compared to C3Z4 and C5Z4 nanomaterials signifies the greater uniformity of Cr^{3+} ions distribution and presence of exchange coupling between Cr^{3+} ion pairs within the nanostructured ZnO that implies the presence of enhanced magnetic homogeneity [43]. The significant reason behind the enhancement of room temperature FM in Cr-doped ZnO nanomaterials is the exchanged coupled Cr^{3+} ion pairs. The EPR spectra observed in Cr-doped ZnO nanomaterials is the Cr^{2+} valance state that has also been investigated in the earlier works of EPR spectroscopy in Cr doped-ZnO nanomaterials. It is expected that the Zn^{2+} ions have been substituted by the Cr^{2+} ions in the lattice site of Cr-doped ZnO wurtzite structure. However, the reported values of g-factor and the peak-to-peak line width in the present work are dissimilar with the earlier reported values of EPR spectra of Cr^{2+}ions doped nanostructured ZnO. Vallin et al. showed that the peak-to-peak line widths of EPR spectra of Cr^{2+} ion doped II-VI semiconducting compounds is 500 G at 20 K [44]. Now, it is expected that the EPR signal of Cr^{2+} ion will be wide and unable to detect correctly. Thus in the present work, it is suggested from the EPR spectra of Cr-doped ZnO nanomaterials that the signal arises due to Cr^{3+} ions instead of Cr^{2+} ions which signifies that the Cr^{3+} ions are bounded in the octahedral site of lattice structure of ZnO and also an unpaired electron confined at the oxygen vacancy site. It may be acceptable that the broad line width of EPR spectra of Cr^{3+} ions overlap with the resonance line of unpaired trapped electron at the oxygen vacancy site. On the basis of BMP model, under external magnetic field, this unpaired electron trapped at the oxygen vacancy site plays the crucial role to exhibit the ferromagnetic ordering within the doped nanostructured ZnO.

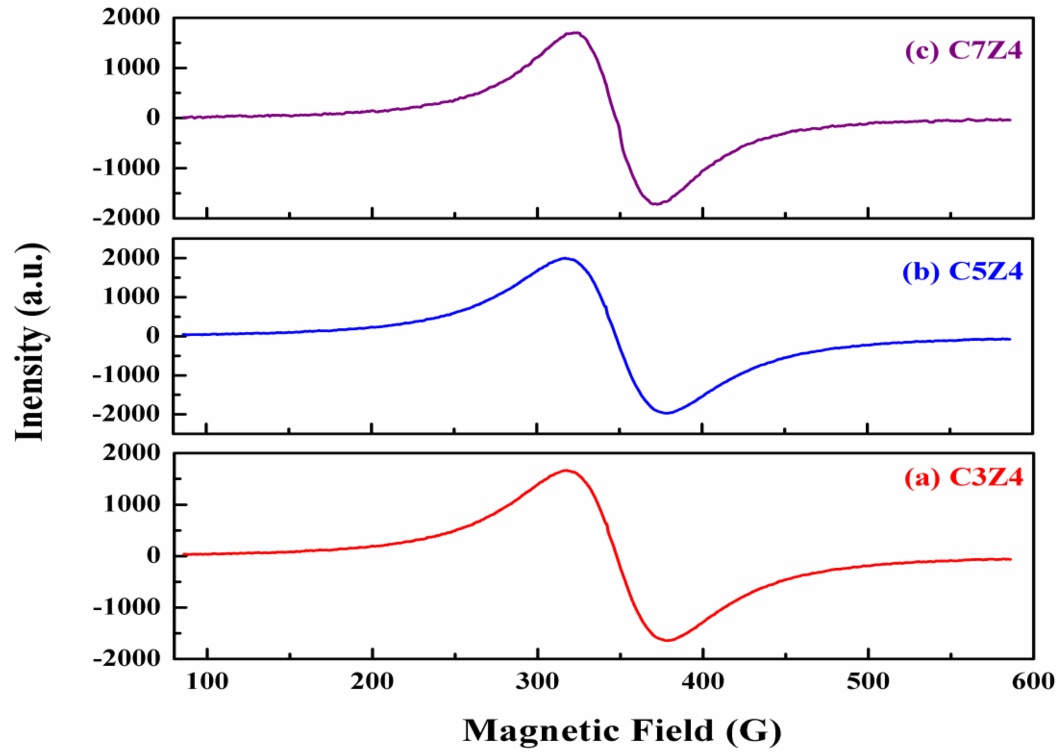

Fig. 5.7 EPR spectra of (a) CZ34, (b) CZ54 and (c) CZ74.

5.3.5 Static magnetic study

With the applied magnetic field of 500 Oe, the zero-field cooled and field cooled (ZFC-FC) magnetization curves as a function of temperature in the range from 300 K down to 10 K of all the specimens have been observed and shown in Figs. 5.8 (a), (b) and (c). From Figs. 5.8, it can be seen that both the FC and ZFC curves have been deviated from each other with the decrease of temperature from 300 K to the 10 K. the variation of FC and ZFC magnetization curves with the decrease of temperature below RT signifies to have paramagnetic/antiferromagnetic (PM/AFM) nature in doped nanostructured ZnO. Also, the existence of magnetic ordering in Cr-doped ZnO nanomaterials has been proven by the bifurcation of FC and ZFC curves at RT. It can be noticed from the magnetic measurement that the bifurcation increases with the increment of Cr^{3+} ions concentration within the host

ZnO nanomaterials. The magnetization value at different temperatures has been measured by the well-known Curie-Weiss law $\chi = \frac{C}{(T-\theta)}$,

Here, χ = M/H, C and θ represents the Curie constant and Curie temperature respectively. The respective fittings as well as the observed data have been shown in the inset of Figs. 5.9(a), (b) and (c) respectively. It has been observed that the poor fitting of all three samples have been deviated from paramagnetic phase. Therefore, we have to approach in a different manner to analyze the M-T data. Recently, few researchers have investigated the simultaneous presence of both ferromagnetic and antiferromagnetic contribution in transition metal (TM) doped ZnO nanomaterials in both experimental and theoretical point of view [45, 46]. In this work, we have fitted the FC *M(T)* data in the standard Block spin-wave model $[M(T) = M(0)(1 - BT^{\frac{3}{2}})]$, where *M(0)* represents the zero temperature magnetization linked with Curie-Weiss model $[M(T) = \frac{C\,H}{(T-\theta)}]$[47]. With adding an extra term $\frac{\mathrm{C\,H}}{(\mathrm{T})}$ in the above equation associated with the FC magnetization have been written as

$$M(T) = \frac{C_1\,H}{(T-\theta)} + \frac{C_2 H}{T} + M(0)\left(1 - BT^{\frac{3}{2}}\right) \tag{5.6}$$

Here
$$B = 2.612\frac{Sg\mu_B}{M(0)}\left(\frac{K_B}{4\pi D}\right)^{\frac{3}{2}} \tag{5.7}$$

And
$$D = 2a^2JS \tag{5.8}$$

Here, the value of the parameter B is inversely proportional to spin-wave stiffness, *J* represents the exchange energy, others symbol possess their usual meaning. From equation (5.4), it can be mentioned that the magnetic interactions can not affect only one subset (second one) of the spins. From the fitting data, the calculated values of C_1 for samples C3Z4, C5Z4 and C7Z4 are 4.378×10^{-5}, 1.01×10^{-4} and 2.03×10^{-3} emuK/gOe, respectively, and the values for C_2 are6.56×10^{-6}, 7.16×10^{-5} and 3.0×10^{-3} emuK/gOe respectively. With the increase in Cr doping concentration, the increasing value of C_1 and C_2 signifies the increase of AFM or PM contribution (since both represents direct functions of N). Therefore, a fitting shown in Figs. 5.8(d) expresses three characteristic consequences (i) Cr^{3+} ions coupled antiferromagnetically with at least one neighboring Cr^{3+} ion, (ii) isolated and completely free Cr^{3+} spin, which follows simple curie behaviour (iii) clustered Cr^{3+} spins with positive exchange integral. Below percolation threshold, the production of isolated, pairs and very small clusters of the dopant have been noticed. It has been noticed in a 3D spin-wave model that the $M(0)$ is proportional to the amount of net spin associated with the ferromagnetic part. From the fitting of C3Z4, C5Z4 and C7Z4 the extracted values of $M(0)$ are 5.0×10^{-5}, 3.63×10^{3} and 4.84×10^{-3} emu/g respectively. With the increase concentration of Cr^{3+} ions, the value of $M(0)$ increases which suggests that more and more Cr^{3+} ions are ferromagnetically coupled. Table 2 represents the contributions of aforesaid Cr^{3+} spin which indicates that the effective spin-spin interactions for C5Z4 and C7Z4 nanomaterials are ferromagnetic in nature at RT which are directly contradictory with the earlier published results [45, 48]. With the with increasing doping concentration of Cr^{3+} ions, net FM moment and PM/AFM moment increased significantly at RT which suggests that the doping plays an important role in magnetization. For C3Z4, C5Z4 and C7Z4 at RT, the FM contribution in the whole magnetization are 28.8%, 89.11% and 57.29% respectively. The FM contributions in the whole magnetization for all the samples decrease with the decrease of temperature, as shown in Table 5.2. Below 50 K, the AFM and PM contribution increases abruptly though the FM contribution remains almost constant there. Thus at low temperature, the abrupt change in M vs T curve is due to uncoupled or antiferromagnetically coupled spins that is studied in the present work. This has been the most significant trend for all DMS materials. So, nearly all dopant spins are isolated or antiferromagnetically coupled for low doping system. The total contribution of FM moment in the net magnetization of C7Z4 is lower as compared to C5Z4 though the net magnetization in C7Z4 is higher. We have already discussed in the EPR study that C7Z4 nanomaterial have more paramagnetic centers than C5Z4. The contribution of net FM moment of C7Z4 is lesser than C5Z4 though the total moment of C7Z4 is larger as compared to C5Z4. The Cr^{3+} ions are randomly distributed in the host lattice, for this type of system the extraction of the magnetic moment (S) and exchange integral (J) are nearly impossible. The value of B has been calculated from the fitting of equation (4) which fits appropriately with the experimental data. One fitting for M vs T curve corresponding to C7Z4 has been depicted in Figs. 5.8(d). The calculated values of B (from fitting) corresponding to C3Z4, C5Z4 and C7Z4 are 9.1×10^{-5}, 7.5×10^{-5} and6.0×10^{-5} $K^{-3/2}$ respectively. The decrease of B value with the increase of doping concentration of Cr^{3+} ion suggests that the system become more disorganized [49]. It is to be noted that this fact is in good agreement with the findings of Rietveld, PL and EPR analysis. Using the SQUID magnetometer, the M vs H data for all the samples at different temperatures (300, 100, 50 and 10 K) in the applied magnetic field range of 0-50000 Oe has been shown in Fig. 9 which depicts clear hysteresis behaviour but the hysteresis loops are not saturated at 50000 Oe. This exhibits the mixed magnetic phase present inside the sample as indicated by M-T curve. Some M-H loops at 10 and 100 K of C3Z4, C5Z4 and C7Z4 nanomaterials have been magnified and displayed in the inset of the respective M-H loops in Fig. 9. The maximum magnetizations are 0.038, 0.055, 0.148 emu/g respectively at 300 K which increases to 0.40, 0.90 and 1.26 emu/g as temperature decreases to 10 K, the corresponding coercive fields and remanent magnetizations at 100 K are 45, 126, 137Oe and 0.00030, 0.0029, 0.0041 emu and at 10 K are 49, 230, 261Oe and 0.00088, 0.0093, 0.0121 emu/g respectively for C3Z4, C5Z4 and C7Z4 nanomaterials. With the increase of Cr concentration, various antiferromagnetic phases may appear in the form of $ZnCr_2O_4$ (T_N ~ 11 K), Cr_2O_3, Cr_3O_4 and Cr metal clusters within the doped ZnO nanomaterials. Though, none of such phases can be observed in Rietveld study or in every characteristic peak of PL spectra. Therefore, RTFM cannot be explained on the basis of secondary phases. Different theories have been proposed in order to understand the origin of RTFM within the Cr-doped ZnO nanomaterials. The increment of structural defects due to the enhancement of doping has been exhibited by the Rietveld, EPR analyses and spin wave stiffness of the samples. Therefore, there is a strong relationship between the ferromagnetism and the structural defect. In order to get the idea behind magnetism in doped specimens, we have investigated magnetization (M) vs magnetic field (H) data in contribution of two magnetic components, one is FM component saturated at low field and other is linear component arises from PM. Considering the above fact, we have fitted the isothermal curve which can be written as

$$M = Nm_s \left[coth\left({}^{Hm_{eff}}\!/_{TK_B} \right) - {}^{TK_B}\!/_{Hm_{eff}} \right] + \chi_m H \qquad (5.9)$$

Here, *M* represents the total magnetization, *N* is number of magnetic spins/cluster (paramagnet), m_s signifies the moment per spin, *H* and *T* are the applied field and temperature respectively and K_B is the Boltzmann's constant [50,51]. The fitting parameters gained from the combined equations have been specified in Table 5.3 and one fitting for C7Z4 sample is shown in Fig. 5.10(d). Due to the weak FM moment with respect to PM/AFM spin, the RT isothermal curve of C3Z4 is not fitted by BMP model. The amount of ferromagnetically active clusters increases with the decrease of temperature as well as with Cr doping concentration which is clearly shown in Table 5.3. These is due to the exchange interaction between oxygen vacancy (V_o) and dopant ions [52]. Due to such interaction, few of the dopant spins align themselves around the oxygen vacancy (V_o) and creates localized ferromagnetically active clusters which are known as "polaron clusters" [53]. Such long range ferromagnetic ordering assigned as direct overlaps between BMPs or indirect BMP-magnetic impurity-BMP interactions [54]. The number of FM spin clusters is nearly 10^{19} as obtained from the fitting is below the percolation limit.

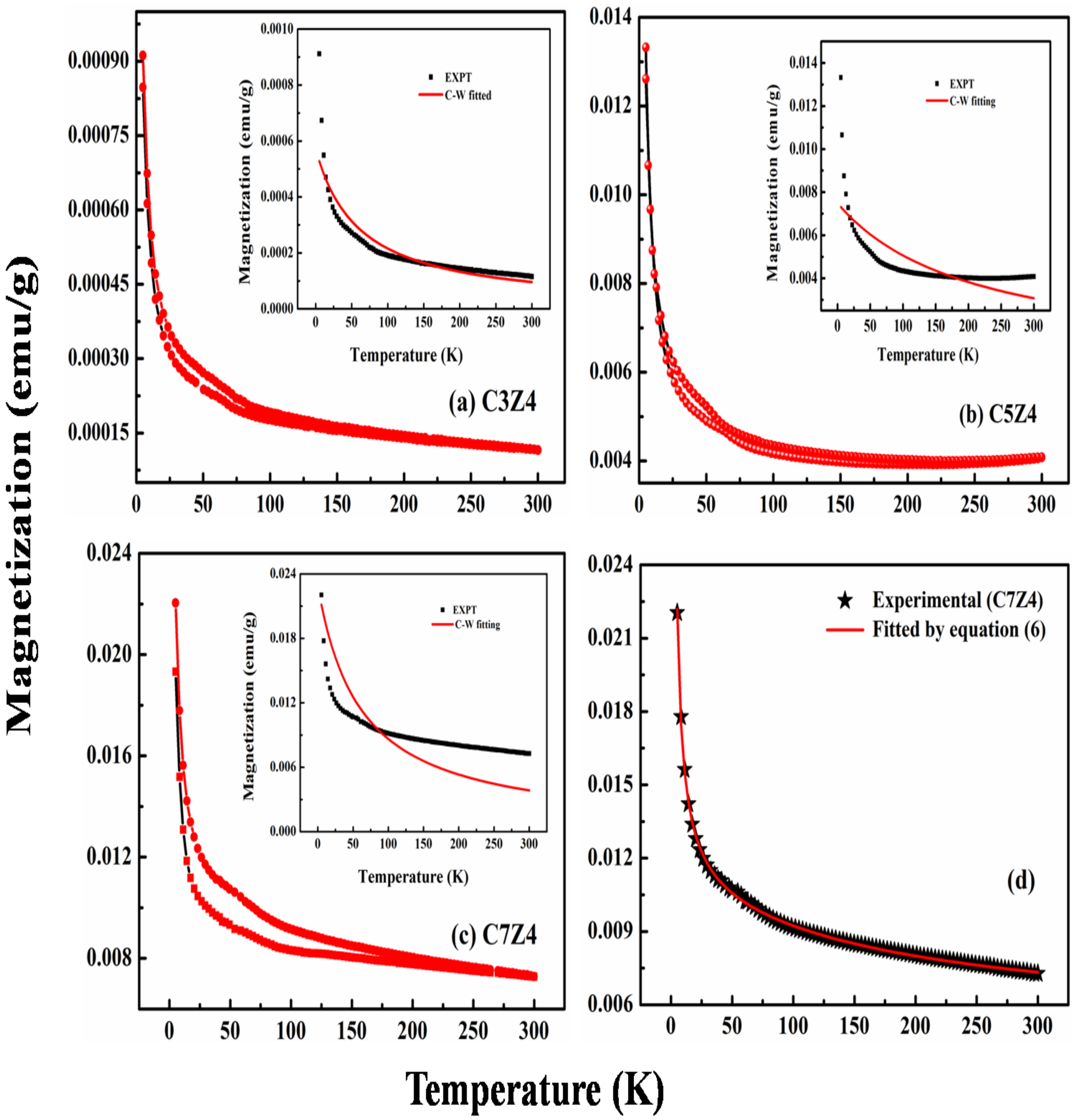

Fig. 5.8 Temperature variation of zero field cooled and field cooled magnetizations of (a) CZ34, (b) CZ54 and (c) CZ74with Curie-Weiss fittings in inset (d) observed magnetization vs. temperature curve of C7Z4 sample and its fittings according to equation 6 in the temperature range of 300 to 5 K.

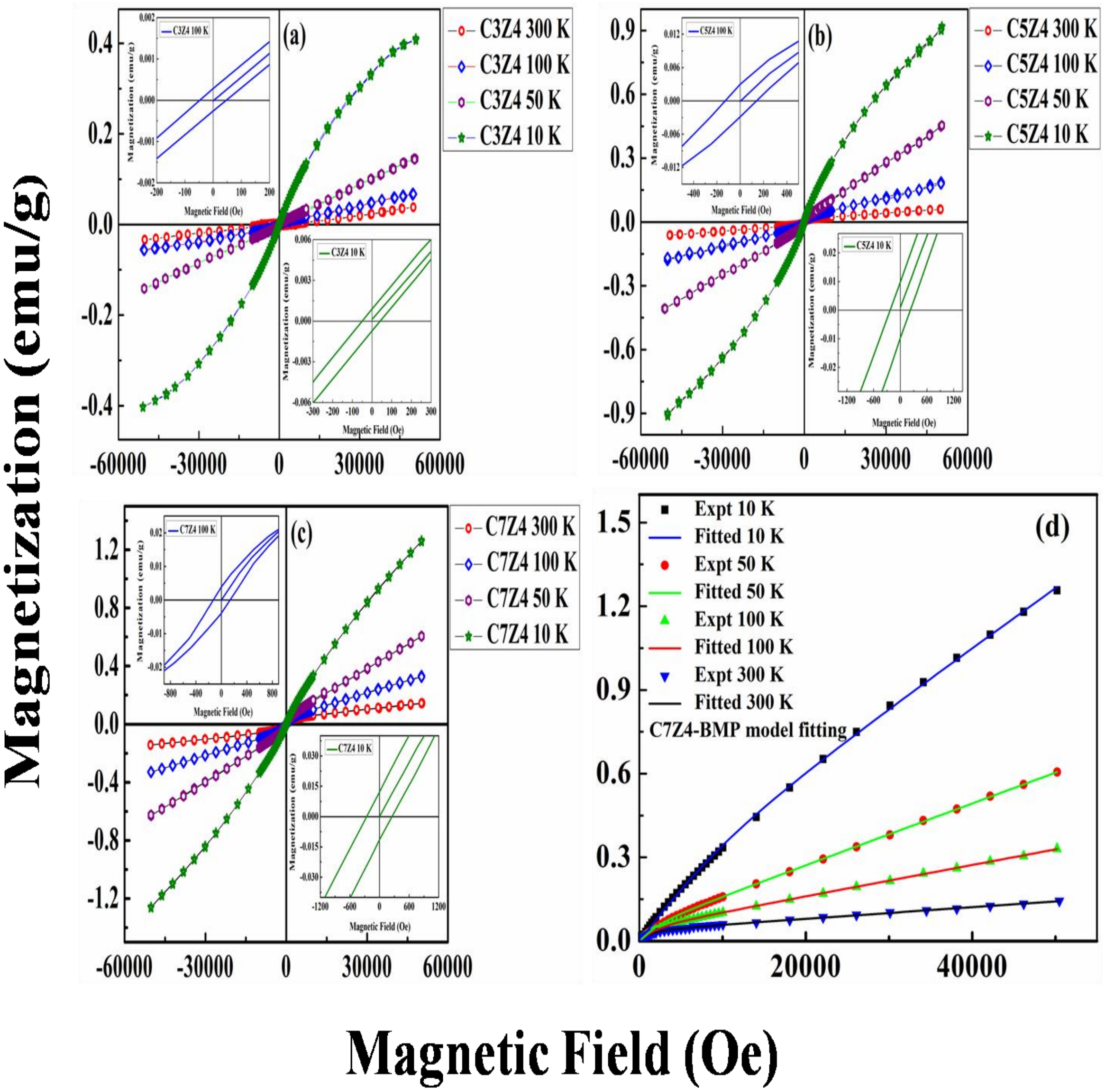

Fig. 5.9 Magnetic hysteresis (M–H) loops observed at 300, 100, 50 and 10 K temperature of the sample (a) CZ34, (b) CZ54 and (c) CZ74 and (d) initial magnetization vs. field curve of C7Z4 sample at 300, 100, 50 and 10 K along with the fitted data using BMP model. Also the magnified image of 10 K M-H loops of each nanomaterials are displayed in the inset of the respective M-H loops.

Table 5.2. Various magnetic parameters of Cr-doped ZnO nanomaterials extracted from static magnetic data.

Sample Name	Temperature (K)	Free Spin (emu/g)	Antiferro (emu/g)	Ferromagnetic (emu/g)	FM (%)
C3Z4	300	1.09×10^{-5}	5.48×10^{-5}	2.66×10^{-5}	28.8
	200	1.64×10^{-5}	7.32×10^{-5}	3.72×10^{-5}	29.3
	100	3.20×10^{-5}	1.10×10^{-4}	4.50×10^{-5}	24.6
	50	6.56×10^{-5}	1.47×10^{-4}	4.84×10^{-5}	18.5
	10	3.28×10^{-4}	2.00×10^{-4}	4.98×10^{-5}	8.6
C5Z4	300	1.28×10^{-4}	1.56×10^{-4}	2.21×10^{-3}	89.1
	200	1.92×10^{-4}	2.26×10^{-4}	2.85×10^{-3}	87.2
	100	3.85×10^{-4}	4.08×10^{-4}	3.35×10^{-3}	81.1
	50	6.83×10^{-4}	7.70×10^{-4}	3.53×10^{-3}	70.8
	10	3.85×10^{-3}	1.47×10^{-3}	3.62×10^{-3}	40.4

C7Z4	300	1.90×10^{-4}	2.27×10^{-3}	3.30×10^{-3}	57.3
	200	2.90×10^{-4}	2.83×10^{-3}	4.01×10^{-3}	56.5
	100	5.90×10^{-4}	3.77×10^{-3}	4.50×10^{-3}	50.8
	50	1.10×10^{-3}	4.50×10^{-3}	4.73×10^{-3}	45.6
	10	5.90×10^{-3}	5.30×10^{-3}	4.83×10^{-3}	30.1

Table 5.3. Result extracted from BMP fitting of Cr-doped ZnO nanomaterials.

Sample Name	Temperature	N (Cluster/gm)	Effective moment (m/cluster)
C3Z4	300	---	---
	100	5.3×10^{13}	5.63×10^{-17}
	50	6.5×10^{14}	5.00×10^{-18}
	10	4.8×10^{17}	2.88×10^{-19}
C5Z4	300	1.6×10^{14}	9.18×10^{-17}
	100	7.8×10^{14}	2.89×10^{-17}
	50	2.0×10^{15}	1.20×10^{-17}
	10	1.0×10^{18}	2.89×10^{-19}

C7Z4	300	5.8×10^{14}	6.78×10^{-17}
	100	3.6×10^{15}	1.41×10^{-17}
	50	8.5×10^{15}	6.51×10^{-18}
	10	2.0×10^{18}	1.93×10^{-19}

5.4 Conclusion

Here, we have investigated the significance of doping concentration of Cr on structural and magnetic property study of host ZnO nanomaterials. XRD study and FESEM analysis of all ZnO nanomaterials exhibit the favoured growth of rod like ZnO nanoparticles along '*a*' axis or (100) Bragg plane. XRD study reveals the increment of oxygen vacancy defects with the increase of doping concentration of Cr^{3+} ions within the nanostructured ZnO. This oxygen vacancy defect plays the crucial role to increase the ferromagnetic ordering within specimens. The existence of paramagnetic and ferromagnetic components and their organized enhancement with the increase of doping concentration of Cr in ZnO nanomaterials is manifested by the investigation of EPR spectra and static magnetic measurement. Under EPR study, we have observed the paramagnetic centers or singly ionized oxygen vacancies in all the doped nanostructured ZnO which increases and distributed uniformly with the increase of dopant concentration. The magnetic hysteresis is not saturated under static magnetic measurement at 5 T external magnetic field which signifies the combination of AFM and PM phases together with the FM phase that has been explained by the BMP model.

Reference:

[1] K. Zhang, T. Holloway, M. Bahoura, A. K. Pradhan, R. Prabakaran, J. Pradhan, S. Smith, J. C. Hall, G. T. Ramesh, D. R. Sahu, J. L. Huang, Proc. SPIE 7291 (2009) 729104.

[2] C. Chang, F. Kimura, T. Kimura, H. Wada, Mater. Lett. 59 (2005) 1037.

[3] S. Li, H. Song, H. Yu, S. Lu, X. Bai, G. Pan, Y. Lei, L. Fan, T. Wang, J. Lumin. 122 (2007) 876.

[4] M. Maekawa, H. Abe, A. Miyashita, S. Sakai, S. Yamamoto, A. Kawasuso, Appl. Phys. Lett. 110 (2018) 172402

[5] M.Z. Shoushtari, A. Poormoghadam, M. Farbod, Material Res. Bulletin 88 (2017) 315.

[6] B. Qi, S. Ólafsson, H.P. Gíslason, Progress in Materials Science 90 (2017) 45.

[7] S.A. Wolf, D.D. Awschalom, R.A. Buhrman, J.M. Daughton, S.V. Molnar, M.L. Roukes, A.Y. Chtchelkanova, D.M. Treger, Science 294 (2001) 1488.

[8] Y. Matsumoto, M. Murakami, T. Shono, T. Hasegawa, T. Fukumura, M. Kawasaki, P. Ahmet, T. Chikyow, S.Y. Koshihara, H. Koinuma, Science 291 (2001) 854.

[9] N. Dogan, A. Bingolbali, L. Arda, J. Magn. Magn. Mater. 373 (2015) 226.

[10] S. Zhou, K. Potzger, Q. Xu, Vacuum 83 (2009) S13-S19.

[11] A. A. Dakhel, M. El-Hilo, J. Appl. Phys. 107 (2010) 123905.

[12] J. Anghel, A. Thurber, D.A. Tenne, C.B. Hanna, A. Punnoose, J. Appl. Phys. 107 (2010) 314.

[13] K. Sato, H.K. Yoshida, Jpn. J. Appl. Phys. 39 (2000) L555.

[14] B.Q. Wang, J. Iqbal, X.D. Shan, G.W. Huang, H.G. Fu, R.H. Yu, D.P. Yu, Mater. Chem. Phys. 113 (2009) 103.

[15] A. Tiwari, V.M. Bhosle, S. Ramachandran, N. Sudhakar, J. Narayan, S. Budak, A. Gupta, Appl. Phys. Lett. 88 (2006) 142511.

[16] B. Wang, J. Iqbal, X. Shan, G. Huang, H. Fu, R. Yu, D. Yu, Mater. Chem. Phys. 113 (2009) 103.

[17] S. B. Singh et al., Nanoscale 6 (2014) 9166.

[18] R.N. Aljawfi, F. Rahman, D.K. Shukla, Mater. Lett. 99 (2013) 18.

[19] T. Dietl, Nat. Mater. 9 (2010) 965.

[20] Chou H, Lin CP, Huang JCA, Hsu HS Phys Rev B 77 (2008) 245210.

[21] A.E. Kandjani, M.F. Tabriz, O.M. Moradi, H.R. Mehr, S.A. Kandjani, M.R. Vaezi, J. Alloys Compd. 509 (2011) 7854.

[22] N. Al-Hardan, M.J. Abdullah, A.A. Aziz, Appl. Surf. Sci. 257 (2011) 8993.

[23] T. Debnath, P. Saha, N. Patra, S. Das, S. Sutradhar, J. Appl. Phys. 123 (2018) 194101.

[24] S. Das, S. Das, S. Sutradhar, Ceramics International 43 (2017) 6932-6941.

[25] S. Das, A. Bandyopadhyay, S. Das, D. Das, S. Sutradhar, J Alloys Compd. 731 (2018) 591.

[26] S. Das, A. Bandyopadhyay, P. Saha, S. Das, S. Sutradhar, J Alloys Compd. 749 (2018) 1.

[27]Y.M. Hu, S.S. Li, C.H. Chia, Appl. Phys. Lett.98, (2011) 052503.

[28] D. Polsongkrama,, P. Chamninok, S. Pukird, L. Chowb, O. Lupan, G. Chai, H. Khallaf, S. Park, A. Schulte, Physica B 403 (2008) 3713.

[29] A. Bandyopadhyay, A.K. Deb, K. Mukhopadhyay, S.K. Roy, P.K. Chakrabarti, J. Mater. Sci. 47 (2012) 2284.

[30] L. Lutterotti, S. Gialanella, Acta Mater. 46 (1998) 101.

[31] S. Kumar, S. Basu, B. Rana, A. Barman, S. Chatterjee, S.N. Jha, D. Bhattacharyya, N.K. Sahoo, A. K. Ghosh, J. Mater. Chem. C 2 (2014) 481.

[32] Ü. Özgür,Y.I. Alivov, C. Liu, A. Teke, M.A. Reshchikov, S. Doğan, V. Avrutin, S.J. Cho, H. Morkoçd, J. Appl. Phys. 98 (2005) 041301.

[33] J.H. Park, Y.J. Lee, J.S. Bae, B.S. Kim, Y.C. Cho, C. Moriyoshi, Y. Kuroiwa, S. Lee, S.Y. Jeong, Nanoscale Res. Lett. 10 (2015) 186.

[34] K.U. Haq, M. Irfan, Md. Masood, M. Saleem, T. Iqbal, I. Ahmad, M.A. Khan, M. Zaffar, M. Irfan, J. semicond. 39 (2018) 043001.

[35] X. Wang, R. Zheng, Z. Liu, Z. Liu, H.P. Ho, J. Xu, S.P. Ringe, Nanotechnolgy, 19 (2008) 455702.

[36] T. Debnath, P. Saha, N. Patra, S. Das, S. Sutradhar, J. Appl. Phys. 123 (2018) 194101.

[37] J. Kennedy, P.P. Murmu, E. Manikandan, S.Y. Lee, J. Alloys Compd. 616 (2014) 614.

[38] X. Wei, B. Man, J. Appl. Phys. 45 (2006) 8586.

[39] Y. Gong, Nanoscale Res. Lett. 2 (2007) 297.

[40] J. Kennedy, D.A. Carder, A. Markwitz, R.J. Reeves, J. Appl. Phys. 107 (2010) 103518.

[41] B. Sathyaseelan, E. Manikandan, K. Sivakumar, J. Kennedy, M. Maaza, J. Alloys Compd. 651 (2015) 479.

[42] A. Kar, S. Kundu, A. Patra, J. Phys. Chem. C 115 (2011)118.

[43] S.S. Sartiman, N.F. Djaja, R. Saleh, Materials Sciences and Applications 4 (2013) 528.

[44] J.T. Vallin, G.D. Watkins, Phys. Rev. B 9 (5) (1974) 2051.

[45] Z.L. Lu, W. Miao, W.Q. Zoua, M.X. Xu, F.M. Zhanga, J. Alloys Compd. 494 (2010) 392.

[46] J. Qi, D. Gao, J. Liu, W. Yang, Q. Wang, J. Zhou, Y. Yang, J. Liu, Appl. Phys. A 100 (2010) 79.

[47] S.J. Potashnik, K.C. Ku, R. Mahendiran, S.H. Chun, R.F. Wang, N. Samarth, P. Schiffer, Phys. Rev. B 66 (2002) 012408.

[48] M. Kobayashi, Y. Ishida, J.I. Hwang, Y. Osafune, A. Fujimori, Y. Takeda, T. Okane, K. Kobayashi, H. Saeki, T. Kawai, and H. Tabata Phys. Rev. B 81 (2010) 075204.

[49] J.J. Beltrán, C.A. Barrero, A. Punnoose, Journal of Physical Chemistry C 118 (2014) 13203.

[50] A. Bandyopadhyay, S. Sutradhar, B.J. Sarkar, A.K. Deb, P.K. Chakrabarti, Appl. Phys. Lett. 100 (2012) 252411.

[51] A. Chanda, S. Gupta, M. Vasundhara, S.R. Joshi, G.R. Mutt, J. Singh, RSC Adv. 7 (2017) 50527.

[52] N.W. Gray, A. Tiwari, J. Appl. Phys. 110 (2011) 033903.

[53] J.M.D. Coey, M. Venkatesan, C.B. Fitzgerald, Nat. Mater. 4 (2005) 173.

[54] C.G. Jin, Y. Yang, Z.F. Wu, L.J. Zhuge, Q. Han, X.M. Wu, Y.Y. Li, Z.C. Fenge, J. Mater. Chem. C 2 (2014) 2992.

CHAPTER 6

Structural, morphological and charge transport properties study of Chromium doped ZnO nanomaterials

6.1 Introduction

In recent years, nanomaterials are the subject of foremost concern of the research community due to their magnificent physical properties like crystallinity, mechanical, optical, magnetic, dielectric and electrical properties etc [1-7]. The modulation of surface to volume ratio, quantum size effect, grain morphology and grain boundary of materials in the nanoscale regime exhibit controls over structural and microstructural symmetry, charge density, band gap energy, microstrain and native defects, etc. [8-10]. Proper choice of host materials, selection of dopants, preparation techniques and the percentage variation of dopants within the host lattice can modulate the physical properties like mechanical, optical, magnetic and charge transport properties, etc. in the selected direction of applications [11-15]. The modulation of dielectric responses in accordance with the morphologies of nanospheres, nanorods, nanowires, nanotubes, etc. is the subject of primary interest. Such materials have massive impact in the electronics industry like, capacitors, sensors, electrochemical transducers, gate electrodes, multiferroics, piezoelectric nano-generators, etc. [16-20]. The electrical transport phenomena and the dielectric properties of nanomaterials are totally contrasting to their bulk counterpart as the nanomaterials have different types of interfaces as well as various forms of defect states. The interfaces present within the nanostructure behave as the source of electric dipoles which modulates the dielectric permittivity of nanomaterials significantly. In recent years, for the reduced scale electronic devices, scientists are giving huge effort to explore new materials with improved super high dielectric response [12]. The influence of dopant selection, dopant concentration and the synthesis procedures on the dielectric response, ac conductivity will give us significant information about charge transport phenomena within the nanostuctured materials. As Cr can enhance the charge carrier density in doped ZnO nanomaterials, (Cr) has been taken as a dopant to modulate the band energy gap as well as the dielectric property of semiconducting ZnO host nanomaterial.

Many articles have been published with chromium (Cr) as a dopant within the structure of ZnO due to its efficiency to modulate the magnetic property of the host ZnO nanomaterials [21-24]. Also, a few researchers have developed the dielectric response of Cr-doped ZnO nanomaterials. The physical properties like optical, magnetic and dielectric properties of ZnO nanomaterials have been modulated systematically with the percentage variation of Cr ions within the lattice structure which have been demonstrated in the earlier published articles. The proper incorporation of Cr ions can modulate the modulate carrier concentration, microstrain and various native defects within the lattice structure of host ZnO nanomaterials. Many published articles have explored the structural, magnetic, optical, and dielectric aspects of Cr-doped ZnO nanostructures [12,25]. But merely reported any detailed analysis on the synthesis process dependent dielectric response of Cr-doped ZnO nanoparticles. This has encouraged us to execute an extensive study on dopant as well as synthesis process dependent dielectric response of Cr-doped ZnO nanomaterial. In our earlier work, the presence of Cr ion modulates the dielectric constant of hydrothermally prepared doped ZnO nanorods within the range of 1.9×10^5 to 5.2×10^5 [12]. Hassan et al. investigated the change in dielectric constant from 20 to 14 of ZnO nanoparticles synthesized by co-precipitation method with Cr doping (0 to 10%) [25]. Aljawfiet al. proclaimed the decrease in dielectric constant from 27 to 9 of ZnO nanoparticles prepared by a sol-gel method due to Cr doping [26]. Interestingly, small size and nearly symmetric structures of nanoparticles synthesized via co-precipitation or similar methods would not have high dielectric constant [25,26]. El-Desoky et al. explored the modulation of dielectric constant from 15 to 75 of ZnO nanoparticles by the variation of annealing temperature from 100 to 500 ^{o}C [27]. Thus, a systematic and quantitative variation is expected due to the percentage change of dopant [12]. Though, a synthesis process like hydrothermal method can produce a very high dielectric value of undoped or doped ZnO nanomaterials. After studying many articles on doped ZnO nanomaterials, all synthesis procedure other than hydrothermal route produce ZnO nanomaterials with small size and nearly symmetric grain structure cannot generate high dielectric constant of ZnO nanomaterials which motivated us to investigate on this research field. It is anticipated that the Cr-doped ZnO nanomaterials synthesized by co-precipitation method have spherical grain structures, where as Cr-doped ZnO nanomaterials synthesized by hydrothermal method have rod like grain structures. Also, the grain size of the rod like structure are more with thick grain boundaries with respect to the spherical grain structures of Cr-doped ZnO nanomaterials. In rod like grain structures of Cr-doped ZnO nanomaterials, the grain boundary effect is quite high. Therefore, the electron tunneling/drifting is low in rod like structures of Cr-doped ZnO nanomaterials due to high grain boundary effect. So in case of rod like structures, in presence of external applied electric field, the polarization effect is expected to be very high and also the dielectric permittivity of the nanomaterials is quite high[12,25-27]. Thus, the essence of this present article is the synthesis procedure that can modulate the dielectric property in a complementary manner.

6.2Experimental

6.2.1 Materials

Different salts like zinc acetate dehydrate $Zn(CH_3COO)_2{\cdot}2H_2O$ (Sigma Aldrich, 99%), chromium acetate $Cr(CH_3COO)_3$ (Sigma Aldrich, 99%) and ammonium hydroxide NH_4OH (concentration ~ 25%) have been taken as the precursors for the synthesis of undoped ZnO and Cr-doped ZnO nanomaterials with the stoichiometry of $Zn_{0.97}Cr_{0.03}O$, $Zn_{0.95}Cr_{0.05}O$, and $Zn_{0.93}Cr_{0.07}O$ via co-precipitation and hydrothermal synthesis routes.

6.2.2 Co-precipitation synthesis of undoped ZnO and Cr-doped ZnO nanoparticles

Cr-doped ZnO nanomaterials with different Cr concentrations ($Zn_{0.97}Cr_{0.03}O$, $Zn_{0.95}Cr_{0.05}O$, and $Zn_{0.93}Cr_{0.07}O$) have beensynthesized by co-precipitation method. A beaker has been used to take the precursor salts i.e. $Zn(CH_3COO)_2{\cdot}2H_2O$ and $Cr(CH_3COO)_3$ in the presence of double distilled water, which has been placed on a magnetic stirrer. Then NH_4OH solution has been added to the previous mixture at a temperature of 60 ^oC in which the pH maintained is at ~ 9. As a result of the reaction, a mix of $Zn(OH)_2$ and $Cr(OH)_3$colloids is formed and collected for washing. After washing the pH becomes ~ 7. The supernatant is then removed, and the precipitates have been dried. The undoped ZnO is also prepared by the same method. Finally, the dried powders of undoped ZnO and different percentage of Cr-doped ZnO have been annealed at 400 ^oC and are defined as C0Z4Cp, C3Z4Cp, C5Z4Cp, and C7Z4Cp.

6.2.3 Hydrothermal synthesis of undoped ZnO and Cr-doped ZnO nanorods

For hydrothermal synthesis route, excess ammonia has been added to the aqueous mixture solution of precursor salts to increase the pH to ~ 11. At this high value of pH, the colloidal suspension of hydrated ions like $Zn(OH)_4^{2-}$ and $Cr(OH)_6^{3-}$have been formed. The colloidal suspension has been taken into a Teflon jacket of stainless-steel autoclave and it is kept inside the oven for 48 hours at 160 ^oC .At the end of these hours, the autoclave has to achieve room temperature (RT) naturally. The solid precipitates have been washed many times in order to reduce the pH to ~ 7. The undoped ZnO is also synthesized by the same method. Finally, the dried powders of undoped ZnO and different Cr-doped ZnO have been annealed at 400 ^oC and defined as C0Z4Ht, C3Z4Ht, C5Z4Ht, and C7Z4Ht. The whole preparation technique of undoped ZnO and 3, 5 and 7% Cr-doped ZnO nanomaterials via co-precipitation (C0Z4Cp, C3Z4Cp, C5Z4Cp, and C7Z4Cp) and hydrothermal synthesis route (C0Z4Ht, C3Z4Ht, C5Z4Ht, and C7Z4Ht) is shown in Fig. 6.1.

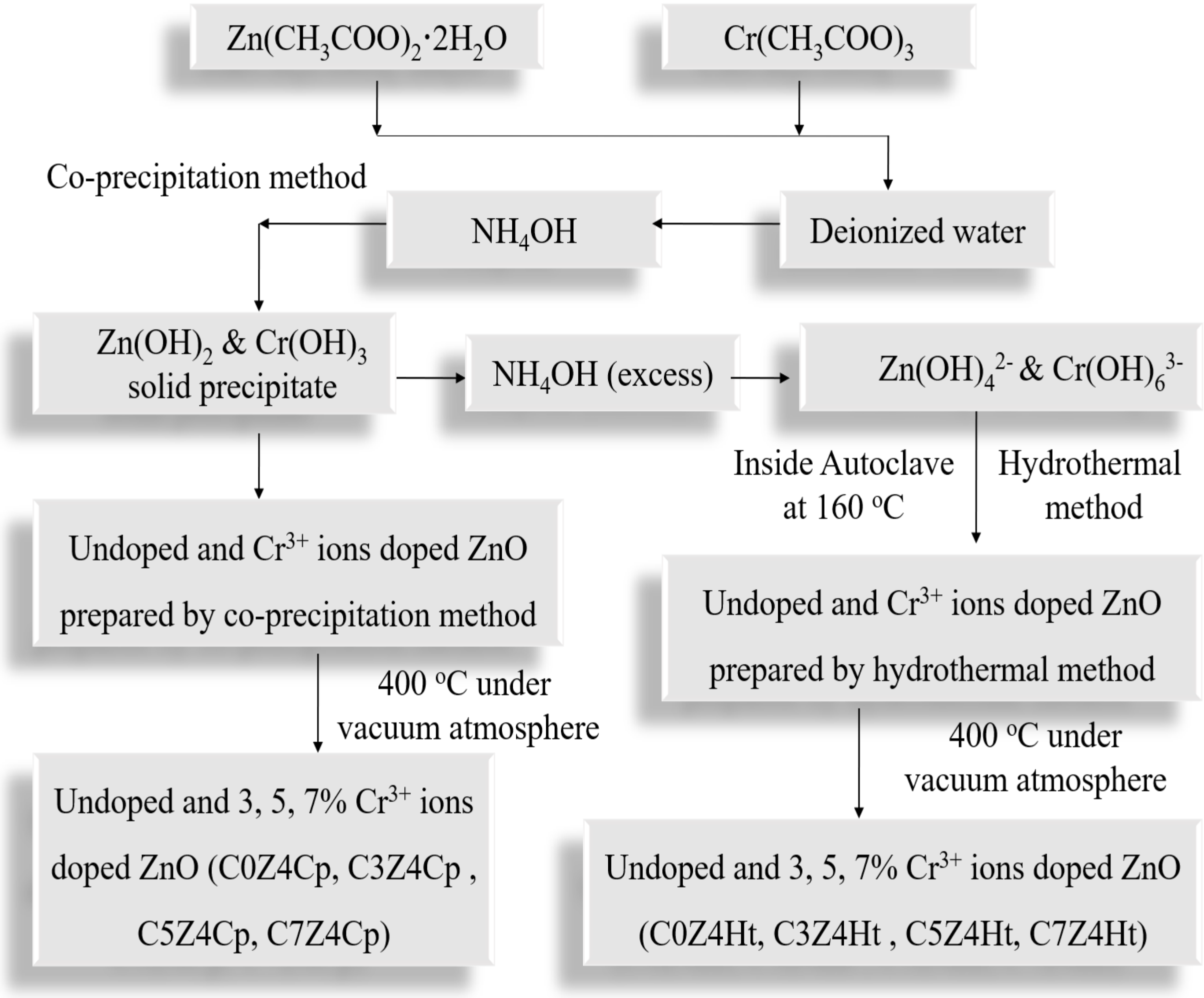

Fig. 6.1 Flowchart of synthesis of undoped ZnO and 3, 5 and 7% Cr^{3+} ion-doped ZnO by co-precipitation and hydrothermal synthesis route.

6.2.4 Characterization techniques

The XRD pattern of all the samples have been recorded in powder X-ray diffractometer, Model D8, BRUKER AXS, using Cu K_α radiation ($\lambda = 1.5405$ Å) in the range of 2θ from 20 to 80°. Field emission scanning electron microscope (FESEM) has been measured by using FESEM, INSPECT F50 (FEI, Netherland). The optical absorption (UV-visible) spectrum has been conducted in the range of 250-500 nm using l25 spectrophotometer, Perkin Elmer, Germany. By using Agilent 4294A Precision Impedance Analyzer, for frequency and temperature-dependent dielectric response measurement and impedance study of C0Z4Cp, C3Z4Cp, C5Z4Cp, C7Z4Cp nanoparticles and C0Z4Ht, C3Z4Ht, C5Z4Ht, and C7Z4Ht nanoparticles of all the undoped and Cr-doped ZnO powder nanomaterials have been measured.

6.3Results and Discussions

6.3.1. XRD Analysis

Fig. 6.2 represents the Rietveld analysis of the X-ray diffraction (XRD) curves for all the samples.With the help of JCPDS file for ZnO (JCPDS file no-36-1451), the peaks obtained from XRD measurement has been assigned.No other impure phases have been detected within the detection limit of XRD which exhibits successful incorporation of Cr ion in host ZnO lattice. The peak broadening in the XRD patterns proves that the nanocrystals and lattice strain are present within the samples. We have esteemed the intensity and sharpness of XRD peaks for hydrothermally synthesized samples are more as compared to co-precipitated samples, which shows better crystallinity of the former as compared to the latter.

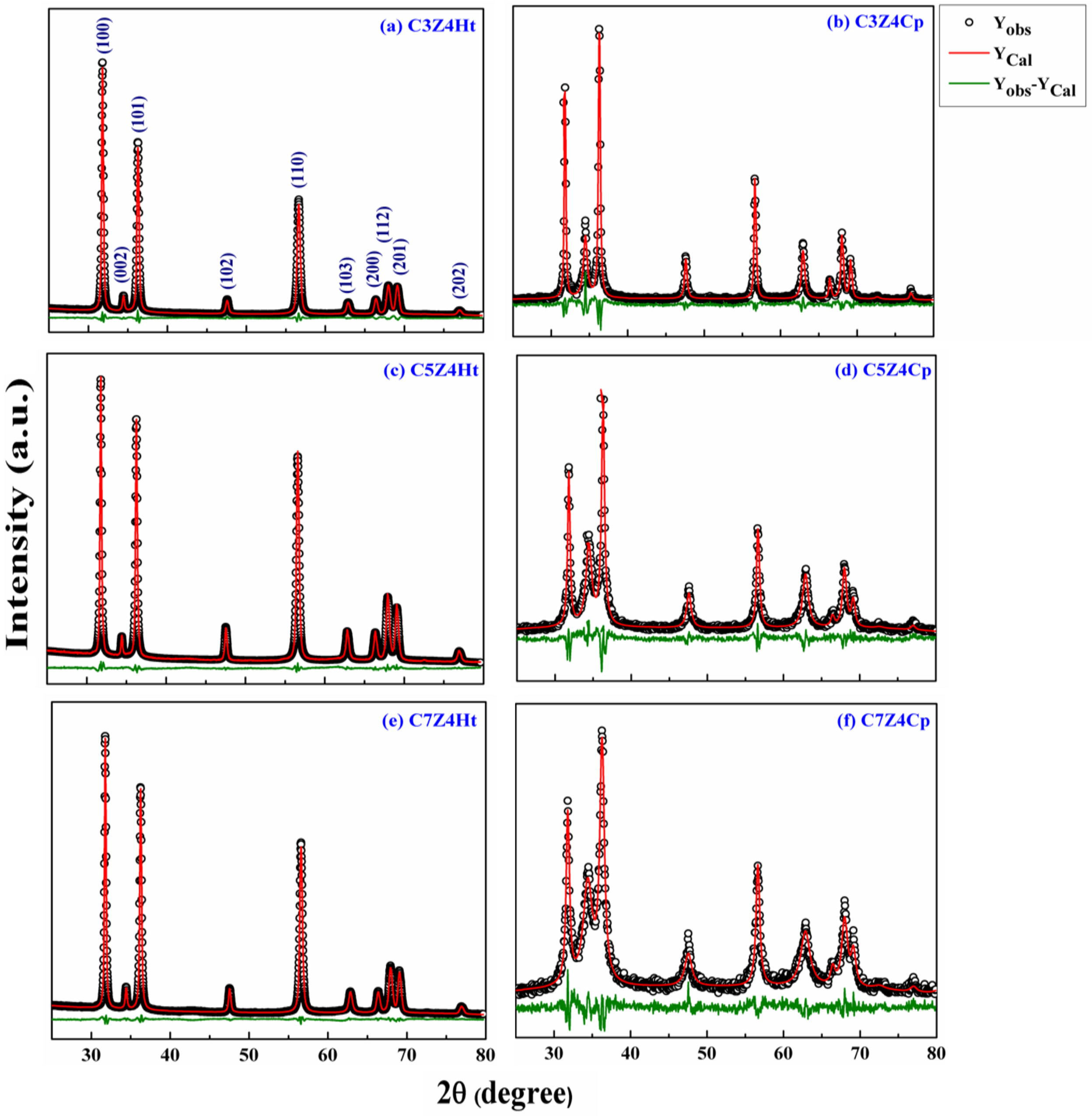

Fig. 6.2 XRD patterns and the Rietveld analysis of the samples (a) C3Z4Ht, (b) C3Z4Cp (c) C5Z4Ht (d) C5Z4Cp (e) C7Z4Ht and (f) C7Z4Cp.

The structural variation between the two sets of samples synthesized by co-precipitation and hydrothermal method is significantly reflected in their corresponding diffraction peaks. The most acute peak for the co-precipitated sample presents the (101) plane, which is in good agreement with standard JCPDS file. Interestingly, all the hydrothermally synthesized samples have a very intense peak corresponding to the (100) plane. Therefore, for a hydrothermally prepared sample a selected growth of the crystal along 'a' axis is observed. ZnO nanorods are aligned in regular fashion along 'a' axis [in comparison to 'c' axis] which proves to be very special for the powder sample. To get a proper observation we have determined an orientation parameter for all the samples. For all six samples, for a specified plane with Miller indices (h, k, l) the respective orientation parameter$\nu_{h_i k_i l_i}$is computed as [28]

$$\boldsymbol{\gamma_{h_i k_i l_i} = \frac{I_{h_i k_i l_i}}{\sum_{i=1}^{n} I_{h_i k_i l_i}}} \tag{6.1}$$

Where the calculation is executed by taking n = 5. For 3% doped hydrothermally prepared samples, the values of $\gamma_{(100)}$, $\gamma_{(002)}$, $\gamma_{(101)}$, $\gamma_{(102)}$and $\gamma_{(110)}$are 0.429, 0.0308, 0.3028, 0.0301 and 0.1997 respectively whereas the corresponding values for co-precipitated samples are 0.298, 0.1174, 0.378, 0.056, 0.149 respectively. For hydrothermally prepared sample, the relative intensity of the plane (002) decreases. It is true for other doping concentrations also. Fig. 6.3 represents the orientation parameter for (100), (002), (101) and (110). The figure exhibits that the intensity of the planes (100) and (110) is higher for samples prepared by hydrothermal method as compared to a standard JCPDS spectra. Therefore, the growth along those planes is secured at the cost of (002), (101) planes. The orientation parameter cannot change instantly with doping for all samples that are incompatible to the previous results [29]. It is already been published that enhanced mobility of the atoms favours the growth of crystal planes [30]. Therefore, it can be understood that hydrothermally synthesized sample will exhibit different properties as compared to the co-precipitated sample.

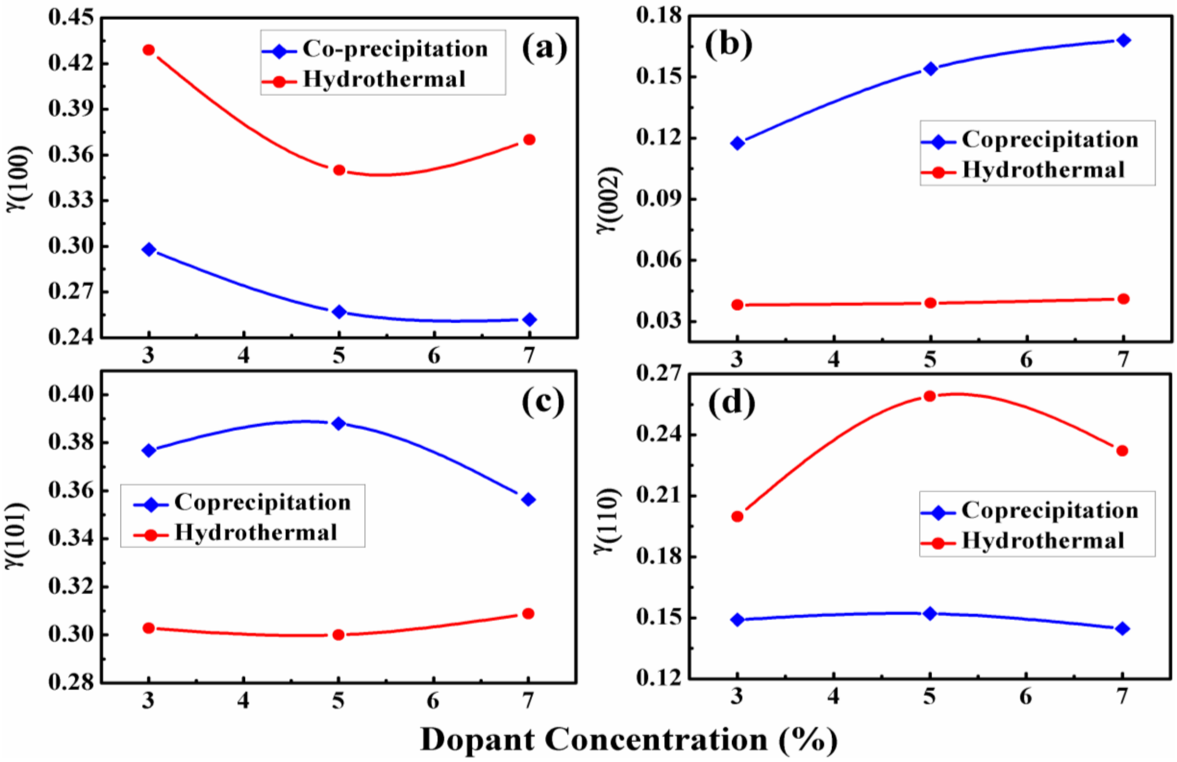

Fig. 6.3 Orientation parameters of 3, 5 and 7% Cr-doped ZnO nanomaterials synthesized by hydrothermal and co-precipitation technique corresponding to the planes(a) (100), (b)(002), (c) (101) and (d) (110)

By using the software MAUD, different structural and microstructural parameters for all the samples have been carried out by the Rietveld analysis [31]. Pseudo Voigot function has been applied to fit the diffraction peaks and six coefficient polynomial functions have been employed to estimate the background. In Fig. 6.2, the observed and the fitted data of the X-ray diffraction (XRD) patterns for all the samples have been exhibited and Y_{obs}(observed intensity), Y_{cal} (calculated intensity) and Y_{obs}-Y_{cal} (comparison between observed and calculated intensities) have been extracted. From the Rietveld analysis of the diffraction pattern followed by Morkoç and Özgür, the values of various structural parameters like degree of distortion *R*, bond length (b), bond angles (θ, β), etc. have been calculated [32,33]. The extracted values have been shown in Table 6.1. The equations for computing the parameters are as follows

$$\boldsymbol{b = uc} \tag{6.2}$$

Where,$u = \frac{1}{3}\frac{a^2}{c^2} + \frac{1}{4}$is known as internal parameter. When the ratio c/a decreases or increases, u increases or decreases just as the values of four tetrahedral distances are found to benearly stable by a distortion of tetrahedral angles

$$\boldsymbol{\theta = \frac{\pi}{2} + arccos\frac{1}{\sqrt{[1+3\frac{c^2}{a^2}(-u+\frac{1}{2})^2]}}} \tag{6.3}$$

$$\boldsymbol{\beta = 2arcsin\frac{1}{\sqrt{[\frac{4}{3}+4\frac{c^2}{a^2}(-u+\frac{1}{2})^2]}}} \tag{6.4}$$

Where, b represents the bond length and bond angles θ and β have been defined as average bond length of the base (Oa-Zn-O_b) and average apex angle of the base (O_b-Zn-O_b), respectively, here O_a and O_b represent O atom at the base of tetrahedral structure. Fig. 6.4 shows the variation of lattice parameter with doping concentration. From the Fig. 6.4and Table 6.1, it is to be noted that for co-precipitated samples, the 'c' axis increases with doping, whereas for hydrothermally prepared sample opposite phenomena is occurred. A linear decrease in lattice parameter 'c' is very much expected as the effective radius of Zn^{2+} (0.74 Å) is larger than Cr^{3+} (0.63 Å). For co-precipitated samples the increase in 'c' is quite interesting. Due to a strong affinity of Cr for the octahedral site in spite of the tetrahedral site, a fraction of the Cr atom resides on the octahedral interstitial site [34]. Also, the lattice parameter 'a' calculated from the refinement increases for all the samples. Due to the existence of a few larger size Cr^{2+} (0.80 Å) ions within the interstitial position of the host lattice, the increase in 'a' for co-precipitated samples is occurred. Though, for hydrothermally prepared samples the increase of '*a*'can be ascribed as the small distortion in Zn tetrahedron. In the direction of *c* and within the plane of *ab*, the Zn tetrahedron has a base and an apex respectively. Now, there will be increase in the average bond angles of base (O_b-Zn-O_b) and decrease in the average apex angles of the base (O_b-Zn-O_a) (in which O_b and O_a represents oxygen atoms present in the base and apex respectively of the tetrahedron) due to incorporation of Cr ions in place of Zn ions which influences a slight rise in '*a*' and a slight fall in '*c*' parameter of the final lattice structure of ZnO [35]. Now, the values of base-apex angles and basal bond angles have been shown in Table 6.1 supporting the above explanation. For all samples the computed bond lengths agree well with the investigated Zn-O bond length (1.9767Å) in the unit cell. For co-precipitated samples, the increase of bond lengths with respect to the rise in dopant concentration has been credited to the segregation of Cr ions in host lattice. Therefore, it is to be noted that a proper incorporation of dopant in place of host cation is possible only for the hydrothermal procedure.

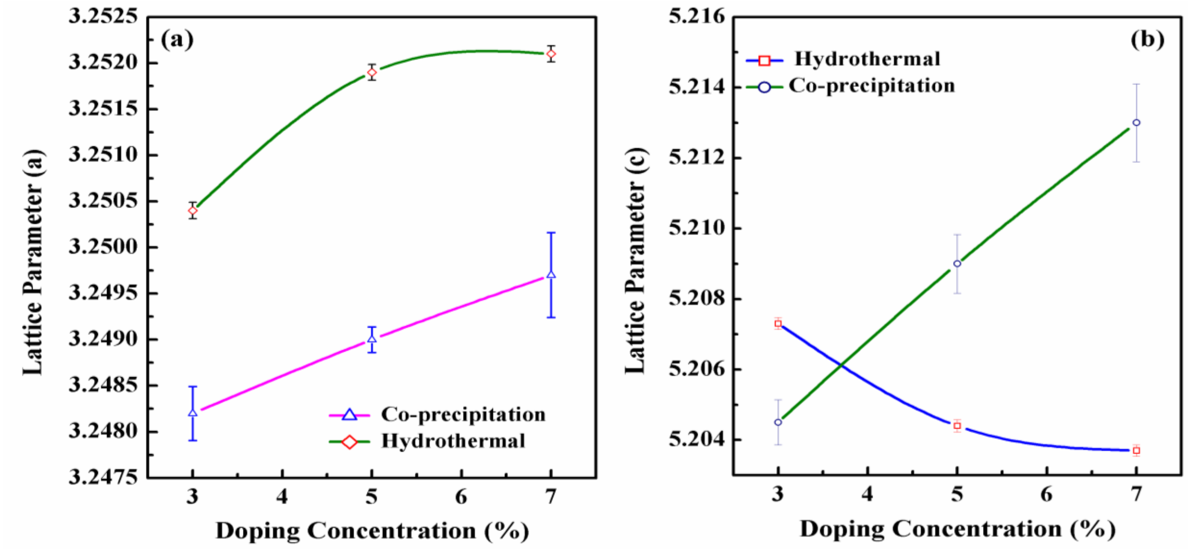

Fig. 6.4 Variation of lattice parameters of **(a)** Lattice parameter a and **(b)** Lattice parameter c as a function of the doping concentrations (3, 5 and 7%) in Cr-doped ZnO nanomaterials synthesized via hydrothermal and co-precipitation route.

The crystal structure of co-precipitated Cr-doped ZnO nanomaterial derived theoretically as procured from the CIF file after the refinement is also assigned in Fig. 6.5 and the theoretically derived crystal structure of hydrothermally prepared Cr-doped ZnO nanomaterial as procured from the CIF file after the refinement has been studied in our earlier publication [24]. It is also need to mention here that to maintain charge neutrality two Cr^{3+} ions replace three Zn^{2+} ions. The equation can be written as

$$\mathbf{3Zn^{2+} = 2Cr^{3+} + V_{Zn}{}^{2+}} \tag{6.5}$$

Therefore, proper substitution will form zinc vacancies/structural disorder inside the crystal which may influence the physical properties of the hydrothermally prepared sample.

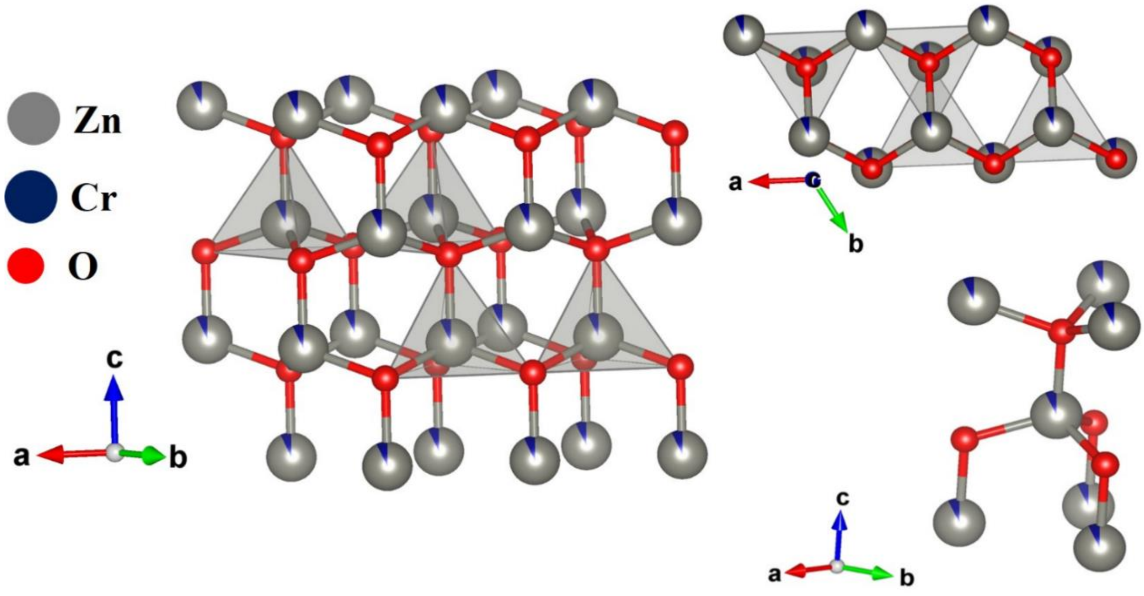

Fig. 6.5 Structural presentation of Cr-doped ZnO nanomaterial synthesized by co-precipitation method.

With increase of doping, the average crystallite size decreases for all the samples which suggest that the grains of the crystal have been stopped from growing due to the substitution of Cr cations within host lattice. The prevention in the movement of the grain boundaries can be explained on the basis of zener pinning discussed in our earlier paper [24]. The rate of decrement of average crystallite size with doping percentage is more for hydrothermally prepared samples. For co-precipitated samples, the increase in doping percentage causes a few larger size Cr^{+2} ions to locate within the interstitial positions which corresponds to slow down the decrement rate. The microstrain (ε) is proportional to the defect concentration within the crystal which is an important parameter. From the refinement for co-precipitated samples, the extracted microstrain varies from 5.90×10^{-5} to 1.01×10^{4}

whereas the microstrain obtained for hydrothermally prepared samples is comparatively higher and varies from 1.03×10^{-3} to 2.1×10^{-3}. It has already been reported that the nanoparticles release the strain through lattice expansion [36]. Also, the oxygen vacancy plays a key role for generating the strain. The stress field present within the grain boundary is reduced by the decrease of oxygen defect concentration and the lattice strain decreases consequently [37]. To study the oxygen vacancy, the oxygen occupancy has been considered as free parameters during the refinement and the oxygen occupancy has been estimated as 0.973, 0.952 and 0.928 respectively for hydrothermally prepared samples, on the other hand oxygen occupancy is one for all co-precipitated samples.

The dislocation density for nanorods is computed from the following equation [38]

$$\boldsymbol{\delta = \frac{15\varepsilon}{aD}} \tag{6.6}$$

Here, ε represents the microstrain, 'a' is the lattice parameter and D signifies the crystallite size. The extracted dislocation density is more for hydrothermally prepared sample. The dislocation density is comparable to defect present in the sample and hardness of the sample. The large dislocation density exhibits that the hydrothermally prepared sample poses more defects than the co-precipitated sample.

Table 6.1. Structural parameters of Cr-doped ZnO nanomaterial synthesized by co-precipitation and hydrothermal method and calculated from Rietveld analysis.

Parameters	**C3Z4Ht**	**C3Z4Cp**	**C5Z4Ht**	**C5Z4Cp**	**C7Z4Ht**	**C7Z4Cp**
Average crystallite diameter (nm)	44 (0.23)	27 (1.80)	35 (1.21)	21 (1.12)	19 (1.63)	16 (0.94)
a (Å)	3.251 (5.97×10^{-5})	3.2482 (2.92×10^{-4})	3.252 (5.46×10^{-5})	3.249 (1.38×10^{-4})	3.252 (5.81×10^{-5})	3.2497 (7.6×10^{-4})

c (Å)	5.207 (1.73×10^{-4})	5.2045 (6.36×10^{-4})	5.205 (1.73×10^{-4})	5.209 (8.32×10^{-4})	5.204 (1.64×10^{-3})	5.213 (1.6×10^{-3})
Degree of distortion (R)	1.019	1.019	1.020	1.018	1.020	1.0178
D_{Zn-O}(Å)	1.978	1.976	1.978	1.978	1.978	1.979
O_b-Zn-O_a (in degree)	108.445	108.447	108.374	108.4899	108.373	108.513
O_b-Zn-O_b (in degree)	110.479	110.493	110.559	110.6199	110.549	110.602
Microstrain (ε)	1.03×10^{-3}	5.90×10^{-5}	1.5×10^{-3}	7.01×10^{-5}	2.1×10^{-3}	1.01×10^{-4}
Dislocation Density	1.08×10^{11}	8.01×10^{9}	1.97×10^{11}	1.15×10^{10}	3.34×10^{11}	1.79×10^{11}

6.3.2 FESEM analysis

Fig. 6.6 represents the FESEM images of some selected samples like C5Z4Ht, C5Z4Cp, C7Z4Ht and C7Z4Cp from the complete group of Cr-doped ZnO nanomaterials. Under hydrothermal synthesis route, FESEM images show rod-like grain morphologies of C5Z4Ht and C7Z4Ht [Fig. 6.6(a) and (c)] and under the co-precipitation method the FESEM images show nearly spherical grain morphologies of C5Z4Cp and C7Z4Cp [Fig. 6.6(b) and (d)]. Based on the kinetic point of view, the formation of rod-like structure of Cr-doped ZnO nanoparticles can be explained. In hydrothermal method, the growth process can be conducted by the development of constituents undergoing growth and these constituents can be blended at the interface of ZnO lattice structure during mechanism of the reaction, the inclusion of ample NH_4OH produces huge amount of $Zn(OH)_4^{2-}$ and $Cr(OH)_6^{3-}$growth constituents [43]. Now, due to a high pH value of the supersaturated aqueous solution, a high pressure exists inside the autoclave. Under high pressure, the hydrated ions are bonded together through a dehydration reaction due to the diffusion of hydrated ions which culminates to a huge clump. When the critical size required to the formation of the grain reaches, the clump gets precipitated. Due to the high intermolecular force and high value of the surface energy of the growth units, the hydrated ions are adsorbed within the primary nuclei of Cr-doped ZnO nano-seeds and transformed into a hexagonal rod-like morphology having the average length of ~ 2-3 µm (measured with ImageJ software) for C5Z4Ht sample is shown in Fig. 6(a) as well as 1-2 µm (measured with ImageJ software) for C7Z4Ht sample is shown in Fig. 6(c). The FESEM images of nearly spherical C5Z4Cp and C7Z4Cp nanoparticles synthesized under the co-precipitation method is shown in Fig. 6.6(b) and (d) which is well established in many published articles. It is to be noted that to make a complete reaction between the precursor elements with NH_4OH, the pH value under co-precipitation method is maintained at ~ 9. C5Z4Cp and C7Z4Cp nanoparticles have smaller grain sizes in the range of ~ 30-40 nm (measured using ImageJ software) that have been depicted in Fig. 6.6(b) and (d). Thus, the typical synthesis process dependent grain growth and grain structure of the Cr-doped ZnO nanomaterials (C3Z4Ht, C5Z4Ht, C7Z4Ht, C3Z4Cp, C5Z4Cp and C7Z4Cp) have been justified with our XRD observation where hydrothermally prepared samples have large crystallite diameter as compared to co-precipitated one. We have studied the energy dispersive spectroscopy (EDX) of some selected samples like C7Z4Ht and C7Z4Cp and the EDX images have been depicted in Fig. 6.6(e) and (f).The EDX spectroscopy of both the samples (C7Z4Ht and C7Z4Cp) suggests the presence of both chromium (Cr) and zinc (Zn) cations within the lattice structure of host ZnO nanomaterials. The elemental study of C7Z4Ht and C7Z4Cp nanomaterials shows the presence of almost 7 wt% of Cr cations within the lattice structure. So, the incorporation of Cr^{3+} ions within the host ZnO nanomaterials is proper. Also, Fig. 6.6(g) to (j) shows the elemental mapping of C7Z4Ht and C7Z4Cp nanomaterials. Though, it is not easy to suggest the complete uniformity of distribution of Cr^{3+} ions within the structure of ZnO nanomaterials. Though, the elemental mapping of both C7Z4Ht and C7Z4Cp nanomaterials shown in Fig. 6.6(g) to (j) exhibit that the distribution of Cr^{3+} and Zn^{2+} ions within the lattice structure of host ZnO nanomaterials do not exist in the form of clusters. Thus, the representative FESEM images of the Cr-doped ZnO nanomaterials are well developed and due to the variation of synthesis process, the variation of grain morphology and size are very prominent.

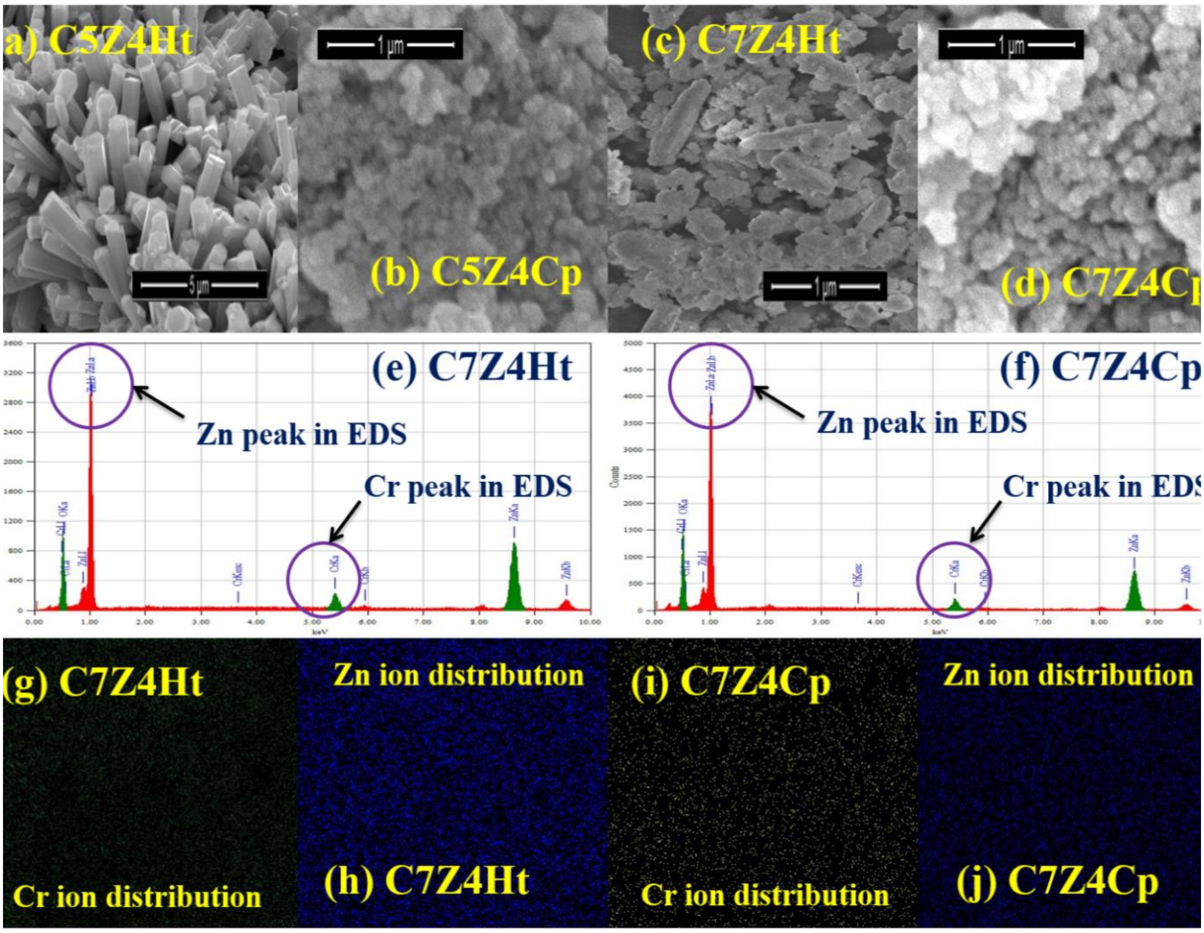

Fig. 6.6 FESEM images of rod-like structures of (a) C5Z4Ht, (c) C7Z4Ht, and spherical structures of (b) C5Z4Cp (d) C7Z4Cp, EDX of (e) C7Z4Ht and (f) C7Z4Cp, the distribution of Cr ions in (g) C7Z4Ht and (i) C7Z4Cp, also the distribution of Zn ions in (h) C7Z4Ht and (j) C7Z4Cp.

6.3.3 UV-visible absorption study and band gap analysis

The absorption spectra of C3Z4Ht, C5Z4Ht and C7Z4Ht nanorods and C3Z4Cp, C5Z4Cp and C7Z4Cp nanospheres have been studied in the wavelength range from 250 to 500 nm. For all the hydrothermally synthesized nanomaterials (C3Z4Ht, C5Z4Ht and C7Z4Ht nanorods), broad absorption peaks have been observed at 283, 282 and 281 nm. Broad absorption peaks at 380, 378 and 376 nm have been observed for C3Z4Cp, C5Z4Cp and C7Z4Cp nanoparticles and depicted in Fig. 6.7(I) and (II), respectively. A clear blue shift has been occurred for C3Z4Ht, C5Z4Ht and C7Z4Ht nanorods as compared to bulk its bulk counterpart (3.35 eV), on the other hand a clear red shift has been detected for C3Z4Cp, C5Z4Cp and C7Z4Cp nanomaterials as compared to the bulk one.

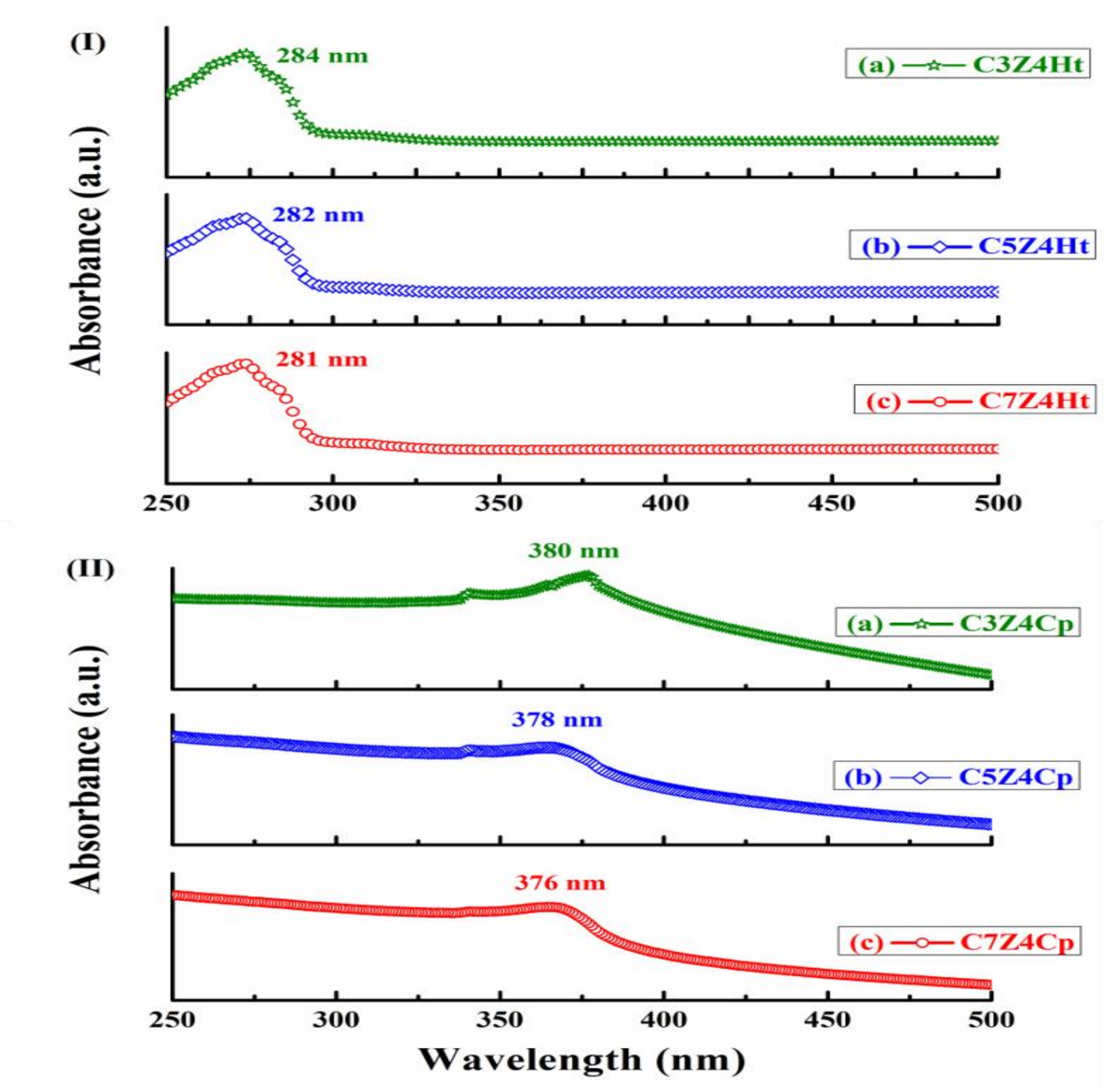

Fig. 6.7 UV-visible absorbance spectra of Cr-doped ZnO nanoparticles prepared by (I) hydrothermal route (a) C3Z4Ht, (b) C5Z4Ht, (c) C7Z4Ht and (II) co-precipitation route (a) C3Z4Cp, (b) C5Z4Cp, (c) C7Z4Cp.

The shift of absorption spectra for C3Z4Cp, C5Z4Cp and C7Z4Cp nanoparticles to the higher wavelength region as compared to C3Z4Ht, C5Z4Ht and C7Z4Ht nanorods has been observed due to the effect of many factors like synthesis process dependent grain morphology, grain size, spin-exchange interactions, percentage of dopants within the ZnO lattice and the presence of different native defects [44-46]. The variation of the absorption spectra of C3Z4Cp, C5Z4Cp and C7Z4Cp nanoparticles can be demonstrated with regard to the exchanging of spins of electrons of the delocalized s or p shells of Zn and O atoms with the electrons of the localized d shell of Cr cations [25]. This indicates the construction of band structure deformation due to the presence of Cr ions within the host ZnO lattice prepared under the co-precipitation method. Now the question arises, why red shift has been occurred for C3Z4Cp, C5Z4Cp and C7Z4Cp nanoparticles. In the co-precipitation process, the small size of C3Z4Cp, C5Z4Cp and C7Z4Cp nanoparticles brings the nanoparticles close to each other which enhance the interactions among the nanoparticles. This will help the s-d, p-d spin-exchange interactions more for C3Z4Cp, C5Z4Cp and C7Z4Cp nanoparticles. Due to these strong spin-exchange interactions, the position of the conduction band edge and the valence band edge of C3Z4Cp, C5Z4Cp and C7Z4Cp nanoparticles have been changed and the value of the band gap energies has been reduced. The calculated band gap energy of respective C3Z4Cp, C5Z4Cp, C7Z4Cp nanoparticles and C3Z4Ht, C5Z4Ht, C7Z4Ht nanorods are 3.02, 3.08, 3.21 and 4.36, 4.38, 4.38 eV. The decrement of bandgap energies of nanoparticles synthesized by co-precipitation route as compared to nanorods synthesized by hydrothermal route upgrade the semiconducting property. Therefore, due to the specific synthesis mechanism based spin-exchange interactions, the spectrum of absorption showing a red shift leads to a modulation of the energy band gap of Cr-doped ZnO nanomaterials.

The bandgap energy has been calculated using the Tauc plot relation given below [12]

$$\alpha h\nu = A(h\nu - E_{gc})^{n} \tag{6.7}$$

Where, hν is the energy of photon and E_g is the optical band gap energy. Here, for direct bandgap semiconductor, the value of n is 1/2. In the Tauc plot, the different values of band gap energies of C3Z4Ht, C5Z4Ht, C7Z4Ht nanorods and C3Z4Cp, C5Z4Cp, C7Z4Cp nanoparticles have been assigned in Fig. 6.8(a-f). The extracted value of optical band gap energies for C3Z4Ht, C5Z4Ht and C7Z4Ht nanorods are 4.36, 4.38 and 4.38 eV, respectively, that are comparatively high with respect to the bulk ZnO and the materials behave like insulator. The optical band gap energies of C3Z4Ht, C5Z4Ht and C7Z4Ht nanorods have been enhanced due to the incorporation of Cr cations in the lattice site of Zn cations and thereby production of huge carrier concentration under hydrothermal synthesis process as compared to bulk ZnO. This large value of carrier concentration gives rise to the phenomena of Moss-Burstein effect of C3Z4Ht, C5Z4Ht and C7Z4Ht nanorods which leads to the broadening of the energy bandgap. Due to the Moss-Burstein effect, the detail of the bandgap modulation has been discussed in our earlier publications [12,43]. The smaller value of grain size of C3Z4Ht, C5Z4Ht, C7Z4Ht nanorods as compared to the bulk ZnO increases the bandgap energy which leads to a blue shift in C3Z4Ht, C5Z4Ht, and C7Z4Ht nanomaterials. The decrease in bandgap energy of C3Z4Cp, C5Z4Cp and C7Z4Cp nanomaterials (3.02, 3.08 and 3.21 eV) is anticipated due to strong s-d, p-d spin-exchange interactions that turn over the effect of size-dependent optical response. The large value of bandgap energy for C3Z4Ht, C5Z4Ht, C7Z4Ht nanorods (4.36, 4.38 and 4.38 eV, respectively) helps to make it a good insulating material for dielectric responses. It is to be mentioned here that the grain size of C3Z4Ht, C5Z4Ht, C7Z4Ht nanorods is in the nanoscale regime and the incorporation of Cr ions are proper and thereby increasing the band gap as compared to the bulk ZnO followed by the phenomena of quantum size effect and Moss-Burstein effect. The bandgap energy has been reduced in the case of C3Z4Cp, C5Z4Cp, and C7Z4Cp nanoparticles due to the presence of closely placed small size nanoparticles which leads to get electron hopping within the structure of C3Z4Cp, C5Z4Cp, and C7Z4Cp nanoparticles and thereby lowering the dielectric constant and ac conductivity as explored in the dielectric section. The relative bandgap energy of C3Z4Ht, C5Z4Ht, C7Z4Ht nanorods need not change much because of the variation of concentration of Cr^{3+} within the ZnO lattice structure. Also, the relative bandgap energy of C3Z4Cp, C5Z4Cp, and C7Z4Cp nanoparticles has been developed due to Moss-Burstein effect. Thus, the physical properties of nanoparticles like bandgap energy can be modulated by the variation of synthesis procedure under which small grain size of Cr-doped ZnO is developed via co-precipitation route and large grain size of Cr-doped ZnO is developed via hydrothermal route.

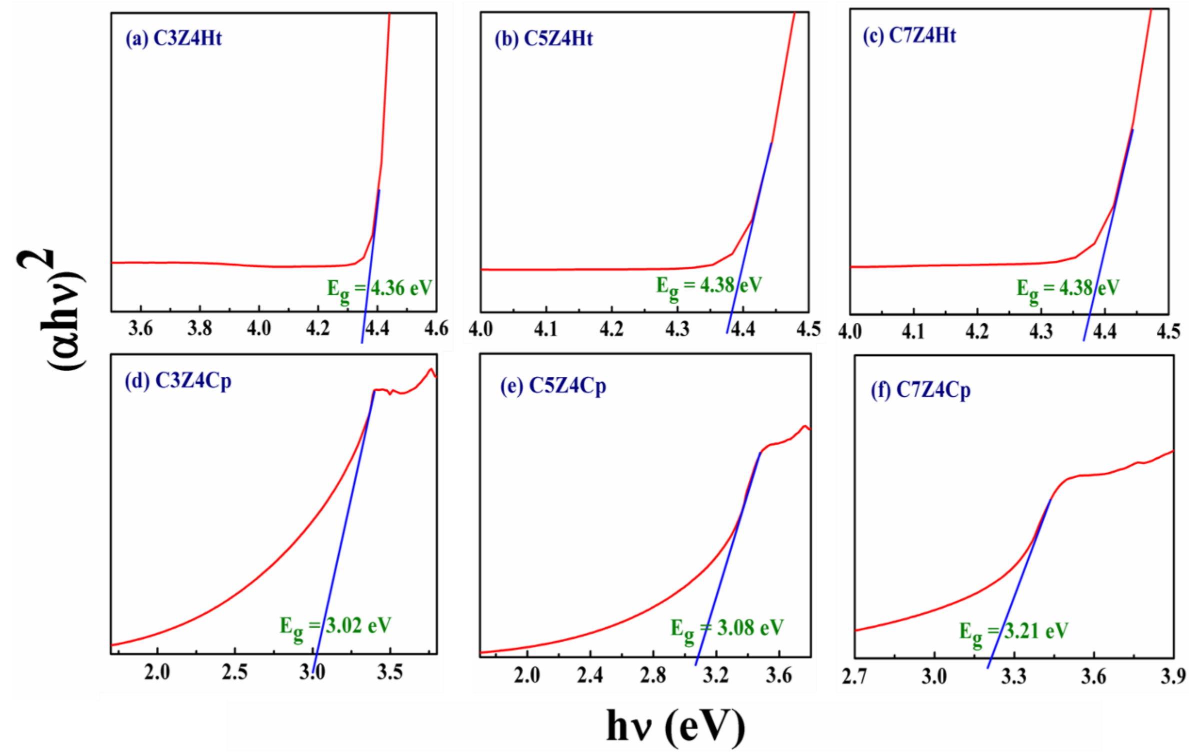

Fig. 6.8 Tauc plot of Cr-doped ZnO synthesized via hydrothermal method (a) C3Z4Ht, (b) C5Z4Ht (c) C7Z4Ht and co-precipitation method (d) C3Z4Cp, (e) C5Z4Cp, (f) C7Z4Cp.

6.3.4 Dielectric study

In this work, the relative dielectric constant of undoped and Cr-doped ZnO nanomaterials (C0Z4Ht, C3Z4Ht, C5Z4Ht, C7Z4Ht) prepared hydrothermally and undoped and Cr-doped ZnO nanomaterials (C0Z4Cp, C3Z4Cp, C5Z4Cp, C7Z4Cp) prepared by co-precipitation method have been extracted by using the equation (6.8).

$$\varepsilon = \varepsilon' - j\varepsilon'' \tag{6.8}$$

In equation (6.8), the former represents the real part of the relative dielectric constant (ε′) and the latter represents the imaginary part of the relative dielectric constant (ε″). In the present report, the outcome of the external oscillating electric field on ε′ and ε″ for the samples taken, have been studied. The real part of the relative dielectric constant (ε′) and imaginary part of the relative dielectric constant (ε″) have been observed for knowing about electrostatic energy storing ability and energy dissipation, in all the undoped and Cr-doped ZnO nanomaterials due to external oscillating field. The value of ε′ and ε″ of C0Z4Ht, C3Z4Ht, C5Z4Ht, C7Z4Ht and C0Z4Cp, C3Z4Cp, C5Z4Cp, C7Z4Cp nanoparticles have been measured by

$$\varepsilon' = \frac{Cd}{\varepsilon_0 A} \tag{6.9}$$

and

$$\varepsilon'' = \varepsilon' \times \tan\delta \tag{6.10}$$

Where, C represents the capacitance of the sample, d is the thickness and A is the area, of the pellet and ε_0 is the free space permittivity. The variation of both ε′ and ε″ as a function of frequencyin the range of 40 Hz to 10^6 Hz for varying temperatures (30, 50 and 100 ^{o}C) of C0Z4Ht, C3Z4Ht, C5Z4Ht, C7Z4Ht and C0Z4Cp, C3Z4Cp, C5Z4Cp, C7Z4Cp nanoparticles respectively have been shown in Fig. 6.9(a-f) and Figures 10(a-f). The massive enhancement The hydrothermally prepared rod-like undoped and Cr-doped ZnO nanomaterials (C0Z4Ht, C3Z4Ht, C5Z4Ht, C7Z4Ht) have massive enhancement in the value of ε′ with respect to the spherical-like undoped and Cr-doped ZnO nanomaterials (C0Z4Cp, C3Z4Cp, C5Z4Cp, C7Z4Cp) in the frequency range from 40 Hz to 10^6 Hz for varying temperatures (30, 50 and 100 ^{o}C) can be demonstrated on the basis of interfacial polarization, the symmetry dependent dielectric response, existence of doping constituents at lattice site and the interstitials within the lattice frame of host ZnO nanoparticles and the fact that electrons hop from one grain of the nanomaterials to another. The hydrothermally synthesized undoped and Cr-doped ZnO nanomaterials are fabricated with good conducting grains and poorly conducting grain boundaries with large thickness which is well supported by the well-known Koop's theory and is explained on the basis of proposition of Maxwell-Wigner-Sillars for inhomogeneous lattices [48-52]. In the presence of applied electric field, the free charge bearers drift within the grains and get bounded at the grain boundaries when they come to the poorly conducting walls of the grains. The free charges within the grain, leads to huge polarizability which develops huge interfacial polarization with super high dielectric constant. The lower range of frequency can also show high value of dielectric constant due to space charge polarization which is attributed to various defects present within the host lattice structure, oxygen vacancies and grain boundary defects, etc. Also, ε' decreases gradually with the increasing frequency and gets saturated at the high-frequency region. Such type of phenomena has been occurred because the electron cannot be able to follow rapid oscillations of the external electric field. The large dielectric constant of hydrothermally synthesized undoped and Cr-doped ZnO has been explored in our early published article [12]. The rod-like C0Z4Ht, C3Z4Ht, C5Z4Ht, C7Z4Ht nanomaterials have structural deformity due to their1D growth along c-axis. The n-type semiconducting nature with excess conduction electron of the host semiconducting ZnO nanomaterial is due to the Cr^{3+} ion present at the lattice site and also the Cr^{3+} ion generated oxygen atom with double ionization (O^{2-}) with regard to the vacancy at the zinc site. The development of these doubly ionized oxygen atoms (O^{2-}) because of the incorporation of Cr^{3+} at the Zn lattice within the ZnO lattice framework can produce excess conduction electron during the annealing process and thereby enhancing the carrier density, which are finally bounded by the grain boundaries of hydrothermally synthesized Cr-doped ZnO nanomaterials and the interfacial polarization of rod-like Cr-doped ZnO nanomaterials (C3Z4Ht, C5Z4Ht and C7Z4Ht) has been enhanced as compared to the undoped ZnO nanomaterials (C0Z4Ht). The hopping of the charge carriers between the grains of the rod-like undoped and Cr-doped ZnO nanomaterials have been prevented due the thick grain boundaries and this enhances overall dielectric contribution of the rod-like nanomaterials irrespective of the presence of Cr ions within the structure of host ZnO lattice. On the other hand, C0Z4Cp, C3Z4Cp, C5Z4Cp, C7Z4Cp nanomaterials exhibit nearly spherical symmetry due to which the resultant dielectric constant is relatively low as compared to C0Z4Ht, C3Z4Ht, C5Z4Ht, C7Z4Ht nanomaterials. It has been observed in the Rietveld Refinement analysis that, for hydrothermally prepared nanoparticles the Cr^{3+} ions have been incorporated at the zinc lattice sites and for co-precipitated nanoparticles the Cr^{3+} ions have also been placed at the octahedral interstitial position within the lattice structure of host ZnO nanomaterials. The interfacial polarization of the hydrothermally synthesized Cr-doped ZnO nanomaterials has been enhanced by the presence of Cr^{3+} ions at the zinc lattice sites, on the other hand the interfacial polarization of the co-precipitated Cr-doped ZnO nanomaterials has been reduced by the presence of Cr^{3+} ions at the octahedral interstitial position within the lattice structure of host ZnO nanomaterials. The hopping effect of the free charge carriers between the grains as well as the grain boundaries increases with the size reduction of grain in the nanomaterials. The C0Z4Cp, C3Z4Cp, C5Z4Cp, C7Z4Cp nanoparticles have smaller size of their grains (diameter ~ 30-40 nm, measured using ImageJ software) as compared to C0Z4Ht, C3Z4Ht, C5Z4Ht, and C7Z4Ht nanorods (length ~1-3 µm and diameter ~ 500 nm, measured using ImageJ software). The grains are much closer to each other and connected with thin grain boundary due to the small size of C0Z4Cp, C3Z4Cp, C5Z4Cp, C7Z4Cp nanomaterials. So, the charge carriers can easily pass through one grain to another through conducting grain boundaries due to electron hopping mechanism. Thus, it exhibits some inconsistency of the modulation in the dielectric constant of the nanaomaterials prepared by co-precipitation method. The decrement in band gap energy of co-precipitated nanoparticles with values of 3.02, 3.08 and 3.21 eV, respectively, shows that the resultant co-precipitated nanomaterials are all semiconducting in nature. The improvement in the conductivity of nanomaterials due to the hopping of charge carriers through grain boundaries and thereby reducing the real part of dielectric constant of C0Z4Cp, C3Z4Cp, C5Z4Cp, C7Z4Cp nanomaterials. Also, the electron hopping phenomenon increases when the specimens are subjected to increase in temperature from 30 °C to 100 °C. The heating effect increases the kinetic energy of the mobile charge carriers and enhances the movement of charge carriers from one grain to the others through grain boundaries and thereby decreasing the dielectric constant of all the undoped and Cr-doped ZnO nanomaterials which is independent of the synthesis procedures (hydrothermal and co-precipitation methods) demonstrated in this report as depicted in Fig. 6.9(a-f). So, the increase in temperature improves the conductivity of these n-type undoped and Cr-doped ZnO nanomaterials and also improves the dielectric constant irrespective of their synthesis procedure. When the synthesis process changes from co-precipitation to hydrothermal, the modulation of ε′ of undoped ZnO and Cr-doped ZnO nanomaterials with various chromium (Cr) concentrations (3, 5 and 7 wt%) has been observed from ~ 487 (C0Z4Cp) to 178276 (C0Z4Ht), 664 (C3Z4Cp) to 475513 (C3Z4Ht), 523 (C5Z4Cp) to 423032 (C5Z4Ht) and 348 (C7Z4Cp) to 404005 (C7Z4Ht) at the applied frequency of 40 Hz and at 30 °C operating temperature, also the value of ε′ changes from ~ 697 (C0Z4Cp) to 17653 (C0Z4Ht), 687 (C3Z4Cp) to 85075 (C3Z4Ht), 151 (C5Z4Cp) to 39719 (C5Z4Ht) and 186 (C7Z4Cp) to 36340 (C7Z4Ht) at the same frequency and at 100 °C temperature, also from ~ 130 (C0Z4Cp) to 4683 (C0Z4Ht), 36 (C3Z4Cp) to 18146 (C3Z4Ht), 57 (C5Z4Cp) to 10256 (C5Z4Ht) and 38 (C7Z4Cp) to 3238 (C7Z4Ht) at the frequency of 10^4 Hz and at 30 °C temperature and from ~ 182 (C0Z4Cp) to 686 (C0Z4Ht), 180 (C3Z4Cp) to 7975 (C3Z4Ht), 43 (C5Z4Cp) to 1545 (C5Z4Ht) and 44 (C7Z4Cp) to 1531 (C7Z4Ht) at the frequency of 10^4 Hz and at 100 °C as presented in Fig. 6.9. Thus, the observed value of ε′ of hydrothermally prepared undoped and Cr-doped ZnO nanomaterials (C0Z4Ht, C3Z4Ht, C5Z4Ht, C7Z4Ht) are comparatively high at RT with a large range of frequency (from 40 Hz to 10^4 Hz) as compared to the undoped and Cr-doped ZnO nanomaterials synthesized by the co-precipitation method (C0Z4Cp, C3Z4Cp, C5Z4Cp, C7Z4Cp). Also, it is to be mentioned here that with the increase of doping concentration of Cr^{3+} ions within the host lattice structure of ZnO, the value of ε′ increases. Finally, as the temperature rises from 30 °C to 100 °C, the value of ε′ decreases. Thus, it can be noted that hydrothermally synthesized rod-like grain structure and the incorporation of Cr^{3+} ions within the lattice structure of ZnO develop a superior dielectric response at RT of semiconducting ZnO nanomaterial.

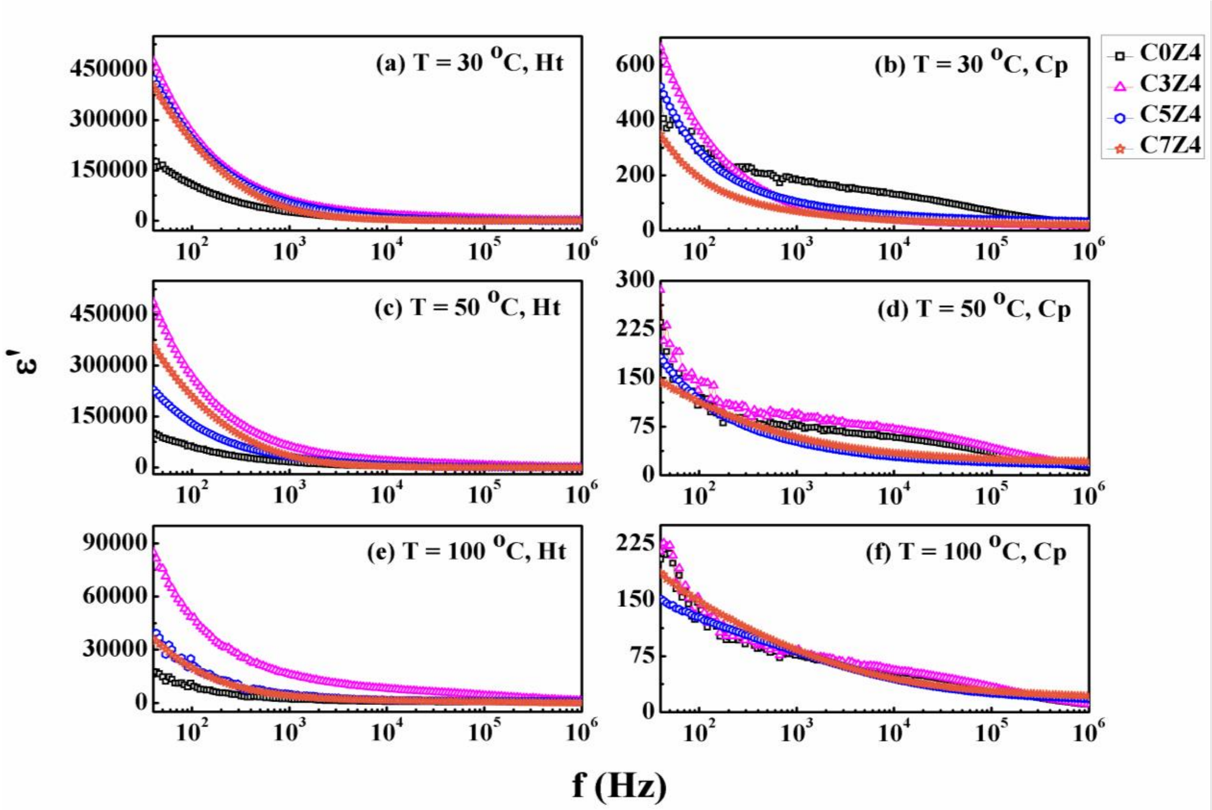

Fig. 6.9 Modulation of real part of dielectric constant (ε′) in relation to frequency of the samples C0Z4Ht, C3Z4Ht, C5Z4Ht and C7Z4Ht at (a) 30 °C, (c) 50 °C, (e) 100 °C and C0Z4Cp, C3Z4Cp, C5Z4Cp and C7Z4Cp at (b) 30 °C, (d) 50 °C, (f) 100 °C.

The imaginary part of the relative dielectric constant (ε″) i.e. the dielectric energy loss has been represented in Figures10(a-f) which exhibits the presence of large space charge polarization effect of C0Z4Ht, C3Z4Ht, C5Z4Ht, and C7Z4Ht nanoparticles with respect to the C0Z4Cp, C3Z4Cp, C5Z4Cp, C7Z4Cp nanomaterials. A very high value of ε″ has been observed for hydrothermally prepared undoped and Cr-doped ZnO nanomaterials (C0Z4Ht, C3Z4Ht, C5Z4Ht, and C7Z4Ht) in the entire frequency range due to the conversion of a large amount of electrical energy into heat energy. Such phenomena occur because of the effect of huge interfacial polarization in the C0Z4Ht, C3Z4Ht, C5Z4Ht, and C7Z4Ht nanomaterials. Under the influence of external alternating the electric field space charge polarization present in C0Z4Ht, C3Z4Ht, C5Z4Ht, and C7Z4Ht nanomaterials aligns its rotational direction following the frequency of the alternating field that reduces at the high frequency region as the polarizations cannot follow the high frequency of the applied electric field. An additional amount of heat energy is produced due to the movement of the free charge carriers within the large size conducting grains. The production of heat loss because of this conduction loss also enhances ε'' of C0Z4Ht, C3Z4Ht, C5Z4Ht, and C7Z4Ht nanomaterials as compared to C0Z4Cp, C3Z4Cp, C5Z4Cp, C7Z4Cp nanomaterials. The measured value of ε'' has been estimated for C0Z4Ht, C3Z4Ht, C5Z4Ht, C7Z4Ht and C0Z4Cp, C3Z4Cp, C5Z4Cp, C7Z4Cp nanomaterials are high for lower frequency (40 Hz) and larger frequency (10^4 Hz) region that has been shown in Fig. 6.10(a-f). Fig. 6.9 and 10 show that the hydrothermally prepared Cr-doped ZnO nanomaterials (C0Z4Ht, C3Z4Ht, C5Z4Ht, and C7Z4Ht) have more localized electrons and also more interfacial polarization effect with respect to C0Z4Cp, C3Z4Cp, C5Z4Cp, C7Z4Cp nanomaterials that consist more delocalized electrons. Now, it is clear from the present work that enhanced dielectric response can be achieved by the proper selection of synthesis procedures of n-type doped ZnO nanomaterials. Also, significant variation of the dielectric response of nanomaterials can be detected due to the variation of dopant concentration as well as the variation of temperature. The enhancement of conduction electrons within the host lattice due to the increase of temperature produces improvement of the dielectric energy loss by the production of more heat energy within ZnO nanomaterials.

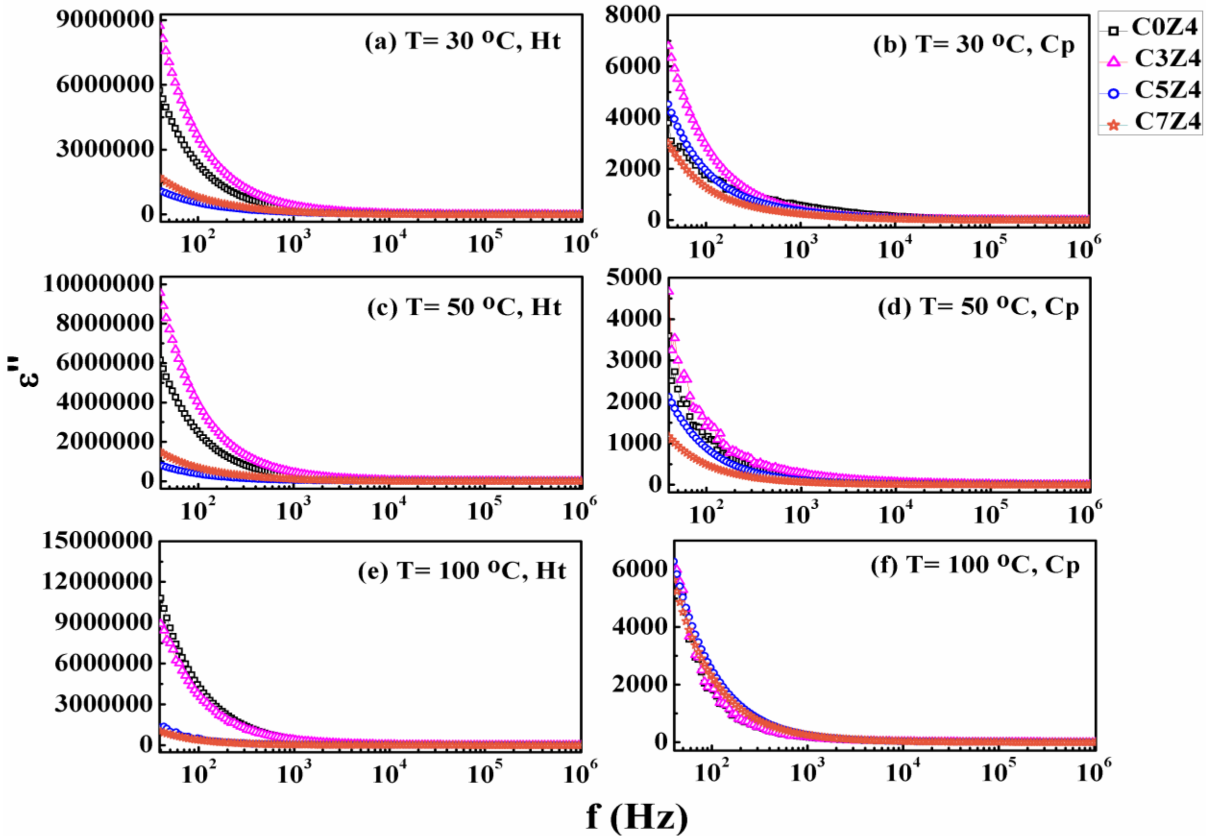

Fig. 6.10 Variation of imaginary part of dielectric constant (ε″) in relation to frequency of the samples C0Z4Ht, C3Z4Ht, C5Z4Ht and C7Z4Ht at (a) 30 ºC, (c) 50 ºC, (e) 100 ºC and C0Z4Cp,C3Z4Cp, C5Z4Cp and C7Z4Cp at (b) 30 ºC, (d) 50 ºC, (f) 100 ºC.

The phase loss or loss tangent (tanδ) of C0Z4Ht, C3Z4Ht, C5Z4Ht, C7Z4Ht and C0Z4Cp, C3Z4Cp, C5Z4Cp, C7Z4Cp respectively, at three different temperatures (30, 50 and 100 ºC) in the frequency range of 40 Hz to 10^6 Hz is represented in Fig. 6.11. The loss tangent (tanδ) for all the samples have been estimated by

$$\tan\delta = \frac{\omega\varepsilon'' + \sigma}{\omega\varepsilon'} \qquad (6.11)$$

Where, w is the angular frequency and σ is the conductivity of the free charge carriers within the nanomaterials. The argument of this present work from both the observation has been made even stronger. The loss tangent (tanδ) C0Z4Ht, C3Z4Ht, C5Z4Ht, C7Z4Ht nanomaterials are more as compared to C0Z4Cp, C3Z4Cp, C5Z4Cp, C7Z4Cp nanomaterials that has been shown in Fig. 6.11(a-f). The tanδ measures the rate of loss of energy of the alternating applied electric field and the observed estimate of rate of loss of energy for an ideal dielectric material is insignificant so it can be used as an ideal capacitor. But for real dielectric substance, the rate of loss of energy enhances with the existence of a factor that is based on resistance known as equivalent series resistance (ESR), that represents a factor that depends on frequency in relation to the active current counterpart (representing the σ in equation 11) through grains that are conducting corresponding to the reactive current counterpart based on relaxation of bound dipoles that depends on frequency (representing $\omega\varepsilon''$ in equation 11). For a dielectric material that is ideal, the ESR estimate will be very low or negligible and for real dielectric substance the ESR estimate will be more. The large tanδ in the hydrothermally synthesized nanoparticles (C0Z4Ht, C3Z4Ht, C5Z4Ht, and C7Z4Ht) have been measured due to the polarization based on the relaxation of dipoles at the interface produced by the charge bearers which are in bound state of undoped and Cr-doped ZnO nanomaterials as well as the equivalent series resistance (ESR) produced by the active current counterpart through these large size grains which are conducting. Also, at high frequency region a distinct hump has been observed in the case of C7Z4Ht nanomaterials at 30 ^{o}C because the orientational and space charge polarization becomes less prominent at high frequency region. So, in the high frequency region, the hump can be assigned as electronic and ionic polarization which has lesser response time as compared to bulk polarization. The resonant occurs in the atomic level at high frequency of the applied external electric field which generates heat corresponds to the greater loss. Thus, it is clear that there is a very good contribution of polarization in the hydrothermally synthesized nanomaterials. The large interfacial polarization effect as well as drift motion of bound charge carriers within the grains of C0Z4Ht, C3Z4Ht, C5Z4Ht, and C7Z4Ht nanomaterials exhibits that the hydrothermally synthesized nanomaterials are super dielectric materials which are useful for different device applications. The value of tanδ also supports the superior dielectric response of the nanomaterials. An observation is made that there is a decrement in the dielectric constant but the conductivity increases with increment of temperature from 30 to 100°C of the dielectric measurement, irrespective of the Cr doping concentration and synthesis procedure. The tanδ value of the nanomaterials has been found elevated with the increase of conductivity due to the enhancement in temperature that has been observed in Fig. 6.11(a-f).

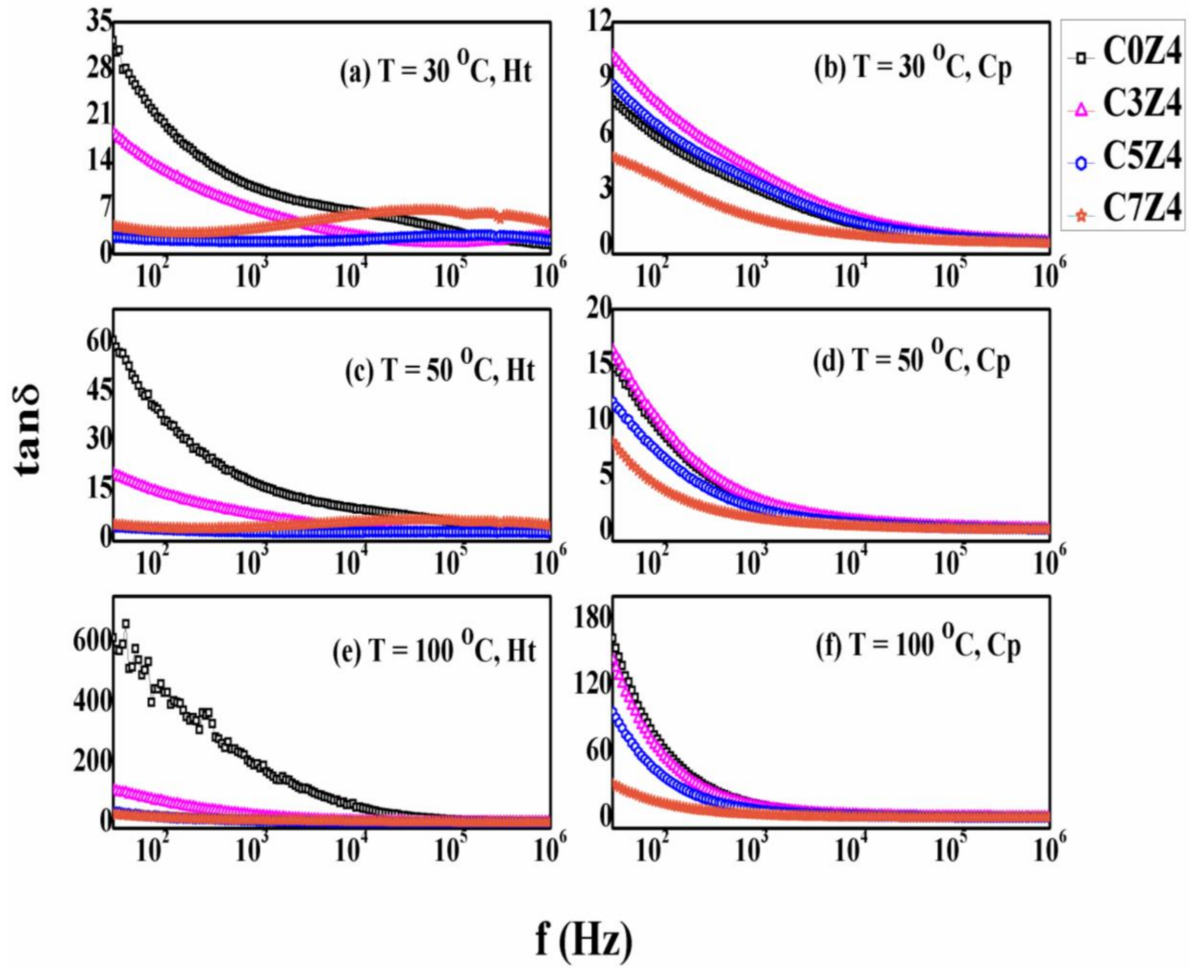

Fig. 6.11 Variation of loss tangent (tanδ) with frequency of the samples C0Z4Ht, C3Z4Ht, C5Z4Ht and C7Z4Ht at (a) 30 °C, (c) 50 °C, (e) 100 °C and C0Z4Cp, C3Z4Cp, C5Z4Cp and C7Z4Cp at (b) 30 °C, (d) 50 °C, (f) 100 °C

The ac conductivity (σ_{ac}) of C0Z4Ht, C3Z4Ht, C5Z4Ht, C7Z4Ht and C0Z4Cp, C3Z4Cp, C5Z4Cp, C7Z4Cp nanoparticles have been shown in Fig. 6.12(a-f). The σ_{ac} is a short-range conductivity because it can only be detected in the low frequency region in the range of 40 Hz to 10^6 Hz. Fig. 6.12 shows that the value of σ_{ac} for C0Z4Ht, C3Z4Ht, C5Z4Ht, C7Z4Ht nanomaterials is higher as compared to C0Z4Cp, C3Z4Cp, C5Z4Cp, C7Z4Cp nanomaterials. A conductivity develops whose range is small because of the drifting of electric charges that are induced by applied oscillating electric field within electric dipoles. The substitution of Cr cations in place of Zn in ZnO lattice as well as the formation of rod-like structure with thick grain boundaries produce and bound the large charge carriers for all the hydrothermally synthesized nanomaterials (C0Z4Ht, C3Z4Ht, C5Z4Ht, C7Z4Ht). Also, the presence of Cr ions at the Zn lattice sites in the ZnO lattice structure produce a large amount of charge carriers for all the co-precipitated nanomaterials (C0Z4Cp, C3Z4Cp, C5Z4Cp and C7Z4Cp) but the presence of small grain size and thin grain boundary produce long range conductivity corresponding to electron hopping phenomenon and the value of this long-range conductivity is not very eminent in the frequency range of 40 Hz to 10^6 Hz. Also, a better semiconducting behavior with a bang gap range of 3.08 to 3.21 eV of co-precipitated nanomaterials reduces the σ_{ac} in the frequency range of 40 to 10^6 Hz in comparison to the hydrothermally synthesized nanomaterials. The σ_{ac} study of the present investigation with a comparatively low value corresponding to the co-precipitated nanomaterials suggests that if a semiconducting nanomaterial is subjected to an alternating electric field the conductivity can only be observed at the surface of the materials and also the frequency-dependent conductivity of the nanomaterial gets reduced. Along with that as mentioned in the XRD section, the presence of Cr^{3+} ions at the interstitial position in the C0Z4Cp, C3Z4Cp, C5Z4Cp, C7Z4Cp nanomaterials reduce the charge carrier density within the ZnO lattice structure in order to neutralize themselves. This decrease in charge carrier density of

C0Z4Cp, C3Z4Cp, C5Z4Cp, C7Z4Cp nanomaterials also reduce the σ_{ac} of the nanomaterials. Also, the value of σ_{ac} in the high-frequency region has been enhanced in the samples that are without doping as well as Cr-doped ZnO due to the fact that at high frequency the rate of hopping of charge between Zn^{2+} and Cr^{3+} ions have been improved. In this report, in the temperature-dependent σ_{ac} study corresponding to the nanomaterials synthesized by both hydrothermal and co-precipitation method no significant modulation has been observed when the measurement temperature increase from 30 to 100^{o}C. The enhancement of conduction charges with the increase in temperature charges can only improve the surface current of the materials keeping their frequency-dependent σ_{ac} constant. In this present work, the observed dielectric value of C0Z4Ht, C3Z4Ht, C5Z4Ht, C7Z4Ht and C0Z4Cp, C3Z4Cp, C5Z4Cp, C7Z4Cp nanomaterials exhibit that the overall dielectric property can be modulated by the proper selection of synthesis mechanism to these n-type doped ZnO nanomaterials.

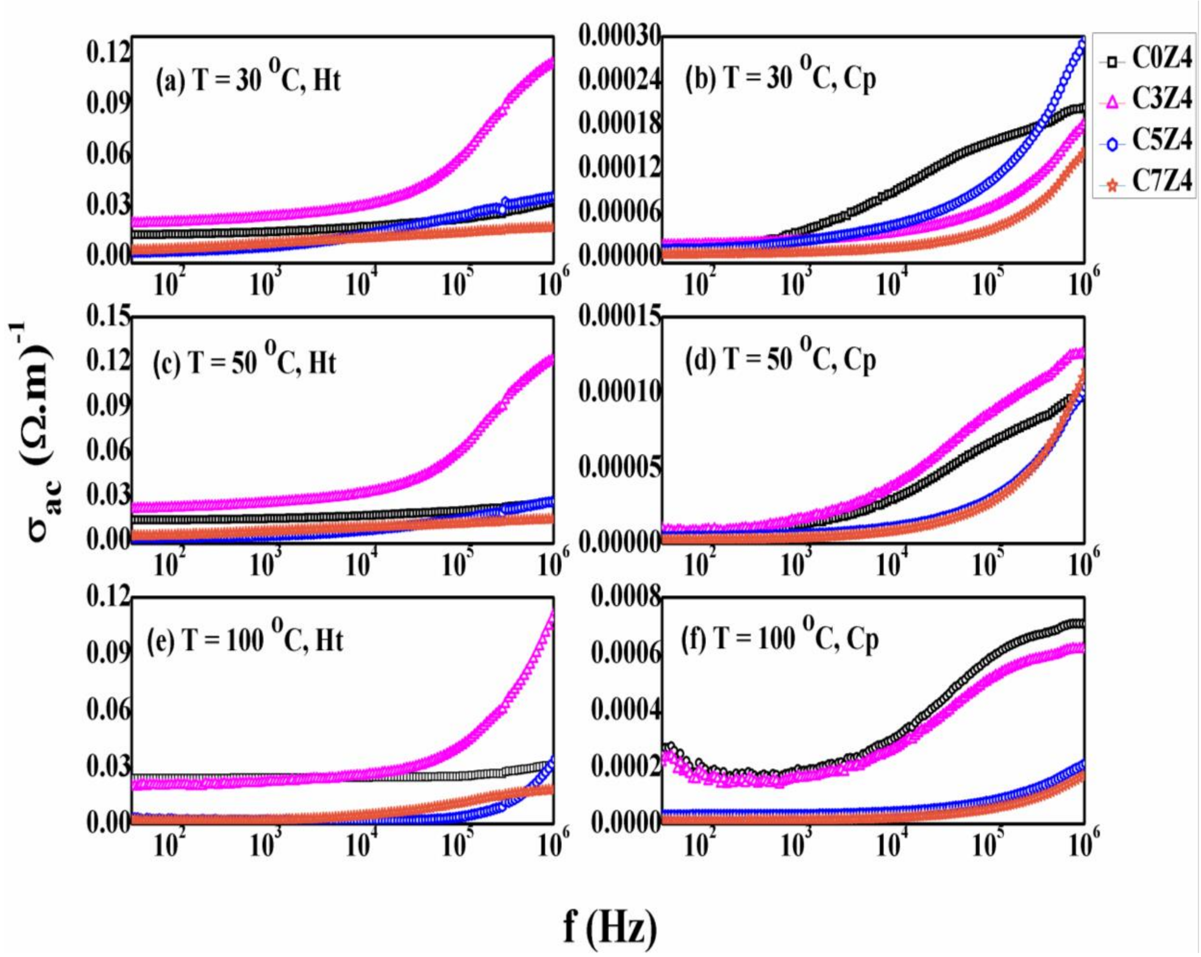

Fig. 6.12 Modulation of ac conductivity (σ_{ac}) with frequency of the samples C0Z4Ht, C3Z4Ht, C5Z4Ht and C7Z4Ht at (a) 30 ^oC, (c) 50 ^oC, (e) 100 ^oC and C0Z4Cp, C3Z4Cp, C5Z4Cp and C7Z4Cp at (b) 30 ^oC, (d) 50 ^oC, (f) 100 ^oC.

6.3.5 Impedance spectroscopy study

To analyze the impedance of grains separated from one another and the electrodes as impedance sources, the impedance spectroscopy study is one of the most important measurements of semiconducting undoped and Cr-doped ZnO nanomaterials [53]. Debye proposed the classical model of complex impedance (Z*) to explain the behavior of impedance of various materials and the complex impedance (Z*) can be written as [54]

$$Z^* = Z' + jZ'' = \frac{R}{1 + j\omega\tau} \tag{6.12}$$

Here, Z' and Z" respectively are the real part of complex impedance and the imaginary part of complex impedance of the corresponding materials [54]

$$\mathbf{Z' = \frac{\boldsymbol{R}}{1 + (\boldsymbol{\omega R C})^2}} \tag{6.13}$$

$$\mathbf{Z'' = \frac{\boldsymbol{\omega R^2 C}}{1 + (\boldsymbol{\omega R C})^2}} \tag{6.14}$$

Here, ω is the angular frequency and τ = RC is the relaxation time. The impedance of these nanomaterials depends on the synthesis mechanism, type of dopants, distribution of dopants grain size, structures, etc [55, 56]. The impedance properties of these undoped and Cr-doped ZnO nanomaterials depend on the microstructural impact of the ZnO lattice structure. In this report the variation in the real part (Z') and imaginary part (Z") of the complex impedance as a function of frequency in the range from 40 Hz to 10^6 Hz for varying temperatures (30, 50 and 100 ^{o}C) have been shown in Fig. 6.13(I) and (II). The Nyquist plot or Cole-Cole plot between the imaginary part (Z") and the real part (Z') of complex impedance (Z*) of C0Z4Ht, C3Z4Ht, C5Z4Ht, C7Z4Ht and C0Z4Cp, C3Z4Cp, C5Z4Cp, C7Z4Cp nanomaterials respectively, at three different temperatures (30, 50 and 100^{o}C) has been shown in Fig. 6.14[57].

Fig. 6.13(I) and (II) represent the change in the real part (Z') and imaginary part (Z") of the complex impedance (Z*) as a function of frequency. The details about different electrical properties like capacitance, resistance, conducting behavior of undoped and Cr-doped ZnO nanomaterials have been provided by both these graphical representations. It is found from the impedance spectra analysis that the value of Z' is high at the low-frequency region and it shows a decrement with the increment of frequency and at it obtains a value that is relatively stable at the high frequency region. Also, the value of Z" is low at low-frequency region and with the increase in frequency it increases and attains a maximum value and further the value of Z" start decreasing with the increase in frequency and gets lower at high frequency region.

The Z' value of all the undoped and doped ZnO nanoparticles reduces either due to the participation of space charges through the grain boundaries or due to the conduction process inside the material. The large value of Z' at lower range of frequency and the reduction in Z' with the rise of frequency exhibits the increase in polarization effect or the short-range ac conductivity (σ_{ac}) of the nanoparticles and the results are consistence with the dielectric property observed in the earlier section. This impedance reduction phenomena for large polarization effect have been observed in all the hydrothermally synthesized undoped and Cr-doped ZnO nanomaterials (C0Z4Ht, C3Z4Ht, C5Z4Ht, C7Z4Ht). For all the hydrothermally synthesized undoped and Cr-doped ZnO nanomaterials (C0Z4Ht, C3Z4Ht, C5Z4Ht, C7Z4Ht), large polarization effect is the main reason for the generation of large capacitive action through the grain boundaries suggests the reduction of Z'. Also, for the hydrothermally synthesized samples, the presence of drift motion of free charge carriers in the conducting large grain structure reduces impedance (large σ_{ac}) of frequency dependent real part (Z') of complex impedance measurement as compared to the co-precipitated undoped and Cr-doped ZnO nanomaterials (C0Z4Cp, C3Z4Cp, C5Z4Cp, C7Z4Cp). For the co-precipitated nanomaterials, the charge carriers will move only at the surface give rise to the reduction of bulk resistance of the co-precipitated nanomaterials. At room temperature, the plots of Z'' versus frequency in Fig. 6.13(II) show wide Debye peaks for C0Z4Cp, C3Z4Cp, C5Z4Cp, C7Z4Cp nanoparticles as compared to the C0Z4Ht, C3Z4Ht, C5Z4Ht, C7Z4Ht nanoparticles manifests the presence of the large reactive imaginary part of impedance for C0Z4Cp, C3Z4Cp, C5Z4Cp, C7Z4Cp nanomaterials appeared due to the presence of the large bulk resistance within the co-precipitated nanomaterials. Also, the plots of the Z'' versus frequency exhibit wide Debye peaks for all the nanomaterials except the hydrothermally synthesized undoped and Cr-doped ZnO nanomaterials (C0Z4Ht, C3Z4Ht, C5Z4Ht, C7Z4Ht) at room temperature because of polarization based on space-charge and due to the presence of space-charge relaxation of co-precipitated undoped and Cr-doped ZnO nanomaterials (C0Z4Cp, C3Z4Cp, C5Z4Cp, C7Z4Cp).

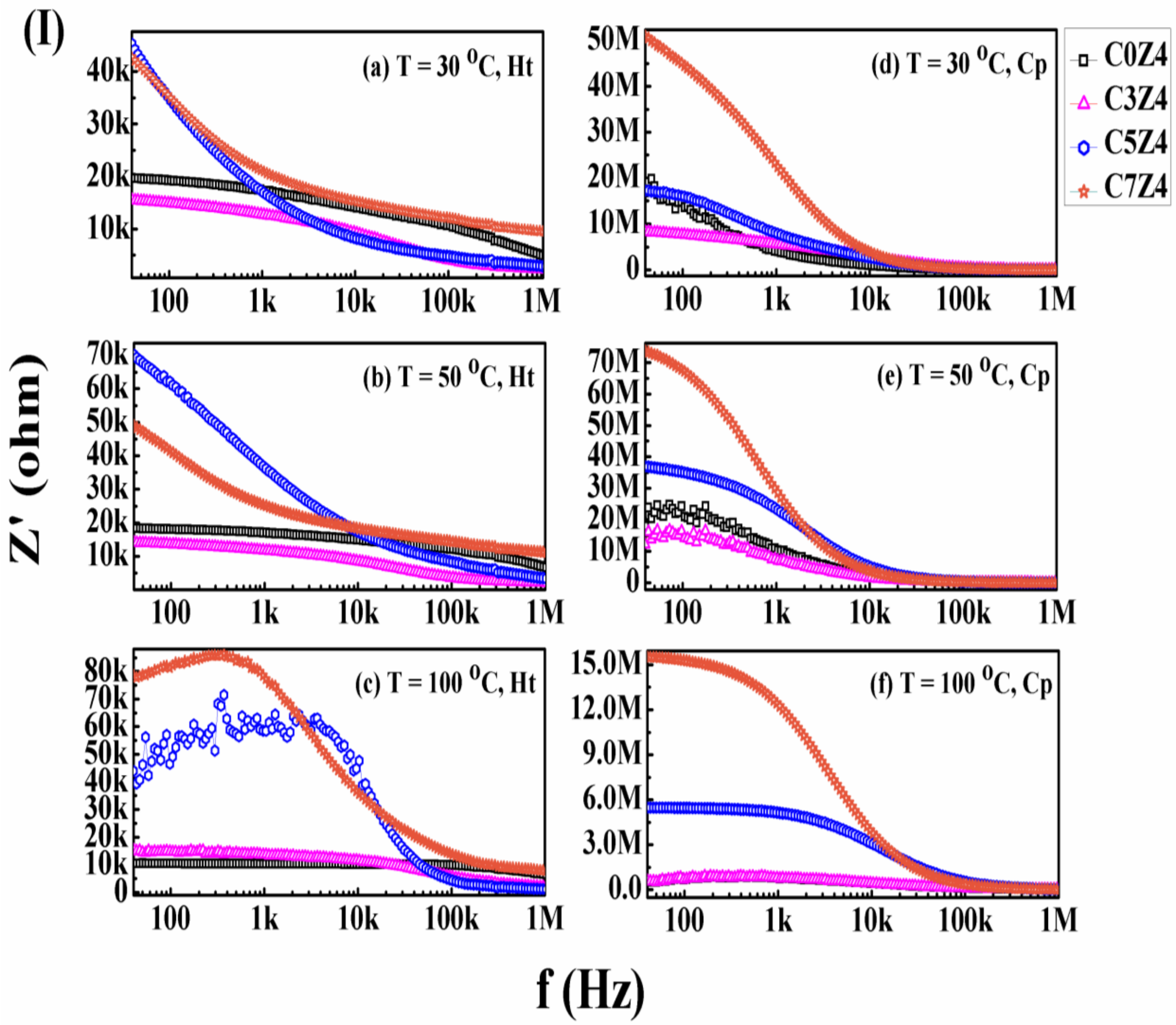

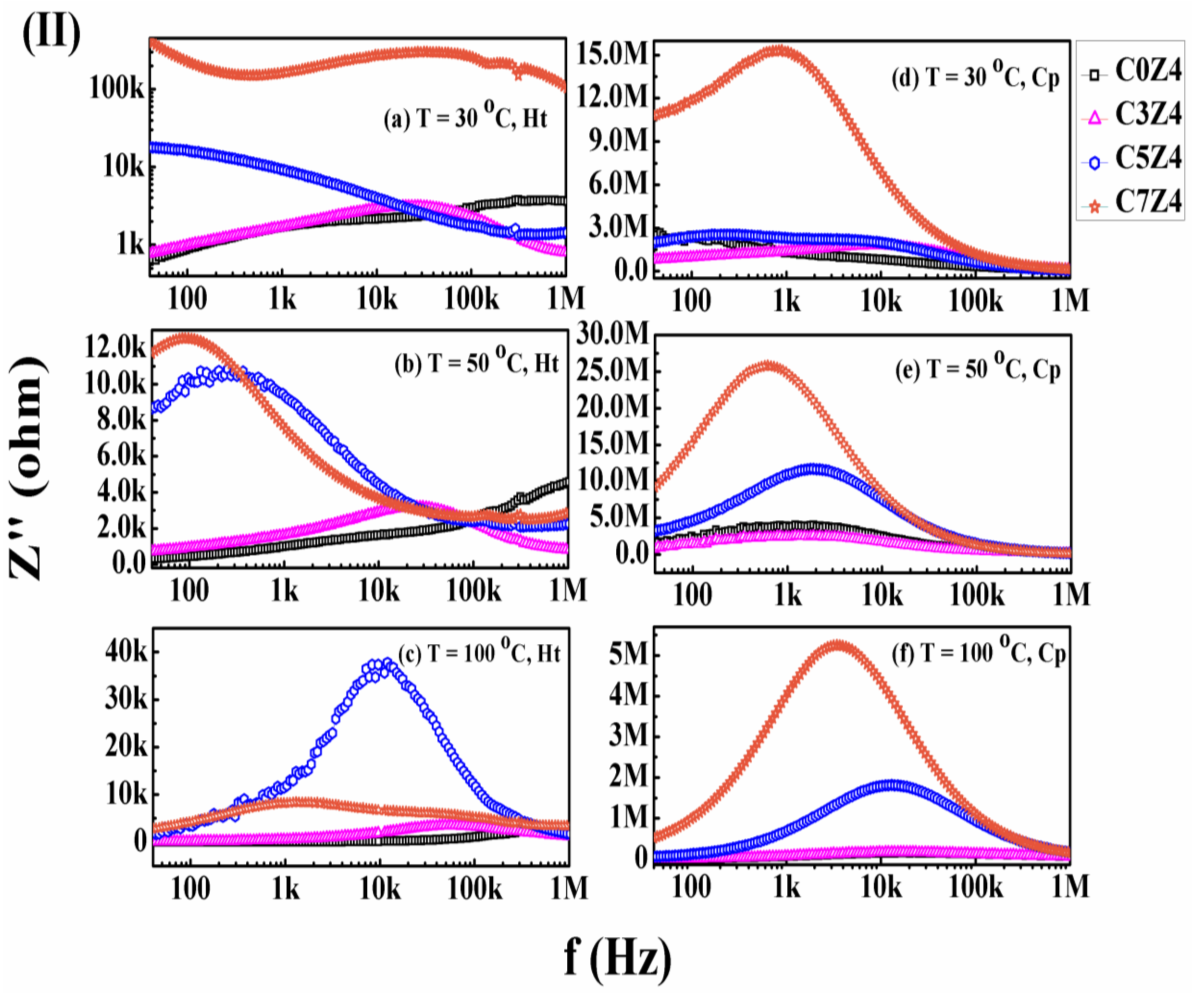

Fig. 6.13 Modulation of (I) real part impedance (Z') and (II) imaginary part of impedance (Z'') with frequency of the samples C0Z4Ht, C3Z4Ht, C5Z4Ht and C7Z4Ht at (a) 30 °C, (b) 50 °C, (c) 100 °C and C0Z4Cp, C3Z4Cp, C5Z4Cp and C7Z4Cp at (d) 30 °C, (e) 50 °C, (f)100 °C.

It is clear from the variation of Z'' as a function of Z' of hydrothermally synthesized Cr-doped ZnO nanomaterials (C0Z4Ht, C3Z4Ht, C5Z4Ht, C7Z4Ht) at all three temperatures (30 °C, 50 °C and 100 °C) coexist two semicircular regions that has been shown in Fig. 6.14(a-c). From Fig. 6.14(a-c), it is quite clear that the tip of the curvature moves to the higher impedance value with the increment of temperature from 30 °C to 100 °C for the undoped and Cr-doped ZnO nanomaterials synthesized by hydrothermally synthesis route. On the other hand, for all the co-precipitated samples (C0Z4Cp, C3Z4Cp, C5Z4Cp, C7Z4Cp) at all the three temperatures (30 ^{o}C, 50 ^{o}C and 100 ^{o}C), the presence of single semicircular regions are very much clear and distinct that have been shown in Fig. 6.14(d-f). Also, for all the undoped and Cr-doped ZnO nanomaterials prepared by co-precipitation method, Fig. 6.14(d) and (e) indicate the peak of the curvature shifts towards the higher impedance value with the enhancement of temperature from 30 ^{o}C to 50 ^{o}C and Fig. 6.14(f) indicates that the peak of the curvature gets reduced to the lower impedance for C0Z4Cp, C3Z4Cp, C5Z4Cp, C7Z4Cp nanomaterials at 100 ^{o}C. Also, the Cole-Cole plots indicate that impedance value for co-precipitated nanomaterials (C0Z4Cp, C3Z4Cp, C5Z4Cp, C7Z4Cp) are comparatively high as compared to the rod-like undoped and Cr-doped ZnO nanomaterials (C0Z4Ht, C3Z4Ht, C5Z4Ht, C7Z4Ht). For hydrothermally prepared nanomaterials (C0Z4Ht, C3Z4Ht, C5Z4Ht and C7Z4Ht), the presence of two semicircular regions is the signature pattern due to both the grain contributions, one is the grain boundary contributions in electric charge transport phenomenon which is a signature pattern with a large dielectric response and the corresponding high internal capacitance through the grains of hydrothermally prepared nanomaterials. On the other hand, for co-precipitated nanomaterials (C0Z4Cp, C3Z4Cp, C5Z4Cp and C7Z4Cp) the presence of a single semicircular region is the signature pattern with only the grain contributions in the electric charge transport phenomena and the low internal capacitance across the grains. This is quite clear of having a low dielectric/polarization response of the co-precipitated nanoparticles. Also, for all the co-precipitated samples (C0Z4Cp, C3Z4Cp, C5Z4Cp and C7Z4Cp), the high value of impedance is the clear indication of having low σ_{ac} corresponding to the low dielectric response of these nanomaterials as compared to the hydrothermally prepared nanomaterials(C0Z4Ht, C3Z4Ht, C5Z4Ht and C7Z4Ht) which have comparatively large σ_{ac} corresponding to the large dielectric response.

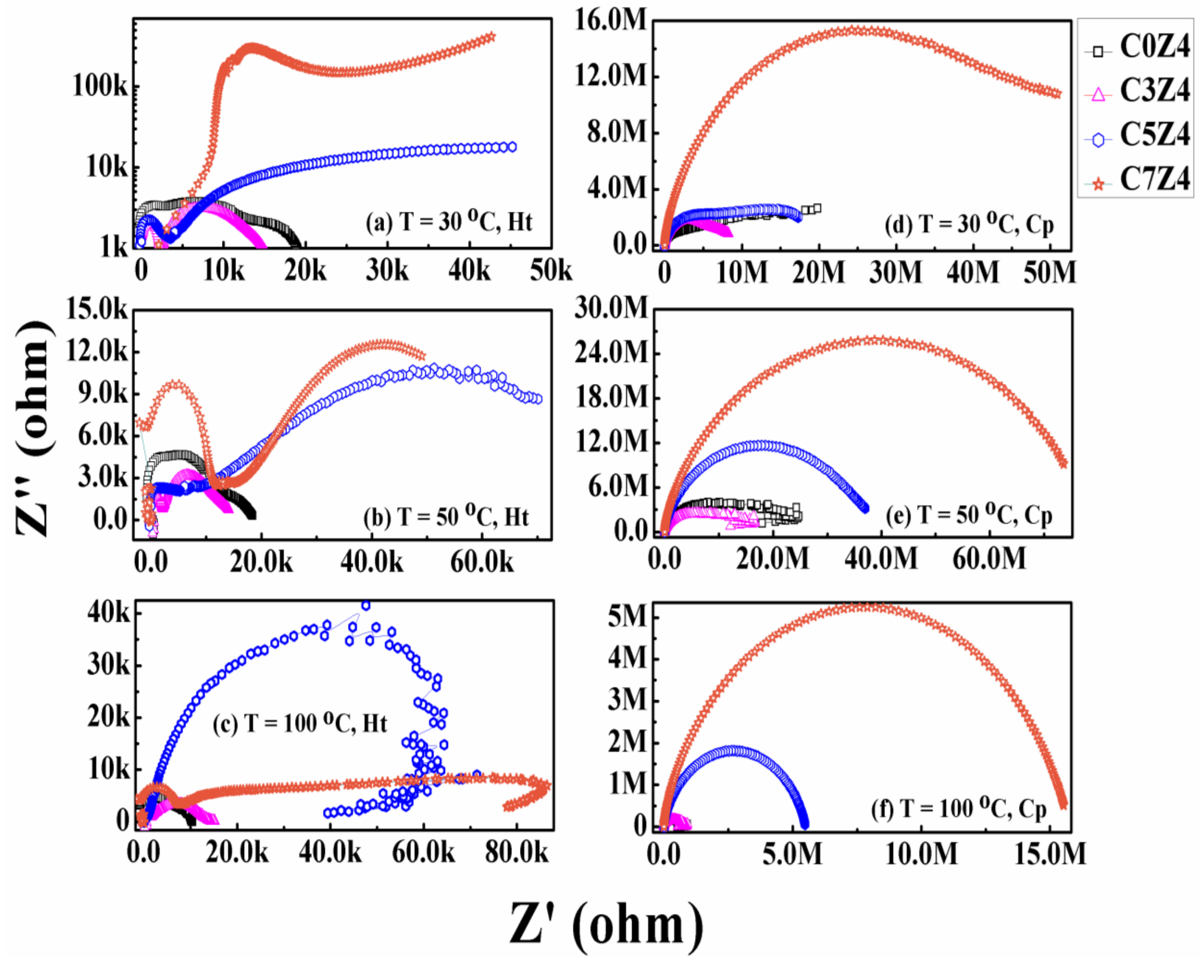

Fig. 6.14 Cole-cole plot between an imaginary part (Z") and the real part (Z') of complex impedance of the samples C0Z4Ht, C3Z4Ht, C5Z4Ht and C7Z4Ht at (a) 30 °C, (c) 50 °C, (e) 100 °C and C0Z4Cp, C3Z4Cp, C5Z4Cp and C7Z4Cp at (b) 30 °C, (d) 50 °C, (f)100 °C.

6.4 Conclusion

The undoped ZnO and Cr-doped ZnO nanoparticles have been obtained through co-precipitation and hydrothermal route. In many articles, the detail of both the synthesis methods have been discussed but no one has investigated the detail comparison of these two methods corresponding to the dielectric response in an extensive manner. FESEM study furnishes clear evidence of co-precipitated Cr-doped ZnO nanomaterials with a nearly spherical shape and hexagonal rod-like grain structure of Cr-doped ZnO nanomaterials under hydrothermal synthesis route. UV-visible absorption spectroscopy study suggests a significant change in bandgap that has been perceived for rod-like Cr-doped ZnO nanomaterial as compared to nearly spherical shaped Cr-doped ZnO nanoparticles. In dielectric response study, for rod-like Cr-doped ZnO nanomaterials, the dielectric constant with ~ 344538 is complementary in nature with dielectric constant ~ 92 of spherical shaped Cr-doped ZnO nanoparticles at low frequency region. For complex impedance study, the Nyquist plot of hydrothermally synthesized rod-like grain structure exhibits the presence of grain and grain boundary effect in the charge transport phenomenon whereas the Nyquist plot for co-precipitated nearly spherical grain structure exhibits the presence of only grain in the electric charge conduction mechanism. It is to be noted here that the selection of dopant and annealing temperature change the physical properties of nanomaterials within an acceptable range but the selection of synthesis mechanism can enhance the physical properties like dielectric response in a complimentary manner. This work inspired us about the preparation of these nanomaterials which will be satisfactory for the fabrication of various device in the field of dielectric applications.

Reference

[1] M.K. Gupta, N. Sinha and B. Kumar, J. Appl. Phys. 112 (2012) 014303.

[2] A. Kar, S. Kundu and A. Patra, J. Phys. Chem. C 115 (2011) 118.

[3] T. Debnath, S. Das, D. Das and S. Sutradhar, J Alloys Compd. 696 (2017) 670.

[4] S. Das, S. Das and S. Sutradhar, J Alloys Compd. 726 (2017) 11.

[5] S. Das, S. Das and S. Sutradhar, Ceram. Int. 43 (6.9) (2017) 6932.

[6] J. Zhou, F. Zhao Y. Wang, Y. Zhang and L. Yang, J. Lumin. 122 (2007) 195.

[7] J.B. Wang, G.J. Huang, X.L. Zhong, L.Z. Sun, and Y.C. Zhou, Appl. Phys. Lett. 88 (2006) 252502.

[8] G. Vijayaprasath, R. Murugan, T. Mahalingam, Y. Hayakawa and G. Ravi, J Alloys Compd. 649 (2015) 275.

[9] A. van Dijken, E.A. Meulenkamp, D. Vanmaekelbergh and A. Meijerink, J. Lumin. 87 (2000) 454.

[10] W. Peng, S. Qu, G. Cong and Z. Wang, Cryst. Growth Des. 6 (2006) 1518.

[11] H. Zeng, G. Duan, Y. Li, S. Yang, X. Xu and W. Cai, Adv. Funct. Mater. 20 (2010) 561.

[12] T. Debnath, P. Saha, N. Patra, S. Das and S. Sutradhar, J. Appl. Phys.123 (2018) 194101.

[13] C.N. Wu, S.Y. Huang, W.C. Lee, Y.H. Chang, T.S. Wu, Y.L. Soo, M. Hong and J. Kwo, Appl. Phys. Lett. 101 (2012) 162403.

[14] K.R. Kittilstved and D.R. Gamelin, J. Am. Chem. Soc. 127 (2005) 5292.

[15] P. Sharma, A. Gupta, K.V. Rao, F.J. Owens, R. Sharma, R. Ahuja, J.M.O. Guillen, B. Johansson and G.A. Gehring, Nature Materials 2 (2003) 673.

[16] E. Broitman, M.Y. Soomro, J. Lu, M. Willander and L. Hultman, Phys. Chem. Chem. Phys., 15 (2013) 11113.

[17] M.L.M. Napi, S.M. Sultan, R. Ismail, K.W. How and Md. K. Ahmad, Materials 12 (2019) 2985.

[18] H.H. Singh and N. Khare, Nano Energy 51 (2018) 216.

[19] D.T. Phan and G.S. Chung, Sensors and Actuators B 187 (2012) 191.

[20] N. Han, P. Hu, A. Zuo, D. Zhang, Y. Tian and Y. Chen, Sensors and Actuators B 145 (2010) 114.

[21] P.E. Amami, J. Das, D.K. Mishra, V.V. Srinivasu, D.R. Sahu , B.K. Roul, Physica B: Condensed Matter, 572 (2019) 60.

[22] Y. Liu, Y. Yang, J. Yang, Q. Guan, H. Liu, L. Yang, Y. Zhang, Y. Wang, M. Wei, X. Liu, L. Fei and X. Cheng, J. Solid State Chem. 184 (2011) 1273.

[23] Y. Liu, J. Yang, Q. Guan, L. Yang, Y. Zhang, Y. Wang, B. Feng, J. Cao, X. Liu, Y. Yang, M. Wei, J Alloys Compd. 486 (2009) 835.

[24] T. Debnath, A. Bandyopadhyay, T. Chakraborty, S. Das and S. Sutradhar, Mater. Res. Bull. 118 (2019) 110480.

[25] M. M. Hassan, W. Khan, A. Azam and A. H. Naqvi, J. Ind. Eng. Chem. 21 (2015) 283.

[26] R. N. Aljawfi, F. Rahman and K. M. Batoo, J. Mol. Struct. 1065 (2014) 199.

[27] M. M. El-Desoky, M.A. Ali, G. Afifi, H. Imam and M. S. Al-Assiri, Silicon 10 (2018) 310.

[28] G. Kenanakis, D. Vernardou, E. Koudoumasand N. Katsarakis, J. Cryst. Growth 311 (2009) 4799-4804.

[29] P. Singh, A. Kumar, Deepak and D. Kaur, J. Cryst. Growth 306 (2007) 303-310.

[30] K. P. Misra, R. K. Shukla, A. Srivastava and A. Srivastava, Appl. Phys. Lett. 95 (2009) 031901.

[31] P. Sahu, M. De, M. Zdujic, Materials Chemistry and Physics 82 (2003) 864-876.

[32] Y. Wang, W. Tang and L. Zhang, J. Mater. Sci. Technol. 31 (2015) 175-181.

[33] S. Chattopadhyay, K.P.Misra, A. Agarwala, A. Shahee, S. Jain, N. Halder, A. Rao, P.D. Babu, M. Saran and A.K. Mukhopadhyay, Ceram. Int. 45 (2019) 23341.

[34] L. Lutterotti and S. Gialanella, Acta Mater. 46 (1998) 101.

[35] H. Morkoç, Ü. Özgür, Zinc Oxide Wiley-VCH Verlag GmbH & Co. KGaA, Weinheim, Germany, 2009. doi:10.1002/9783527623945.

[36] U. Ozgur, Y.I. Alivov, C. Liu, A. Teke, M.A. Reshchikov, S. Doğan, V. Avrutin, S.J. Cho and H. Morkoç, J. Appl. Phys. 98 (2005) 041301.

[37] L.B. Duan , X.R. Zhao, J.M. Liu, T. Wang and G.H. Rao, Appl. Phys. A 99 (2010) 679.

[38] S. Kumar, S. Basu, B. Rana, A. Barman, S. Chatterjee, S.N. Jha, D. Bhattacharyya, N.K. Sahoo, A.K. Ghosh, J. Mater. Chem. C 2 (2014) 481.

[39] Y. Zhao and J. Zhang, J. Appl. Cryst. 41 (2008) 1095–1108.

[40] S. Tsunekawa, K. Ishikawa, Z.-Q. Li, Y. Kawazoe, and A. Kasuya, Phys. Rev. Lett. 85 (2000) 3440.

[41] B. Chowdhury, P. Chetri and A. Chowdhury, J. Exp. Nanosci. 10 (2015) 103.

[42] S. Kahraman, H. A. C-etinkara, F. Bayansal, H.M. C-akmak and H.S. Güder, Philos. Mag. 92 (2012) 2150.

[43] W.-J. Li, E.-W. Shi, W.-Z. Zhong and Z.-W. Yin, J. Crystal Growth 203 (1999) 186.

[44] Y. Chen and X.L. Xu, Physica B: Condensed Matter 406 (2011) 3121.

[45] J. W. Li, L.W. Yang, Z.F. Zhou, P.K. Chu, X.H. Wang, J. Zhou, L.T. Li and C.Q. Sun, J. Phys. Chem. C 114 (2010) 13370.

[46] B. Wei, K. Zheng, Y. Ji, Y. Zhang, Z. Zhang and X. Han, Nano Lett. 12 (2012) 4595.

[47] S. Das, S. Das,A. Roychowdhury, D. Das and S. Sutradhar, J Alloys Compd. 708 (2017) 231.

[48] S. Das, A. Bandyopadhyay, S. Das, D. Das and S. Sutradhar, J Alloys Compd. 731 (2018) 591.

[49] S. Das, S. Das, D. Das and S. Sutradhar, J Alloys Compd. 691 (2017) 739.

[50] K.W. Wagner, Am. Phys. 40 (1973) 817.

[51] J. Maxwell, Electric and Magnetism 2 New York Oxford University Press (1973).

[52] C.G. Koops, Phys. Rev. 83 (1951) 121.

[53] K.S. Hemalatha, G. Sriprakash, M.V.N.A. Prasad, R. Damle and K. Rukmani, J. Appl. Phys. 118 (2015) 154103.

[54] M.A. Rahman and A.K.M.A. Hossain, Phys. Scr. 89 (2014) 025803.

[55] M.A. Dar, K.M. Batoo, V. Verma, W.A. Siddiqui and R.K. Kotnala, J Alloys Compd. 493 (2010) 553.

[56] K.M. Batoo, Physica B 406 (2011) 382.

[57] T.F. Khoon, J. Hassan, Z.A. Wahab, R.S. Azis, Engineering Science and Technology, an International Journal 19 (2016) 2081.

CHAPTER 7

Reprint of published papers

Journal of Alloys and Compounds 696 (2017) 670–681

Contents lists available at ScienceDirect

Journal of Alloys and Compounds

journal homepage: http://www.elsevier.com/locate/jalcom

Optical, magnetic and dielectric properties of ZnO:Y nanoparticles synthesized by hydrothermal method

Tanumoy Debnath [a, b], Sukhen Das [b], Dipankar Das [c], Soumyaditya Sutradhar [a, *]

[a] Department of Physics, Amity University, Rajarhat, Kolkata 700156, India
[b] Department of Physics, Jadavpur University, Jadavpur, Kolkata 700032, India
[c] UGC-DAE Consortium for Scientific Research, III/LB-8, Kolkata 700098, India

ARTICLE INFO

Article history:
Received 2 November 2016
Received in revised form
18 November 2016
Accepted 19 November 2016
Available online 21 November 2016

Keywords:
Diluted magnetic semiconductor
Nanoparticles
Magnetic properties
Space charge polarization

ABSTRACT

Y^{3+} ions doped zinc oxide nanoparticles were prepared by hydrothermal method. The desired nanocrystalline phase and intrinsic defects inside the host ZnO nanoparticles was obtained by taking the as prepared samples, doped with different Y^{3+} ion concentrations, at 400 °C for 6 h in vacuum atmosphere. The crystallinity and morphology of all the samples were investigated using X-ray diffraction (XRD) and field emission scanning electron microscopy (FESEM). Atomic vibrational mode of the samples has been investigated by FTIR spectroscopy. The formation of oxygen vacancy and the trapping of electron in Y^{3+} ions doped ZnO nanorods were also confirmed by PL and Raman analysis which are very useful for the determination of different types of defect in the sample. Magnetic measurement shows the presence of room temperature ferromagnetism in the samples which has been successfully explained by the vacancy assisted bound magnetic polaron model. Frequency as well as temperature dependent dielectric constant of the samples was also investigated. High value of dielectric constant in the Y^{3+} ions doped ZnO sample was obtained.

1. Introduction

Zinc oxide (ZnO) is a well known II–VI semiconducting material with direct band gap energy (3.37 eV) and large exciton binding energy (60 meV) and it has attracted considerable interest in the research community [1–3]. Although ZnO had been considered for research in the past decades and the renewed interests are focused on the low-dimensional nanostructures, such as nanoparticles, nanowires, nanorods, and nanotubes, due to brand new elementary physical properties and applications of nano-devices [4–7]. Advance studies on the performance enhancement of these low-dimensional nanostructures of ZnOs for various device applications have been performed by various growth methods, such as coprecipitation method, hydrothermal methods, metal organic vapor-phase epitaxy method and pulsed laser deposition and doped with impurity atoms, such as Ag, Li, and P [8–14]. Besides, effective mass production process of ZnO nanowires by a modified carbothermic reduction method has also been reported [15]. Recent researches denoted that nanostructured ZnO with large surface area is very much suitable for ultraviolet and photovoltaic device applications, such as light-emitting diodes, nanolasers, photodetectors, field emitters, chemical sensors, and photo-electrodes in dye-sensitized solar cells [16–21]. Recently, the observation of ferromagnetic ordering at room temperature (RT) along with high Curie temperature in III-V and II-VI semiconductors has also attracted a great deal of attentions [22–24]. RT ferromagnetic ordering of transition metal ions doped ZnO nanoparticles has been also theoretically predicted and experimentally confirmed for spintronic applications [25,26]. In order to construct diluted magnetic semiconductors (DMSs), ZnO nanostructures have been doped with magnetic metal elements, such as Mn, Co, or Ni [27]. Recently, some research works have declared that ferromagnetic ordering had been obtained from undoped and doped nanostructured ZnO and suggested to be induced by intrinsic defects [28]. Non-magnetic elements, such Bi or Li, have been doped into ZnO and RT ferromagnetism has been also observed [29,30]. Therefore, ferromagnetic ordering would not originate from the non-magnetic dopant since they do not contribute to ferromagnetism. Based on the earlier reports, one of the most useful ways to approach the optical, magnetic and dielectric properties of these nanostructured materials is the doping with careful choice of

---

* Corresponding author.
E-mail address: sds.phy1@gmail.com (S. Sutradhar).

http://dx.doi.org/10.1016/j.jallcom.2016.11.270
0925-8388/© 2016 Elsevier B.V. All rights reserved.

elements. By choosing suitable rare-earth dopant, modification of the properties can be anticipated. In recent times many research works have been reported on rare-earth (Dy^{3+}, Tb^{3+}, Tm^{3+}, Gd^{3+}, etc.) doped ZnO nanoparticles. The enhance optical, magnetic and dielectric properties of the rare-earth doped ZnO nanoparticles have been observed due to the presence of intrinsic defects in the structure of the doped ZnO nanomaterials. The various types of intrinsic defects such as, oxygen vacancies, zinc vacancies, interstitials and others in the structure of the doped ZnO nanomaterials develop because the ionic radius of those dopant ions are sufficiently large as compared to the ionic radius of the host zinc ion. In this connection the ionic radius of yttrium ion (0.89 Å) is quite larger than the ionic radius of the zinc ion (0.74 Å). So the substitution of Zn ion by the large size yttrium ion can produce large internal strain which in turn can generate large numbers of intrinsic defects in the structure of ZnO. Also the major benefits of yttrium doping are (i) it can reduce the energy band gap of ZnO [31] (iii) Y^{3+} surface improvement hinders crystallite growth [32] (iii) the surface isolation of Y^{3+} boosts oxygen vacancies creation [32]. All these facts motivated us to explore the optical, magnetic and dielectric properties of Y^{3+} ions doped ZnO nanoparticles. In these direction Y^{3+} ions doped ZnO has been considered recently for extensive research for the very interesting optical properties shown by them. So far of our knowledge, the optical properties of Y^{3+} ions doped ZnO have been reported by many researchers but the detail magnetic or dielectric properties of Y^{3+} ions doped ZnO have not yet been reported [33–35]. In this paper, optical, magnetic and dielectric properties of nanocrystalline Y^{3+} ions doped ZnO prepared by hydrothermal method have been reported. The origin of the ferromagnetic ordering at room temperature (RT) and the intrinsic defect induced dielectric properties in the Y^{3+} ions doped ZnO nanoparticles was also discussed. Based on the reports, this material is suitable for many electromagnetic device applications.

2. Experimental

2.1. Materials

Y^{3+} ions doped nanoparticles of ZnO were prepared by hydrothermal method. All the precursor materials used for the preparation of $Zn_{1-x}Y_xO$ ($x = 0.03$, 0.05 and 0.07) are zinc acetate dihydrate $Zn(CH_3COO)_2 \cdot 2H_2O$ (Sigma Aldrich, 99%), yttrium nitrate hexahydrate $YN_3O_9 \cdot 6H_2O$ (Sigma Aldrich, 99%), ammonium hydroxide NH_4OH (concentration ~ 25%). All the chemicals were taken with analytical grade.

2.2. Synthesis of Y^{3+} ions doped ZnO nanoparticles by co-precipitation method

Nanoparticles of Y^{3+} ions doped ZnO were prepared by using simple co-precipitation method. zinc acetate dihydrate $Zn(CH_3COO)_2 \cdot 2H_2O$ and yttrium nitrate hexahydrate $YN_3O_9 \cdot 6H_2O$ were the precursor materials taken in milli-Q water (resistivity value 16–17 MΩ cm @ 25 °C, Heal force ASTM Type-I Easy Series model) and the aqueous solution of both the salts were taken in a beaker. The beaker was then placed over a magnetic stirrer. Molar concentration of yttrium salt that has been taken in the aqueous solution was set at 3, 5, and 7% to that of the molar concentration of zinc salt. The mixed solution was then stirred for 4 h to get homogeneous solution of the precursor salts. Thereafter NH_4OH solution added in the precursor solution for co-precipitation and the final pH of the solution was kept at ~10. Rigorous stirring process was maintained during the whole course of the sample preparation by co-precipitation method. After that the co-precipitated particles were collected properly for washing. The whole course of washing of the co-precipitated particles has been done several times by using milli-Q water and ethyl alcohol to neutralize the pH as well as to remove the extra ions. A through washing process brings up the pH of the as-prepared particles back to ~6.

2.3. Nucleation of Y^{3+} ions doped ZnO nanoparticles by hydrothermal process

After washing the precipitation was dissolved in milli-Q water to form a 40 ml solution and it was taken into Teflon jacket. The Teflon jacket has been taken in the autoclave and the autoclave was placed in an oven at 160 °C for 2 days. Hydrothermal technique initiates the nucleation of the ZnO nanoparticles inside the Teflon jacket which was executed under the effect of high pressure and temperature resulting from thermal expansion of air initially present in it. This ambiance inside Teflon jacket favours the surface growth of rod like ZnO nanoparticles. After 2 days the autoclave was permitted to cool down naturally to RT. The supernatant was then removed and the solid precipitates at the underside of the Teflon jacket were collected and washed several times with milli-Q water to remove unreacted reagents from precipitation. It was then dried in a vacuum desiccator at RT. Now the dried powder was sintered at 400 °C in vacuum atmosphere to eliminate unreacted precursor waste and to get better crystallographic phase formation. The sample name and the corresponding sample specifications were given in Table 1.

2.4. Characterization techniques

The XRD pattern of all the samples were recorded in powder X-ray diffractometer, Model D8, BRUKER AXS, using Cu K_α radiation ($\lambda = 1.5405$ Å) in the range of 2θ from 10 to 80°. Field emission scanning electron microscope (FESEM) was employed for morphological study using INSPECT F50 (FEI, Netherland). FTIR measurement of the samples was recorded in JASCO FTIR instrument - 410 (USA). The photoluminescence spectroscopy (PL) study was also done using a spectroflurometer, Perkin Elmer Germany with an excitation wavelength (λ_{ex}) of 325 nm. The Raman spectroscopy study was employed using Newport RS 2000TM. Magnetization versus applied magnetic field ($M - H$) data of the samples at RT and at different low temperatures was recorded by a SQUID magnetometer (MPMS XL 7, Quantum Design), where the maximum applied field was 50 kOe. Electrical conduction mechanism was investigated by dielectric measurement using Agilent 4294A Precision Impedance Analyzer.

3. Result and discussions

3.1. XRD and FESEM analysis

XRD patterns of undoped ZnO and Y^{3+} ions doped ZnO nanoparticles were depicted in Fig. 1. All the peaks have been assigned with the help of the JCPDS (file no. 36-1451). All the peaks in the XRD pattern of Fig. 1 are matched very well with that of the desired phase of the hexagonal wurtzite structure of ZnO (space group

Table 1
The sample name and the corresponding sample specifications for undoped and Y^{+3} ions doped ZnO samples.

Sample specification	Sample details
ZnO	Undoped ZnO
ZnOY3	3% yttrium ions doped ZnO ($Zn_{0.97}Y_{0.03}O$)
ZnOY5	5% yttrium ions doped ZnO ($Zn_{0.95}Y_{0.05}O$)
ZnOY7	7% yttrium ions doped ZnO ($Zn_{0.93}Y_{0.07}O$)

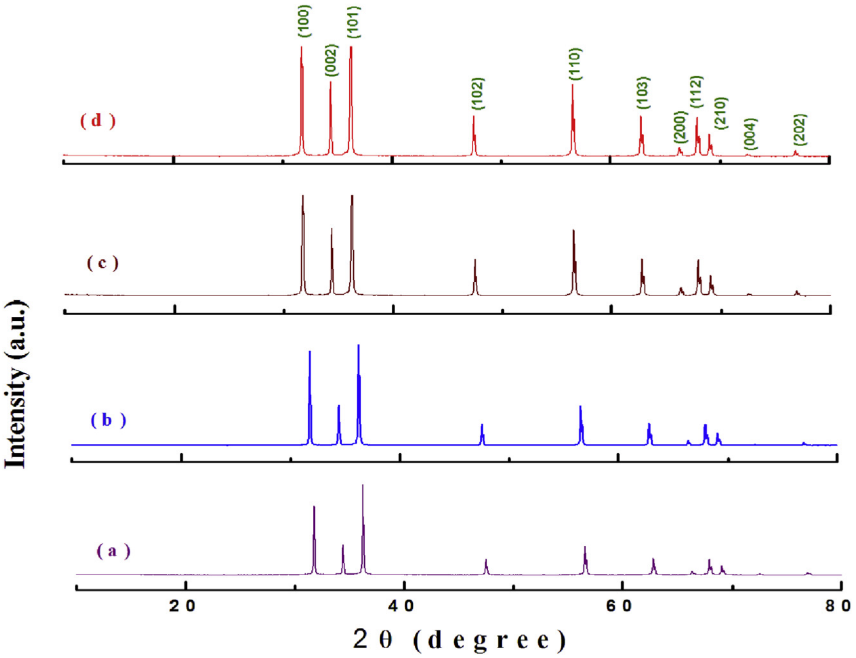

Fig. 1. XRD patterns of the samples (a) ZnO, (b) ZnOY3, (c) ZnOY5 and (d) ZnOY7.

$P6_3mc$). Also, no peak corresponding to any other impurity phase like Y_2O_3 etc. has been found in the XRD patterns. This indicates the homogeneous incorporation of Y^{3+} ions at the tetrahedral site of Zn^{2+} ions in the wurtzite structure of ZnO. The average nanocrystallite diameter of undoped ZnO and Y^{3+} ions doped ZnO nanoparticles was calculated from the broadening of the peak (101) of each sample by using the well known Debye-Scherrer equation.

$$<D>_{(101)} = \frac{0.9\lambda}{\beta_{\frac{1}{2}}\cos\theta} \quad (1)$$

It is noticed that the average nanocrystallite diameter increases with the increased doping percentage of Y^{3+} ions in the ZnO nanoparticles. The observed change in nanocrystallite diameter occurs due to the presence of distortional effect in the host ZnO lattice by the incorporation of the doped Y^{3+} ions. The corresponding value of micro strain (ε) of the doped ZnO nanoparticles is also given in Table 2 using the formula

$$Micro\ strain(\varepsilon) = \frac{\beta_{\frac{1}{2}}cos\theta}{4} \quad (2)$$

The other important information pertaining to the microstructural analysis such as unit cell parameters ‘a’ and ‘c’, c/a ratio, volume per unit cell (V), bond length (L), internal positional parameter (u) and dislocation density (δ) calculated from the XRD data for different doped ZnO samples are given in Table 2. Now for Y^{3+} ions in the ZnO nanoparticles, lattice parameter ‘a’ is found to be higher as compared to undoped ZnO nanoparticles and ‘c’ is found to be lower as compared to undoped ZnO nanoparticles. The increase/decrease in lattice constants with increasing concentration of Y^{3+} ion in the ZnO nanostructure confirms the substitution of Y^{3+} ions at Zn sites as the bigger ionic radius (0.89 Å) of Y^{3+} ions as compared to Zn^{2+} ion (0.74 Å) produces internal lattice strain. Doping of Y^{3+} ions into ZnO nanostructure should lead the increase/decrease of a and c-axis lattice constants and consequently, the shift of all diffraction peaks towards lower 2θ angle. The ratio of c/a has also been measured to show a good agreement with perfectly hexagonal close packed structure. The volume of unit cell for hexagonal system has been calculated from the following equation

$$V = 0.866 \times a^2 \times c \quad (3)$$

Increased value of cell volume (V) indicates the substitution of Y^{3+} ions in the tetrahedral site of Zn. Dislocation density (δ) is a prominent signature of the occurrence of defect in the Y^{3+} ions doped ZnO samples. Dislocation density is defined as the length of dislocation lines per unit volume of the crystal and has been calculated using equation

Table 2

Structural parameters calculated from XRD data are average nanocrystallite diameter (D), lattice parameter (a, c), c/a ratio, micro strain (ε), unit cell volume (V), bond length (L) and dislocation density (δ).

Average crystallite		Lattice parameter (Å)		c/a ratio	Micro strain (ε) (10^{-4})	Unit cell volume V (Å)^3	Zn–O bond length (Å)	Dislocation density (Å)$^{-2}$ δ (10^{-6})
Sample	Diameter D (nm) (101)	a	c					
ZnO	84.44	3.2514	5.212	1.605	3.728	47.66	1.9783	1.158
ZnOY3	87.06	3.2516	5.209	1.603	3.966	47.69	1.9787	1.312
ZnOY5	88.86	3.2518	5.207	1.601	4.061	47.74	1.9791	1.375
ZnOY7	89.19	3.2520	5.204	1.600	4.132	47.78	1.9796	1.432

$$\delta = \frac{1}{D^2} \tag{4}$$

The Zn–O bond length has been calculated using the relationship

$$L = \sqrt{\frac{a^2}{3} + \left(\frac{1}{2} - u\right)^2 c^2} \tag{5}$$

Where the u is the positional parameter for wurtzite structure and it can be calculated from the equation

$$u = \frac{a^2}{3c^2} + 0.25 \tag{6}$$

It is observed that bond length increases gradually with the increase in Y^{3+} ions content in the ZnO nanostructure. This can be due to the fact that once Y^{3+} ions replace Zn^{2+} ions, Y–O bonds are also created in Zn–O lattice, whose bond length is higher than Zn–O bond length.

The structural morphology of all the samples has been observed and some representative micrographs are shown in Fig. 2. Fig. 2a–d shows the morphology of undoped ZnO and Y^{3+} ions doped ZnO nanoparticles obtained by means of FESEM. It is clear from Fig. 2a–d that the micrographs of all the samples are rod like in nature with hexagonal cross-section. Fig. 2a represents the micrograph of undoped ZnO nanoparticles and it shows rod like structure and the entire rod like structures are very much clear and distinguishable from one another and the clustering occurred in the micrographs formed large size grains. Fig. 2b–d shows the micrographs of ZnOY3, ZnOY5 and ZnOY7 nanoparticles respectively. In all the micrographs the structural morphology of Y^{3+} ions doped ZnO nanoparticles are also rod like in nature with the same signature of orientation to that of undoped ZnO nanoparticles. The change in morphology with the increase in doping percentages signifies the successful incorporation of the Y^{3+} ions in the structure of ZnO nanoparticles. Interestingly, all the nanorods in different micrographs are nearly uniform in size and the particles are not yet agglomerated.

3.2. FTIR studies

The FTIR spectra of undoped ZnO and other Y^{3+} ions doped ZnO samples are shown in Fig. 3. FTIR spectroscopy is an important measurement to investigate the atomic vibrational mode of bonded molecules in undoped ZnO and Y^{3+} ions doped ZnO powders annealed at 400 °C. It is quite clear from Fig. 3 that a weak doublets at around 2366, 2348, 2347 and 2357 cm^{-1} of the samples of

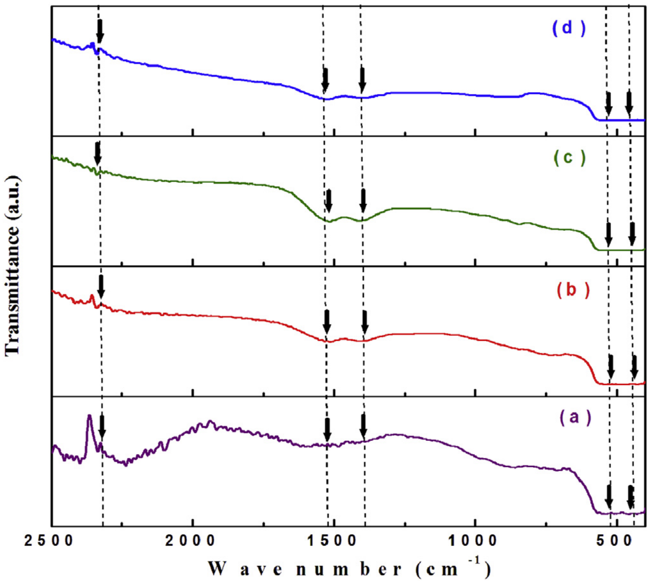

Fig. 3. FTIR transmittance spectra of the samples (a) ZnO, (b) ZnOY3, (c) ZnOY5 and (d) ZnOY7.

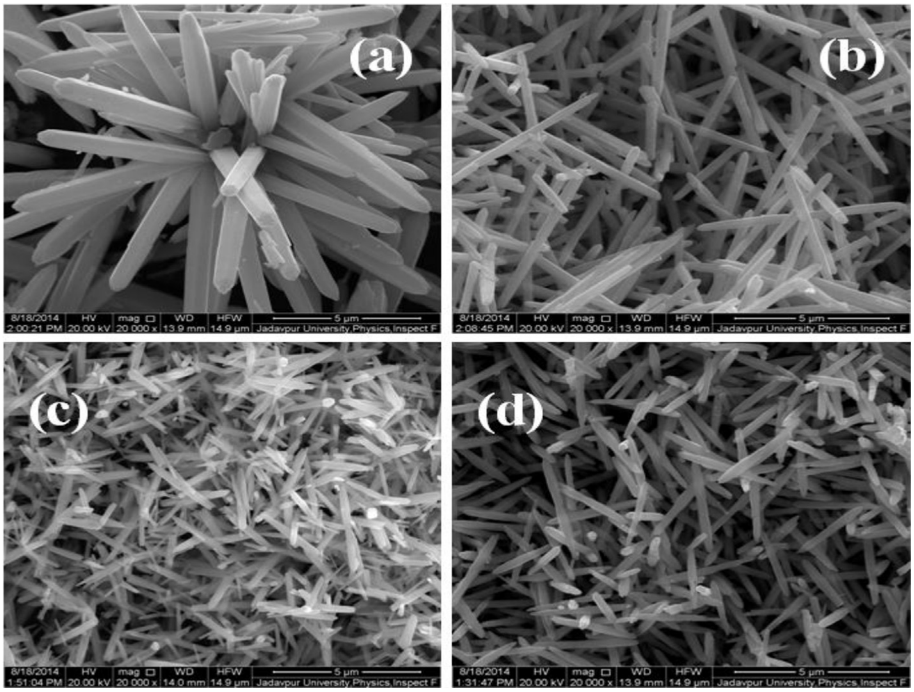

Fig. 2. SEM images of the samples (a) ZnO, (b) ZnOY3, (c) ZnOY5 and (d) ZnOY7.

undoped ZnO and Y^{3+} ions doped ZnO (ZnOY3, ZnOY5 and ZnOY7) respectively, have been ascertained due to the presence of CO_2 molecule in air [36]. It is not related to any kind of impurity present in the samples. The samples might have trapped some CO_2 from the atmosphere during measurement and this absorbed CO_2 raise these modes. The peak recorded at about 1513, 1529, 1536, 1348 cm^{-1} and 1406, 1413, 1401, 1404 cm^{-1} of the samples of undoped ZnO, ZnOY3, ZnOY5 and ZnOY7, respectively, appears due to the C=O stretching (symmetric and asymmetric) mode arises from the absorbed CO_2 resides on the outer surface of the ZnO nanoparticles [37]. Among the three infrared absorption bands in the range of 400–600 cm^{-1}, the two most strong absorption bands are observed at 443-452 cm^{-1}, which may be attributed due to Zn–O stretching of ZnO nanoparticles. The band observed at 525-531 cm^{-1} may be attributed due to the existence of oxygen deficiency and/or oxygen vacancy (V_o) present in ZnO which is naturally formed during the annealing of the samples in vacuum atmosphere. However, the mismatch between the ionic radii of Zn^{2+} ion (~0.74 Å) and Y^{3+} ion (~0.89 Å) results in more number of different kinds of structural/vacancy defects such as oxygen vacancies, zinc interstitials and zinc vacancies in the host ZnO nanoparticles. The presence of different kinds of defects and their consequences will be discussed in the later sections.

3.3. *Photoluminescence studies*

Photoluminescence study is an important tool to find out optical properties of the samples. RT photoluminescence spectra for all the samples have been measured and are given in Fig. 4(I)(a-d) respectively. Photoluminescence study on undoped ZnO and Y^{3+} ions doped ZnO nanorods was carried out with excitation wavelength of 325 nm at RT. The PL spectra of undoped ZnO and Y^{3+} ions doped ZnO nanorods show a sharp UV emission at 360 and 388 nm. In ultraviolet region, the emission were found almost at the same position for all the samples which arises due to the recombination of free excitons through exciton-exciton collision process and are generally assigned as a near-band-edge (NBE) emission band. In visible region violet emission at 411 nm is attributed due to the electronic transition from zinc interstitial level (I_{Zn}) to top of the valance band. Blue emission located at 454 nm is designated due to the electronic transition from zinc interstitial level (I_{Zn}) to zinc vacancy level (V_{Zn}) for all the samples [38]. Green emission at 498 nm in all the samples is assigned due to electronic transition from bottom of the conduction band to the oxygen vacancy level (V_o). A clear red shift of excitonic emission peak of in all the samples were detected which can be assumed to be due to incorporation of Y^{3+} ions within ZnO matrix. This prediction is in well agreement with our analysis of defect in Raman spectroscopy measurement discussed later. A comparison between undoped ZnO and Y^{3+} ions doped ZnO nanorods shows that the relative intensity of Y^{3+} ions doped ZnO nanorods is smaller than that of undoped ZnO nanorods, illustrating that Y^{3+} ions doping can increase the intrinsic defects and oxygen vacancies in doped ZnO nanorods [39–42].

3.4. *Raman spectroscopy studies*

Raman spectra were taken for undoped ZnO and Y^{3+} ions doped ZnO nanorods in the range of 50–550 cm^{-1}. Raman spectroscopy is a nondestructive procedure to obtain more information about microstructure of undoped ZnO and Y^{3+} ions doped ZnO nanorods such as, its quality of crystallinity, structural disorderness and intrinsic defects etc. The wurtzite ZnO consists six Raman-active phonon modes at 101 [E_2 (low)], 225 [2E_2 (low)], 330 (E_{2H}-E_{2L}), 380 [A_1 (TO)], 410 [E_1 (TO)] and 437 cm^{-1} [E_2 (high)] respectively, at RT and the corresponding Raman spectrum have been shown in Fig. 4(II) (a) [43–45]. As compared to undoped ZnO, low frequency E_2 mode [E_2 (low)] in Y^{3+} ions doped ZnO samples exhibits a blue shift from 100 cm^{-1} to 108 cm^{-1} and the high frequency E_2 mode [E_2 (high)] in Y^{3+} ions doped ZnO samples exhibits a blue shift from 428 cm^{-1} to 437 cm^{-1}. Generally, the shift in the position and reduction in intensity of Raman modes appear due to the local stress arising as a result of the formation of structural defects and local lattice distortions due to the incorporation of Y^{3+} ions into the Zn^{2+} lattice sites inside the ZnO nanostructure. In the present case, Y^{3+} ion doping can be considered as a main factor which causes the lattice distortions due to the mismatching in the ionic radius between Zn^{2+} ion (~0.76 Å) and Y^{3+} ion (~0.89 Å). The peak at 329 cm^{-1} is referred as E_2 (high)–E_2 (low) mode (E_{2H}–E_{2L}) and

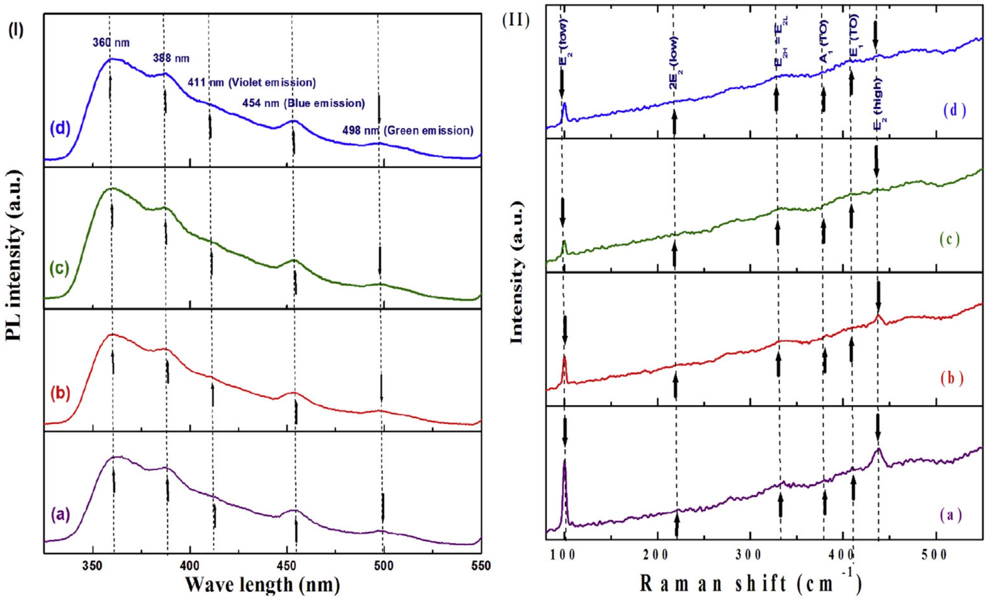

Fig. 4. (I) Photoluminescence spectra of the samples (a) ZnO, (b) ZnOY3, (c) ZnOY5 and (d) ZnOY7 and (II) Characteristic Raman vibrational modes of the samples (a) ZnO, (b) ZnOY3, (c) ZnOY5 and (d) ZnOY7.

arises from zone-boundary phonon scattering. The peaks around 530-560 cm^{-1} occur due to E_1 symmetry with LO modes. It has been accepted that the E_1 (LO) peak is caused by the defect due to oxygen vacancy, zinc interstitial defect states and free carriers. Therefore, the observation of E_1 (LO) peak indicates that oxygen vacancies or zinc interstitials present in the sample of Y^{3+} ions doped ZnO nanoparticles pronounced variation in width and position of E_{2H} mode (428-437 cm^{-1}) which is characteristic of wurtzite structure in different percentage of Y^{3+} ions doped ZnO compared to the undoped ZnO were noticed. This variation in frequency is a consequence of the formation of local defect, lattice strain or distortion which causes phonon localization and creates corresponding peak shift. It can be mentioned here that these changes are not due to laser induced heating in the nanostructure. Therefore it confirms the change in isotopic mass of atom constituting ZnO by the substitution of Y atom.

3.5. Static magnetic measurement

We have measured the magnetic field (H) dependent magnetization (M) curves at various temperatures (300, 150 and 10 K) using SQUID magnetometer in the applied magnetic field range from 0 to 50 kOe. The M − H curves of ZnOY3 and ZnOY7 exhibit ferromagnetic (FM) phase with almost saturation magnetization at RT (see Fig. 5a, and f), while at low temperature (10 K) the observed hysteresis loops are not saturated which indicates the co-existence of paramagnetic (PM) phase together with the FM phase [46,47]. Thus in these samples the PM contribution dominates over FM contribution at lower temperatures. On the other hand, in case of ZnOY5 the hysteresis loops are not saturated at all temperatures even at highest magnetic field which certainly indicates the co-existence of PM phase and FM phase at all temperatures (see Fig. 5c, d and e). Our result is in consistent with previous results obtained by the other researchers. For example Liu et al. obtained similar result for V-doped ZnO sample where magnetic contribution occurs due to dominated PM phase and weak FM phase [48]. Jing et al. also reported the co-existence of PM and FM phase in Er-doped ZnO system in their work [49]. The variations in maximum magnetization (M_{max}), remanent magnetization (M_r) and coercive field (H_c) for different Y^{3+} ions doped ZnO samples have been given in Table 3. A similar result was also found by other researchers for Nd doped ZnO thin films and transition metal doped ZnO nanoparticles [50,51]. Now to get the information about the origin of observed RT ferromagnetism in Y^{3+} ions doped ZnO, the amount of structural defects/oxygen vacancy is absolutely an inevitable factor according to the previous literature. The FTIR, Raman spectra and PL results imply that all the Y^{3+} ions doped ZnO samples have a single wurtzite phase without any secondary phases. So the effect of secondary impurity on the magnetic contribution in the present case can be ruled out. However, in the samples of Y^{3+} ions doped

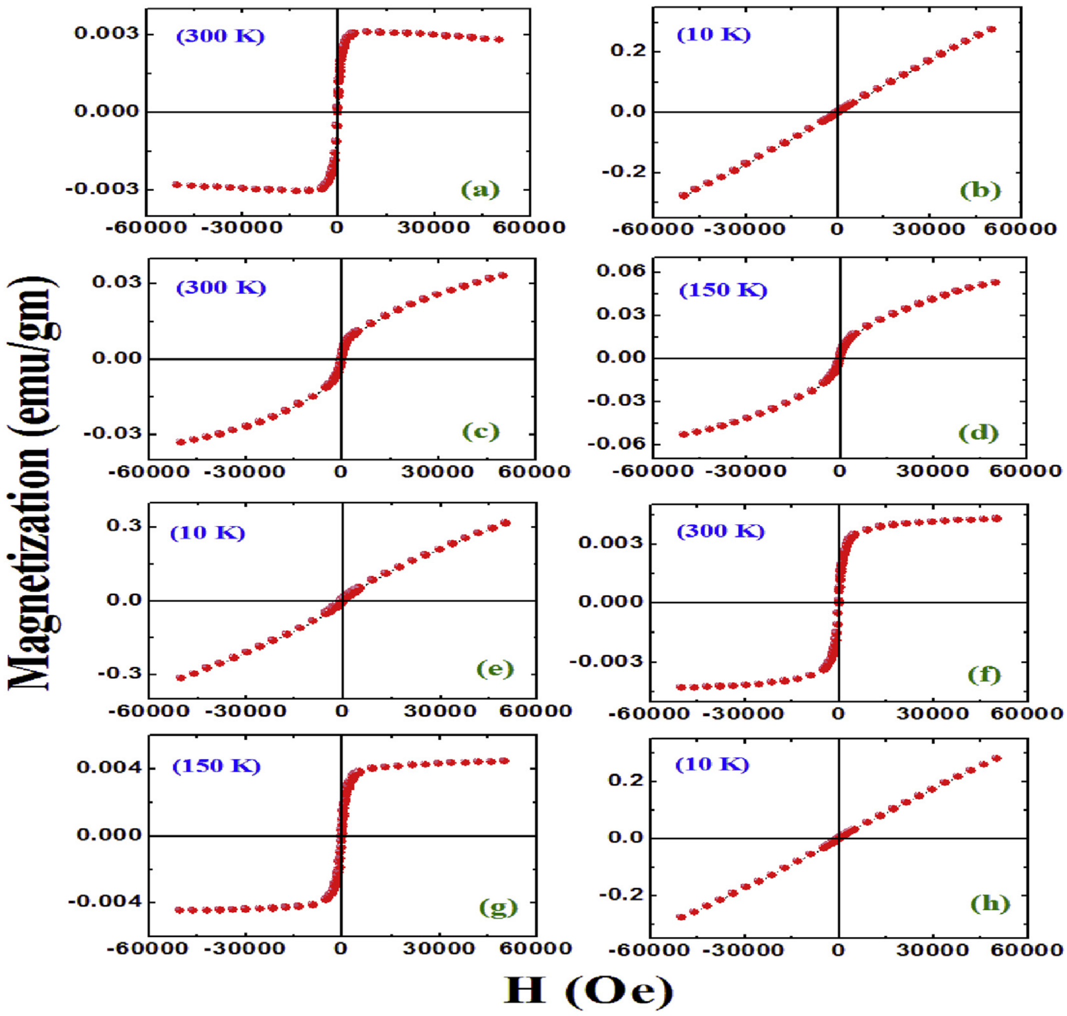

Fig. 5. Static hysteresis (M–H) loops of different sample ZnOY3 (a) 300 K and (b) 10 K, ZnOY5 (c) 300 K, (d) 150 K and (e) 10 K and ZnOY7 (f) 300 K, (g) 150 K and (h) 10 K.

Table 3
Maximum Magnetization (M_{max}), Remanence (M_r), Coercivity (H_c) of the samples (a) ZnOY3, (b) ZnOY5 and (c) ZnOY7 recorded at different temperature from 300 K to 10 K.

Sample ID	Measuring temperature (T) (In K)	Maximum magnetization (M_{max}) (emu/g)	Remanence (M_r) (emu/g)	Coactivity (H_c) (Oe)
ZnOY3	300	0.0028	0.000165	59.18
	10	0.2755	0.000720	89.44
ZnOY5	300	0.0334	0.000662	80.05
	150	0.0530	0.000730	155.97
	10	0.3173	0.006301	464.25
ZnOY7	300	0.0043	0.000108	40.25
	150	0.0044	0.000365	124.30
	10	0.2809	0.001070	160.13

ZnO nanoparticles the observed ferromagnetism cannot arise from carrier-mediated mechanism because of the low electron concentration in Y^{3+} ions doped ZnO samples which is confirmed by dielectric measurement of the samples. The value of dielectric constant of all the samples indicates semi-insulating nature of the materials, which is in consistent with the theory predicted by Dietl et al. [52]. Although the exact mechanism of intrinsic ferromagnetism in ZnO-based DMSs is still under debate but the defects are considered as the most essential factor to play an important role in observed ferromagnetism. Kohan et al. calculated formation energies and electronic structure of native point defects in ZnO by using the first-principle pseudo potential method [53]. Their calculation showed that, the two most common defects in ZnO are likely to be oxygen vacancy and zinc vacancy (V_o and V_{Zn}). In particular, oxygen vacancy (V_o) has lower formation energy than the zinc vacancy (V_{Zn}) and hence should be more abundant in Zn-rich conditions and correspondingly, zinc vacancy (V_{Zn}) should dominate in O-rich conditions. So, it is quite reasonable to conclude

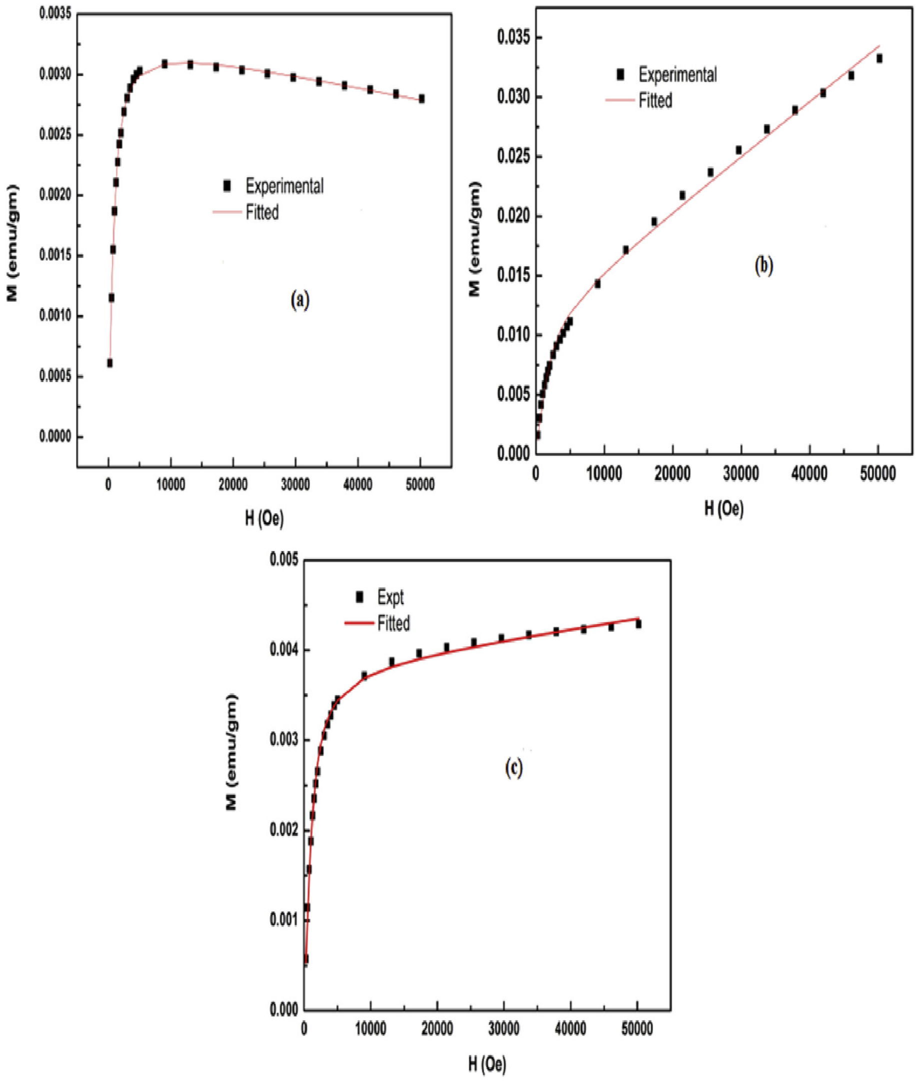

Fig. 6. Initial Magnetization vs field curve fitted by BMP model at 300 K (a) ZnOY3, (b) ZnOY5 and (c) ZnOY7.

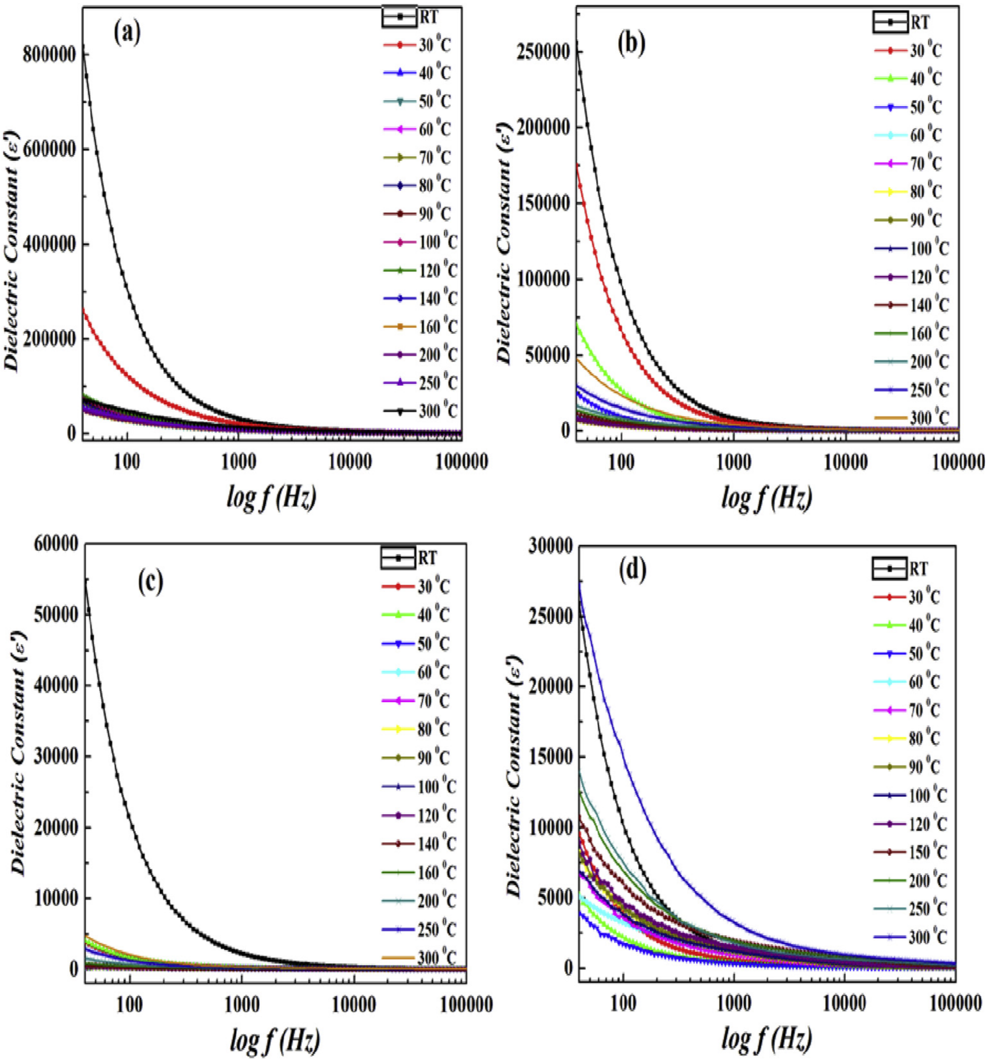

Fig. 7. Variation of Dielectric constant with frequency for samples (a) ZnO, (b) ZnOY3, (c) ZnOY5 and (d) ZnOY7.

that abundant Oxygen vacancy and a part of zinc vacancy may exist in the Y^{3+} ions doped ZnO samples. The analyses of result of Raman, FTIR and PL observations also indicate the presence of defects particularly oxygen vacancies in the sample. It has been observed that the oxygen vacancy (V_o) contributed much more than zinc vacancy (V_{Zn}) for the dilute ferromagnetism, as the doping of trivalent ions would induce more oxygen vacancy (V_o) [54]. Considering the low dopant density and unsaturated hysteresis loop at lower temperature, the ferromagnetic behavior may be explained by the BMP model introduced by Coey et al. which is suitable for low conductive or high resistive (as evident from dielectric behavior) samples having localized carriers [55]. In the present case, a locally trapped electron in oxygen vacancy (V_o) plays an important role for the spin orientations of neighboring Y^{3+} ions. The magnetic exchange interaction between oxygen vacancies (V_o) and Y^{3+} ions align some of the Y^{3+} spins around the oxygen vacancies (V_o), forming BMPs. If sufficient oxygen vacancies (V_o) are not present in the sample, neighboring Y^{3+} ions which were coupled via oxygen vacancies (V_o) (ferromagnetic exchange) are now being coupled by an oxygen bond (super exchange interaction), causing destruction of magnetic ordering. That is why oxygen vacancies (V_o) play an important role in RTFM. According to Coey's model, the measured magnetization due to interaction between BMPs can be described as [56].

$$M = M_0L(x) + \chi_m H \tag{7}$$

Here the first term signifies the contribution due to BMP and the second term appears due to the presence of paramagnetic part [57]. According to the above equation, the sample is observed as mixed up state of BMPs where localized charge carrier strongly interacts with doped Y^{3+} ions. The fraction of doped Y^{3+} ions which do not contribute in the BMP interaction are anticipated to behave like an independent paramagnetic part and contribute towards the paramagnetism. The spontaneous moment of the system can be written as

$$M_0 = Nm_s \tag{8}$$

where m_s is the actual spontaneous moment of each BMP and N is the number of BMPs per unit volume. The Langevin function is

$$(x) = cothx - \frac{1}{x} \tag{9}$$

where x can be written as

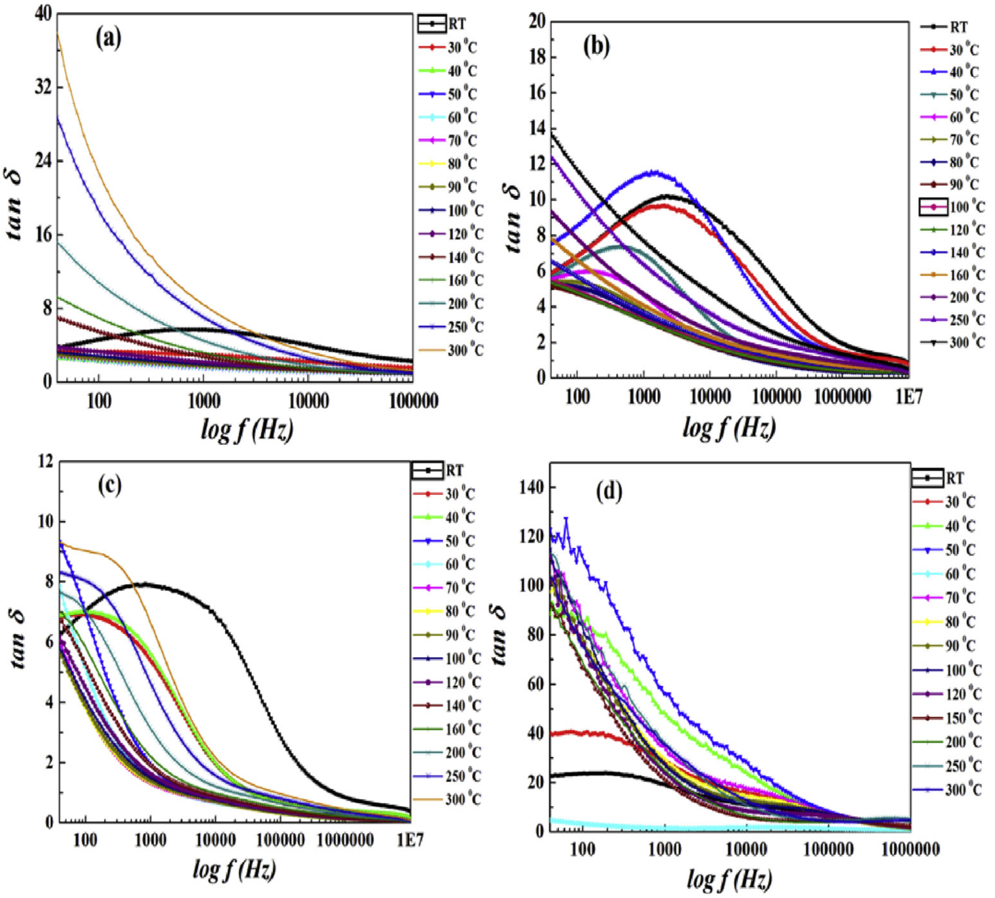

Fig. 8. Plot of loss tangent (tanδ) vs frequency at different temperature for the samples (a) ZnO, (b) ZnOY3, (c) ZnOY5 and (d) ZnOY7.

$$x = Hm_{eff} \Big/ TK_B \qquad (10)$$

here m_{eff} is the effective spontaneous magnetic moment of each BMP. It is to be noted here that we have neglected the interaction between the BMPs and thus fitting procedure is done by pretending $m_s = m_{eff}$. The respective fittings of M − H curve at RT of all the samples are shown in Fig. 6(a–c). It is evident from the fitting that in case of ZnOY5 sample the paramagnetic contribution is almost ~40 times greater than that of other two samples. Thus hysteresis curve of ZnOY5 at RT does not reach its saturation value compared to other two doped samples due to the presence of PM phase. Note that, in all the cases the number of BMPs at RT are of the order of ~10^{13}-10^{14} but as the temperature decreases the number of BMPs increases up to ~10^{17}-10^{18}. Thus at higher temperature the Y^{3+} ions are distributed as a part of uncoupled spin or isolated BMPs which results fraction of BMPs can overlap and leads to FM phase mixed with PM phase. As temperature decreases further, the polaron concentration increases and their overlapping produces larger FM contribution and prominent hysteresis loop with enhanced magnetization, coercivity and remanence in some cases. On the other hand, paramagnetic contribution also increases with decrease of temperature which in turn results the robust increase of net magnetization at lower temperature as well as non-saturation of hysteresis loop. For a given sample M_0 is found to increase which is due to interaction between BMPs and the paramagnetic matrix. The possible reason for low value of m_{eff} at lower temperature may be due to the reduced size of the BMPs [58]. The origin of such reduced BMP size can be due to the presence of competing magnetic interaction [59]. The distribution of Y^{3+} ions in ZnO host matrix can be divided into three parts (i) AFM coupled Y^{3+} ions with at least one neighboring Y^{3+} ions, (ii) isolated Y^{3+} ions, which behave paramagnetically and contribute to magnetization at low temperature and (iii) the Y^{3+} ions within BMPs which couple ferromagnetically via the donor electrons associated with defects. Variation in Y concentration in ZnO leads to a change in the nature of magnetic coupling resulting in a change of its magnetic state. In ZnOY7, the average distance between the neighboring Y atoms is reduces due to the increased concentration of Y^{3+} ions (7 at %), which will favor direct exchange interaction. The exchange coupling between Y-Y adjacent neighbors in ZnO is expected to be antiferromagnetic due to overlapping of Y d-states with the valence band. Thus increase of Y^{3+} ions concentration above 5% results the increase of first contribution i.e. antiferromagnetic exchange between two neighboring Y^{3+} ions which results decrease of magnetization of ZnOY7 compared to that of the others.

3.6. Dielectric measurement

The effect of sintering temperature and applied alternating electric field on the real part of dielectric constant (ε') and loss tangent (tanδ) of the samples have been studied. Here the value of the real part of dielectric constant (ε') and loss tangent (tanδ) has been determined to understand the effect of electrostatic energy storing ability and energy dissipation, respectively by the material in presence of applied alternating electric field. Dielectric constant (ε') or relative permeability of the sample has been calculated by using the formula

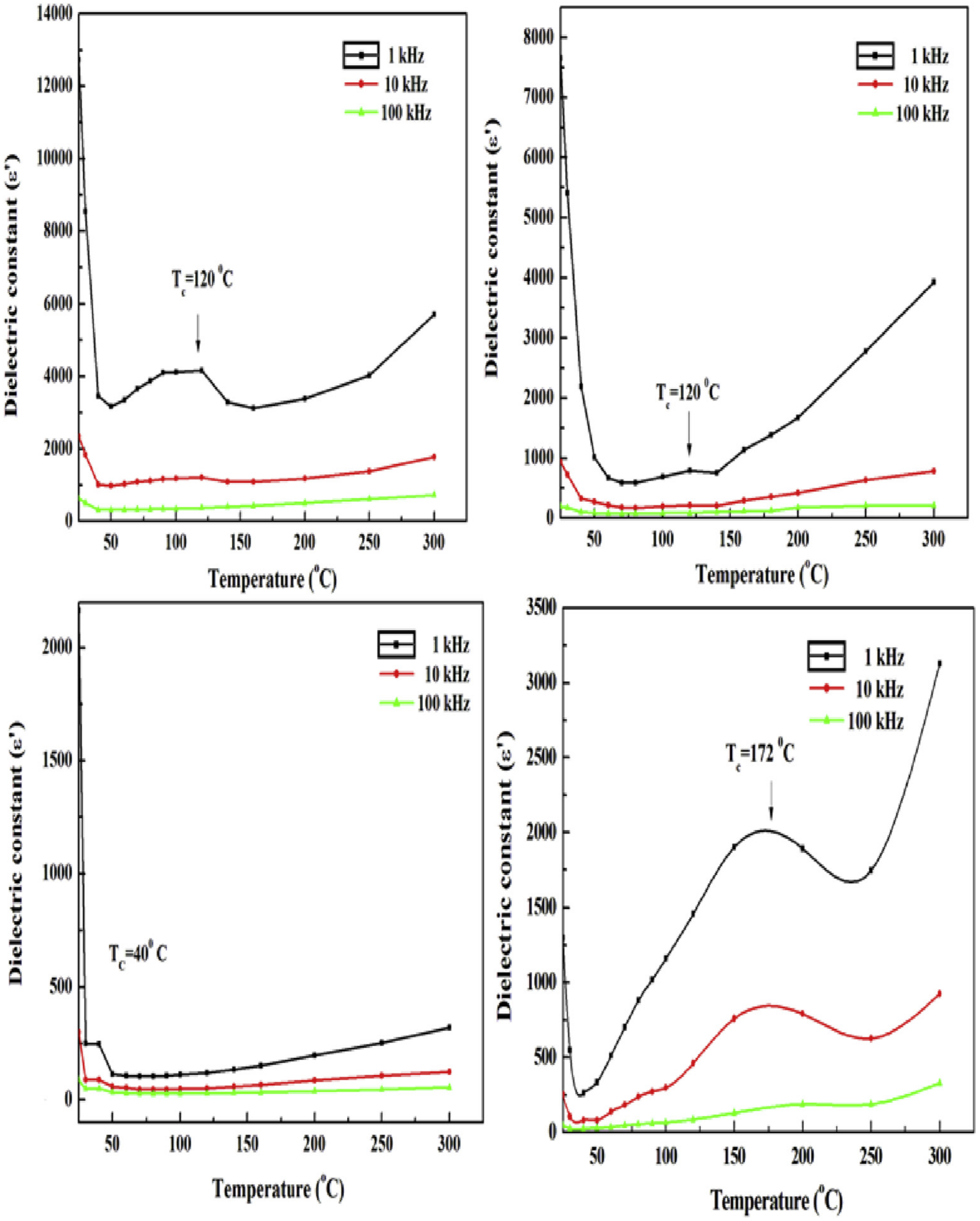

Fig. 9. Variation of dielectric constant with temperature for the samples (a) ZnO, (b) ZnOY3, (c) ZnOY5 and (d) ZnOY7.

$$\varepsilon' = \frac{Cd}{\varepsilon_0 A} \tag{11}$$

Where, C is the capacitance of the sample, d and A are thickness and area, respectively of the pellet and ε_0 is the free space permittivity. Fig. 7 shows the variation of real part of dielectric constant (ε') as a function of frequency for undoped ZnO and Y^{3+} ions doped ZnO nanoparticles, ranging from 40 Hz to 0.1 MHz at different temperatures. The observed large value of the real part of dielectric constant (ε') can be explained on the basis of electron hopping between Zn^{2+} and Y^{3+} ions in the nanostructures of Y^{3+} ions doped ZnO, which act as permanent electric dipoles under the presence of the applied alternating electric field. The observed frequency dependent dielectric behavior can also be explained by Maxwell-Wagner type of relaxation. Some microscopic phenomenon like electronic, ionic, dipolar and space charge polarization etc. significantly contribute towards the dielectric behavior of nanostructured materials. High value of dielectric constant at low frequency region may also appear due to the contribution from the space charge polarization. All these different types of polarization in the Y^{3+} ions doped ZnO nanoparticles can be obtained due to the fact that the predominance of the different defects such as grain boundary defects, oxygen vacancies etc. It is also observed that the value of real part of dielectric constant (ε') decreased with increase in frequency. The trend of this decrement is rapid at low frequency and then reaches at a constant value at higher frequency [60,61]. The polarization decreases with the increase in frequency, approaching to frequency independent behavior which is due to the fact that beyond a certain frequency of external field the hopping of the electrons between different metal ions (Zn^{2+}, Y^{3+}) can not follow the alternating field and hence lagging behind the applied electric field. The variation of dielectric loss (tanδ) versus frequency of the applied electric field in the range from 40 Hz to

10 MHz (maximum) with temperature as the function is shown in Fig. 8. The dielectric loss (tanδ) represents the energy dissipation in the dielectric system. It can be observed that initially dielectric loss (tanδ) increases with the increase of the frequency, showing relatively higher value and afterwards it decreases with the increase of frequency for the undoped ZnO and Y^{3+} ions doped ZnO nanoparticles which might be due to the presence of space charge polarization in the sample. On the other hand, the high value of loss has been obtained for undoped ZnO sample compared to the 3 and 5% Y^{3+} ions doped ZnO nanoparticles and it increases again for 7% Y^{3+} ions doped ZnO nanoparticles. Therefore, it can be concluded that the Y^{3+} ions doped ZnO nanostructure can be applied for the high frequency device applications. Fig. 9 shows the temperature variation in the range of 30–350 °C of the real part of dielectric constant (ε') for the undoped ZnO and Y^{3+} ions doped ZnO nanoparticles. The measurement has been taken for three different frequencies i.e., 1 kHz, 10 kHz and 100 kHz, respectively. In all the cases the curve shows ferroelectric to paraelectric transition but the transition temperatures are different for different samples [62]. It is noted that the maximum value of the real part of dielectric constant is quite high. This high value of the real part of dielectric constant (ε') may be attributed to the presence of the interfacial polarization inside the samples. This doped ZnO nanoparticles with high dielectric property would be suitable for application in devices.

4. Conclusions

Y^{3+} ions doped ZnO nanorods have been successfully synthesized using co-precipitation process followed by hydrothermal method. For the first time the correlation between the Y^{3+} ions doped induced intrinsic defects in the Y^{3+} ions doped ZnO nanorods and their structural, optical, magnetic and dielectric properties were studied in details. It was found that the doping of Y^{3+} ions results in the increase of many different intrinsic defects which also affects the corresponding structural, optical, magnetic and dielectric properties of the ZnO nanorods. The XRD spectra show that crystallization is suppressed by the doping of Y^{3+} ions in the ZnO nanorods. The increase of visible emission in room temperature PL spectra and E_1 (LO) intensity in Raman spectra demonstrates that the doping of Y^{3+} ions will increase the doping-induced intrinsic defects in the ZnO nanorods. Magnetization curve measurements show the room temperature ferromagnetism in the doped ZnO nanorods and the maximum of coercivity was obtained with 5% Y^{3+} ions doped ZnO nanorods. The dielectric data of the nanorods shows that the samples are very much suitable for the high frequency device applications. Finally, the combination of the optical, magnetic and dielectric measurement results reveals that the oxygen defects play a crucial role in all properties and it introduces ferromagnetism at RT which can be enhanced by the critical doping percentage of Y^{3+} ions in the ZnO nanorods.

Acknowledgments

We gratefully acknowledge Dr. Achintya Singha of Bose Institute, Kolkata for Raman spectroscopy measurement.

References

[1] Z.L. Wang, J. Phys. Condens. Mater. 16 (2004) 829.
[2] N. Tahir, A. Karim, K.A. Persson, S.T. Hussain, A.G. Cruz, Md. Usman, Md. Naeem, R. Qiao, W. Yang, Y.D. Chuang, Z. Hussain, J. Phys. Chem. C 117 (2013) 8968.
[3] G. Li, H. Wang, Q. Wang, Y. Zhao, Z. Wang, J. Du, Y. Ma, Nano. Res. Lett. 10 (2015) 112.
[4] V. Gandhi, R. Ganesan, H.H.A. Syedahamed, M. Thaiyan, J. Phys. Chem. C 11 (2014) 9715.
[5] C. Wu, L. Shen, Y.C. Zhang, Q. Huang, Mater. Lett. 65 (2011) 1794.
[6] L.W. Yang, X.L. Wu, T. Qiu, G.G. Siu, P.K. Chu, J. Appl. Phys. 99 (2006) 074303.
[7] K. Jayanthi, S. Chawla, A.G. Joshi, Z.H. Khan, R.K. Kotnala, J. Phys. Chem. C 114 (2010) 18429.
[8] G.M. Kumar, P. Elanchezhiyan, J. Kawakita, M. Subramanian, R. Jayavel, Cryst. Eng. Comm. 12 (2010) 1887.
[9] F.F. Comjani, U. Willer, S. Kontermann, W. Schade, Phys. Status Solidi A 210 (10) (2013) 2219.
[10] C. Xu, K. Yang, Y. Liu, L. Huang, H. Lee, J. Cho, H. Wang, J. Phys. Chem. C 112 (2008) 19236.
[11] L. Mino, D. Gianolio, F. Bardelli, C. Prestipino, E.S. Kumar, F. Bellarmine, M. Ramanjaneyulu, C. Lamberti, M.S. Ramachandra Rao, J. Phys. Condens. Matter 25 (2013) 385402.
[12] C.X. Mei, J. Yong, G.X. Yong, Z.X. Wei, Chin. Phys. B 21 (2012) 116801.
[13] Z. Zhang, K.E. Knutsen, T. Merz, A.Y. Kuznetsov, B.G. Svensson, L.J. Brillson, J. Phys. D. Appl. Phys. 45 (2012) 375301.
[14] S. Sarkar, D. Basak, RSC Adv. 4 (2014) 39095–39100.
[15] C.S. Kim, Y.B. Chung, W.K. Youn, N.M. Hwang, Aerosol Sci. Technol. 43 (2009) 120.
[16] D.K. Hwang, M.S. Oh, J.H. Lim, Y.S. Choi, S.J. Park, Appl. Phys. Lett. 91 (2007) 121113.
[17] G. Visimberga1, E.E. Yakimov, A.N. Redkin, A.N. Gruzintsev, V.T. Volkov, S. Romanov, G.A. Emelchenko, Phys. Status Solidi C 7 (2010) 1668.
[18] C.H. Chen, S.J. Chang, S.P. Chang, M.J. Li, I.C. Chen, T.J. Hsueh, C.L. Hsu, Chem. Phys. Lett. 476 (2009) 69.
[19] C.C. Lin, W.H. Lin, C.Y. Hsiao, K.M. Lin, Y.Y. Li, J. Phys. D. Appl. Phys. 41 (2008) 045301.
[20] T. Zhang, Y. Zeng, H.T. Fan, L.J. Wang, R. Wang, W.Y. Fu, H.B. Yang, J. Phys. D. Appl. Phys. 42 (2009) 045103.
[21] A. Umar, A. Al-Hajry, Y.B. Hahn, D.H. Kim, Electrochem. Acta 54 (2009) 5358.
[22] B. Pal, P.K. Giri, J. Appl. Phys. 108 (2010) 084322.
[23] J.J. Wu, S.C. Liu, M.H. Yang, Appl. Phys. Lett. 85 (2004) 6.
[24] X.W. Zhang, W.J. Fan, Y.H. Zheng, S.S. Li, J.B. Xia, Appl. Phys. Lett. 90 (2007) 253110.
[25] Z. Dai, A. Nurbawono, A. Zhang, M. Zhou, Y.P. Feng, G.W. Ho, C. Zhang, Chem. Phys. 134 (2011) 104706.
[26] P. Kaur, S.K. Pandey, S. Kumar, N.S. Negi, C.L. Chen, S.M. Rao, M.K. Wu, Appl. Nanosci. 5 (2015) 975–981.
[27] Z.Y. Chen, Z.Q. Chen, B. Zou, X.G. Zhao, Z. Tang, S.J. Wang, J. Appl. Phys. 112 (2012) 083905.
[28] J. Yun, R. Qu, Z. Zhang, J. Li, Adv. Condens, Matter Phys. 2014 (2014) 627975.
[29] R.T. Ginting, H.B. Lee, S.T. Tan, C.H. Tan, Md. H.H. Jumali, C.C. Yap, J.W. Kang, Md. Yahaya, J. Phys. Chem. C 120 (2016) 771.
[30] C.L. Pueyo, S. Dilger, M.R. Wagner, M. Gerigk, A. Hoffmann, S. Polarz, Cryst. Eng. Comm. 16 (2014) 1525.
[31] T.M. Hammad, J.K. Salem, R.G. Harrison, Nano 4 (2009) 225.
[32] I. Atriabak, A. Bueno-Lopez, A. Garcia-Garcia, J. Mol. Catal. A Chem. 300 (2009) 103.
[33] J. Yang, R. Wang, L. Yang, J. Lang, M. Wei, M. Gao, X. Liu, J. Cao, X. Li, N. Yang, J. Alloys. Compd. 509 (2011) 3606.
[34] J.H. Zheng, J.L. Song, Q. Jiang, J.S. Lian, Appl. Surf. Sci. 258 (2012) 6735.
[35] S.K. Sharma, D.Y. Kim, J. Mater. Sci. Technol. 32 (2016) 12–16.
[36] S. Anandan, S. Muthukumara, Opt. Mater 35 (2013) 2241.
[37] C. Gua, J. Huanga, Y. Wua, M. Zhaia, Y. Sunc, J. Liub, J. Alloys. Compd. 509 (2011) 4499.
[38] X. Wei, B. Man, J. Appl. Phys. 45 (2006) 8586.
[39] P.P. Murmu, J. Kennedy, B.J. Ruck, G.V.M. Williams, A. Markwitz, S. Rubanov, in: AIP Conf. Proc 1525, 2013, pp. 300–304.
[40] J. Kennedy, P.P. Murmu, E. Manikandan, S.Y. Lee, J. Alloys. Compd. 616 (2014) 614.
[41] P.P. Murmu, J. Kennedy, B.J. Ruck, S. Rubanov, Electron. Mater. Lett. 11 (2015) 998.
[42] J. Kennedy, B. Sundrakannan, R.S. Katiyar, A. Markwitz, Z. Li, W. Gao, Curr. Appl. Phys. 8 (2008) 291.
[43] R.P. Wang, G. Xu, P. Jin, Phys. Rev. B 69 (2004) 113303.
[44] J.B. Wang, H.M. Zhong, Z.F. Li, W. Lu, J. Appl. Phys. 97 (2005) 086105.
[45] J.D. Ye, S.L. Gu, S.M. Liu, Y. Shi, Q. Chen, Appl. Phys. Lett. 88 (2006) 101905.
[46] J. Kennedy, G.V.M. Williams, P.P. Murmu, B.J. Ruck, Phys. Rev. B 88 (2013) 214423.
[47] P.P. Murmu, J. Kennedy, G.V.M. Williams, B.J. Ruck, S. Granville, S.V. Chong, Appl. Phys. Lett. 101 (2012) 082408.
[48] S.H. Liu, H.S. Hsu, C.R. Lin, C.S. Lue, J.C. Huang, Appl. Phys. Lett. 90 (2007) 222505.
[49] J. Qi, D. Gao, J. Liu, W. Yang, Q. Wang, J. Zhou, Y. Yang, J. Liu, Appl. Phys. A 100 (2010) 79.
[50] A. Dakhel, M. El-Hilo, J. Appl. Phys. 107 (2010) 123905.
[51] J. Anghel, A. Thurber, D.A. Tenne, C.B. Hanna, A. Punnoose, J. Appl. Phys. 107 (2010) 314.
[52] T. Dietl, Nat. Mater 9 (2010) 965.
[53] A.F. Kohan, G. Ceder, D. Morgan, Phys. Rev. B 61 (2000) 15019.

[54] H. Shi, P. Zhang, S.S. Li, J.B. Xia, J. Appl. Phys. 106 (2009) 023910.
[55] J.M.D. Coey, M. Venkatesan, C.B. Fitzgerald, Nat. Mater 4 (2005) 173.
[56] A. Bandyopadhyay, S. Sutradhar, B.J. Sarkar, A.K. Deb, P.K. Chakrabarti, Appl. Phys. Lett. 100 (2012) 25241.
[57] A. Bandyopadhyay, A.K. Deb, S. Kobayashi, K. Yoshimura, P.K. Chakrabarti, 611 (2014) 324.
[58] S. Mohanty, S. Ravi, Solid State Commun. 150 (2010) 1570.
[59] T. Bora, B. Samantaray, S. Mohanty, IEEE Trans. Mag. 47 (2011) 3991.
[60] S. Bhattacharya, S.K. Saha, D. Chakravorty, Appl. Phys. Lett. 76 (2000) 3896.
[61] M.K. Gupta, N. Sinha, B. Kumar, J. Appl. Phys. 112 (2012) 014303.
[62] M.K. Gupta, B. Kumar, J. Alloys. Compd. 509 (2011) L208.

Hydrothermal process assists undoped and Cr-doped semiconducting ZnO nanorods: Frontier of dielectric property

Tanumoy Debnath, Papiya Saha, Nesla Patra, Sukhen Das, and Soumyaditya Sutradhar

Citation: Journal of Applied Physics **123**, 194101 (2018); doi: 10.1063/1.5017792
View online: https://doi.org/10.1063/1.5017792
View Table of Contents: http://aip.scitation.org/toc/jap/123/19
Published by the American Institute of Physics

JOURNAL OF APPLIED PHYSICS **123**, 194101 (2018)

Hydrothermal process assists undoped and Cr-doped semiconducting ZnO nanorods: Frontier of dielectric property

Tanumoy Debnath,[1,2] Papiya Saha,[1,2] Nesla Patra,[1] Sukhen Das,[2] and Soumyaditya Sutradhar[1,a)]
[1]*Department of Physics, Amity University, Rajarhat, Kolkata 700156, India*
[2]*Department of Physics, Jadavpur University, Jadavpur, Kolkata 700032, India*

(Received 30 November 2017; accepted 1 May 2018; published online 18 May 2018)

The influence of the hydrothermal synthesis route on the grain morphology and thereby the modulation of dielectric response of undoped and Cr^{3+} ion doped semiconducting ZnO nanoparticles is investigated in this report. The X-ray diffraction study reveals that all the samples are in a polycrystalline single phase of a hexagonal wurtzite structure of ZnO. The field emission scanning electron microscopy study reveals the rod like structure of all the samples. The formation of synthesis route dependent morphology and the morphology dependent physical property of all the samples are the characteristic features of the present work and to date it has not been considered as the specific tool of dielectric property modulation by anyone else. The ultraviolet-visible measurement signifies the superior control over the charge density of the host semiconducting material due to the presence of Cr^{3+} ions in the structure of ZnO. In the photoluminescence measurement, no significant peak has been observed in the visible region. The frequency and temperature dependent dielectric constants of all the samples were investigated. The consequences of the dielectric measurement suggest that the hydrothermal synthesis route influences the growth mechanism of the semiconducting nanoparticles mostly towards the rod like structure and the doping element influences the charge density, nature of defects, and the defect densities inside the structure of ZnO nanomaterials. All these factors together make the semiconducting ZnO nanomaterials more effective for tailor made applications in magneto-dielectric devices. *Published by AIP Publishing.*
https://doi.org/10.1063/1.5017792

I. INTRODUCTION

Over the last few decades, nanomaterials have gained much attention from various research groups of theoretical and experimental backgrounds as an advanced research topic since they have a small grain dimension, large grain boundary, quantum size effect, and sufficiently large surface to volume ratio in contrast to their bulk counterpart.[1–3] In the nanoscale regime, all the characteristic physical properties of nanomaterials, e.g., microstructural, mechanical, thermal, optical, magnetic, dielectric, and electrical, show modulation due to the variation of structural symmetry, grain morphology, band gap, charge density, micro strain, and numerous other intrinsic defects caused by the choice of a proper synthesis route and nature of dopants.[4–7] In recent years, many different undoped and doped semiconducting metal oxide nanomaterials such as indium oxide (In_2O_3), titanium oxide (TiO_2), silicon oxide (SiO_2), tin oxide (SnO_2), zirconium oxide (ZrO_2), zinc oxide (ZnO), etc., have been considered as the subject of comprehensive investigation for their interesting physical properties and applications in various optical, magnetic, dielectric, and magneto-electronic devices.[8–20] In this direction, zinc oxide (ZnO) with a direct band gap energy of 3.37 eV and a high excitation binding energy of 60 meV is a well known II–VI semiconductor material having n-type semiconducting behaviour.[21–23] But in the case of doped ZnO nanoparticles, both n-type and p-type behaviours are expected. However, it is necessary to mention here that the nature (n-type/p-type) of the semiconducting nanomaterials of doped ZnO or any other doped metal oxide nanomaterials depends on the selective choice of dopants.[24,25] ZnO has also attracted considerable interest of the research community due to its fundamental and technological importance. Although ZnO nanoparticles have been considered the prime topic of experimental research over the past few decades, the enhanced interest is now given on the undoped and doped ZnO nanostructures with a very low-dimension. In this regard, nanospheres, nanowires, nanoflowers, nanobolt, nanorods, nanotubes, etc., are the most interesting nanostructures due to their brand new elementary physical properties and many fascinating applications in future devices.[26–30] Also, in many articles, it has been reported that different physical and chemical properties of ZnO nanomaterials can be modulated by the choice of a proper doping mechanism and dopants.[31–33] Selective dopants, based on their atomic radius and charge valence state, can produce immense impact on the growth mechanism of the nanomaterial as well as the formation of native defects inside the nanostructures. In our previous publications, we have shown that dopants with a 3+ valence state can produce different types of vacancies in the form of zinc vacancies and oxygen vacancies.[5,12] These native defects in the form of vacancies can produce the effect of quantum confinement by reducing the average size of the ZnO nanomaterials. This

---

[a)] Author to whom correspondence should be addressed: sds.phy1@gmail.com quantum confinement is responsible for the change of the band gap of the nanomaterials towards a high frequency region commonly known as a blue shift.[34,35] Many articles also report that the presence of oxygen vacancies can produce room temperature ferromagnetism in the doped ZnO nanomaterials.[36] Also, the dielectric property of the ZnO nanomaterial can be immensely influenced due to the presence of native defects in the form of grain size modulation, grain boundary modulation, zinc vacancies, zinc interstitials, dandling bond, oxygen vacancies, etc., by the effect of a proper choice of dopants and doping engineering, which is the main theme of this work. Moreover, the undoped and doped semiconducting ZnO nanomaterials have numerous other exciting physical and chemical properties such as a high degree of transparency, high electron mobility, superior optical emission, and excellent chemical stability. All these can be achieved by the proper selection of the synthesis technique among the conventional techniques such as the co-precipitation method, sol-gel method, hydrothermal method, solvothermal method, solid state reaction method, mechanical milling method, pulsed laser deposition method, etc., formulated over the years.[37–40] These nanostructured undoped or doped semiconducting ZnO nanomaterials, prepared by the above-mentioned chemical/physical synthesis routes, are very much suitable for ultraviolet and photovoltaic device applications such as light-emitting diodes, nanolasers, photodetectors, field emitters, chemical sensors, and photoelectrodes in dye-sensitized solar cells, supercapacitors, etc.[41–49] Along with the choice of the synthesis technique, the superior control over the various physical properties such as charge densities, dielectric constant, conductivity, etc., can be made by the choice of suitable doping elements. Both these factors, e.g., selection of the synthesis technique and choice of dopants, play the key roles in the modulation of some specific physical properties and tailor made applications can be obtained from these semiconducting nanomaterials. By the careful selection of transition metal ions (Co^{2+}, Cu^{2+}, Ni^{2+}, Mn^{2+}, etc.) and/or rare earth ions (Gd^{3+}, Er^{3+}, Eu^{3+}, Tb^{3+}, Yb^{3+}, Sm^{3+}, etc.), further modulation of the physical properties of zinc oxide in the desired direction is expected.[50–53]

In the present work, among all other synthesis techniques, the hydrothermal preparation technique has been selected for the synthesis of undoped and Cr^{3+} ion doped semiconducting ZnO nanoparticles. In this synthesis process, the morphology of the nanoparticles can be made cylindrical or rod like and this fact has already been proved and also mentioned but insignificantly in various articles published by the various research groups.[54–58] In addition, the proper choices of temperature, pressure, time, and the pH value of hydrothermal synthesis are the key factors for the development of the desired and detectable rod like structure of undoped and Cr^{3+} ion doped semiconducting ZnO nanoparticles. These cylindrical or rod like microstructures are very much essential and they also play the key role in the modulation of some specific physical properties, one of which is the goal of our present work. The targeted modulation of the dielectric properties of the undoped and Cr^{3+} ion doped semiconducting ZnO nanomaterial prepared by hydrothermal synthesis route as compared to the dielectric properties investigated so far by other researchers in different synthesis routes is the endeavor of our present work. So far, no one has mentioned or focussed on the specific synthesis route dependent dielectric property of the semiconducting nanomaterials. We have done it for the first time and the explanation is given in this report. In this report, among all other elements from different groups of transition and/or rare earth elements, chromium (Cr) has been selected as the dopant for the further enhancement of the dielectric and other physical properties such as optical, magnetic, and electrical. One of the reasons for the selection of chromium is that the radius of Zn^{2+} (0.74 Å) is comparable to that of Cr^{3+} (0.63 Å) and it indicates that when Cr^{3+} ions are doped into the wurtzite lattice structure of ZnO, the Cr^{3+} ions can substitute the Zn^{2+} ions from the crystal lattice position of ZnO and this substitution creates a large amount of microstrain and various intrinsic defects inside the lattice structure of ZnO. A high value of the dielectric constant in the nanoscale regime can be obtained by the proper choice of trivalent cations as the dopant along with the other two basic factors such as semiconducting nanomaterials and the hydrothermal synthesis route. Basically, the selected trivalent cationic dopant, i.e., Cr^{3+} ions can improve the amount of free charge density inside the ZnO nanomaterials which reside at the surface of the poorly conducting grain boundaries in the presence of externally applied electric field. The comparable ionic radius of the Cr^{3+} ion with the Zn^{2+} ion makes the incorporation of the Cr^{3+} ion into the ZnO lattice very easy and induces more free electrons inside ZnO. Thus, the substitution process with the Cr^{3+} ion and thereby the production of free charge density inside ZnO will be more effective than any other usual trivalent dopants such as Gd^{3+}, Er^{3+}, Y^{3+}, Al^{3+}, and Co^{3+}. In addition, Cr^{3+} ion substitution mediated intrinsic defects have various forms, e.g., oxygen vacancy defects, zinc vacancy defects, interstitials, dandling bond, and others. Now these intrinsic defects in the lattice structure and the enhancement of the charge density of the doped semiconducting ZnO nanoparticles are developed because of the presence of both the ionic radius mismatching and 3+ vacant states of the chromium atoms, and in addition to that, the hydrothermal synthesis route is also responsible for this. The successful substitution of doped cations in the wurtzite lattice structure of Zn^{2+} induces a large number of cationic vacancies to maintain electrical neutrality in the ZnO matrix. Also, in the present study, the Cr^{3+} ion has been selected as the potential dopant for the substitution of Zn^{2+} ions from the ZnO wurtzite lattice structure because theoretical calculations indicate that Cr^{3+} ion doped ZnO should exhibit stable ferromagnetism. In addition, it has to be mentioned here that the enhancement of ferromagnetic behaviour of doped ZnO nanomaterials by two cations has been considered as the topic of recent research due to their reliable usefulness in the data storage industry and many other interesting applications.[59,60] However, in the present work, we have not considered the comprehensive optical and magnetic properties of the Cr^{3+} ion doped ZnO nanoparticles and will be considered in our research work at the later time. In the present report, we have done our study on the dielectric property of the undoped and Cr^{3+} ion doped semiconducting ZnO nanoparticles and the dielectric response of the doped samples has been enhanced largely with respect to the undoped one, and also for the undoped ZnO, the dielectric response has been improved in comparison to the other reports.

II. EXPERIMENTAL

A. Materials

The nanoparticles of $Zn_{1-x}Cr_xO$ (x = 0.03, 0.05, and 0.07) with different compositions were prepared by the first co-precipitation method and there after the co-precipitated materials were taken for the controlled nucleation process by the hydrothermal synthesis method. The detailed preparation technique was also given in our earlier reports.[5,12] Zinc acetate dehydrate $Zn(O_2CCH_3)_2·2H_2O$ (Sigma Aldrich, 99%), chromium acetate $Cr(CH_3COO)_3$ (Sigma Aldrich, 99%), and ammonium hydroxide NH_4OH (concentration ∼25%) were used as the precursor materials with analytical grade and without any further purification.

B. Synthesis of Cr^{3+} ion doped ZnO nanoparticles by the co-precipitation method

Nanoparticles of Cr^{3+} ion doped ZnO nanoseeds were prepared by using a simple co-precipitation method. Zinc acetate dihydrate $Zn(CH_3COO)_2·2H_2O$ and chromium acetate $Cr(CH_3COO)_3$ were the precursor materials taken in a beaker with triple distilled water. The beaker was then placed over a magnetic stirrer. The stoichiometry of chromium salt that has been taken in the aqueous solution was set at three different concentrations such as 3%, 5%, and 7% to that of the zinc salt. The mixed solution was then stirred for several hours to get a homogeneous solution of the precursor salts. Thereafter, NH_4OH solution was added into the precursor solution for co-precipitation and the final pH of the solution was kept at ∼10. A rigorous stirring process was continued during the whole course of the sample preparation under a co-precipitation method. After that, the newly prepared colloidal solution of $Zn(OH)_2$ for undoped ZnO and the colloidal mixture of $Zn(OH)_2$ and $Cr(OH)_3$ for Cr^{3+} ion doped ZnO were collected properly for washing. The whole course of washing of the co-precipitated particles has been done several times by using triple distilled water and ethyl alcohol to neutralize the pH as well as to remove the extra ions. A thorough washing process brings up the pH of the as-prepared particles back to ∼6.

C. Nucleation of Cr^{3+} ion doped ZnO nanoparticles by a hydrothermal process

After the completion of the washing process, the newly prepared colloidal solution of $Zn(OH)_2$ for undoped ZnO and the colloidal solution of $Zn(OH)_2$ and $Cr(OH)_3$ for Cr^{3+} doped ZnO were dissolved in the mixture of triple distilled water to form a 40 ml solution. The excess ammonia was added into the aqueous solution to enhance the pH value of the solution and it was then taken into a Teflon jacket. The Teflon jacket has been taken in an autoclave, and the autoclave was placed in an oven at 160 °C for 48 h. The hydrothermal technique initiates the nucleation process of the undoped and Cr^{3+} ion doped ZnO nanoseeds towards the rod like structure inside the Teflon jacket which was executed under the effect of high pressure and temperature resulting from thermal expansion of air initially present in the Teflon jacket. This ambience inside the Teflon jacket favours the surface as well as interfacial growth of undoped and Cr^{3+} ion doped ZnO nanoseeds into rod like structures. After 48 h, the autoclave was permitted to cool down naturally to RT. The supernatant was then removed, and the solid precipitates at the bottom of the Teflon jacket were collected and washed several times with triple distilled water to remove unreacted reagents from precipitation. It was then dried in a vacuum desiccator at RT. Now the dried powder was sintered at 400 °C in a vacuum atmosphere to eliminate unreacted precursor waste and to get better crystallographic phase formation. The synthesis mechanism is shown in Fig. 1, and the detailed synthesis procedure is given in Sec. III B. The sample name and the corresponding sample specifications are given in Table I.

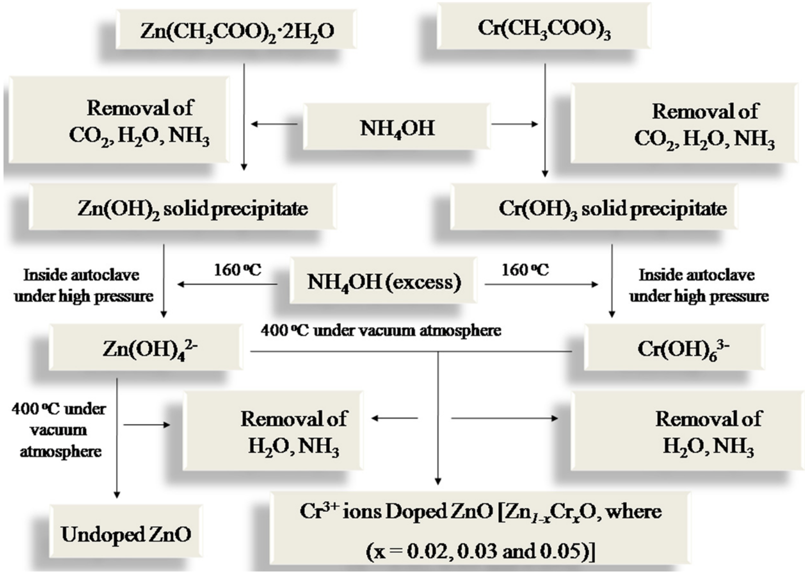

FIG. 1. Flowchart of the preparation of undoped and Cr^{3+} ion doped ZnO by the hydrothermal synthesis route.

TABLE I. The sample name and the corresponding sample specifications for undoped and Cr^{+3} ion doped ZnO samples.

Sample name	Sample specification
PZ4	Undoped ZnO sintered at 400 °C
CZ34	3% Cr^{3+} ion doped ZnO ($Zn_{0.97}Cr_{0.03}O$) sintered at 400 °C
CZ54	5% Cr^{3+} ion doped ZnO ($Zn_{0.95}Cr_{0.05}O$) sintered at 400 °C
CZ74	7% Cr^{3+} ion doped ZnO ($Zn_{0.93}Cr_{0.07}O$) sintered at 400 °C

D. Characterization techniques

The XRD pattern of all the samples was recorded in a powder X-ray diffractometer, Model D8, BRUKER AXS, using Cu K_α radiation ($\lambda = 1.5405$ Å) in the range of 2θ from 20° to 80°. A field emission scanning electron microscope (FESEM) was employed for the morphological study using an INSPECT F50 (FEI, Netherland). The optical absorption (UV-visible) spectrum of the synthesized nanoparticles was taken in the range of 240–350 nm using a l25 spectrophotometer, Perkin Elmer, Germany. The photoluminescence (PL) spectroscopy was also carried out using a spectroflurometer, Perkin Elmer, Germany, with an excitation wavelength (λ_{ex}) of 300 nm. The electrical conduction mechanism was investigated by dielectric measurements using an Agilent 4294A Precision Impedance Analyzer.

III. RESULTS AND DISCUSSION

A. XRD analysis

X-ray diffractograms of undoped ZnO (PZ4) and Cr^{3+} ion doped ZnO nanoparticles (CZ34, CZ54, and CZ74) are depicted in Fig. 2. The positions and relative intensities of diffraction peaks of undoped and Cr^{3+} ion doped ZnO nanoparticles are in good agreement with the hexagonal wurtzite structure of ZnO (space group $P6_3mc$). All the peaks have been assigned with the help of the JCPDS (file No. 36-1451). Also, no peak corresponding to any other impurity phase has been detected in the XRD patterns. This specific pattern indicates the homogeneous and successful incorporation of Cr^{3+} ions at the tetrahedral site of Zn^{2+} ions in the wurtzite structure of ZnO. The average crystallite diameters of undoped and Cr^{3+} ions doped ZnO nanoparticles were calculated from the broadening of the peak (100) of each sample by using the well known Debye-Scherrer equation

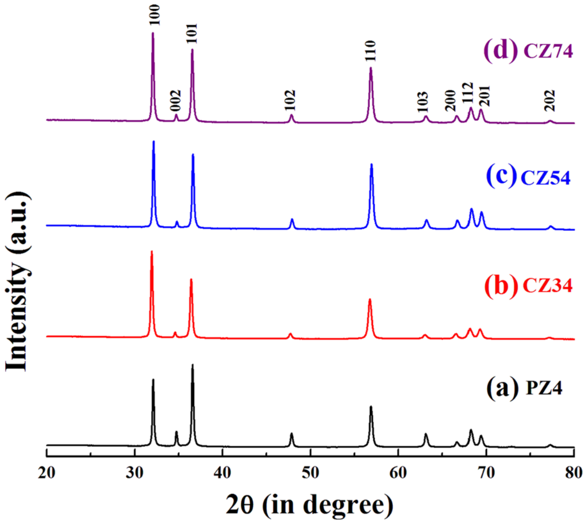

FIG. 2. XRD patterns of the samples (a) PZ4, (b) CZ34, (c) CZ54, and (d) CZ74.

$$\langle D\rangle_{(100)} = \frac{0.9\lambda}{\beta_{\frac{1}{2}}\cos\theta}. \tag{1}$$

Here, D is the crystallite diameter, λ is the wavelength of the incident X-ray beam, θ is the corresponding Braggs angle, and $\beta_{\frac{1}{2}}$ is the full width at half maximum (FWHM) of the (100) peak. The crystallite diameters (D) for different samples were found within the range of 34–40 nm. The different values of interplaner spacing (d) were calculated from the following Bragg's equation:

$$2d\sin\theta = n\lambda, \tag{2}$$

where "n" is the order of diffraction, "λ" is the wavelength of the X-rays, and "θ" is the angle of diffraction. The lattice parameter of hexagonal undoped and Cr^{3+} ion doped ZnO was calculated from the relation

$$\frac{1}{d^2} = \frac{4}{3}\frac{h^2 + hk + k^2}{a^2} + \frac{l^2}{c^2}. \tag{3}$$

Here, "a" and "c" are the lattice parameters and h, k, and l are the Miller indices, respectively, and d is the interplanar spacing of the specific plane (hkl). The crystallite diameters and the corresponding lattice parameters of PZ4, CZ34, CZ54, and CZ74 nanoparticles are given in Table II and it was found that both got reduced with the increasing doping percentage of Cr^{3+} ions in the wurtzite structure of ZnO. Also, the intensity of the peak along the (002) crystalline plane of the Cr^{3+} ion doped ZnO nanoparticles decreases and the intensity of the peak along the (100) crystalline plane increases with respect to the undoped ZnO nanoparticles. This change in the crystalline plane indicates the preferred growth of the doped ZnO nanoparticles along the (100) plane, and this change also indicates the successful incorporation of Cr^{3+} ions inside the structure of ZnO nanomaterials.

The observed change in the crystallite diameter and lattice parameter occurs due to the presence of a distortional effect in the host ZnO lattice by the incorporation of the Cr^{3+} ions. Actually, with the increasing doping percentage of Cr^{3+} ions in the wurtzite ZnO, more and more zinc vacancies would create inside the structure of ZnO to maintain charge equality. This induced cationic vacancies/zinc vacancies created by Cr^{3+} ion doping in the ZnO matrix (up to 7%) are responsible for the decrease in the crystallite diameter. It is well known that during doping three Zn^{2+} ions are substituted by the two Cr^{3+} ions and due to that the effective diameter of the nanocrystallite gets reduced with respect to undoped ZnO. For higher doping percentages of Cr^{3+} ions in the host lattice, the average nanocrystalline diameters decrease gradually. This is a clear evidence of having Cr^{3+} ions in the host lattice of ZnO. Moreover, the XRD measurement shows that no unwanted phase of Cr_2O_3 has been found

TABLE II. Structural parameters calculated from XRD data are the crystallite diameter (D), lattice parameters (a and c), micro strain (ε), unit cell volume (V), bond length (L), and dislocation density (δ).

		Lattice parameter (Å)		Micro strain (10^{-4})			
Sample	Average crystallite diameter D (nm) (100)	a	c	ε	Unit cell volume V $(\text{Å})^3$	Zn-O bond length (Å)	Dislocation density $(\text{Å})^{-2}$ δ (10^{-6})
PZ4	39.62	3.24	5.18	8.787	47.09	1.9583	6.371
CZ34	36.47	3.23	5.17	9.581	46.71	1.9666	7.518
CZ54	35.83	3.21	5.15	9.671	45.95	1.9554	7.789
CZ74	34.73	3.20	5.13	10.022	45.49	1.9597	8.291

in any of the given three doped ZnO nanomaterials, not even with 3%, 5%, and 7% Cr^{3+} ion doped ZnO samples. Thus, the overall XRD information of undoped and doped ZnO indicates that Cr^{3+} ions are present inside the lattice structure of ZnO by replacing some of the Zn^{2+} ions from their lattice position and without the formation of any oxide phase related to chromium. In addition, the radius of the Cr^{3+} ion (0.63 Å) is different from that of the Zn^{2+} ion (0.74 Å), and this difference in the dimension of the ionic radius induces internal lattice strain inside the lattice structure of Cr^{3+} ion doped ZnO nanomaterials. The corresponding values of internal lattice strain/micro strain (ϵ) of the Cr^{3+} ion doped ZnO nanoparticles are more when compared to those of the undoped ZnO nanoparticles and they increase gradually with the increasing doping percentages of Cr^{3+} ions in the structure of ZnO. The values of internal lattice strain/microstrain (ϵ) for all the samples are given in Table II using the formula

$$\text{Microstrain}\,(\epsilon) = \frac{\beta_{\frac{1}{2}}\cos\theta}{4}. \tag{4}$$

The volume of the unit cell for the hexagonal system has been calculated from the following equation:

$$\mathrm{V} = 0.866 \times \mathrm{a}^2 \times \mathrm{c}. \tag{5}$$

The decreasing value of the unit cell volume (V) with the increasing doping percentage of Cr^{3+} ions also indicates the substitution of Zn^{2+} ions from the tetrahedral site of ZnO by the Cr^{3+} ions. Dislocation density (δ) is a prominent signature of the presence of various forms of defects in the Cr^{3+} ion doped ZnO samples. Dislocation density can be defined as the length of dislocation lines present per unit volume inside the crystal lattice and has been calculated using the following equation:

$$\delta = \frac{1}{D^2}. \tag{6}$$

It has been observed from the measured value of dislocation density (δ) that the magnitude of dislocation density increases with the increasing doping percentage of Cr^{3+} ions in the ZnO nanostructure. Such types of variations of dislocation density indicate that the magnitude of defects increases with the increasing doping percentage of Cr^{3+} ions in the ZnO nanostructure.

The Zn-O bond length has been calculated using the relationship

$$\mathrm{L} = \sqrt{\frac{a^2}{3} + \left(\frac{1}{2} - u\right)^2 c^2}, \tag{7}$$

where u is the positional parameter for the wurtzite structure and it can be calculated from the following equation:

$$\mathrm{u} = \frac{a^2}{3c^2} + 0.25. \tag{8}$$

It has been observed that the bond length increases gradually with the increase in the Cr^{3+} ion content in the ZnO nanostructure. This occurs due to the fact that once Zn^{2+} ions are replaced by the Cr^{3+} ions, the Cr-O bonds are also created inside the ZnO lattice, whose bond length is higher than the Zn-O bond length. All the parameters extracted from the XRD analysis are clear evidence of the presence of structural irregularities/defects in doped ZnO nanomaterials and all these will help the nanomaterials to enormously modulate their different physical properties such as dielectric properties significantly.

B. FESEM analysis

The XRD analysis shows that due to the incorporation of Cr^{3+} ions into the structure of ZnO, various forms of defects have been generated and these defects inside the structure of the hexagonal rod like ZnO nanomaterials are responsible for the enhancement of the dielectric property. But, so far, the cause behind the growth mechanism of the undoped and Cr^{3+} ion doped ZnO nanomaterials into the rod like morphology from its initial nanoseed like structure has not been explained in this report. The explanation is given in Sec. III B with some representative micrographs shown in Fig. 3 and it will help us to understand the reason behind the

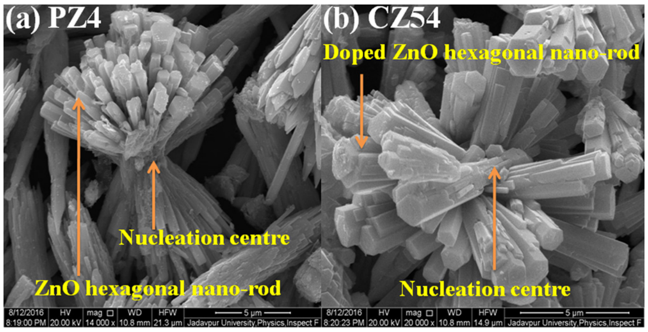

FIG. 3. SEM images of the samples (a) PZ4 and (b) CZ54.

formation of rod like morphology of undoped and Cr^{3+} ion doped ZnO nanomaterials under a hydrothermal synthesis route. It follows that the crystal growth mechanism of nanomaterials can be explained from the kinetic point of view. In this direction, it has to be assumed that the growth mechanism mainly contains the formation of growth units and the incorporation of growth units into the crystal lattice at the interface. The formation of micro/nano-structures with rod like morphologies for all the samples mostly depends on the pH value of aqueous solution. We have found that the rod like morphologies of all the samples were formed with the pH value close to 9 or 10, which is relatively very high. At this high pH and at high temperature (∼160 °C), sufficient numbers of growth units in the form of $Zn(OH)_4{}^{2-}$ and $Cr(OH)_6{}^{3-}$ would develop in the aqueous solution when the solution is subjected under the autoclave and inside the Teflon jacket. The formation of $Zn(OH)_4{}^{2-}$ and $Cr(OH)_6{}^{3-}$ inside the solution for undoped and doped ZnO samples under the hydrothermal synthesis route is shown in Fig. 1. Now, in the supersaturation solution, due to the diffusion of ions under high pressure of the autoclave, and also due to deregulation movement among molecules and ions, growth units $Zn(OH)_4{}^{2-}$ in the case of undoped ZnO and $Zn(OH)_4{}^{2-}$ and $Cr(OH)_6{}^{3-}$ in the case of undoped and doped ZnO are bounded together in the solution through a dehydration reaction and decomposed into a large size cluster of $Zn_iO_j(OH)_k{}^{(i\text{-}2j-2k)-}$ and $Cr_iO_j(OH)_k{}^{(i\text{-}2j-2k)-}$ and when the critical size of the cluster reaches the value required for the formation of ZnO powder, the cluster of $Zn_iO_j(OH)_k{}^{(i\text{-}2j-2k)-}$ is precipitated. A similar phenomenon is expected for the Cr^{3+} ion doped ZnO with selective stoichiometry. It has to be mentioned here that the subscripts *i*, *j*, and *k* represent the numbers of Zn^{2+}, Cr^{3+}, O^{2-}, and OH^- within the crystal, respectively. Thereafter, the ions are adsorbed in the primary nuclei due to the high value of surface energy and intermolecular force and the ZnO nanoseeds are grown in the form of hexagonal rodlike structures. This type of morphology may also be formed due to excessive air pressure present inside the Teflon jacket. At high pH, the solubility of NH_3 decreases and it comes out from the solution. The liberation of NH_3 from the solution produces high pressure inside the Teflon jacket. At such a high pressure, the early stage of reaction contains sufficient numbers of growth units which will be diffused and decomposed into a large size grain, and results in distinct rodlike structures. In this way, the high pH and high pressure help the undoped and doped ZnO nanoseeds to grow into the nano rodlike structures through the hydrothermal process. From Fig. 3, it is clear that the micrographs of all the samples are rodlike in nature with a hexagonal cross-section being the signature morphology of the ZnO nanomaterials prepared by the hydrothermal synthesis route. Figure 3(a) represents the micrograph of PZ4 and it shows a rodlike structure, where individual rods are very much clear and distinguishable from one another. In addition, a very important and interesting observation has been found in the FESEM analysis. It has been found that the clustering effect occurs within the very small size nanostructure, and finally, they grow into large size microstructures. Figure 3(b) shows the micrograph of CZ54 where the morphology of CZ54 is also rodlike in nature and similar to that of PZ4, but the size of the microstructure of CZ54 is large as compared to PZ4. From the FESEM micrograph, it has been found that the length and cross-section of the microstructure of the doped sample (CZ54) are larger than those of the undoped sample (PZ4). The crystallite diameter of the doped samples decreases gradually with the increasing Cr^{3+} doping percentages as compared to the PZ4, but from the FESEM micrographs, it is quite clear that the microstructure of the doped samples increases gradually with the increasing Cr^{3+} doping percentages as compared to the PZ4. Actually, the surface energy of the nanoparticle increases with decreasing crystallite diameter.[47] Large surface energy comprises the large growth rate of the nanoparticles at a certain temperature. Thus, the samples of a small nanocrystallite diameter can produce large microstructures of the material and it happens especially in the process of hydrothermal synthesis where diffusion and decomposition of the growth units play an important role in the formation of the microsize grains under high pH and high pressure. Therefore, the microstructures of the doped ZnO samples increase gradually with increasing doping percentages of Cr^{3+} ions with reference to the undoped ZnO. In addition, the change in morphology and the variation of the microstructure with the increase in Cr^{3+} ion doping percentages signify the successful incorporation of the Cr^{3+} ions into the structure of ZnO nanoparticles. Interestingly, all the nanorods in different micrographs for a particular sample are nearly uniform in size and not yet agglomerated.

C. UV-visible absorption study

UV-visible absorption spectroscopy is taken to investigate the optical properties of direct band gap semiconducting materials. In addition, the band gap energy of undoped ZnO and Cr^{3+} ions doped semiconducting ZnO nanoparticles can be estimated using UV-visible absorption spectroscopy. The band gap energy of the semiconductor material changes with the crystal imperfection developing inside the material induced by the doping concentration of the foreign elements. The optical absorption spectra of undoped ZnO and Cr^{3+} ion doped semiconducting ZnO nanoparticles have been investigated in the wavelength range of 240–350 nm and are depicted in Fig. 4. Various positions of absorption edges of the doped ZnO samples show blue shift with respect to the undoped ZnO sample with the increase in Cr^{3+} ion concentration inside the semiconducting host ZnO nanoparticles. The absorbance can vary with various factors such as particle size, band gap, oxygen vacancy, surface roughness, defects in the grain structure, etc., in the semiconducting host ZnO nanoparticles. ZnO is one of the well known direct band gap semiconductors, and the optical band gap of the nanoparticles was estimated using the following Tauc plot relation:

$$\alpha \mathrm{h}\nu = \mathrm{A}(\mathrm{h}\nu - \mathrm{E_g})^{\mathrm{n}}, \tag{9}$$

where $\mathrm{h}\nu$ and $\mathrm{E_g}$ are the photon energy and the optical band gap energy, in eV, respectively. Other two terms α is the absorption coefficient ($\alpha = 2.303\mathrm{A/t}$, here A is the absorbance and t is the thickness of the cuvette) and A is a

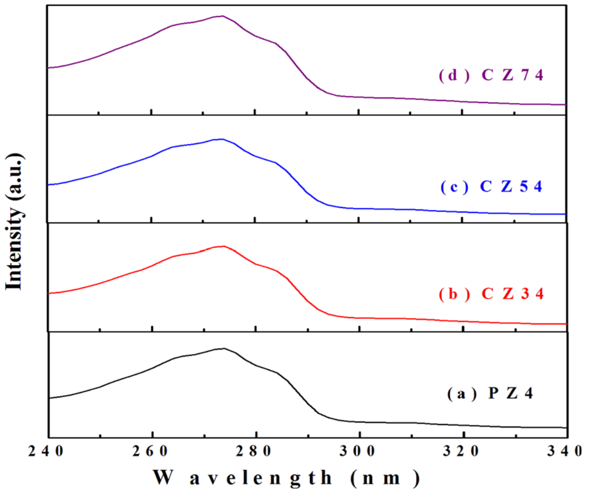

FIG. 4. UV-visible absorbance spectra of the samples (a) PZ4, (b) CZ34, (c) CZ54 and (d) CZ74.

constant, respectively. The value of n = 1/2, 3/2, 2, or 3 depends on the nature of the electronic transition responsible for absorption and n = 1/2 for the direct band gap semiconductor. In the Tauc plot, an investigation of the linear region of a plot of $(\alpha h\nu)^2$ on the abscissa vs. photon energy $(h\nu)$ on the ordinate gives the different values of the optical band gap for different samples and is given in Fig. 5. The band gap energy sharply increases from 4.32 to 4.40 eV with the increase in Cr^{3+} ion doping percentage. Similar observation was reported by Mariappan *et al.*[61] The calculated value of the band gap energy of undoped ZnO nanoparticles is relatively higher as compared to that of their bulk counterpart and it shows a clear blue shift in the absorption band edge which could be attributed to the very well known quantum size effect of direct band gap semiconductors, indicating the increase in the band gap with the decrease in the particle size.[62–64] It has been explained in Sec. III A that with the increasing doping percentage of Cr^{3+} ions in the ZnO, more and more zinc vacancies would create inside the structure of wurtzite ZnO nanoparticles. These induced cationic vacancies/zinc vacancies, created by Cr^{3+} ion doping in the ZnO nanoparticles, are responsible for the decrease in the particle size and lattice parameter and increase in the band gap energy. Along with the quantum confinement, the enhancement in band gap energy with the increase in Cr^{3+} ion doping percentage can also be explained on the basis of the Moss-Burstein effect. ZnO is a well known n-type semiconductor having donor electrons. In the Cr^{3+} ion doped ZnO nanomaterial, three Zn^{2+} ions are substituted by two Cr^{3+} ions to maintain the charge neutrality. Now, the third oxygen with two excess electrons (O^{2-}) becomes neutral just by releasing the extra electrons present within it. These extra electrons are the donor electrons and they enhance the resultant charge density of the doped semiconducting ZnO nanomaterials with the increasing percentages of Cr^{3+} ions. In addition, in Cr^{3+} ion doped semiconducting ZnO nanoparticles, the donor electrons generally occupy the state at the bottom of the conduction band. According to the Pauli principle, those electrons are restricted to get a doubly occupied state. Due to the vertical nature of optical transition, these valence electrons need extra energy to be excited into the higher energy state in the conduction band and that causes broadening of the energy band gap. When Cr^{3+} ions are

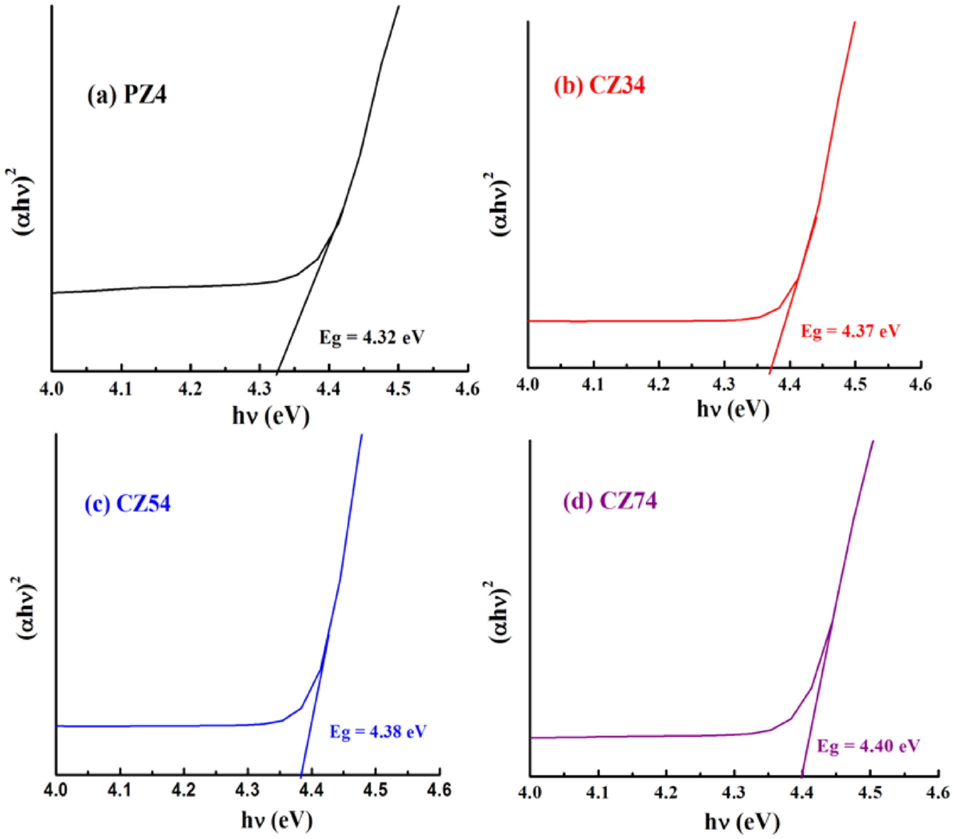

FIG. 5. Plot of $(\alpha h\upsilon)^2$ vs $(h\upsilon)$ of the samples (a) PZ4, (b) CZ34, (c) CZ54 and (d) CZ74.

implanted into the ZnO wurtzite structure by replacing Zn^{2+} ions, free charge carriers are released within the ZnO structure. Therefore, the top most electronic state level of the valence band becomes vacant and the Fermi level shifted inside the conduction band filling up all the electronic state level just below it. Absorption transition then occurs in between the top of the valence band and the Fermi level inside the conduction band. Therefore, this upward shift of the absorption band edge toward the high photon energy is the main reason for the significant increase in the bang gap energy for Cr^{3+} ion doped ZnO nanoparticles. The above observation indicates that the increase in the band gap occurs due to both decreases in the particle size known as quantum confinement and the increase in free charge carrier or donor electrons inside the grain structure known as the Moss-Burstein effect. The quantum confinement makes the optical property insignificant, but the Moss-Burstein effect increases charge density which in turn increases the dielectric constant of the host semiconducting ZnO nanomaterials.

D. Photoluminescence study

Room temperature photoluminescence (PL) spectra of all the undoped and Cr^{3+} ion doped ZnO nanomaterials have been observed, and the PL spectrum is shown in Fig. 6. The proper selection of the preparation technique, stoichiometry, choice of dopant, and post sintering process are all very sensitive for the outcome of PL measurements. The surface morphologies and microstructural defects for the undoped and Cr^{3+} ion doped ZnO samples in the nanoscale range are mostly controlled by the above-mentioned factors, and the corresponding PL intensity is directly correlated with surface morphologies and various forms of defects created in or around the nanomaterials. The PL study of undoped and Cr^{3+} ion doped ZnO nanoparticles was carried out with an excitation wavelength of 290 nm. The PL spectra of undoped and Cr^{3+} ion doped ZnO nanoparticles show a prominent UV emission at 326 and 336 nm. In the ultraviolet region, the emissions of both undoped and doped ZnO nanomaterials were found almost at the same position and these peaks appeared due to the recombination of free excitons through the exciton-exciton collision process and are generally assigned to a near-band-edge (NBE) emission band. In the visible region, violet emission at 396 nm is attributed due to the electronic transition from the zinc interstitial level (I_{Zn}) to the top of the valence band and this peak has been found for all the undoped and Cr^{3+} ion doped ZnO samples. A clear change in the intensity of the excitonic emission peak for all the samples was detected which can be assumed due to incorporation of Cr^{3+} ions within the ZnO matrix. But in the visible region and at different positions corresponding to the blue, green, and red emissions, no prominent peaks have been observed in any of the present samples. It has been mentioned in earlier reports that UV and visible emission are competing with each other and nanocrystals with a large size and a nearly perfect crystalline structure generally show stronger UV emission. In the case of the rodlike nanostructure prepared by the hydrothermal process, it has been found that the intensity ratio of the UV emission to visible emission is very high, whereas a weak intensity ratio of the UV emission to visible emission and strong intensity ratio of the visible emission to UV emission is expected for the spherical or nearly spherical nanomaterials. It has to be mentioned here that the transfer of optical energy emission from the UV region to the visible region, as well as their intensity in the case of doped ZnO nanoparticles, depends on the number of surface defects as well as the defect centers present inside the lattice structure of Cr^{3+} ion doped ZnO nanomaterials. If there are a large number of surface defects, which is expected to be more in the case of the spherical structure and less in the case of the rodlike structure, and a large variety of defect centers are present inside ZnO samples, the electronic transition between two energy states is possible, but if the defect centers related to deep hole trapped levels above the valence band are present at the surface, the photogenerated electrons will be trapped at the surface of the Cr^{3+} ion doped ZnO nanomaterials and the visible emission gets reduced. In the present research on Cr^{3+} ion doped ZnO samples, very fewer numbers of surface defects are present due to the rodlike structure of all the samples and also fewer numbers of defect centers are present in the ZnO related to deep donor levels, deep acceptor levels, and oxygen vacancies and most of the defect centers are available related to deep hole trapped levels at the surface. So, from FESEM and PL measurements, it can be inferred that in the hydrothermal process the rodlike structures of doped ZnO nanoparticles can be obtained and this process is not very much suitable for the better modulation of the optical properties. Also, in Fig. 6, if we compare the individual PL intensities of all the samples, it can be found that the UV emission intensity decreases with the increasing percentages of Cr^{3+} ions in the ZnO and the luminescence band of Cr^{3+} ion doped ZnO nanoparticles is slightly larger than that of undoped ZnO nanoparticles, illustrating that the doping effect of Cr^{3+} ions can increase the surface defects and oxygen vacancies slightly in ZnO nanoparticles.

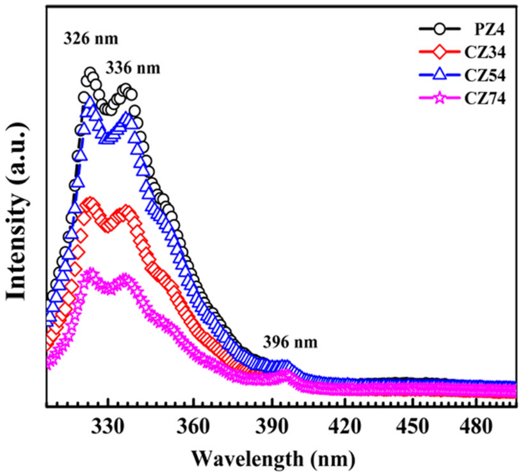

FIG. 6. Photoluminescence spectra of the samples (a) PZ4, (b) CZ34, (c) CZ54, and (d) CZ74.

E. Dielectric study

The shape and dopant dependent dielectric response of undoped and doped semiconducting ZnO nanomaterials are an important field of research for the advancement of science and technology. It can give us superior control over the dielectric property of the nanomaterials in a very simple way. So far, it has been observed in many articles that the dielectric response of the semiconducting ZnO based nanomaterials fairly depends on their grain morphologies. Basically, the shape dependent different physical properties are competing with each other. Sometimes, a particular physical property shows superiority over other physical properties when it evolves with a meticulous structure, whereas the same physical property becomes less significant or even insignificant with respect to the others when the same material appears with other structural forms. In this direction, the spherical structure prepared by different soft chemical routes such as sol-gel, co-precipitation, etc., comprises relatively low values of the dielectric constant and the rodlike structure of ZnO based nanomaterials, rather in true sense most of the semiconducting transition metal oxide nanomaterials (doped or undoped) prepared by the hydrothermal synthesis route comprises relatively high or ultrahigh values of the dielectric constant. The dielectric constant of the rodlike structure prepared by the hydrothermal synthesis route can be found within the range of 10^5 or 10^6, and the materials are called super dielectric materials (SDM). These SDMs are highly acceptable for advanced research in the field of super capacitor application, high electric breakdown strength applications, sensor applications, ferroelectric or piezoelectric applications, and many more. To date, no one has given emphasis on this study and the reason behind the shape dependent dielectric response of ZnO based nanomaterials is yet to explain. Here, in this section, we have tried to find out the possible reasons behind these high or ultrahigh values of the dielectric constant of the nanomaterials, and in this regard, we have discussed the dielectric response of undoped and Cr^{3+} ion doped ZnO nanomaterials. Also, in this section, we have discussed how the synthesis technique modulates and enhances the dielectric response of the nanomaterials. The dielectric constant is represented by

$$\varepsilon = \varepsilon' - j\,\varepsilon''. \tag{10}$$

The first term is the real part of the dielectric constant (ε'), and the second term is the imaginary part of the dielectric constant (ε''). The effect of externally applied alternating electric field and temperature on ε' and ε'' of all the samples has been measured. Here, the values of ε' and ε'' have been determined to understand the effect of electrostatic energy storing ability and energy dissipation, respectively, by the material in the presence of externally applied alternating electric field. The real part of the dielectric constant (ε') and the imaginary part of the dielectric constant (ε'') of all the samples have been calculated by using the formula

$$\varepsilon' = \frac{Cd}{\varepsilon_0 A} \tag{11}$$

and

$$\varepsilon'' = \varepsilon' \times \tan\delta, \tag{12}$$

where C is the capacitance of the sample, d and A are thickness and area of the pellet, respectively, and ε_0 is the free space permittivity. Figure 7 shows the variation of ε' as a function of frequency for undoped and Cr^{3+} ion doped ZnO nanoparticles, ranging from 40 Hz to 1 kHz at different temperatures (RT to 200 °C), and Fig. 8 represents the ε'' for undoped and Cr^{3+} ion doped ZnO nanoparticles with the 40 Hz to 10 kHz frequency range and at different temperatures (RT to 80 °C). The observed enhancement of both ε' and ε'' of the Cr^{3+} ion doped ZnO nanomaterials (CZ34, CZ54, and CZ74) with respect to the undoped ZnO

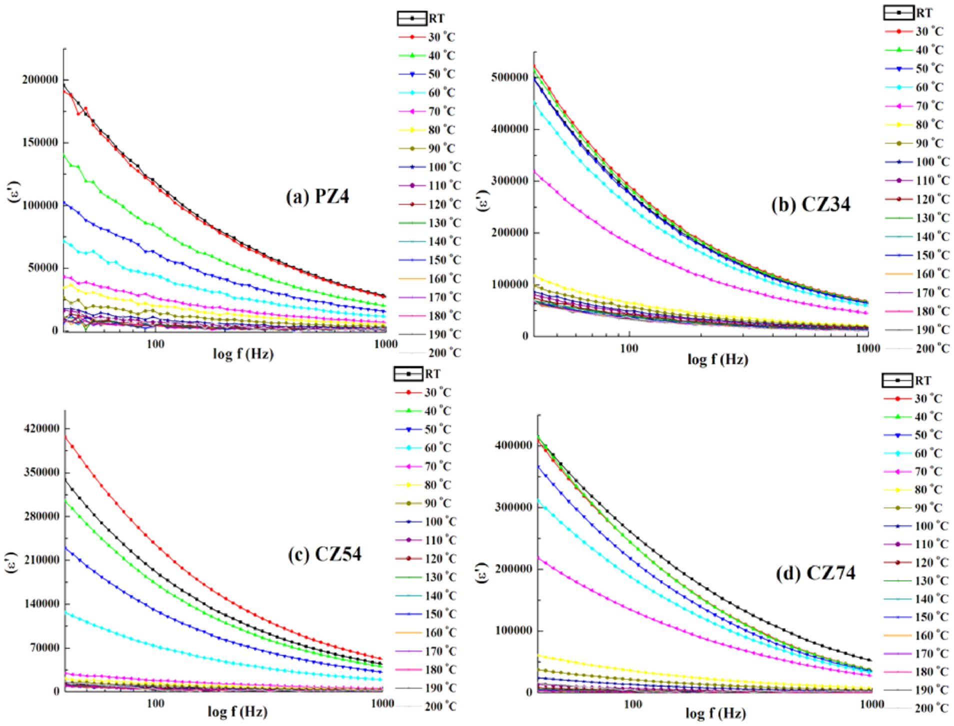

FIG. 7. Variation of real part of dielectric constant (ε') with frequency at different temperatures of the samples (a) PZ4, (b) CZ34, (c) CZ54, and (d) CZ74.

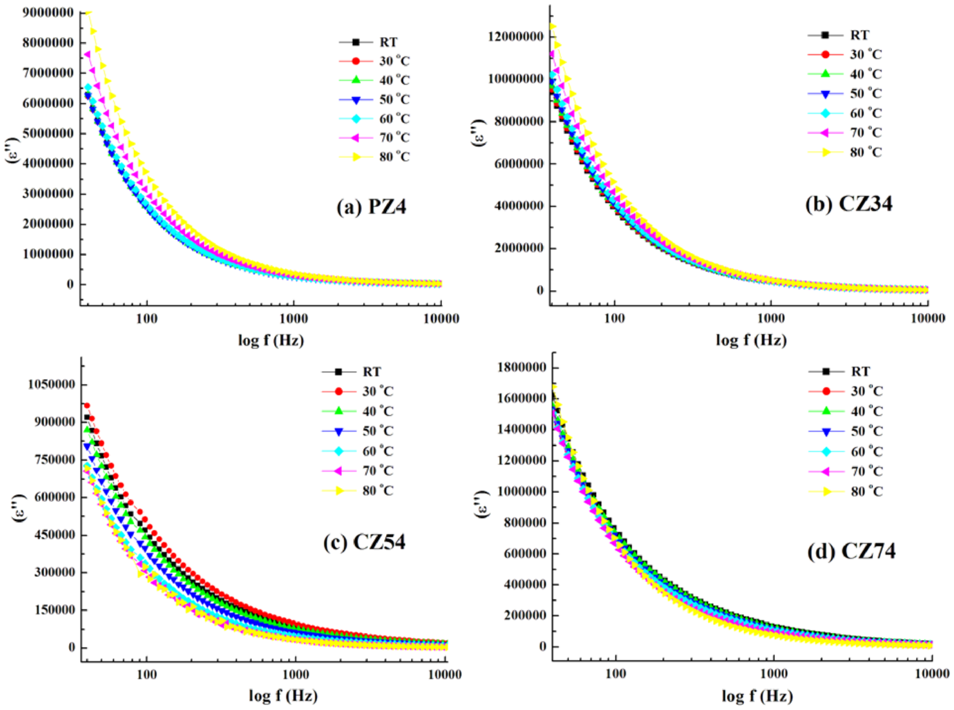

FIG. 8. Variation of imaginary part of dielectric constant (ε'') with frequency at different temperatures of the samples (a) PZ4, (b) CZ34, (c) CZ54, and (d) CZ74.

nanomaterial (PZ4) can be explained on the basis of electron hopping between Zn^{2+} and Cr^{3+} ions in the nanostructures of Cr^{3+} ion doped ZnO, which act as permanent electric dipoles under the presence of the externally applied alternating electric field. The observed frequency dependent dielectric response of the nanomaterials can be explained on the basis of Koop's theory which, on the other hand, depends on the Maxwell-Wagner-Sillars model for the nanostructures.[65–67] According to this model, a dielectric medium is expected to be made of well conducting grains and each grain is isolated from its surroundings by the poorly conducting grain boundary. Under the influence of externally applied alternating electric field, the free charge carriers (generated inside the material due to the effect of Cr^{3+} ion doping) can easily drift inside the grains but they are accumulated at the grain boundaries. These accumulation of free charge carriers at the edge of the grain boundaries process large polarizability on the materials, which in turn produces large polarization and ultrahigh dielectric constant of the materials. Some microscopic phenomena such as electronic, ionic, dipolar, and space charge polarization significantly contribute towards the dielectric response of nanomaterials. A high value of dielectric constant in a low frequency region may also appear due to the contribution that comes from the interfacial/space charge polarization in inhomogeneous nanostructures. All these different types of polarization in the Cr^{3+} ion doped ZnO nanoparticles can be obtained due to the presence of the different defects such as grain boundary defects, interstitials, vacancies, dandling bonds, etc. It is also observed that the values of both ε' and ε'' decreased with the increase in frequency of the externally applied alternating electric field. The tendency of this decrement is fast in the low frequency region, and finally, it reaches a constant value at a higher frequency.[1,68] The polarization decreases with the increase in frequency, approaching frequency independent behavior, and this type of behaviour is observed due to the fact that beyond a certain frequency range of the externally applied alternating electric field the hopping of the electrons between different metal cations (Zn^{2+}, Cr^{3+}) cannot follow the frequency and hence lagging behind the frequency. In the present work, the dielectric constants of CZ34, CZ54, and CZ74 are higher as compared to those of PZ4, but the dielectric constants of CZ54 and CZ74 decrease gradually as compared to those of CZ34. This ultrahigh value of the dielectric constant, highest ever found for Cr^{3+} ion doped ZnO nanoparticles as well as for any other nanomaterials (∼524 160 at 40 Hz), has been observed for the sample CZ34. The high dielectric constant of CZ34, CZ54, and CZ74 as compared to that of PZ4 appears due to the presence of Cr^{3+} ions in the nanostructure of ZnO as discussed earlier, along with other factors such as the large grain size, thin grain boundary, etc. The presence of Cr^{3+} ions inside the ZnO nanostructure enhances defects and by this way improves inhomogeneties in the nanostructures. In addition, the charge hopping mechanism between the metal cations becomes more effective due to the presence of Cr^{3+} ions along with Zn^{2+} ions inside the doped ZnO nanostructure. All these phenomena improve the dielectric constant of CZ34, CZ54, and CZ74 as compared to PZ4. It has been observed that ε' decreases with the increase in the Cr^{3+} ion concentration. The increase in the real part of the dielectric constant (ε') indicates the formation of more numbers of microstructures of undoped or doped ZnO grains surrounded by insulating grain boundaries, and the decrease in the real part of the dielectric constant (ε') indicates the formation of fewer numbers of microstructures with undoped or doped ZnO grains surrounded by insulating grain boundaries and also suggests the variation of interfacial states across the grain boundaries. The grain size of CZ34 is less as compared to that of CZ54 and CZ74, and it increases gradually for both CZ54 and CZ74. As it has been already mentioned that the dielectric constant is a function of the number of grains or the amount of effective grain boundaries present in the samples, the large grain structure reduces the number of grains or the amount of effective grain boundaries in the samples, and thereby it reduces the dielectric constant of the materials.[64] Since the grain size increases gradually for both CZ54 and CZ74 as compared to CZ34 (explanation given in Sec. III B), the dielectric constant for both CZ54 and CZ74 decreases gradually as compared to that of CZ34.

Here, it is necessary to mention that though the dielectric constant of a nanomaterial depends on the number of grains and the grain boundaries present inside the material, the expected presence of rodlike nanostructures inside the microstructures plays the most crucial role in the modulation of the dielectric constant of the material. The fundamental cause for this speculation regarding the dielectric constant has been discussed in this section. It has also been mentioned in the earlier discussion that the enhancement of the dielectric constants of CZ34, CZ54, and CZ74 as compared to that of PZ4 appears due to the presence of Cr^{3+} ions in the structure of ZnO (electron hopping effect) and the decrement of the dielectric constants with increasing percentages of Cr^{3+} ions in the structure of ZnO (grain size effect), but the overall enhancement of the dielectric constants by multi-fold of all the undoped and doped ZnO samples as compared to any other previous reports is yet to be explained. To date, no one has explained why the dielectric constants of rodlike undoped or doped ZnO samples are so much large with respect to any other structures reported earlier and how we could achieve this ultrahigh dielectric constant for undoped or doped ZnO samples preferable for many important device applications. In the present case, the nanostructures are accumulated inside the microstructure, and finally, they can be obtained with preferable growth along the c-axis. This type of growth of the nanostructures inside the microstructure appears due to the hydrothermal synthesis route in which nanostructures grow under high pH value and high pressure. Different synthesis routes other than the hydrothermal synthesis route can produce nanostructures with different geometrical shapes such as spherical, flack, bolt, flower, etc. All these structures are quite different from the rodlike nano- as well as microstructures developed under the hydrothermal synthesis route and may not be suitable to get the ultrahigh value of the dielectric constant. Each rodlike nanostructure acts as a nano-dipole and the cumulative effect of all the nano-dipoles inside the microstructures contribute towards the resultant dielectric constant of the material. In general, the dielectric constant depends on the cumulative effect of dipole moments for the dipoles present inside the system and the value of the dipole moment for each dipole depends on the product of the amount of total charge at the interface with the free path length. Now, for the doped ZnO sample (CZ34), larger path length and also more free charge carriers can be found inside each microstructure in comparison to the undoped ZnO sample (PZ4) and it shows a larger dielectric constant. But with the increasing percentages of Cr^{3+} ions in the ZnO structure, the dielectric constant decreases due to (i) the step-down effect of the number of grain boundaries and (ii) the step-down effect of the effective grain boundary thickness. It has to be mentioned here that the dielectric constant of the material depends on the thickness of the grain boundary. Thinner the grain boundary layer, the higher is the dielectric constant. In comparison to CZ34, both CZ54 and CZ74 contain more numbers of growth units and so that the grain boundary thickness of both CZ54 and CZ74 will be more than that of CZ34 and this will reduce the dielectric constant of the materials accordingly. In addition, the main contribution of the dielectric constant of the material is due to the presence of space charge polarization which, on the other hand, depends on the number of microstructural grains and grain boundaries. As discussed in Sec. III B that the number of microstructural grains and grain boundaries are more inside CZ34 as compared to CZ54 and CZ74, so CZ34 shows large value of dielectric constant as compared to others. Thus, the rodlike nano- as well as microstructures of the undoped and doped ZnO materials under hydrothermal synthesis route acts as the frontier of dielectric property and it is probably the most effective way to get the ultrahigh value of dielectric constant for most of the undoped and doped semiconducting transition metal oxide nanomaterials. In the future, we will extend our research work on different other semiconducting oxide nanomaterials and with different other dopants to generalize this fact more significantly.

The variation of dielectric loss (tan δ) versus frequency of the applied alternating electric field in the range from 40 Hz to 10 kHz with temperature as the function is shown in Fig. 9. The dielectric loss (tan δ) represents the energy dissipation in the dielectric system and it is considered to be caused by the domain wall resonance. According to Eq. (12), dielectric loss (tan δ) is expressed as the ratio of the imaginary part of the dielectric constant (ε'') to the real part of the dielectric constant (ε'). Figure 9 shows the variation of dielectric loss (tan δ) as a function of frequency at different temperatures (RT to 80 °C). From Fig. 9, it is quite clear that the dielectric loss (tan δ) decreases with the increase in frequency at different temperatures. This type of variation of dielectric loss (tan δ) appears due to the space charge polarization. According to Eq. (12), dielectric loss (tan δ) is proportional to the imaginary part of the dielectric constant (ε''), so exhibits similar dispersion behavior. It is also noticeable that dielectric loss (tan δ) is maximum when there is no doping and decreases gradually with the increase in the Cr^{3+} ion doping percentage. Hence, we can conclude that these Cr^{3+} ion doped samples show the capability to be used in high frequency device applications. None of the plots display small peaks in the higher frequency region which represents the relaxation processes or loss peaks. The peaking behavior occurs when the hopping frequency of the localized electric charge carrier approximately equals to that of frequency of the externally applied alternating electric field.

Figure 10 shows the temperature variation in the range of 25–120 °C of the real part of dielectric constant (ε') for the undoped ZnO and Cr^{3+} ion doped ZnO nanoparticles. The measurement has been taken for three different frequencies, i.e., 1 kHz, 10 kHz, and 100 kHz, respectively. In all the cases, the curve shows ferroelectric to paraelectric transition at around 30 °C. It is noted that the maximum value of the real part of dielectric constants (ε') for all the samples is

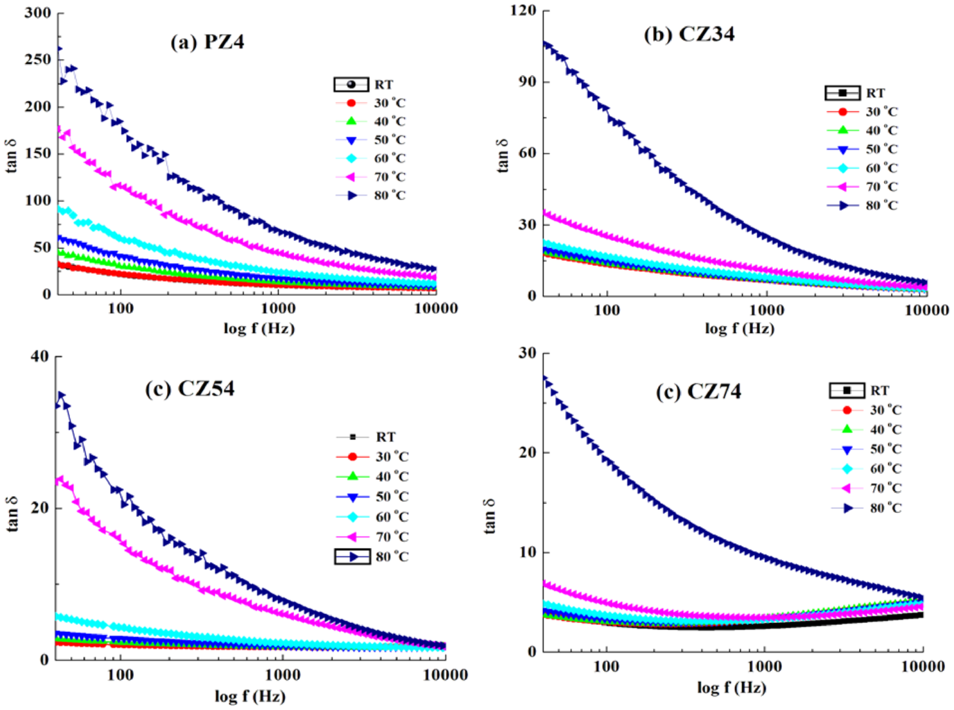

FIG. 9. Plot of dielectric loss (tan δ) vs frequency at different temperature of the samples (a) PZ4, (b) CZ34, (c) CZ54, and (d) CZ74.

quite high and the highest value of the real part of dielectric constant (ε') (~65595) has been found at 1 kHz frequency and specifically for 3% Cr^{3+} ion doped ZnO (CZ34) system. This high value of ε' may be attributed to the presence of the interfacial polarization inside the samples.

In addition, it has to be mentioned here that the bulk ZnO is an n-type semiconducting material with large free electron density inside the material, but in the nanoscale regime, a large amount of grain boundaries are present inside the ZnO nanomaterials. Although the ZnO grains are good conductors, the grain boundaries are poor conductors. Therefore, when the ZnO nanomaterial consists of large numbers of grain boundaries and the ZnO nano-grains are separated from one another by poorly conducting grain boundaries, the conduction property of the nanomaterial does not hold good. Thus, the motion of free charge particles inside ZnO nanomaterial is completely restricted by the grain boundaries. Now, in the presence of external electric field, the free charge particles reside at the surface of poorly conducting grain boundaries inside ZnO nanomaterials and thereby enhance interfacial polarization inside the sample. On the other hand, the charge density and the corresponding interfacial polarization inside the ZnO nanomaterials can be enhanced largely over the usual amount of charge density of

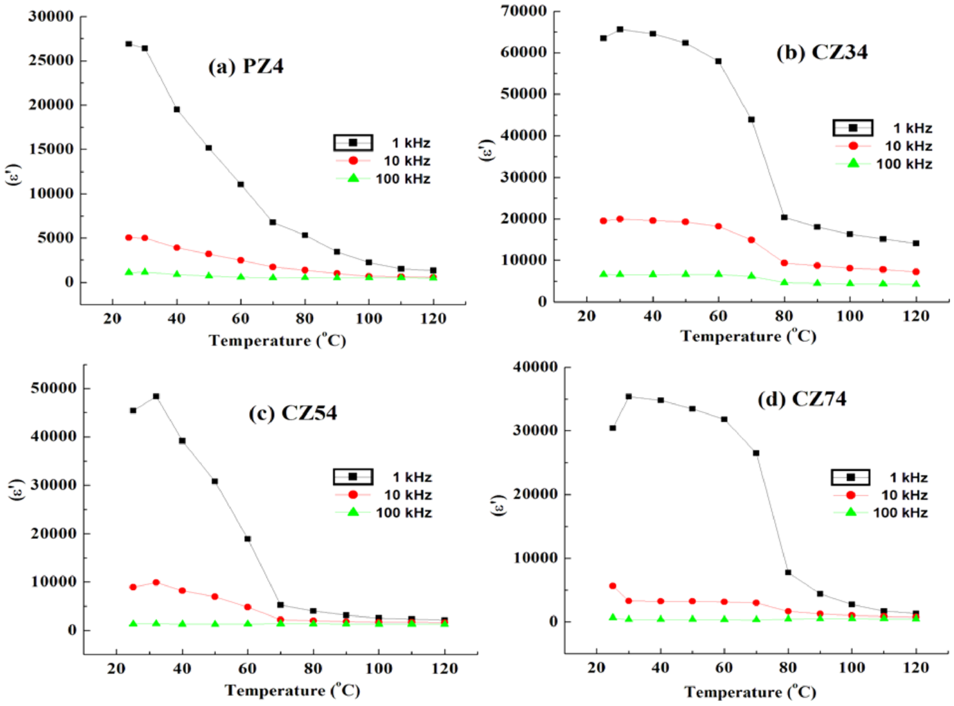

FIG. 10. Variation of real part of dielectric constant (ε') with temperature at different frequencies of the samples (a) PZ4, (b) CZ34, (c) CZ54, and (d) CZ74.

the host ZnO nanomaterial by the doping of Cr^{3+} ions. Cr^{3+} is an important transition metal element and it has a close ionic radius parameter to that of Zn^{2+}, which means that Cr^{3+} can easily penetrate into the ZnO crystal lattice or substitute Zn^{2+} ions from the host crystal lattice.[69] Due to this specific nature of Cr^{3+} ions, three Zn^{2+} ions can be replaced very easily by two Cr^{3+} ions to maintain electrical neutrality, and due to this distribution of Cr^{3+} ions inside the structure of ZnO, both free charge carriers and cationic vacancy in form of zinc vacancy are generated. The doubly ionized oxygen atom (O^{2-}) corresponding to each zinc vacancy inside the structure of ZnO can liberate its excess electron to be neutralized itself and thereby the process further improves the free charge density and the corresponding interfacial polarization of ZnO nanomaterial. In addition, the oxygen vacancy generates inside ZnO in this process. It has to be mentioned here that the main contribution of the dielectric property comes from the interfacial polarization of the ZnO nanomaterial, but the presence other native defects such as zinc vacancy, zinc interstitial, and oxygen vacancy inside the structure of the ZnO nanomaterial can also further improve the dielectric constant of the nanomaterial over the expected value. Thus, it can be inferred that the doping of a trivalent cation such as the Cr^{3+} ion inside the structure of ZnO nanomaterial is one of the key factors for the significant improvement of the dielectric constant of the nanomaterial. Thus, these Cr^{3+} ion doped ZnO nanoparticles with high dielectric property would be suitable for application in devices.

IV. CONCLUSION

In this work, we have carried out an experimental study to modulate the dielectric property in highly crystalline Cr^{3+} ion doped semiconducting ZnO nanoparticles prepared by the hydrothermal synthesis route. All the nanostructures as well as microstructures of undoped and Cr^{3+} ions doped semiconducting ZnO nanomaterials have been grown up into hexagonal rodlike structures under high pH and high pressure of hydrothermal process and the presence of rodlike structures of all the undoped and doped ZnO samples has been confirmed by the FESEM micrograph. It has been found in the present work that these rodlike structures of undoped and doped semiconducting ZnO samples are playing the key role in the modulation of the dielectric property, and the normal dielectric materials with a moderate dielectric constant having any form of microstructures other than rodlike structures can be achieved as the super dielectric material with a very high value of the dielectric constant when the material is found in the rodlike structures. It has to be mentioned here that this hydrothermal synthesis route is not only effective for the improvement of the dielectric response of the undoped and doped ZnO samples, but it is also very effective and probably the inevitable one for all the other semiconducting metal oxide nanomaterials when it is the question of their dielectric response and dielectric constant. In addition, the substitution of Cr^{3+} ions improves the charge density, and thereby it enhances the dielectric response of the semiconducting host ZnO nanomaterials. Thus, by using the low cost hydrothermal synthesis route, many undoped and TM or REE ion doped semiconducting oxide materials can be prepared into rod like structures with an exceptionally high dielectric constant. Furthermore, a high dielectric constant (∼524 160 at 40 Hz) in Cr^{3+} ion doped ZnO nanoparticles was observed at the low frequency side and a ferroelectric to paraelectric phase transition at 30 °C was observed at various frequencies. Such a high value of the dielectric constant of undoped and Cr^{3+} ion doped ZnO nanoparticles improves its dielectric property towards nanoscale charge storage devices, sensor device applications, high electric breakdown strength for non-conducting coating materials, and ferroelectric or piezoelectric applications, which is an essential requirement for device applications in the field of modern technology.

[1] M. K. Gupta, N. Sinha, and B. Kumar, J. Appl. Phys. **112**, 014303 (2012).
[2] A. Kar, S. Kundu, and A. Patra, J. Phys. Chem. C **115**, 118 (2011).
[3] A. Patra, P. Ghosh, P. Saha Chowdhury, M. A. R. C. Alencar, W. Lozano, B. N. Rakov, and G. S. Maciel, J. Phys. Chem. B **109**, 10142 (2005).
[4] K. L. Kelly, E. Coronado, L. L. Zhao, and G. C. Schatz, J. Phys. Chem. B **107**, 668 (2003).
[5] T. Debnath, S. Das, D. Das, and S. Sutradhar, J. Alloys Compd. **696**, 670 (2017).
[6] Y. Yang, W. Guo, X. Wang, Z. Wang, J. Qi, and Y. Zhang, Nano Lett. **12**, 1919 (2012).
[7] K. Jagiello, B. Chomicz, A. Avramopoulos, A. Gajewicz, A. Mikolajczyk, P. Bonifassi, M. G. Papadopoulos, J. Leszczynski, and T. Puzyn, Struct. Chem. **28**, 635 (2017).
[8] A. Kar and A. Patra, J. Phys. Chem. C **113**, 4375 (2009).
[9] B. Liu, H. M. Chen, C. Liu, S. C. Andrews, C. Hahn, and P. Yang, J. Am. Chem. Soc. **135**, 9995 (2013).
[10] N. H. Hong, M. B. Kanoun, S. Goumri-Said, J. H. Song, E. Chikoidze, Y. Dumont, A. Ruyter, and M. Kurisu, J. Phys.: Condens. Matter **25**, 436003 (2013).
[11] N. H. Hong, J. Sakai, N. T. Huong, A. Ruyter, and V. Brizé, J. Phys.: Condens. Matter **18**, 6897 (2006).
[12] S. Das, S. Das, D. Das, and S. Sutradhar, J. Alloys Compd. **691**, 739 (2017).
[13] G. Z. Xing, Y. Wang, J. I. Wong, Y. M. Shi, Z. X. Huang, S. Li, and H. Y. Yang, Appl. Phys. Lett. **105**, 143905 (2014).
[14] G. Z. Xing, D. D. Wang, C.-J. Cheng, M. He, S. Li, and T. Wu, Appl. Phys. Lett. **103**, 022402 (2013).
[15] Y. Sun and Q. Li, Chin. J. Liq. Cryst. Disp. **31**, 635 (2016).
[16] Z. Zhu, B. Bai, O. You, Q. Li, and S. Fan, Light: Sci. Appl. **4**, e296 (2015).
[17] A. Karabchevsky, A. Mosayyebi, and A. V. Kavokin, Light: Sci. Appl. **5**, e16164 (2016).
[18] C. Yuyu and T. Zhen, Chin. Opt. **10**(1), 86 (2017).
[19] L. Tong, Z. Mei-ling, W. Fei, Z. Da-ming, and W. Guo-ping, Chin. Opt. **10**(2), 219 (2017).
[20] L. Ma, S. Ma, H. Chen, X. Ai, and X. Huang, Appl. Surf. Sci. **257**, 10036 (2011).
[21] Z. L. Wang, J. Phys. Condens. Mater. **16**, 829 (2004).
[22] N. Tahir, A. Karim, K. A. Persson, S. T. Hussain, A. G. Cruz, Md. Usman, Md. Naeem, R. Qiao, W. Yang, Y. D. Chuang, and Z. Hussain, J. Phys. Chem. C **117**, 8968 (2013).
[23] G. Li, H. Wang, Q. Wang, Y. Zhao, Z. Wang, J. Du, and Y. Ma, Nano. Res. Lett. **10**, 112 (2015).
[24] X. Yang, A. Wolcott, G. Wang, A. Sobo, R. C. Fitzmorris, F. Qian, J. Z. Zhang, and Y. Li, Nano Lett. **9**, 2331 (2009).
[25] B. Chavillon, L. Cario, A. Renaud, F. Tessier, F. Cheviré, Md. Boujtita, Y. Pellegrin, E. Blart, A. Smeigh, L. Hammarström, F. Odobel, and S. Jobic, J. Am. Chem. Soc. **134**, 464 (2012).
[26] K. Zhang, T. Holloway, M. Bahoura, A. K. Pradhan, R. Prabakaran, J. Pradhan, S. Smith, J. C. Hall, G. T. Ramesh, D. R. Sahu, and J. L. Huang, Proc. SPIE **7291**, 729104 (2009).
[27] C. Chang, F. Kimura, T. Kimura, and H. Wada, Mater. Lett. **59**, 1037 (2005).
[28] S. Li, H. Song, H. Yu, S. Lu, X. Bai, G. Pan, Y. Lei, L. Fan, and T. Wang, J. Lumin. **122**, 876 (2007).

[29] Y. Mao, J. Y. Huang, R. Ostroumov, K. L. Wang, and J. P. Chang, J. Phys. Chem. C **112**, 2278 (2008).
[30] Y. He, Y. Tian, and Y. Zhu, Chem. Lett. **32**, 862 (2003).
[31] V. Ney, S. Ye, T. Kammermeier, A. Ney, H. Zhou, J. Fallert, H. Kalt, F.-Y. Lo, A. Melnikov, and A. D. Wieck, J. Appl. Phys. **104**, 083904 (2008).
[32] H. S. Hsu, J. C. A. Huang, Y. H. Huang, Y. F. Liao, M. Z. Lin, C. H. Lee, J. F. Lee, S. F. Chen, L. Y. Lai, and C. P. Liu, Appl. Phys. Lett. **88**, 242507 (2006).
[33] V. Gandhi, R. Ganesan, H. H. A. Syedahamed, and M. Thaiyan, J. Phys. Chem. C **118**, 9715 (2014).
[34] H. Yu, J. Li, R. A. Loomis, L.-W. Wang, and W. E. Buhro, Nat. Mater. **2**, 517 (2003).
[35] K.-F. Lin, H. M. Cheng, H.-C. Hsu, and W.-F. Hsieh, Appl. Phys. Lett. **88**, 263117 (2006).
[36] W. Yan, Q. Jiang, Z. Sun, T. Yao, F. Hu, and S. Wei, J. Appl. Phys. **108**, 013901 (2010).
[37] P. P. Murmu, J. K. Kennedy, B. J. Ruck, A. Markwitz, G. V. M. Williams, and S. Rubanov, Nucl. Instrum. Methods Phys. Res., Sect. B **272**, 100 (2012).
[38] H. M. Zhou, D. Q. Yi, Z. M. Yu, L. R. Xiao, and J. Li, Thin Solid Films **515**, 6909 (2007).
[39] N. Fathy and M. Ichimura, J. Cryst. Growth **294**, 191 (2006).
[40] M. Jin, J. Feng, Z. De-heng, M. Hong-lei, and L. Shu-ying, Thin Solid Films **357**, 98 (1999).
[41] Y. Wang, N. Liu, Y. Chen, C. Yang, W. Liu, J. Su, L. Lia, and Y. Gao, RSC Adv. **5**, 104386 (2015).
[42] C. E. Small, S. Chen, J. Subbiah, C. M. Amb, S. W. Tsang, T. H. Lai, J. R. Reynolds, and F. So, Nat. Photonics **6**, 115 (2012).
[43] S. C. Pillai, J. M. Kelly, R. Ramesh, and D. E. McCormack, J. Mater. Chem. C **1**, 3268 (2013).
[44] M. H. Huang, S. Mao, and H. Feick, Science **292**, 1897 (2001).
[45] G. S. Kino and R. S. Wagner, J. Appl. Phys. **44**, 1480 (1973).
[46] P. K. Shrestha, Y. T. Chun, and D. Chu, Light: Sci. Appl. **4**, e259 (2015).
[47] Y. Y. Lai, Y. P. Lan, and T. C. Lu, Light: Sci. Appl. **2**, e76 (2013).
[48] G. Li-li, L. Jun-sheng, Z. Miao, and Z. Yue-lin, Chin. J. Liq. Cryst. Disp. **29**, 499 (2014).
[49] G. Li-li, L. Song-fei, C. Tian-fu, and Z. Xue, Chin. J. Liq. Cryst. Disp. **30**, 925 (2015).
[50] A. S. H. Hameed, C. Karthikeyan, A. P. Ahamed, N. Thajuddin, N. S. Alharbi, S. A. Alharbi, and G. Ravi, Sci. Rep. **6**, 24312 (2016).
[51] W. H. Nam, Y. S. Lim, S. M. Choi, W. S. Seo, and J. Y. Lee, J. Mater. Chem. **22**, 14633 (2012).
[52] C. J. Cong, L. Liao, J. C. Li, L. X. Fan, and K. L. Zhang, Nanotechnology **16**, 981 (2005).
[53] J. Luo, J. K. Liang, Q. L. Liu, F. S. Liu, and Y. Zhang, J. Appl. Phys. **97**, 086106 (2005).
[54] O. Lupan, T. Pauporté, B. Viana, V. V. Ursaki, I. M. Tiginyanu, V. Sontea, and L. Chow, J. Nanoelectron. Optoelectron. **7**, 712 (2012).
[55] S. Baruah and J. Dutta, Sci. Technol. Adv. Mater. **10**, 013001 (2009).
[56] F. Solís-Pomar, E. Martínez, M. F. Meléndrez, and E. Pérez-Tijerina, Nanoscale Res. Lett. **6**, 524 (2011).
[57] S. López-Romero and M. García-H, 2013 World J. Condens. Matter Phys. **3**, 152 (2013).
[58] S. B. Kondawar, S. A. Acharya, and S. R. Dhakate, Adv. Mater. Lett. **2**, 362 (2011).
[59] J. J. Lee, G. Z. Xing, J. B. Yi, T. Chen, M. Ionescu, and S. Li, Appl. Phys. Lett. **104**, 012405 (2014).
[60] D. D. Wang, G. Z. Xing, F. Yan, Y. S. Yan, and S. Li, Appl. Phys. Lett. **104**, 022412 (2014).
[61] R. Mariappan, V. Ponnuswamy, P. Suresh, R. Suresh, and M. Ragavendar, Superlattices Microstruct. **59**, 47 (2013).
[62] R. Viswanatha, S. Sapra, B. Satpati, P. V. Satya, B. N. Dev, and D. D. Sarma, J. Mater. Chem. **14**, 661 (2004).
[63] A. L. Schoenhalz, J. T. Arantes, A. Fazzio, and G. M. Dalpian, J. Phys. Chem. C **114**, 18293 (2010).
[64] A. Mclaren, T. Valdes-Solis, G. Li, and S. C. Tsang, J. Am. Chem. Soc. **131**, 12540 (2009).
[65] K. W. Wagner, Ann. Phys. **40**, 817 (1973).
[66] J. Maxwell, *Electric and Magnetism 2* (Oxford University Press, New York, 1973).
[67] C. G. Koops, Phys. Rev. **83**, 121 (1951).
[68] S. Bhattacharya, S. K. Saha, and D. Chakravorty, Appl. Phys. Lett. **76**, 3896 (2000).
[69] B. K. Roberts, A. B. Pakhomov, V. S. Shutthanandan, and K. M. Krishnan, J. Appl. Phys. **97**, 10D310 (2005).

Materials Research Bulletin 118 (2019) 110480

Contents lists available at ScienceDirect

Materials Research Bulletin

journal homepage: www.elsevier.com/locate/matresbu

Influence of different Cr concentrations on the structural and ferromagnetic properties of ZnO nanomaterials prepared by the hydrothermal synthesis route

Tanumoy Debnath[a,b], Atul Bandyopadhyay[c], Tanmoy Chakraborty[a], Sukhen Das[b], Soumyaditya Sutradhar[a,*]

[a] Department of Physics, Amity University, Kolkata, 700156, West Bengal, India
[b] Department of Physics, Jadavpur University, Kolkata, 700032, West Bengal, India
[c] Department of Physics, University of Gour Banga, Malda, West Bengal, 732103, India

ARTICLE INFO

Keywords:
Hydrothermal synthesis
Nanorods
Paramagnetic centers
Ferromagnetism
Bound magnetic polaron

ABSTRACT

ZnO nanomaterials with different doping concentrations of Cr ions have been prepared by the hydrothermal method. The crystallographic parameters have been estimated by Rietveld analysis. The diffraction pattern indicates the preferential growth of the nanomaterials along '*a*' axis. Photoluminescence (PL) and electron paramagnetic resonance (EPR) spectra reveal the presence of various defect states and singly ionized oxygen vacancy in all the Cr-doped ZnO nanomaterials. M-T curve suggests that all the magnetic phases (para, ferro, and antiferro) are present in the total magnetization of the Cr-doped ZnO nanomaterials. The calculation shows that 7% Cr-doped ZnO has the highest magnetic moment among others, though the ferromagnetic contribution (˜ 89.1%) in the total magnetization is more for 5% Cr-doped ZnO sample. The widely accepted bound magnetic polaron theory has been proposed here to explain the modulation of the magnetic behavior of doped ZnO nanomaterials due to the variation of the doping concentration of Cr ions.

1. Introduction

ZnO is one of the most promising and widely studied II-VI semiconductor materials with a large direct band gap energy of 3.37 eV and a large exciton binding energy of 60 meV. ZnO nanostructures such as nanospheres, nanorods, nanobolts, nanoflowers, nanowires, etc. with size modulations show fascinating optical, dielectric and many other physical properties which establish this nanostructure ZnO as the most significant candidate for the fabrication of nano-devices [1–3]. Moreover, in recent reports, it has already been established through experimental observation that ZnO nanomaterial can possess feeble magnetic ordering though its origin is still under doubt [4,5]. The small spin-orbit coupling and corresponding large spin coherence length make ZnO a potential candidate/host for spintronic devices [6]. In this direction, few atomic percentages of transition metal (TM) doping can generate some fascinating physical properties of ZnO and these can be integrated with magnetic properties to satisfy the needs for formulating spin-based devices such as spin-valve transistors, non-volatile memory, logic device and many more [7,8]. The TM doping also initiates the debates about the generation of room temperature ferromagnetism (RTFM) in ZnO due to the possible existence of ferromagnetic clusters/secondary phases related to the well known magnetic metal cations (Co, Ni, Fe). These secondary phases are the most vital concerns in any diluted magnetic system as a source of the spurious magnetic signal [9,10]. Therefore, the non-ferromagnetic element doping in the lattice structure of host ZnO is the most constructive method to find out the origin of intrinsic ferromagnetism. Another serious issue is the low magnetization value (nearly ˜ 10^{-4} to 10^{-3} emu/g) of TM doped ZnO nanomaterials which restrict their application in high-speed data processing systems [11,12]. This particular drawback related to the magnetic response of TM doped ZnO nanomaterials and the requirement for the fabrication of high-speed next-generation logic device has motivated us to do research work on the Cr doped ZnO system. Here in the present work, Cr is chosen as the preferred TM dopant because (i) Sato and Katayama-Yoshida et al., predicted theoretically that FM in Cr-doped ZnO is more stable and energetically favourable than most widely studied Co-doped ZnO [13], (ii) Cr^{3+} ion has smaller atomic radius (0.63 Å) than the atomic radius of Zn^{2+} ion (0.74 Å) and expected to easily enter into ZnO crystal lattice or substitute Zn position in the crystal forming a solid solution [14], (iii) Cr metal is

---

* Corresponding author.
E-mail address: sds.phy1@gmail.com (S. Sutradhar).

https://doi.org/10.1016/j.materresbull.2019.05.005
Received 6 January 2019; Received in revised form 16 April 2019; Accepted 7 May 2019
Available online 11 May 2019

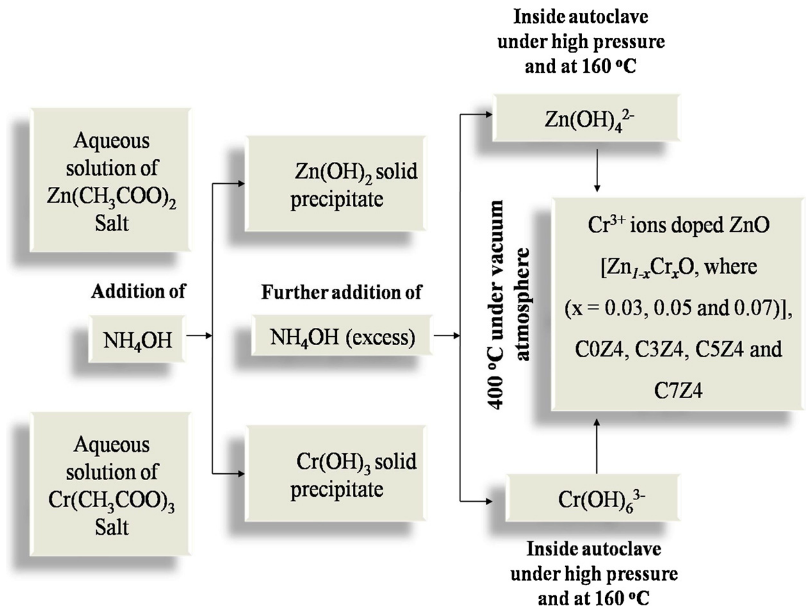

Fig. 1. Flowchart of the preparation of undoped and Cr-doped ZnO by hydrothermal synthesis route.

paramagnetic at high temperature and antiferromagnetic below 311 K. These features make Cr a promising doping element to distinguish intrinsic FM, (iv) trivalent Cr^{3+} ions exhibit $3d^3$ high-spin configuration, which may help to produce large magnetic moments in the host lattice and (v) we expect that substitution of divalent zinc cations by the trivalent chromium cations can produce a large number of defect states inside the structure of ZnO such as zinc vacancy defect, zinc interstitial defect, oxygen vacancy defect, dangling bond, etc. to maintain the charge neutrality which may initiate desired magnetic ordering [15,16]. After the detail experimental and theoretical observations, it is now accepted that the structural defects are basically the cause of the RTFM in TM doped ZnO. [17,18]. In addition exchange interaction between magnetic moments localized at the TM sites mediated by free charge carriers known as Ruderman–Kittel–Kasuya–Yosida (RKKY) is also believed to be the other reason for magnetic ordering [19,20]. In this direction only a few reports are available and the systems have been reported to display the presence of ferromagnetic, paramagnetic or spin glass behavior, depending on the sample preparation parameters [21,22]. Thus contradictory results on magnetic ordering still open up a void space for the researchers to work with Cr-doped ZnO nanomaterials. Subsequently, to date, no consensus has been reached regarding the coupling mechanism or the origin of the magnetic ordering of TM doped ZnO. In line with this, we have doped various concentrations of Cr^{3+} ions (3, 5 and 7%) in host ZnO nanomaterial. In the present study, we have used the hydrothermal synthesis route which gives us a better opportunity to develop ZnO nanomaterials, particularly, for the preparation of TM doped ZnO nanomaterials. The goal of this study is to reveal the exact origin of magnetic ordering as well as to evaluate and substantiate the influence of Cr content on the structural and magnetic properties of ZnO nanomaterial.

2. Experimental

2.1. Materials and methods

In the present article different measurements were conducted on Cr-ions doped ZnO nanomaterials for the determination of structural, magnetic and other co-related physical properties. Cr-doped ZnO nanomaterials with different compositional ratio, i.e., $Zn_{1-x}Cr_xO$ (x = 0.00, 0.03, 0.05 and 0.07) were prepared by co-precipitation method followed by hydrothermal synthesis route. The detail preparation technique has been provided in our earlier publications [23–26]. Zinc acetate dehydrate $Zn(CH_3COO)_2{\cdot}2H_2O$ (Sigma Aldrich, 99%), chromium acetate $Cr(CH_3COO)_3$ (Sigma Aldrich, 99%) were used as the precursor salts with analytical grade and without any further purification, and ammonium hydroxide NH_4OH (concentration ˜ 25%) was also used in the co-precipitation process. Zinc acetate dihydrate Zn $(CH_3COO)_2{\cdot}2H_2O$ and chromium acetate $Cr(CH_3COO)_3$ salts were taken in a beaker with triple distilled water. The solutions of precursor salts were stirred on a magnetic stirrer for an hour at a temperature of 60 °C and NH_4OH solution was added in the solutions of precursor salts for the synthesis of both undoped and Cr-doped ZnO nanoseeds. Excess ammonia was added in the aqueous solution to enhance the pH value of the resultant solution to ˜ 10 and the resultant solution was then transferred into the Teflon jacket. The Teflon jacket was placed in the stainless steel autoclave and the whole system was placed inside a hot air oven at 160 °C for 48 hrs. After 48 hrs the system was allowed to cool down naturally to RT. The supernatant was removed from the Teflon jacket and the solid precipitates at the bottom of the Teflon jacket were collected for washing. The solid precipitates were washed several times with triple distilled water and ethyl alcohol. The solid precipitates were kept inside the vacuum oven at 50 °C for another 48 hrs in order to make it dry and finally, the dried as-prepared powder samples of undoped and Cr-doped ZnO nanomaterials were collected. Now, the as-prepared nanomaterials were annealed at 400 °C to get the desired crystallographic phase of the resultant undoped and Cr-doped ZnO nanomaterials. The whole synthesis mechanism has been depicted in Fig. 1.

In the present study, the crystal growth mechanism of undoped and Cr-doped ZnO nanomaterials into rod-like grain structure can be explained on the basis of the kinetic point of view. Under the hydrothermal synthesis route, growth mechanism is assisted by the formation of growth units and thereafter the growth units will assimilate at the interface of the ZnO lattice site. The high pH value of aqueous solution ˜ 10 also plays the most significant role in the development of microstructures with rod-like in nature for undoped and Cr-doped ZnO nanomaterials. During the reaction process, the addition of excess NH_4OH helps to create a large number of growth units in the form of hydrated ions such as $Zn(OH)_4^{2-}$ and $Cr(OH)_6^{3-}$. Now, the high pressure inside autoclave helps to get diffusion of hydrated ions and the deregulation movement between the molecules and ions. These hydrated ions are finally bonded together through a dehydration reaction and as a result, they decomposed into a large size cluster. As the size of the cluster satisfies the critical limit required to form grain, the cluster gets precipitated. Thus, this hydrothermal synthesis route is very much helpful for the modulation of grain structures of undoped and Cr-doped ZnO nanomaterials into rod-like in nature as well as this process also helps to get large internal strain inside the lattice structure of host ZnO nanomaterials. This internal lattice strain is one of the important factors due to which the desired modification in various physical properties such as optical and magnetic properties can be made and it has been discussed in the XRD section.

2.2. Characterization techniques

The XRD patterns of all the samples were recorded in powder X-ray diffractometer, Model D8, BRUKER AXS, using Cu K_α radiation ($\lambda = 1.5405$ Å) in the range of 2θ from 20 to 80°. Field emission scanning electron microscope (FESEM) was employed for morphological study using INSPECT F50 (FEI, Netherland). The photoluminescence (PL) emission spectroscopy was also conducted by using a spectroflourometer, Perkin Elmer Germany with an excitation wavelength (λ_{ex}) of 325 nm. The electron paramagnetic resonance (EPR) measurement was conducted by using the EPR spectrometer model E500 Bruker. Magnetization versus applied magnetic field (M-H) data of the samples at RT and at different low temperatures was recorded by a SQUID magnetometer (MPMS XL 7, Quantum Design), where the maximum applied field was 50000 Oe.

3. Result and discussions

3.1. XRD analysis

The structural properties of undoped and Cr-doped ZnO nanomaterials have been investigated by the use of X-ray diffraction (XRD) patterns and the respective patterns of all the samples viz., (C0Z4, C3Z4, C5Z4, and C7Z4) have been depicted in Fig. 2(a)-(d). The XRD patterns of these samples are in good agreement with the JCPDS (File no. 36-1451) standard data of the wurtzite hexagonal lattice structure of ZnO. The X-ray diffraction patterns of all the undoped and Cr-doped ZnO nanomaterials exhibit a series of diffraction peaks corresponding to Bragg planes (100), (002), (101), (102), (110), (103), (200), (112), (201) and (202) with the space group *P63mc*. Rietveld refinement has been considered in the present report and the corresponding analysis tells us that the samples are all in the single phase of the hexagonal wurtzite lattice structure of ZnO and no trace of any other impurities have been observed within the detection limit of powder XRD pattern. The maximum doping percentage of Cr ion in the present study is 7% and this higher doping percentage may influence the Cr ions to occupy vacant octahedral (Cr^{3+}) and tetrahedral (Cr^{6+}) sites sequentially inside the host ZnO lattice. These site selections of higher valency Cr ions act as precursors for different secondary oxide phases such as antiferromagnetic Cr_2O_3 and $ZnCr_2O_4$, paramagnetic Cr_2O_3 and ferromagnetic CrO_2, etc. These secondary phases are the sources of various forms of magnetic responses and they are not intrinsic in nature [27]. It is to be mentioned here that we are very much concerned about the phase purity for Cr-doped ZnO nanomaterials throughout the entire course of sample preparation. Since the formation of any secondary phase in Cr-doped ZnO nanomaterials may mislead us to draw conclusions about the intrinsic behavior of the FM ordering at RT present in the samples. It has been noticed from Fig. 2 that all the undoped and Cr-doped ZnO nanomaterials have a common preferential growth pattern along (100) Bragg plane whereas the slandered JCPDS file shows that the intensity of (101) plane is high as compared to the (100) plane. The preferential growth of the ZnO nanomaterials along '*a*' axis has been appeared due to the nucleation of the undoped and Cr-doped ZnO nanoseeds along (100) plane under high pressure and temperature of the autoclave during the hydrothermal synthesis route. Also, this nucleation process under high pressure and temperature of the autoclave influences the resultant products of ZnO to be evolved as rods like in nature. The well-ordered alignment of ZnO nanorods along '*a*' axis [compared to '*c*' axis] is very much scarce in available literature and perhaps for the first time, this type of growth pattern of undoped and Cr-doped ZnO nanorods have been found. The lower intensity of (002) peaks for all the samples is also in good agreement with the fact that the growth of all the undoped and Cr-doped ZnO nanorods has appeared along '*a*' axis rather than '*c*' axis. The degree of *a*-orientation can be illustrated by the relative texture coefficient as shown in equation 1 [28]

$$TC_{100} = \frac{\frac{I_{100}}{I^0_{100}}}{\frac{I_{100}}{I^0_{100}} + \frac{I_{101}}{I^0_{101}}} \tag{1}$$

Where I_{100} and I_{101} are the measured diffraction intensities due to (100) and (101) planes of undoped and Cr-doped ZnO nanorods and I^0_{100} and I^0_{101} are the diffraction intensities of standard ZnO sample as obtained from JCPDS (File no. 36-1451). The texture coefficients for C0Z4, C3Z4, C5Z4, and C7Z4 are 0.678, 0.672, 0.674 and 0.683 respectively, which indicates that the preferential growth of all the ZnO nanomaterials has appeared along (100) plane. This growth pattern is almost independent of Cr doping concentration and the nucleation of ZnO nanoseeds into ZnO nanorods along (100) plane depends mostly on the preparation techniques/parameters such as pH value of the solution, pressure, and temperature inside the autoclave, etc. under hydrothermal synthesis route.

The X-ray powder diffraction (XRPD) profile at any diffraction angle (θ) can be described as:

$$Y_c(2\theta) = [B \times (I_S \times I_A)](2\theta) + Bkg \tag{2}$$

Here *B* is the true specimen broadening describing the microstructural broadening, I_S is the symmetric part of the instrumental function, I_A is the asymmetric part of the instrumental function and *Bkg* is the background of the diffraction pattern [29]. In the present article, the structural (lattice parameters, unit cell volume, etc.) and microstructural (coherent domain size/crystallite size, microstrain, etc.) parameters have been estimated from Rietveld analysis with the help of the software MAUD [30]. Small values of χ^2 (goodness-of-fit quality factor) and different profile parameters viz, R_p (profile fitting R-value), R_{wp} (weighted profile R-value) recommend that Cr-doped ZnO nanomaterials are all in single crystallographic phase corresponding to the hexagonal wurtzite structure of ZnO. The observed patterns are all well fitted by the generated patterns in the Rietveld refinement and the parameters are reproducible too. The lattice parameters (*a* and *c*) extracted from Rietveld refinement are plotted in Fig. 3 as a function of Cr doping concentration (x). The values of lattice parameters (*a* and *c*), extracted from Rietveld refinement for the variation of Cr doping concentration have been shown in Table 1. From Table 1, it is quite clear that the lattice parameters (*a* and *c*) do not change significantly due to the increase in Cr doping concentration inside the structure of host ZnO nanomaterials. However, a closer observation (Fig. 3) reveals that there is a small increase in the lattice parameter '*a*' and a small decrease in the lattice parameter '*c*' due to the increase in Cr doping concentration in host ZnO nanomaterials. In the present study, the change in lattice parameters (*a* and *c*) has also been observed due to the generation of distortion effect in the host ZnO lattice structure by the incorporation of the Cr^{3+} ions. Actually, with the increasing doping percentage of Cr^{3+} ions ($Zn_{1-x}Cr_xO$ (x = 0.03, 0.05 and 0.07)), more and more zinc vacancies would generate inside the lattice structure of host ZnO to maintain charge equality. These induced zinc vacancies generated due to the doping of Cr^{3+} ions in the ZnO lattice are responsible for the change in the lattice parameters (*a* and *c*). During doping of Cr^{3+} ions in the lattice structure of host ZnO, three Zn^{2+} ions get removed from host lattice by the two Cr^{3+} ions and due to that, the effective lattice parameters of the nanocrystallite gets changed with respect to undoped ZnO. Also, the decrease in '*c*' may be appeared due

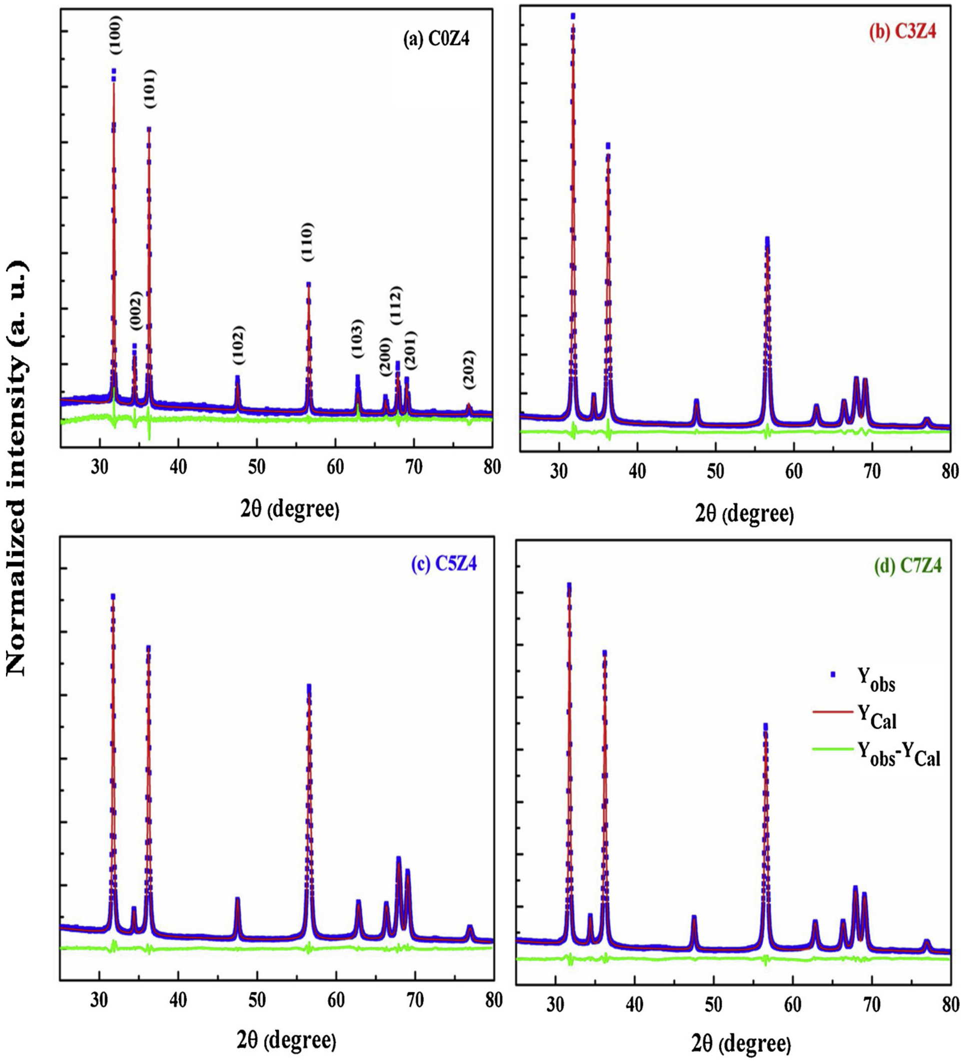

Fig. 2. XRD patterns along with the Rietveld analysis of the samples (a) undoped ZnO (C0Z4), (b) 3% Cr-doped ZnO (CZ34), (c) 5% Cr-doped ZnO (CZ54) and (d) 7% Cr-doped ZnO (CZ74).

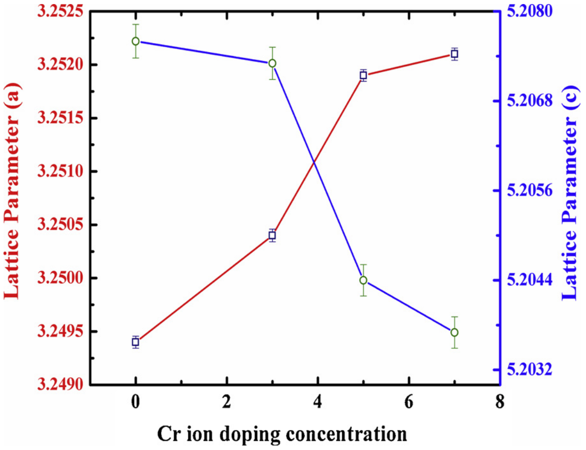

Fig. 3. Variations of lattice parameters ‘a’ and ‘c’ as a function of Cr ion doping concentration in ZnO.

to the incorporation of smaller size Cr^{3+} ion (0.63 Å) at the site of Zn^{2+} (0.74 Å) ions inside the lattice structure of host ZnO. However, the increase of the lattice parameter ‘*a*’ cannot be accounted by this logic and this change has been appeared due to the small distortion at Zn-tetrahedron. Normally in the wurtzite ZnO structure, the Zn-tetrahedron has its base in the *ab*-plane and the apex along the *c*-direction. Now, the replacement (doping) of Zn^{2+} ions by Cr^{3+} ions increases the average basal bond angles (O_b-Zn-O_b) of the wurtzite ZnO structure and it also decreases the average base-apex angles (O_b-Zn-O_a) (where O_b and O_a are oxygen atoms in the base and at the apex respectively, of the tetrahedron) leading to the small increment in the lattice parameter ‘*a*’ and small decrement in the lattice parameter ‘*c*’ of the resultant ZnO lattice structure [31]. To substantiate this explanation, we have

Table 1
Structural parameters of undoped and Cr-doped ZnO nanomaterials extracted from Rietveld analysis.

Parameters	C0Z4	C3Z4	C5Z4	C7Z4
Crystallite Size (nm)	57	44	35	29
a (Å)	3.249	3.251	3.252	3.252
c (Å)	5.208	5.207	5.205	5.204
B_{iso}	1.262	1.403	1.750	1.101
Δg_o	1.000	0.027	0.048	0.072
Degree of distortion (R)	1.018	1.019	1.020	1.020
$D_{Zn\text{-}O}$ (Å)	1.977	1.978	1.978	1.978
O_b-*Zn*-O_a (in degree)	108.468	108.445	108.374	108.373
O_b-*Zn*-O_b (in degree)	110.422	110.479	110.559	110.549
Microstrain	5.62×10^{-4}	1.03×10^{-3}	1.5×10^{-3}	2.1×10^{-3}

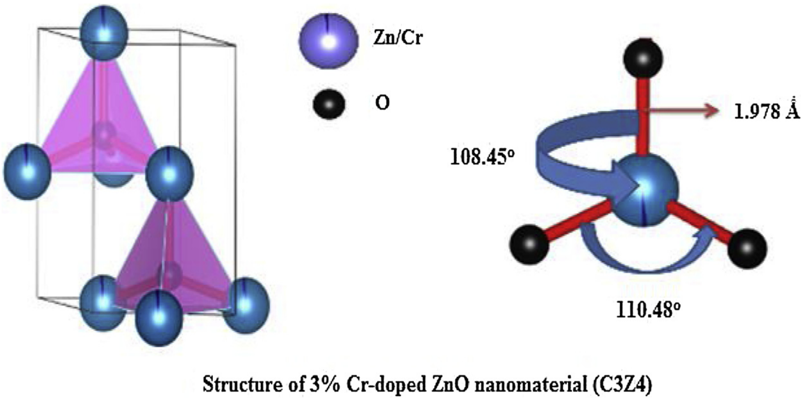

Fig. 4. Structure representation of 3% Cr-doped ZnO.

evaluated the bond angles as well as the bond lengths of undoped and Cr-doped ZnO nanomaterials from Rietveld analysis and the corresponding values are also presented in Table 1. The values of bond angles and bond lengths reveal that the base-apex angles decrease from 108.47° to 108.45° and basal bond angle increases from 110.42° to 110.48°. The representative crystal structure of one such Cr-doped ZnO nanomaterials i.e., 3% Cr-doped ZnO nanomaterial (C3Z4) has been derived from Rietveld analysis and the structure has been shown in Fig. 4. Therefore, the distortion in the Zn-tetrahedron arises due to the variations of bond lengths and bond angles between the lattice atoms. The other factors such as zinc antisites, oxygen vacancies, and extended defects are also responsible for the enhancement of the lattice constant as proposed by Ozagur et al. [32]. An additional Rietveld refinement has been performed in the present report in order to understand the presence of oxygen occupancies in each Cr-doped ZnO nanomaterial. The oxygen occupancy estimated for C0Z4, C3Z4, C5Z4, and C7Z4 nanomaterials are 1, 0.973, 0.952, and 0.928 respectively. The variation of the oxygen occupancy for each sample has been defined as [33]

$$\Delta g_{o(ZnO)} = g_{o(ZnO)} - \frac{g_{o(Cr-doped\ ZnO)}}{g_{o(ZnO)}} \tag{3}$$

Where g_o refers to oxygen site occupancy. The positive value of all the Cr-doped ZnO nanomaterials (summarized in Table 1) indicates that oxygen vacancy increases with the increase of Cr doping concentration inside the lattice structure of host ZnO.

Therefore, we conclude that Cr^{3+} ions get incorporated successfully in the lattice structure of host ZnO and it influences both oxygen vacancies and lattice distortion in the Cr-doped ZnO nanomaterials. The degree of distortion (R) has been calculated by the following relation:

$$R = \sqrt{\frac{8}{3}}\frac{a}{c} \tag{4}$$

The value of R is 1 for an ideal structure. The gradual increase of R has been shown in Fig. 5 and it suggests that R increases with increasing Cr-concentration. In order to determine the size and strain parameters of undoped and Cr-doped ZnO nanomaterials, the whole profile has been fitted again by the isotropic size strain model. The average crystallite size in the present study decreases from 57 to 29 nm when Cr doping concentration varies from 0% to 7%. It indicates that the presence of Cr ions in the ZnO lattice structure prevents the growth of crystal grains and it also slows down the motion of the grain boundaries. The interruption on the movement of the grain boundaries can be well explained by Zener pinning [34]. If the retarding force of the moving boundary is attached to the zinc interstitial and if the concentration of Cr ions is more than the driving force required for grain growth, then the particle growth will be restricted and the particle cannot grow any longer. Subsequently, the substitution of Zn^{2+} ions by the Cr^{3+} ions produces crystal defects which act as nucleation center [35]. Therefore, crystal growth is inhibited. The lattice strain of C0Z4, C3Z4, C5Z4, and C7Z4 has also been estimated from Rietveld analysis and the corresponding values have been provided in Table 1. In the present study, undoped and Cr-doped ZnO nanomaterials are all prepared by the hydrothermal method. Now, under the hydrothermal synthesis route inside autoclave high pressure has been developed in the lattice structure of host ZnO nanomaterials which also develops large internal compressive stress on the crystal planes in the host ZnO structure. This large internal compressive stress on undoped and Cr-doped ZnO nanomaterials also develops large internal strain on the lattice structure. Now, it is well known that the large internal lattice strain can shift the position of any particular XRD peak towards the higher 2θ value. Along with the internal lattice strain present inside the host lattice structure of ZnO due to the high pressure effect under the hydrothermal synthesis route, the addition amount of internal lattice strain would develop inside the lattice structure of the host ZnO due to the presence of Cr^{3+} ions as dopant. It is to be mentioned here that the radius of Cr^{3+} ion (0.63 Å) is different from the radius of Zn^{2+} ion (0.74 Å). Therefore, when Zn^{2+} ions are substituted by Cr^{3+} ions the internal lattice strain inside the lattice structure of Cr-doped ZnO nanomaterials would develop due to this difference in the dimension of the ionic radius of these two cations. The corresponding values of the internal lattice strain/microstrain of Cr-doped ZnO nanoparticles are more as compared to the undoped ZnO nanoparticles and it increases gradually with the increasing doping percentages of Cr^{3+} ions in the structure of host ZnO nanomaterials. In the present report, the values of internal lattice strain/microstrain for all the nanomaterials (C0Z4, C3Z4, C5Z4, and C7Z4) are given in Table 1 and the values are in good agreement with that of the enhancement of lattice distortion observed in the lattice structure of Cr-doped ZnO nanomaterials. Thus, the improvement of the internal lattice strain due to the incorporation of the

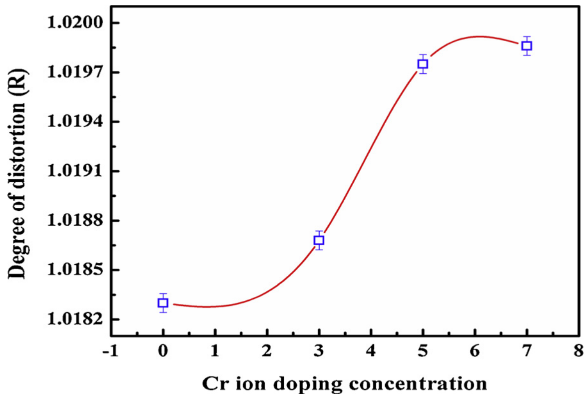

Fig. 5. Variations of the degree of distortion (R) as a function of Cr ion concentration in ZnO.

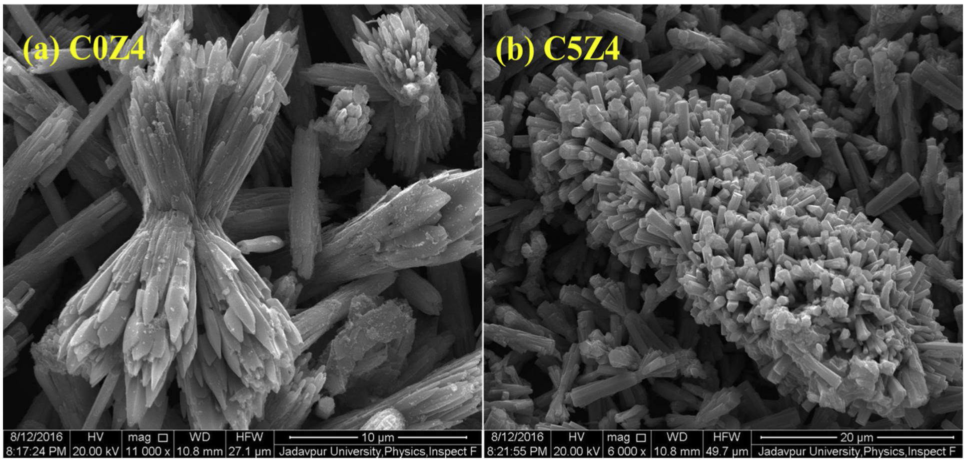

Fig. 6. FESEM images of the samples (a) C0Z4 and (b) C5Z4.

Cr^{3+} ions in the structure of host ZnO nanomaterials is the main cause behind this shift in diffraction peak positions in the XRD observation.

3.2. FESEM analysis

In order to get a clear idea about the growth mechanism and the variation of surface morphologies of undoped and Cr-doped ZnO nanomaterials under the hydrothermal synthesis route, the FESEM measurement has been conducted and some selected micrographs have been shown in Fig. 6. Fig. 6 (a) and (b), respectively, show the surface morphologies of undoped ZnO (C0Z4) and 5% Cr-doped ZnO (C5Z4) nanomaterials observed in their FESEM measurements. It is quite clear from Fig. 6(a) and (b) that the micrographs of both the samples are rod-like in nature and a clear variation of their morphologies has also been observed in the representative micrographs. Fig. 6(a) represents the micrograph of undoped ZnO nanomaterial (C0Z4) and it shows the rod-like structure of C0Z4 with the needle like end. In the given micrograph all the rod-like structures are very much clear and distinguishable from one another, though the presence of agglomeration effect at the growth centers of C0Z4 cannot be ruled out completely. Fig. 6(b) shows the micrograph of 5% Cr-doped ZnO nanomaterial (C5Z4). In the given micrograph the surface morphology of C5Z4 is also rod-like in nature with hexagonal ends and it also shows a similar pattern that we have observed for C0Z4. Thus, the formation of rod-like grain morphologies of C0Z4 and C5Z4 nanomaterials from their nanoseeds like structures is the signature pattern of hydrothermal synthesis of undoped or Cr-doped ZnO nanomaterials. Now, the formation of growth units in form of hydrated ions like, $Zn(OH)_4{}^{2-}$ and $Cr(OH)_6{}^{3-}$ under high pH (˜ 10) and thereafter the diffusion process of these hydrated ions under high pressure and temperature (˜ 160 °C) in the aqueous solution, actually controls the growth mechanism of the undoped and Cr-doped ZnO nanomaterials under hydrothermal process. The detail of the growth mechanism of undoped and Cr-doped ZnO nanomaterials has been given in our earlier publication [23]. After the end of the hydrothermal process, the structural variations have been observed for both the rod-like C0Z4 and C5Z4 nanomaterials. The first one shows its rod-like structure with the needle like end and the latter one shows its rod-like structure with a nearly uniform hexagonal end. This change in surface morphologies of both C0Z4 and C5Z4 nanomaterials appears due to the presence of elemental dissimilarity in form of Cr^{3+} ions between undoped ZnO and Cr-doped ZnO nanomaterials. The presence of Cr^{3+} ions inside Cr-doped ZnO nanomaterials has changed the requisite conditions for the formation of precipitation of Cr-doped ZnO nanomaterials under hydrothermal synthesis route in comparison to that of undoped ZnO nanomaterials [36]. These changes in grain morphologies due to the presence of dopant ions inside host nanomaterials have also been reported in our earlier publication [23]. Thus, these changes in morphology with the doping of Cr^{3+} ions in the structure of ZnO signify the successful incorporation of the Cr^{3+} ions inside the wurtzite lattice structure of ZnO nanomaterials. Interestingly, all the nanorods in different micrographs are nearly uniform in size and the particles are not much agglomerated.

3.3. Photoluminescence study

Photoluminescence (PL) spectra of all the hydrothermally prepared Cr^{3+} ions doped ZnO nanomaterials (C3Z4, C5Z4, and C7Z4) have been measured and the corresponding broad PL spectra have been deconvoluted. These deconvoluted PL spectra for all the Cr-doped ZnO nanomaterials have been depicted in Fig. 7(a-c). The schematic diagram of band gap energies of the given PL spectra corresponding to each sample has also been depicted in Fig. 7(d). It is well accepted that the PL emission spectra depend on many factors associated with the resultant nanomaterials such as preparation technique, stoichiometry, selection of dopant, doping percentage and annealing temperature, etc. All these factors are responsible for the desired outcome of PL emission spectra. Depending on the above mentioned factors the grain morphology and various native defect states in form of oxygen vacancy defects (V_o), oxygen interstitial defects (I_o), zinc vacancy defects (V_{Zn}), zinc interstitial defects (I_{Zn}), etc., present inside the structure of Cr-doped ZnO nanomaterials can be modulated and the corresponding PL emission spectra vary accordingly. The PL study of Cr-doped ZnO nanomaterials has been conducted with an excitation wavelength of 325 nm. The PL spectra of all the Cr-doped ZnO nanomaterials (C3Z4, C5Z4, and C7Z4) show a broad UV emission peak centered at 380 nm. In the ultraviolet region, the emission peak of Cr-doped ZnO nanomaterials has been found almost at the similar positions for all the nanomaterials and the emission peak has been developed due to the recombination of free excitons through the exciton-exciton collision process. Also, the emission peak can be appeared in the UV region due to the transition of free excitons present in the energy states close to the conduction band to the energy states close to the valance band and this recombination process is called near-band-edge (NBE) emission [37]. Also, a broad emission peak centered at 442 nm has been observed for C3Z4, C5Z4, and C7Z4 nanomaterials. In the visible region and at 442 nm the blue emission peak has been observed in Fig. 7 due to the presence of electronic transition between the zinc interstitial (I_{Zn}) and the zinc vacancy (V_{Zn}) level present inside the lattice structure of C3Z4, C5Z4, and C7Z4 nanomaterials [38]. It is quite well known that in the process of doping three Zn^{2+} ions are successfully substituted by three Cr^{3+} ions. Also, no peak related to any secondary phase like Cr_2O_3 has been observed in any of the Cr-doped ZnO nanomaterials. Thus, three

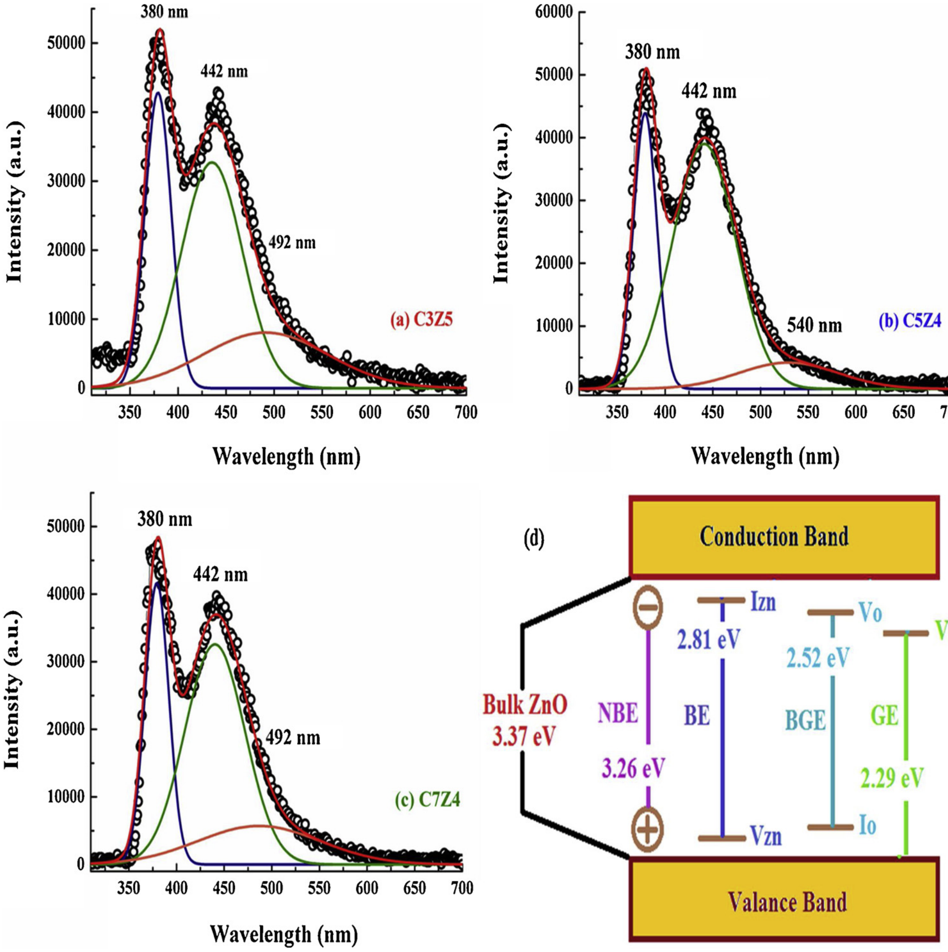

Fig. 7. Deconvoluted Photoluminescence spectra of the samples (a) CZ34, (b) CZ54 and (c) CZ74 and (d) Schematic diagram proposed for different relaxation processes in Cr-doped ZnO nanomaterials.

Zn^{2+} ions are properly replaced by two Cr^{3+} ions inside the wurtzite lattice structure of hexagonal ZnO nanomaterials and due to this substitution Zn vacancies are formed. Also, these substituted Zn^{2+} ions will take the interstitial positions inside the ZnO lattice structure. Thus, these Zn vacancies (V_{Zn}) and Zn interstitials (I_{Zn}) are mainly responsible for the development of the emission peak at 442 nm corresponding to the blue emission for C3Z4, C5Z4, and C7Z4 nanomaterials. Now, at 492 nm the blue-green emission peak has been formed for C3Z4 and C7Z4 nanomaterials. At 492 nm, the blue-green emission peak has been formed due to the surface defects in the ZnO nanomaterials and the corresponding electronic transition between the oxygen vacancy defects (V_o) and oxygen interstitial defects (I_o) [38]. Another peak at 540 nm has been observed for C5Z4 nanomaterial corresponding to the green emission and this peak has been formed due to the presence of surface defects and the corresponding transitions due to oxygen vacancies (V_o) in C5Z4 nanomaterials [39]. In the PL spectrum, the defect states related to the oxygen vacancies (V_o) and oxygen interstitials (I_o) have been developed in the structure of Cr-doped ZnO nanomaterials during the sintering process of Cr-doped ZnO nanomaterial. The observed PL spectra of Cr-doped ZnO nanomaterials in the present study are also consistent with the works published by Kennedy et al. and Sathyaseelan et al. [40,41]. It is also to be noted here that the oxygen vacancy (V_o) concentration present in the Cr-doped ZnO nanomaterials plays the most significant role for the improvement of the ferromagnetism in the Cr-doped ZnO nanomaterials.

3.4. EPR study

The formation of oxygen vacancy defect states in the Cr-doped ZnO nanomaterials has been identified by the room temperature electron paramagnetic resonance (EPR) measurement. In static magnetic measurements, ferromagnetic ordering has been observed in all the Cr-doped ZnO nanomaterials (C3Z4, C5Z4, and C7Z4) and this particular feature of Cr-doped ZnO nanomaterials has motivated us to do further investigation on EPR analysis of these samples. The observed variations of EPR spectra, as a function of the magnetic field of C3Z4, C5Z4, and C7Z4 nanomaterials have been depicted in Fig. 8. Fig. 8(a), (b) and (c) represent the EPR spectra of C3Z4, C5Z4, and C7Z4 nanomaterials, respectively. The EPR spectra of all the Cr-doped ZnO nanomaterials show broad line width and it is quite clear from the given figure that the line width decreases and intensity of EPR spectra increase with the increasing amount of Cr doping concentration in the host ZnO structure. Also, it has been observed in the EPR spectra of all the Cr-doped ZnO nanomaterials that the patterns of the spectra are almost symmetrical Lorentzian in shape. The resonant signal corresponding to an effective value of g-factor of C3Z4, C5Z4, and C7Z4 nanomaterials has been estimated by the equation given below [42]

$$g = \frac{h\gamma}{BH} \tag{5}$$

where H is the static field (gauss or G), γ is the frequency (Hz), B is the Bohr magnetron equal to 9.274×10^{-21} erg/G, and h is Planck's constant equal to 6.626×10^{-27} erg.s/cycle. The values of g-factors of C3Z4, C5Z4, and C7Z4 nanomaterials estimated from the room

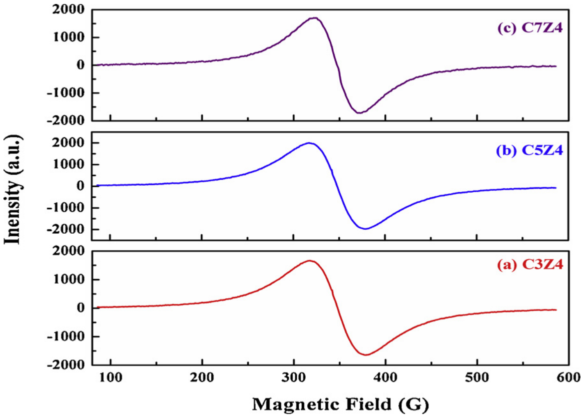

Fig. 8. EPR spectra of the samples (a) CZ34, (b) CZ54 and (c) CZ74.

temperature EPR spectra show enhancement with the increasing doping concentration of Cr ions in the structure of ZnO nanomaterial. The higher value of g-factor of C5Z4 nanomaterial as compared to C3Z4 nanomaterial and the higher value of g-factor of C7Z4 nanomaterial as compared to C5Z4 nanomaterial reveal the improvement of the concentration of paramagnetic centers, i.e., singly ionized oxygen vacancies (V_o^+) with the increasing concentration of Cr^{3+} ions in the structure of host ZnO nanomaterials. But the presence of a considerable concentration of paramagnetic centers in both C3Z4 and C5Z4 nanomaterials cannot be ruled out and the presence of paramagnetic centers or singly ionized oxygen vacancies (V_o^+) in all the samples have been substantiated by the presence of paramagnetic and ferromagnetic behaviors in static magnetic measurement. In the EPR spectra, the presence of a higher concentration of paramagnetic centers in the C7Z4 nanomaterial can also be substantiated by the higher value of EPR intensity. Also, it has been found that the EPR resonant peak of C7Z4 nanomaterial is sharper than that of C3Z4 and C5Z4 nanomaterials. The sharp resonant peak of C7Z4 nanomaterial with a higher value of g-factor as compared to C3Z4 and C5Z4 nanomaterials signify the presence of improved magnetic homogeneity due to the greater uniformity of Cr^{3+} ion distribution inside the structure of host ZnO as well as the presence of a typical exchange coupled Cr^{3+} ion pairs inside ZnO [43]. This exchange coupling between the Cr^{3+} ion pairs plays the most significant role in the development of FM at RT in Cr-doped ZnO nanomaterials. Now, based on the earlier works on EPR spectroscopy of Cr doped-ZnO nanomaterials, one can easily relate the EPR spectra detected in the Cr-doped ZnO nanomaterials to the Cr^{2+} valance state. Thus, it is quite expected that the Cr^{2+} ion in the Cr-doped ZnO will substitute for the Zn^{2+} ion from the lattice site of the ZnO wurtzite structure. However, the values of the g-factor in the present work and the peak-to-peak line width are in contradiction with the reported values of the EPR spectra of Cr^{2+} ions in the ZnO host material. In this direction, Vallin et al. showed that the EPR spectra of Cr^{2+} ion in most of the II-VI compounds have been found with peak-to-peak line widths

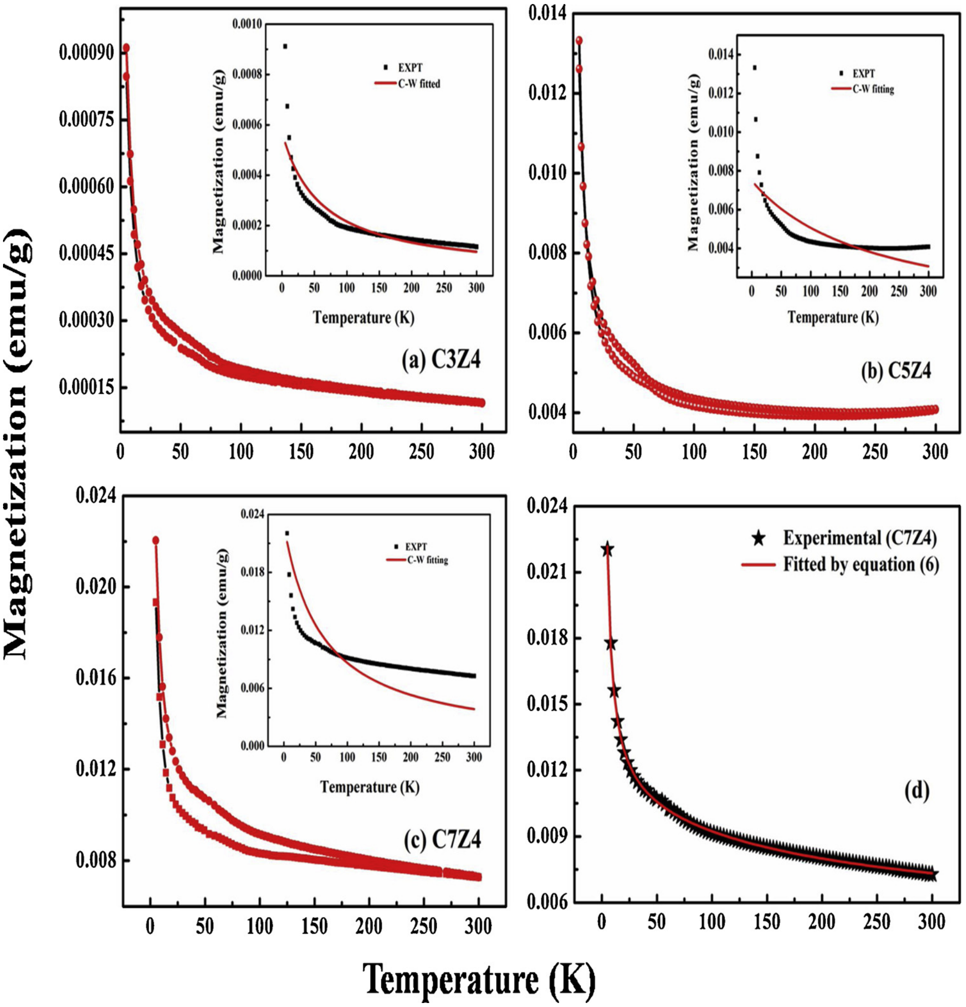

Fig. 9. Temperature variation of zero field cooled and field cooled magnetizations of (a) CZ34, (b) CZ54 and (c) CZ74 with Curie-Weiss fittings in the inset (d) observed magnetization vs. temperature curve of C7Z4 sample and its fitting according to equation 6 in the temperature range of 300 to 5 K.

of 500 G at 20 K [44]. Therefore, the expectation is that at RT, the EPR signal of Cr^{2+} ion will be broader and unable to observe properly in the EPR spectra. Additionally, the study on Cr doped GaAs revealed that the Cr^{3+} valence state is predominant if the chromium concentration significantly exceeds the concentration of shallow donors in the ZnO crystal structure. Thus, from the observed data of EPR spectra of Cr-doped ZnO nanomaterials in the present work, we believe that the EPR signal appears due to the Cr^{3+} ions instead of the Cr^{2+} ions and it can be suggested that Cr^{3+} ions are localized in the octahedral site of the host ZnO lattice structure and correspond not only to the Cr^{3+} ions observed in the doped-ZnO nanomaterials but also to an unpaired electron trapped at the oxygen vacancy site. It is possible that the broad line width of the Cr^{3+} ions overlaps with the resonance line of an unpaired electron trapped at the oxygen vacancy site. Under certain condition, this trapping of an unpaired electron at the oxygen vacancy site plays the most significant role to show ferromagnetic ordering in Cr-doped ZnO nanomaterials under external magnetic field which can be explained on the basis of BMP model.

3.5. Static magnetic study

Zero-field-cooled and field-cooled (ZFC-FC) magnetization curves with the applied magnetic field of 500 Oe has been observed as a function of temperature from 300 K down to 10 K of all the Cr-doped ZnO nanomaterials and the respective curves have been shown in Fig. 9 (a), (b) and (c). In the given Fig. 9, both FC and ZFC curves have been diverging from each other below RT. The observed variation of ZFC-FC magnetization with the decrease of temperature from 300 K down to 10 K is a clear indication of having paramagnetic/antiferromagnetic (PM/AFM) behavior in the Cr-doped ZnO nanomaterials. The bifurcation of FC and ZFC curves at RT signifies the presence of magnetic ordering in the Cr-doped ZnO nanomaterials. Also, it has been observed in the magnetic measurement that the bifurcation between FC and ZFC curves increases with the increasing concentration of Cr^{3+} ions in the structure of host ZnO nanomaterials. The measured value of magnetization recorded at different temperatures are tried to fit in the well-known Curie-Weiss law $\chi = \frac{C}{(T-\theta)}$, where χ= M/H, C is the Curie constant and θ is the Curie temperature and the respective fittings along with the observed data are shown in the inset of Fig. 10 (a), (b) and (c) respectively. The poor fitting established that all three samples have deviated from the paramagnetic phase and we have to analyze the M-T data in different approaches. Very recently, few research works have been published on the experimental and theoretical study of transition metal (TM) doped ZnO nanomaterials, where the researchers have shown the simultaneous existence of both ferromagnetic orderings with an antiferromagnetic contribution [45,46]. This has motivated us to do further investigation of the magnetic property study of Cr-doped ZnO nanomaterials. In the present work, we have tried to fit the FC *M(T)* data by the standard Block spin-wave model [$M(T) = M(0)(1 - BT^{\frac{3}{2}})$], where *M(0)* is the zero temperature magnetization associated with the Curie-Weiss model [$M(T) = \frac{CH}{(T-\theta)}$] [47]. The fitting is not adequate unless we are adding an extra term $\frac{\mathrm{CH}}{(\mathrm{T})}$ in the equation of *M(T)*. Thus, in the present case, the *M(T)* data associated with FC magnetization can be written as

$$M(T) = \frac{C_1 H}{(T - \theta)} + \frac{C_2 H}{T} + M(0)\left(1 - BT^{\frac{3}{2}}\right) \tag{6}$$

Here

$$B = 2.612\frac{Sg\mu_B}{M(0)}(\frac{K_B}{4\pi D})^{\frac{3}{2}} \tag{7}$$

And

$$D = 2a^2JS \tag{8}$$

Where B is a parameter inversely proportional to spin-wave stiffness, J is the exchange energy and other symbols have their usual meaning. An important observation from the equation (4) is that only one subset (the second one) of the spins are not affected by magnetic interactions. The extracted values of C_1 from the fitting data for the samples C3Z4, C5Z4, and C7Z4 are 4.378 × 10^{-5}, 1.01 × 10^{-4} and 2.03 × 10^{-3} emuK/gOe, respectively, whereas those for C_2 are 6.56 × 10^{-6}, 7.16 × 10^{-5} and 3.0 × 10^{-3} emuK/gOe respectively. The rise in the value of C_1 and C_2 indicates a progressive increment of the AFM or PM contribution (since both are direct functions of N) with an increase in Cr doping concentration. Therefore, good fitting [one respective fitting is shown in Fig. 9(d)] confirms that the distribution of Cr^{3+} ions in the ZnO host lattice can produce three distinctive effects on the Cr-doped ZnO nanomaterials and they are (i) antiferromagnetically coupled Cr^{3+} ions with at least one neighboring Cr^{3+} ion, (ii) isolated Cr^{3+} spin, which is completely free and it follows simple Curie behavior (iii) clustered Cr^{3+} spins having positive exchange integral. These features are quite expected for all the Cr-doped ZnO nanomaterials because the distribution of the Cr^{3+} ions inside the structure of ZnO is random in nature. As a result, the formation of isolated, pairs and very small clusters of dopant have been observed below the percolation threshold. In a 3D spin-wave model, $M(0)$ is proportional to the number of net spin corresponding to the ferromagnetic contribution. The values of $M(0)$ as extracted from the fitting of C3Z4, C5Z4, and C7Z4 are 5.0 × 10^{-5}, 3.63 × 10^{-3} and 4.84 × 10^{-3} emu/g respectively. Therefore the higher $M(0)$ value with Cr dopant concentration implies that more and more Cr^{3+} ions are ferromagnetically coupled in ZnO host lattice with the increasing amount of Cr^{3+} ions. The contributions of the aforesaid Cr^{3+} spin are given in Table 2, and it indicates that the dominant spin-spin interactions are ferromagnetic in nature at RT for C5Z4 and C7Z4 nanomaterials. This observation is in direct contradiction with other published results [45,48]. The net FM moment, as well as PM/AFM moment at RT, increased significantly with increasing doping concentration of Cr^{3+} ions which implies that the doping of Cr^{3+} ions plays a significant role in magnetization. The FM contributions in the entire magnetization for C3Z4, C5Z4, and C7Z4 at RT are 28.8%, 89.11%, and 57.29% respectively. It is evident from Table 2 that FM contributions in the entire magnetization for all the samples decrease with the lowering of temperature. The AFM and PM component increases abruptly below 50 K whereas the FM component remains nearly constant there. Thus the abrupt change in M vs T curve at low temperature is due to uncoupled or antiferromagnetically coupled spins which is now quantitatively established in the present work. This is the most common trend found in almost all DMS materials. Therefore, for the low doping system, most of the dopant spins are isolated or antiferromagnetically coupled. It is to be noted that though the net magnetization is higher in C7Z4 the total contribution of the FM moment in net magnetization is lower as compared to C5Z4. In EPR analysis, we have already discussed that C7Z4 nanomaterial consists of more paramagnetic centers than C5Z4. Though the total moment of C7Z4 is higher in comparison to C5Z4 the overall contribution of the total FM moment of C7Z4 is smaller than C5Z4. It is to be noted here that for this type of system where Cr^{3+} ions are distributed randomly in host lattice, the determination of the magnetic moment (S) and exchange integral (J) are almost impossible. The equation (4) fits properly with the experimental data and the value of B has been extracted from the fitting only. One corresponding fitting for M vs T curve for C7Z4 has been shown in Fig. 9(d). The extracted values of B (from fitting) for C3Z4, C5Z4, and C7Z4 are 9.1 × 10^{-5}, 7.5 × 10^{-5} and 6.0 × 10^{-5} $K^{-3/2}$ respectively. The decrease of B with Cr^{3+} ion doping indicates that the system becomes more disordered with the increase of Cr doping concentration [49]. This fact also is in agreement with the findings obtained from Rietveld, PL and EPR analysis.

The M vs H data for all the samples at various temperatures (300, 100, 50 and 10 K) using the SQUID magnetometer in the applied magnetic field range from 0-50000 Oe has been depicted in Fig. 10. Fig. 10 shows clear hysteresis behavior of all the samples but the

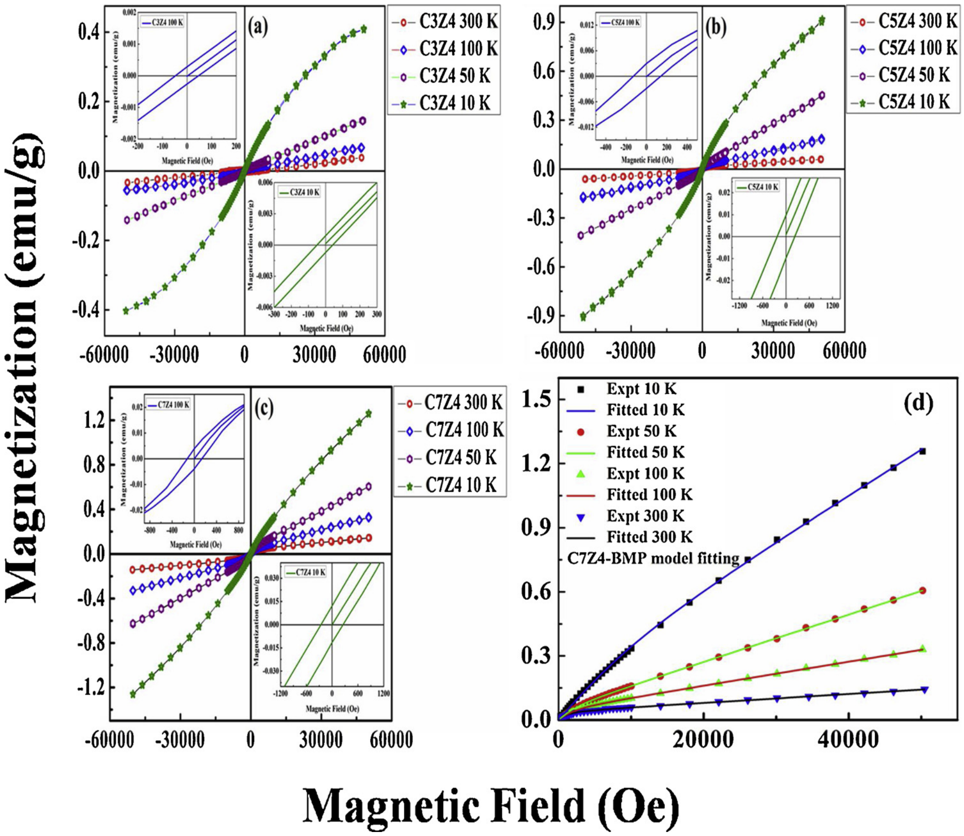

Fig. 10. Magnetic hysteresis (M–H) loops observed at 300, 100, 50 and 10 K temperature of the sample (a) CZ34, (b) CZ54 and (c) CZ74 and (d) initial magnetization vs. field curve of C7Z4 sample at 300, 100, 50 and 10 K along with the fitted data using the BMP model. Also, the magnified images of 10 K M-H loops of each nanomaterial are displayed in the inset of the respective M-H loops.

observed hysteresis loops are not saturated even at 50000 Oe which indicates the mixed magnetic phase within the sample as predicted by the M-T curve. Some representative M-H loops of C3Z4, C5Z4, and C7Z4 nanomaterials at 10 and 100 K have been magnified at the low magnetic field and they have been displayed in the inset of the respective M-H loops of Fig. 10. The maximum magnetizations at 300 K for are 0.038, 0.055, 0.148 emu/g respectively which reaches to 0.40, 0.90 and 1.26 emu/g as temperature decreases to 10 K with the corresponding coercive fields and remanent magnetizations of C3Z4, C5Z4, and C7Z4 nanomaterials at 100 and 10 K are 45, 126, 137 Oe and 0.00030, 0.0029, 0.0041 emu/g and 49, 230, 261 Oe and 0.00088, 0.0093, 0.0121 emu/g respectively. In the preceding analysis, we have already shown that the contribution to the magnetization of all three magnetic phases (FM, PM, and AFM) increases with a decrease in temperature. It is well known that RTFM in DMS is often linked with the extrinsic origins, such as unintentional sample contamination and metal/secondary phase clustering/aggregation. In principle, as the Cr doping concentration increases, different antiferromagnetic phases may appear in the form of $ZnCr_2O_4$ (T_N ˜ 11 K), Cr metal clusters, Cr_2O_3 and Cr_3O_4 inside the doped-ZnO nanomaterials. However, none of the phases can be detected in Rietveld analysis or in any characteristic peaks of PL spectra. The antiferromagnetic character is also not evident in the M-T curve. Even, if these phases are present in small quantities, none of them can produce ferromagnetism, except the CrO_2 phase (T_c ˜ 386 K). However, CrO_2 is unstable and decomposes under normal conditions. Therefore, RTFM in our Cr-doped sample cannot be explained by the secondary phases. In order to get the idea about the origin of RTFM in the Cr-doped ZnO nanomaterials, a variety of different theories have been proposed. The Rietveld, EPR analyses and spin wave stiffness of the samples have already indicated the enhancement of structural defects due to the enhancement of doping. We believe that the strong correlation between ferromagnetism and the

Table 2
Various magnetic parameters of Cr-doped ZnO nanomaterials extracted from static magnetic data.

Sample Name	Temperature (K)	Free spin (emu/g)	Antiferro (emu/g)	Ferromagnetic (emu/g)	FM (%)
C3Z4	300	1.09×10^{-5}	5.48×10^{-5}	2.66×10^{-5}	28.8
	200	1.64×10^{-5}	7.32×10^{-5}	3.72×10^{-5}	29.3
	100	3.20×10^{-5}	1.10×10^{-4}	4.50×10^{-5}	24.6
	50	6.56×10^{-5}	1.47×10^{-4}	4.84×10^{-5}	18.5
	10	3.28×10^{-4}	2.00×10^{-4}	4.98×10^{-5}	8.6
C5Z4	300	1.28×10^{-4}	1.56×10^{-4}	2.21×10^{-3}	89.1
	200	1.92×10^{-4}	2.26×10^{-4}	2.85×10^{-3}	87.2
	100	3.85×10^{-4}	4.08×10^{-4}	3.35×10^{-3}	81.1
	50	6.83×10^{-4}	7.70×10^{-4}	3.53×10^{-3}	70.8
	10	3.85×10^{-3}	1.47×10^{-3}	3.62×10^{-3}	40.4
C7Z4	300	1.90×10^{-4}	2.27×10^{-3}	3.30×10^{-3}	57.3
	200	2.90×10^{-4}	2.83×10^{-3}	4.01×10^{-3}	56.5
	100	5.90×10^{-4}	3.77×10^{-3}	4.50×10^{-3}	50.8
	50	1.10×10^{-3}	4.50×10^{-3}	4.73×10^{-3}	45.6
	10	5.90×10^{-3}	5.30×10^{-3}	4.83×10^{-3}	30.1

Table 3
Result extracted from the BMP fitting of Cr-doped ZnO nanomaterials.

Sample Name	Temperature (K)	N (Cluster/g)	Effective moment (m/cluster)
C3Z4	300	——	——
	100	5.3×10^{13}	5.63×10^{-17}
	50	6.5×10^{14}	5.00×10^{-18}
	10	4.8×10^{17}	2.88×10^{-19}
C5Z4	300	1.6×10^{14}	9.18×10^{-17}
	100	7.8×10^{14}	2.89×10^{-17}
	50	2.0×10^{15}	1.20×10^{-17}
	10	1.0×10^{18}	2.89×10^{-19}
C7Z4	300	5.8×10^{14}	6.78×10^{-17}
	100	3.6×10^{15}	1.41×10^{-17}
	50	8.5×10^{15}	6.51×10^{-18}
	10	2.0×10^{18}	1.93×10^{-19}

structural defect may set the magnetic ordering in the present samples. The preceding analysis also shows that the size of the magnetically active clusters can produce magnetic properties. In order to understand the reason behind the magnetic behavior in these Cr-doped ZnO nanomaterials, we have further analyzed magnetization (M) versus magnetic field (H) data in a combination of two magnetic components i.e. FM component which is saturated at low field and a linear component due to PM. Considering this we tried to fit the isothermal curve that can be written as

$$M = Nm_s \left[coth\left({Hm_{eff}}\Big/{T\, K_B} \right) - {T\, K_B}\Big/{Hm_{eff}} \right] + \chi_m H \tag{9}$$

Where M is the total magnetization, N is the number of magnetic spins/cluster (paramagnet) m_s is the moment per spin, H is the applied field, T is the temperature and K_B is Boltzmann's constant [50,51]. Table 3 enumerates the fitting parameters obtained from the combined equations and one corresponding fitting for C7Z4 is shown in Fig. 10(d). The RT isothermal curve for C3Z4 is not fitted by the BMP model due to feeble FM moment as compared to PM/AFM spin. Table 3 clearly shows that the number of ferromagnetically active clusters increases with the decrease in temperature and also increases with Cr doping concentration. This, in turn, increases the net FM moment with the increase of Cr doping concentration. This has already been shown in Table 2. The ferromagnetically active clusters are formed due to the exchange interaction between oxygen vacancy (V_o) and dopant ions [52]. This interaction helps to align few of the dopant spins around the oxygen vacancy (V_o) and forms localized ferromagnetically active clusters. They are phrased as "polaron clusters" in literature [53]. Therefore, there is a strong relationship between structural disorder and magnetization. Within this framework, long-range FM ordering could be triggered by either direct overlaps between BMPs or indirect BMP-magnetic impurity-BMP interactions [54]. The highest number of FM spin clusters obtained from the fitting is nearly 10^{19} which is still below the percolation limit. Therefore, the latter case is apparently more applicable as the samples are highly insulating (as reported in our earlier work) and it consists of sufficient magnetic impurities. The present analysis reveals that the oxygen vacancies alone are not adequate to establish robust ferromagnetism as the Cr doping is dispensable.

4. Conclusion

In summary, we report here the influence of Cr doping concentration on the structural and magnetic response of host ZnO nanomaterials prepared by cost effective hydrothermal synthesis route. XRD analysis and FESEM study of all the ZnO nanomaterials reveal the preferential growth of the rods like ZnO nanomaterials along '*a*' axis or (100) Bragg plane. This preferential growth is the consequence of the hydrothermal synthesis technique on the growth technique of the ZnO nanomaterials. The XRD analysis also shows the enhancement of oxygen vacancy defects with the increasing doping concentration of Cr^{3+} ions in the structure of host ZnO nanomaterials. This oxygen vacancy defect plays the most significant role to enhance the ferromagnetic ordering in the Cr-doped ZnO nanomaterials. The presence of both paramagnetic and ferromagnetic contributions in all the Cr-doped ZnO nanomaterials and their systematic enhancement with the increasing Cr doping concentration is substantiated by the observation of EPR spectra and static magnetic measurement. The paramagnetic centers or singly ionized oxygen vacancies are found to present in all the Cr-doped ZnO samples under EPR study, which on the other hand increases and distributed more uniformly with the increasing Cr ion concentration. The observed magnetic hysteresis loops under static magnetic measurement are not saturated up to 50000 Oe external magnetic field which indicates the presence of a mixed phase of AFM and PM phases collectively with the FM phase. The enhancement in magnetization is due to the additive effects of grain boundary defect and indirect interaction between oxygen vacancies and dopant ions which has been explained by the BMP model.

References

[1] K. Zhang, T. Holloway, M. Bahoura, A.K. Pradhan, R. Prabakaran, J. Pradhan, S. Smith, J.C. Hall, G.T. Ramesh, D.R. Sahu, J.L. Huang, Proc. SPIE 7291 (2009) 729104.
[2] C. Chang, F. Kimura, T. Kimura, H. Wada, Mater. Lett. 59 (2005) 1037.
[3] S. Li, H. Song, H. Yu, S. Lu, X. Bai, G. Pan, Y. Lei, L. Fan, T. Wang, J. Lumin. 122 (2007) 876.
[4] M. Maekawa, H. Abe, A. Miyashita, S. Sakai, S. Yamamoto, A. Kawasuso, Appl. Phys. Lett. 110 (2018) 172402.
[5] M.Z. Shoushtari, A. Poormoghadam, M. Farbod, Material Res. Bulletin 88 (2017) 315.
[6] B. Qi, S. Ólafsson, H.P. Gíslason, Progress in Materials Science 90 (2017) 45.
[7] S.A. Wolf, D.D. Awschalom, R.A. Buhrman, J.M. Daughton, S.V. Molnar, M.L. Roukes, A.Y. Chtchelkanova, D.M. Treger, Science 294 (2001) 1488.
[8] Y. Matsumoto, M. Murakami, T. Shono, T. Hasegawa, T. Fukumura, M. Kawasaki, P. Ahmet, T. Chikyow, S.Y. Koshihara, H. Koinuma, Science 291 (2001) 854.
[9] N. Dogan, A. Bingolbali, L. Arda, J. Magn. Magn. Mater. 373 (2015) 226.
[10] S. Zhou, K. Potzger, Q. Xu, 83 (2009) S13.
[11] A.A. Dakhel, M. El-Hilo, J. Appl. Phys. 107 (2010) 123905.
[12] J. Anghel, A. Thurber, D.A. Tenne, C.B. Hanna, A. Punnoose, J. Appl. Phys. 107 (2010) 314.
[13] K. Sato, H.K. Yoshida, Jpn. J. Appl. Phys. 39 (2000) L555.
[14] B.Q. Wang, J. Iqbal, X.D. Shan, G.W. Huang, H.G. Fu, R.H. Yu, D.P. Yu, Mater. Chem. Phys. 113 (2009) 103.
[15] A. Tiwari, V.M. Bhosle, S. Ramachandran, N. Sudhakar, J. Narayan, S. Budak, A. Gupta, Appl. Phys. Lett. 88 (2006) 142511.
[16] B. Wang, J. Iqbal, X. Shan, G. Huang, H. Fu, R. Yu, D. Yu, Mater. Chem. Phys. 113 (2009) 103.
[17] S.B. Singh, et al., Nanoscale 6 (2014) 9166.
[18] R.N. Aljawfi, F. Rahman, D.K. Shukla, Mater. Lett. 99 (2013) 18.
[19] T. Dietl, Nat. Mater. 9 (2010) 965.
[20] H. Chou, C.P. Lin, J.C.A. Huang, Hsu HS Phys Rev B 77 (2008) 245210.
[21] A.E. Kandjani, M.F. Tabriz, O.M. Moradi, H.R. Mehr, S.A. Kandjani, M.R. Vaezi, J. Alloys Compd. 509 (2011) 7854.
[22] N. Al-Hardan, M.J. Abdullah, A.A. Aziz, Appl. Surf. Sci. 257 (2011) 8993.
[23] T. Debnath, P. Saha, N. Patra, S. Das, S. Sutradhar, J. Appl. Phys. 123 (2018) 194101.
[24] S. Das, S. Das, S. Sutradhar, Ceramics International 43 (2017) 6932–6941.
[25] S. Das, A. Bandyopadhyay, S. Das, D. Das, S. Sutradhar, J Alloys Compd. 731 (2018) 591.
[26] S. Das, A. Bandyopadhyay, P. Saha, S. Das, S. Sutradhar, J Alloys Compd. 749 (2018) 1.
[27] Y.M. Hu, S.S. Li, C.H. Chia, Appl. Phys. Lett. 98 (2011) 052503.
[28] D. Polsongkrama, P. Chamninok, S. Pukird, L. Chowb, O. Lupan, G. Chai, H. Khallaf, S. Park, A. Schulte, Physica B 403 (2008) 3713.
[29] A. Bandyopadhyay, A.K. Deb, K. Mukhopadhyay, S.K. Roy, P.K. Chakrabarti, J. Mater. Sci. 47 (2012) 2284.
[30] L. Lutterotti, S. Gialanella, Acta Mater. 46 (1998) 101.
[31] S. Kumar, S. Basu, B. Rana, A. Barman, S. Chatterjee, S.N. Jha, D. Bhattacharyya, N.K. Sahoo, A.K. Ghosh, J. Mater. Chem. C 2 (2014) 481.
[32] Ü. Özgür, Y.I. Alivov, C. Liu, A. Teke, M.A. Reshchikov, S. Doğan, V. Avrutin, S.J. Cho, H. Morkoçd, J. Appl. Phys. 98 (2005) 041301.
[33] J.H. Park, Y.J. Lee, J.S. Bae, B.S. Kim, Y.C. Cho, C. Moriyoshi, Y. Kuroiwa, S. Lee, S.Y. Jeong, Nanoscale Res. Lett. 10 (2015) 186.
[34] K.U. Haq, M. Irfan, Md. Masood, M. Saleem, T. Iqbal, I. Ahmad, M.A. Khan, M. Zaffar, M. Irfan, J. semicond. 39 (2018) 043001.
[35] X. Wang, R. Zheng, Z. Liu, Z. Liu, H.P. Ho, J. Xu, S.P. Ringe, Nanotechnolgy 19 (2008) 455702.
[36] T. Debnath, P. Saha, N. Patra, S. Das, S. Sutradhar, J. Appl. Phys. 123 (2018) 194101.
[37] J. Kennedy, P.P. Murmu, E. Manikandan, S.Y. Lee, J. Alloys Compd. 616 (2014)

614.
[38] X. Wei, B. Man, J. Appl. Phys. 45 (2006) 8586.
[39] Y. Gong, Nanoscale Res. Lett. 2 (2007) 297.
[40] J. Kennedy, D.A. Carder, A. Markwitz, R.J. Reeves, J. Appl. Phys. 107 (2010) 103518.
[41] B. Sathyaseelan, E. Manikandan, K. Sivakumar, J. Kennedy, M. Maaza, J. Alloys Compd. 651 (2015) 479.
[42] A. Kar, S. Kundu, A. Patra, J. Phys. Chem. C 115 (2011) 118.
[43] S.S. Sartiman, N.F. Djaja, R. Saleh, Materials Sciences and Applications 4 (2013) 528.
[44] J.T. Vallin, G.D. Watkins, Phys. Rev. B 9 (5) (1974) 2051.
[45] Z.L. Lu, W. Miao, W.Q. Zoua, M.X. Xu, F.M. Zhanga, J. Alloys Compd. 494 (2010) 392.
[46] J. Qi, D. Gao, J. Liu, W. Yang, Q. Wang, J. Zhou, Y. Yang, J. Liu, Appl. Phys. A 100 (2010) 79.
[47] S.J. Potashnik, K.C. Ku, R. Mahendiran, S.H. Chun, R.F. Wang, N. Samarth, P. Schiffer, Phys. Rev. B 66 (2002) 012408.
[48] M. Kobayashi, Y. Ishida, J.I. Hwang, Y. Osafune, A. Fujimori, Y. Takeda, T. Okane, K. Kobayashi, H. Saeki, T. Kawai, H. Tabata, Phys. Rev. B 81 (2010) 075204.
[49] J.J. Beltrán, C.A. Barrero, A. Punnoose, Journal of Physical Chemistry C 118 (2014) 13203.
[50] A. Bandyopadhyay, S. Sutradhar, B.J. Sarkar, A.K. Deb, P.K. Chakrabarti, Appl. Phys. Lett. 100 (2012) 252411.
[51] A. Chanda, S. Gupta, M. Vasundhara, S.R. Joshi, G.R. Mutt, J. Singh, RSC Adv. 7 (2017) 50527.
[52] N.W. Gray, A. Tiwari, J. Appl. Phys. 110 (2011) 033903.
[53] J.M.D. Coey, M. Venkatesan, C.B. Fitzgerald, Nat. Mater. 4 (2005) 173.
[54] C.G. Jin, Y. Yang, Z.F. Wu, L.J. Zhuge, Q. Han, X.M. Wu, Y.Y. Li, Z.C. Fenge, J. Mater. Chem. C 2 (2014) 2992.